UNIVERSITÀ
DEGLI STUDI
DI BRESCIA

DOTTORATO DI RICERCA IN

Ingegneria Meccanica e Industriale

IIND-03/C Metallurgia

CICLO XXXVI

Characterization of Nitinol alloy produced by laser powder bed fusion for biomedical applications

Dottoranda:

Maria Beatrice Abrami

Relatori:

Prof.ssa Annalisa Pola

Prof.ssa Marialaura Tocci

Tutor:

Prof. Dermot Brabazon

Coordinatore:

Prof. Pietro Poesio

ABSTRACT

Negli ultimi anni, le tecniche di manifattura additiva hanno visto un rapido sviluppo e si sono progressivamente inserite in diversi ambiti industriali per la produzione di componenti con geometrie complesse, che difficilmente sarebbero realizzabili tramite le convenzionali tecniche di produzione sottrattive. In particolare, questi processi hanno suscitato un notevole interesse nel campo biomedicale grazie alla possibilità di produrre impianti personalizzati sulla base delle necessità del paziente.

Tra i materiali di interesse in questo settore vi è il Nitinol (NiTi), una lega quasi-equiatomica di nichel e titanio che costituisce il materiale metallico a memoria di forma più diffuso. Attualmente, il NiTi prodotto tramite tecniche convenzionali è largamente utilizzato per la fabbricazione di componenti biomedicali, in particolare per dispositivi endovascolari, grazie all'elevata biocompatibilità e resistenza a corrosione unite alle sue proprietà peculiari di memoria di forma e superelasticità. La fabbricazione additiva di dispositivi biomedicali in NiTi è molto promettente grazie ai benefici che offre. Tuttavia, la sua realizzazione è ancora ostacolata dalla complessa natura di tali processi e dalla mancanza di una caratterizzazione esaustiva delle proprietà del materiale così prodotto.

Il NiTi è infatti un materiale le cui proprietà sono molto sensibili a svariati fattori, quali la composizione chimica o le lavorazioni meccaniche e i trattamenti termici subiti, che sono comunemente effettuati per migliorare le proprietà funzionali della lega. Di conseguenza, ogni step di produzione, nonché i parametri coinvolti, ha un impatto significativo sulle caratteristiche finali del componente. Ciò richiede sforzi considerevoli e studi approfonditi nello sviluppo di nuovi iter di produzione. In particolare, la messa a punto di trattamenti termici per il raggiungimento delle proprietà desiderate è uno step essenziale e delicato, che richiede quindi di essere esaminato caso per caso. In questo contesto, il presente lavoro ha l'obiettivo di caratterizzare l'effetto di diversi trattamenti termici su leghe NiTi prodotte tramite fusione laser a letto di polvere, al fine di migliorarne le proprietà attraverso modifiche microstrutturali.

Le prime due sezioni del lavoro introducono teoricamente al processo considerato e al NiTi, riferendosi principalmente alla descrizione delle sue proprietà funzionali (memoria di forma e superelasticità), caratteristiche microstrutturali e metodi di produzione.

Le successive due sezioni del lavoro riguardano l'attività sperimentale svolta.

Nella terza sezione è stata analizzata l'influenza di trattamenti termici di invecchiamento diretto sulle proprietà superelastiche del NiTi, attraverso prove di compressione cicliche condotte a varie temperature. Ad oggi, l'invecchiamento diretto dopo fusione laser a letto di polvere è una pratica ancora poco esplorata per il NiTi. Tuttavia, la sua implementazione contribuirebbe a rendere l'iter di produzione tramite manifattura additiva più attrattivo a causa del risparmio energetico e di costi dovuti all'assenza della fase di solubilizzazione. Le molteplici prove effettuate hanno consentito di ricavare una mappa temperatura-sforzo di utilizzo del materiale, caratterizzandone esaustivamente il comportamento. I campioni sottoposti agli innovativi trattamenti di invecchiamento diretto proposti sono stati inoltre analizzati tramite microscopia elettronica a trasmissione.

La quarta sezione esamina l'effetto dei trattamenti termici sulla modifica delle temperature di trasformazione, con l'obiettivo di ripristinare una microstruttura adatta per l'ottenimento della superelasticità a seguito dell'evaporazione del nichel durante il processo. Una delle principali problematiche che caratterizza la produzione di NiTi tramite manifattura additiva è infatti l'evaporazione del nichel, come risultato delle elevate temperature raggiunte a causa dell'azione del laser. Ciò comporta numerose complicazioni sia nella gestione del processo che nel controllo delle proprietà del componente, le quali possono differire in modo considerevole anche solo con una piccola variazione del contenuto di nichel.

CONTENTS

In recent years, additive manufacturing techniques have experienced rapid development and have progressively integrated into various industrial sectors to produce components with complex geometries, difficult to realize through the conventional subtractive manufacturing techniques. In particular, these processes have garnered significant interest in the biomedical field due to the possibility to produce customized implants based on patient needs.

In this sector, one of the materials of interest is Nitinol (NiTi), a near-equiatomic alloy of nickel and titanium that constitutes the most widespread shape memory metallic material. Currently, conventionally produced NiTi is widely used for fabricating biomedical components, especially endovascular devices, owing to its high biocompatibility and corrosion resistance combined to its unique shape memory and superelastic properties. Additive manufacturing of NiTi biomedical devices is very promising thanks to the advantages involved, however, its realization is still hindered by the complex nature of such processes and the lack of an exhaustive characterization of the properties of the material thus produced.

NiTi is a material whose properties are highly sensitive to various factors, such as chemical composition, mechanical processing, and heat treatments, which are commonly performed to enhance the functional properties of the alloy. Consequently, each production step, together with the parameters involved, significantly impacts on the final features of the component. This necessitates considerable efforts and in-depth studies in developing new production processes. In particular, the tuning of heat treatments to achieve the desired properties is an essential and sensitive step, requiring a case-by-case examination. In this context, the present work aims at characterizing the effects of different heat treatments on NiTi alloys produced through laser powder bed fusion (L-PBF), with the objective to enhance their properties through microstructural modifications.

The first two sections of this work provide theoretical insights on L-PBF and NiTi, mainly focusing on the description of its functional properties (shape memory and superelasticity), microstructural characteristics, and production methods.

The subsequent two sections present the experimental activities conducted.

In the third section, the influence of direct aging heat treatments on the superelastic properties of NiTi was analyzed through cyclic compression tests conducted at various

temperatures. To date, direct aging after L-PBF is still an unexplored practice for NiTi. However, its implementation would contribute to make the production through additive manufacturing more attractive due to the notable savings of energy and cost resulting from the absence of the solution treatment phase. The multiple tests conducted allowed the obtainment of a temperature-stress diagram for the use of the alloy, exhaustively characterizing its behavior. In addition, the samples subjected to the innovative direct aging treatments proposed were analyzed through transmission electron microscopy.

The fourth section addresses the effects of heat treatments on the modification of the transformation temperatures, aiming at restoring a microstructure suitable for superelasticity after nickel evaporation during the process. One of the main challenges in producing NiTi through additive manufacturing is in fact the nickel evaporation, resulting from the high temperatures reached due to the laser action. This leads to numerous complications in managing the process and controlling the component properties, which can significantly differ even with a small variation in the nickel content.

INDEX

LIST OF FIGURES

page

LIST OF TABLES

SECTION 1.

LASER POWDER BED FUSION

1.1 ADDITIVE MANUFACTURING

According to the ASTM F2792 "Standard Terminology for Additive Manufacturing Technologies", additive manufacturing (AM) is:

> *"A process of joining materials to make objects from 3D model data, usually layer upon layer, as opposed to subtractive manufacturing methodologies." [1]*

AM technologies build up a three-dimensional object from a CAD or digital 3D models by using metals, polymers, ceramic composites, or biological materials [2]. The main difference with the traditional manufacturing process (cutting, forming, casting, etc.) is that shaping takes place by adding material layer by layer until the part is complete. On the contrary, the traditional processes are subtractive, meaning that shaping from the raw material to the final component occurs by removing material from a larger piece.

AM was developed in the 1980s primarily for prototype parts and then evolved rapidly up to recent years, where it has been used to build end-use components with high mechanical properties. The unique nature of these technologies and the deriving advantages are responsible for their success and constant expansion. Compared to the conventional methods, AM allows a significant reduction of the material waste, as well as higher production efficiency and higher process sustainability. Furthermore, it is possible to manufacture geometrically complex components that would be difficult or impossible to manufacture otherwise. This results in almost total freedom in the design, as well as lower costs in the post-processing. Lastly, AM technologies provide a quick time-to-market for the production of customized parts.

These qualities make AM of considerable interest in the biomedical, automotive, aerospace and military fields but its expansion is expected in other numerous industrial sectors.

Concerning metallic materials, there are several AM techniques that differ according to the state of aggregation of the feedstock material and to the source of energy used for the fusion. The most prevalent processes to manufacture alloys are laser powder bed fusion (L-PBF), electron beam powder bed fusion (EB-PBF), directed energy deposition (DED) and binder jetting.

1.2 LASER POWDER BED FUSION

Laser powder bed fusion (L-PBF), also known as selective laser melting (SLM), constitutes the most common, evolved and successful AM process for metallic materials [3]. A wide range of engineering alloys can be manufactured through this technique, such as steels, aluminum, titanium, cobalt-chrome and nickel alloys. A schematic representation of L-PBF is displayed in Fig. 1.1.

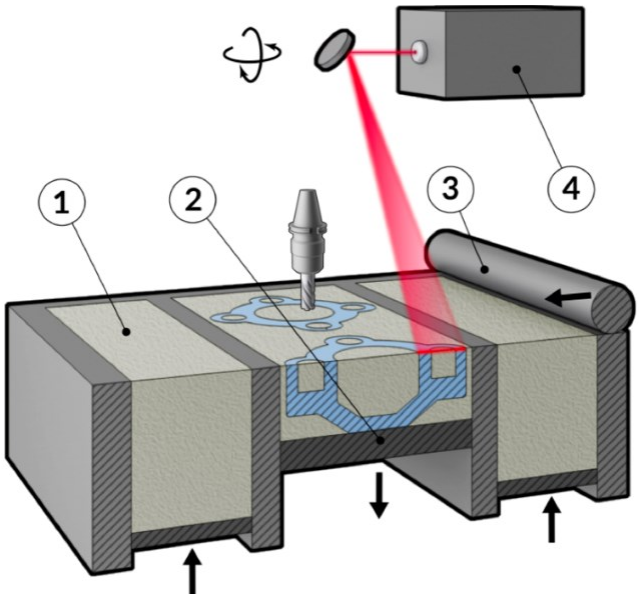

Fig. 1.1. L-PBF process [4].

A powder bed located on a building platform (2, Fig. 1.1) is hit by a laser beam (4), which is used to melt the powder bed just in selected locations. By melting the current layer, also a partial melting of the previous layer takes place, allowing the full bonding between consecutive layers, as displayed in Fig. 1.2. Once the laser finishes its scanning on the first layer, the first cross section of the component is completed, and the building platform lowers by a defined layer thickness. Then, new powder is spread from the powder reservoir (1) over the building platform using a roller or a blade (3). The melting of successive layers repeats until the completion of the component. During the process, argon or nitrogen gas saturates the building chamber to prevent oxidation and to facilitate the removal of condensate created during the melting process.

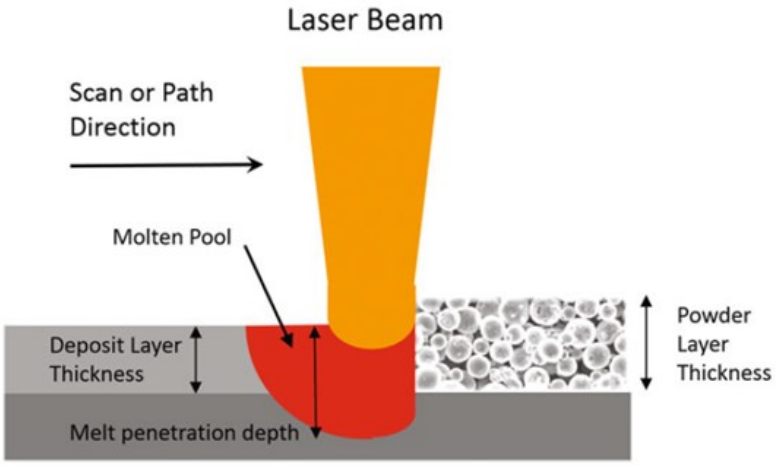

Fig. 1.2. Schematization of the scanning of the laser showing the melt penetration depth up to the previous layer [3].

The evolution of L-PBF over the years allowed the building of fully dense and near net-shape metal components directly from digital 3D models, sometimes without post-processing [3, 5]. Among the others, this technology allows higher manufacturing reliability and lower processing time, as well as better quality, due to the finer microstructures and the better surface finishing obtainable [5, 6]. Furthermore, mechanical properties of metallic components fabricated through L-PBF are nearest to those of parts manufactured through tradition processes. Similarly to other AM methods, L-PBF offers freedom of design, high precision and the possibility of customization, as well as the reduction of waste.

The main limitations of L-PBF are associated with the complexity of the process, due to the wide number of parameters involved and the related management complexity. The process parameters are responsible for the melting of powders and for the quality of the bonding between the adjacent layers, which determines the density and overall quality of the final component. Furthermore, they strongly affect the presence of the typical process defects. The control of the process parameters is therefore crucial for reaching the full potential of L-PBF. As the other AM processes, L-PBF parts usually require post-processing to achieve the desired surface finishing, due to the partially fused powder present on the as-built surfaces. Another limitation of this technique concerns the volume of the building chamber, which makes the production of large parts limited. In addition, L-PBF is best suited for low/medium production volumes, since high-volume production is usually not cost-effective compared to other manufacturing methods [7, 8].

1.2.1 Solidification theory and microstructure

L-PBF is characterized by cooling rates of about 10^6 K/S, which is significantly higher than those of conventional processes, e.g. about 10-10^2 K/s for the casting processes [9]. This, together with the high thermal gradients achieved (10^7 K/m), involves non-equilibrium solidification and consequently significant changes in the macro-features and micro-features of the component compared to the traditional methods. High solidification rates can in fact generate highly refined microstructures, suppress solid-state diffusion and produce non-equilibrium or meta-stable phases [3].

The structure resulting from L-PBF is anisotropic and characterized by the overlap of successive layers. Peculiar features resulting from L-PBF are illustrated in Fig. 1.3: melt pools along the building direction (z) because of the progressive melting of small volumes of powder, while the scanning plane (xy) is characterized by scan tracks following the laser path. The typical semi-circular shape of melt pools derives from the Gaussian distribution of the laser energy. These patterns constitute the typical macro-features observable at low magnification optical microscopy, which include also defects as pores, lack of fusion, balling, warpage, or delamination.

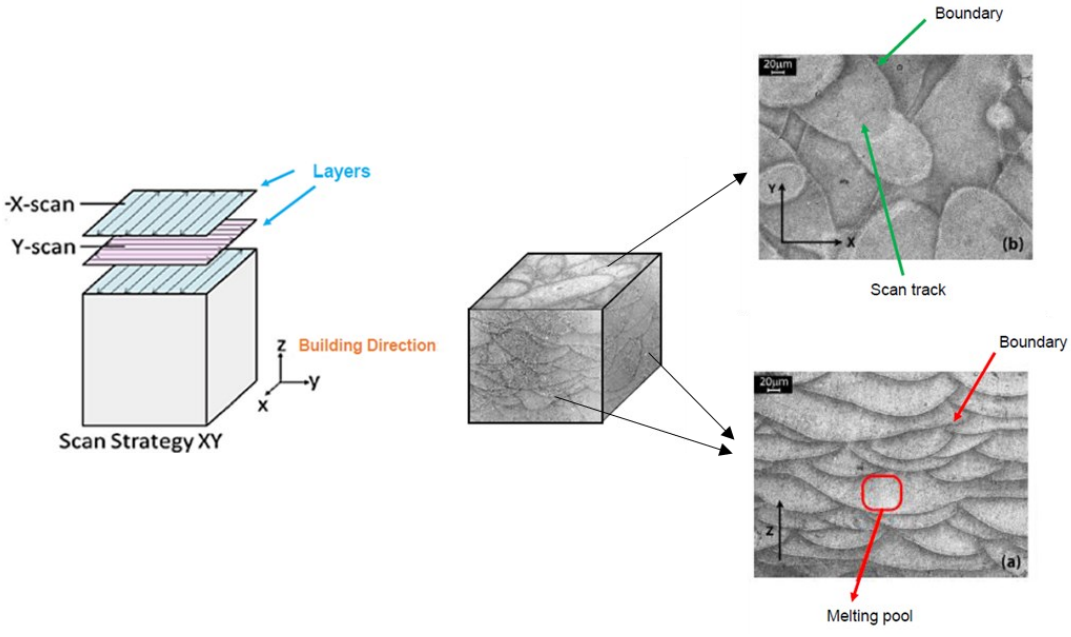

Fig. 1.3. Schematic representation of a cubic part produced via L-PBF and the resulting anisotropic structure: (a) melt pools along z and (b) scan tracks in xy.

Similarly to what happens in fusion welding, solidification during L-PBF is characterized by epitaxial growth at the solid-liquid interface, i.e. the interface between the substrate solid metal and the liquid in contact with it (Fig. 1.4a). Therefore, under the

condition of melt superheating, nucleation of grains starts from the pre-existing substrate. As crystallization is initiated at the boundary of the melt pool, grains continue growing toward its thermal center in the form of columnar grains. This kind of solidification allows grains to orientate according to the preferential orientation of the grains present on the surface of the pre-deposited layer (the "parent grain"), which is energetically favorable for the crystallization, and following the direction of heating transfer, i.e. the temperature gradient, perpendicular to the solid-liquid interface. This gives rise to the particular semi-circular geometry of the melt pool (Fig. 1.4b), described above. Thus, the columnar grains forming from the epitaxial solidification grow following the direction of the temperature gradient and extend between one melt pool and the above one. Since grains are generally aligned and oriented along certain directions, L-PBF pars are often characterized by a certain degree of anisotropy [6].

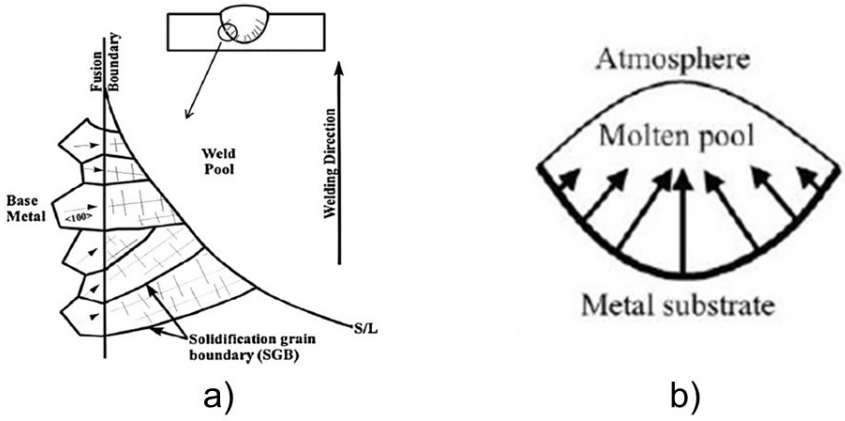

Fig. 1.4. (a) Epitaxial solidification and growth of the molten zone [10], (b) solidification of the melt pool during the L-PBF process [11].

The solidification mode of the melt pool mainly depends on the laser energy density and the interaction time between the laser and the material. The most important factors affecting the solidification mode are the temperature gradient $G = \mathrm{d}T/\mathrm{d}x$, the solidification rate $R = \mathrm{d}x/\mathrm{d}t$ and the cooling rate $G \cdot R = \mathrm{d}T/\mathrm{d}t$. Through these critical parameters together with the ratio G/R, it is possible to construct the solidification map of a material (Fig. 1.5). In detail, the type of resulting microstructure is controlled by G/R, while its scale by $G \cdot R$. With the successive decrease of G/R, the microstructure experiences morphological evolution from planar to cellular, columnar dendritic and equiaxed dendritic. Instead, with higher $G \cdot R$ the resulting microstructure is finer and vice versa. Since the molten pool is characterized by different temperature gradients, crystallization rates, and distribution of the undercooling due to the Gaussian distribution of the laser energy, various grain

morphologies (also called substructures) usually appear in the solidified microstructure, which constitute the micro-features of L-PBF parts [10]. The most observed substructures in L-PBF parts are the planar or cellular ones.

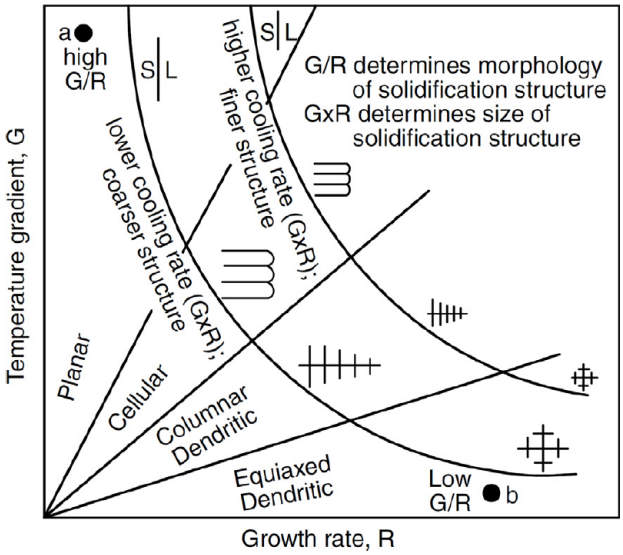

Fig. 1.5. Effect of temperature gradient G and growth rate R on the morphology and size of solidification microstructure [6, 12].

1.2.2 Process parameters

The main process parameters of L-PBF are laser power P (W), scanning speed v (mm/s), layer thickness t (mm) and hatch spacing h (mm), which are represented in Fig. 1.6. These constitute the most common parameters used to optimize the process, since they affect the volumetric energy density (Eq. 1.1) available to melt the powders and strongly influence the presence of defects in the built component.

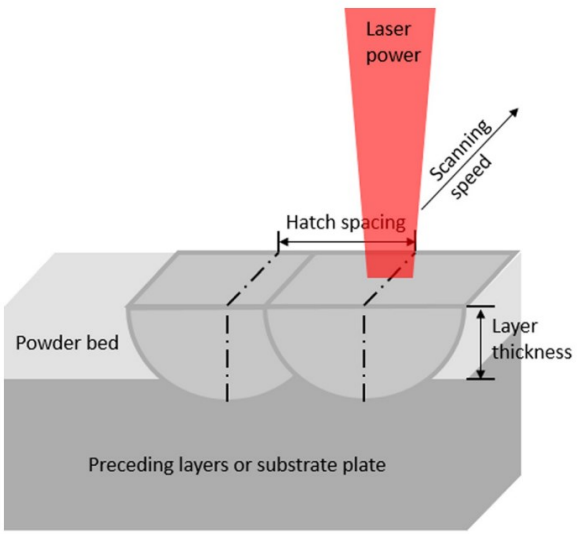

Fig. 1.6. L-PBF main process parameters [5].

Insufficient energy leads to lack of wetting of molten pool with the previous layer, which often results in balling defect (Fig. 1.7). This is usually due to a combination of low laser power, high scanning speed and large layer thickness. On the other hand, extensive material evaporation can appear as result of high laser power and low scanning speed, which often leads to the "keyhole" melting mode (Fig. 1.7). When the keyhole mode takes place, temperatures up to the boiling point can be reached, leading to partial evaporation and to the appearance of deep melt pools with high depth-to-width ration. This results in instability of the melt pool and entrapped gas that can generate small keyhole pores [13, 14]. The desired melting mode is the "conduction" one, which is characterized by a roughly semi-cylindrical shape of the melt pools, and which leads more process stability and less presence of defects [14]. In addition, inappropriate hatch spacing does not allow melt line to be completely fused together, thus causing the presence of porosities in the built parts. It is therefore evident that the optimization of these parameters and their combination is crucial for obtaining L-PBF near full-dense components [5]. This can be done by building process parameters maps similar to the one in Fig. 1.7, which highlights the process window where stable processing conditions are achieved [13].

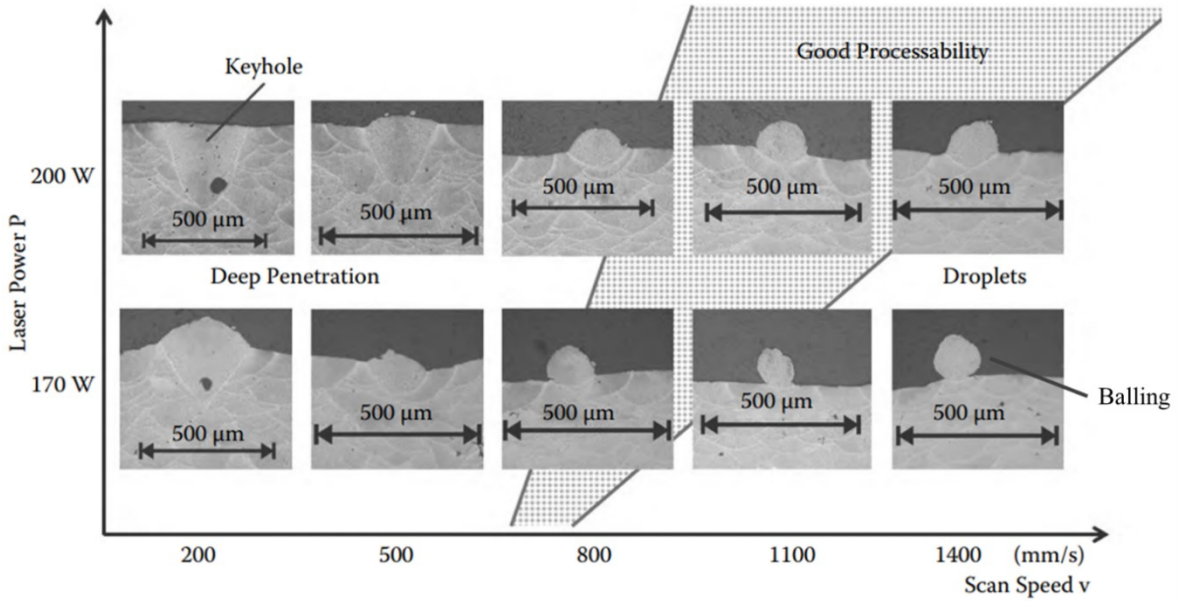

Fig. 1.7. Cross section micrographs of single scan tracks manufactured with different process parameters [13].

A common way to define the volumetric energy density VED (J/mm^3) is through Eq. 1.1, which provides a useful and effective overview of the effects of the key process parameters:

$$VED = \frac{P}{v\ h\ t}$$

Eq. 1.1

An alternative equation for VED is as follows, where the hatch spacing is replaced by the spot size of the laser s (mm):

$$VED = \frac{P}{v\ s\ t}$$

Eq. 1.2

Besides the parameter previously mentioned, there are other factors that play a significant role on the quality of L-PBF parts and therefore need to be properly adjusted, such as the laser scan strategy, the distribution, size, morphology of the used powder, the chamber environment, or the preheating temperature of the platform.

1.2.3 Defects

Several defects can arise after processing alloys through L-PBF, which can originate mainly from the characteristics of the used powder (raw material) and the control of the process parameters.

Typical defects related to the powder are:

- non-metallic inclusions such as nitrides, sulfides, carbides or oxides (Fig. 1.8a);
- internal porosities due to the inert gases (e.g. Ar, He, N) entrapped during atomization techniques or to the powder solidification shrinkage (Fig. 1.8b);
- morphological defects such as satellites which can affect the powder flowability (Fig. 1.8c);
- oxidation of powder coming from storage or handling of powder;
- presence of recycled powder that has different features compared to the virgin powder.

The presence of these defects in the powder used during L-PBF negatively impacts the properties of the component, and also limits the repeatability and precision of the process.

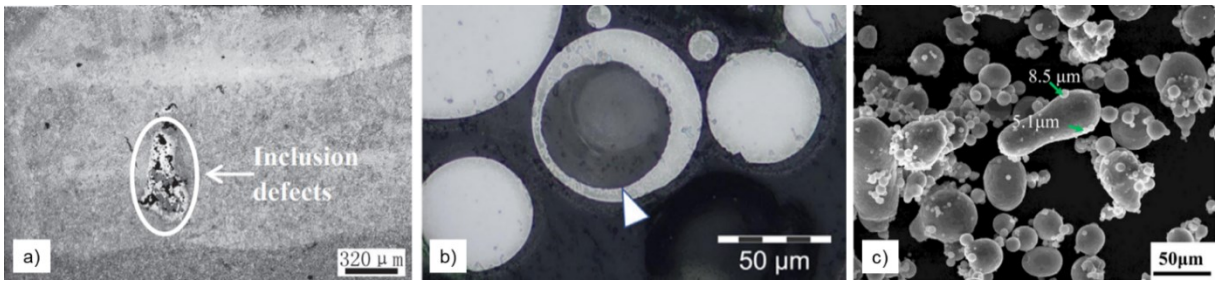

Fig. 1.8. Examples of defects related to the powder: a) inclusions [15], b) porosity [16], c) satellites [17].

On the other hand, process-related defects form during the process itself and generally result from an inadequate choice of the parameters. The main ones are:

- Gas porosities, typically characterized by a rounded shape (Fig. 1.9). These are due to the absorption of the surrounding gas or moisture, or to improper process parameters generating keyhole pores.

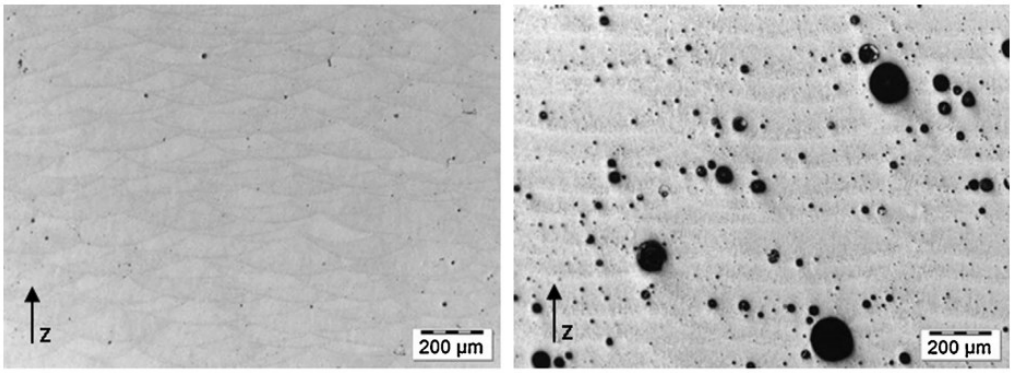

Fig. 1.9. Gas pores in samples built with different process parameters [18].

- Lack of fusion defects, typically characterized by an irregular shape (Fig. 1.10). They originate from un-melted metal powder or from insufficient energy provided to the powder bed, generating insufficient melt and poor bonding between consecutive layers.

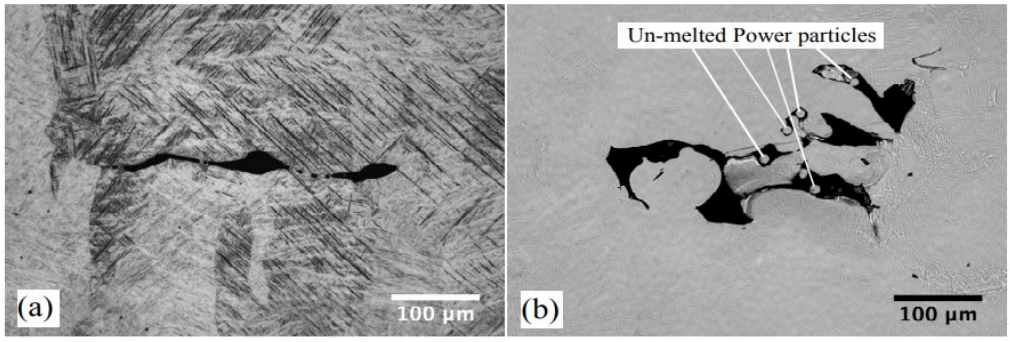

Fig. 1.10. Lack of fusion defects a) due to poor bonding and b) with un-melted powder inside [19].

- Balling, a surface defect that causes high roughness and surface irregularities, typically associated with an insufficient energy input to the powder bed (Fig. 1.11).

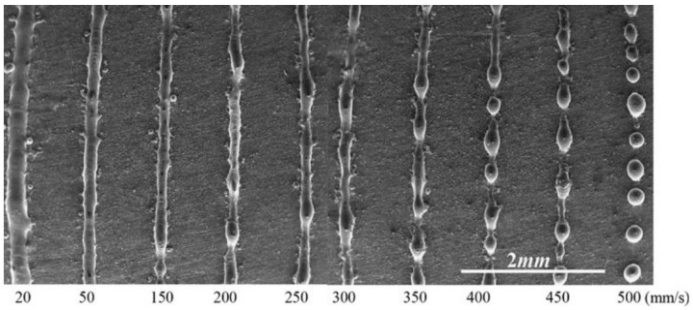

Fig. 1.11. SEM images displaying the balling characteristics of single scan tracks manufactured with different scan speed [20].

- Laser spatter induced by the recoil pressure of vapor that causes small droplets to be expelled from the melt pool and then to land into the powder bed, generating oxidation and contamination, as well as the loss of elements.

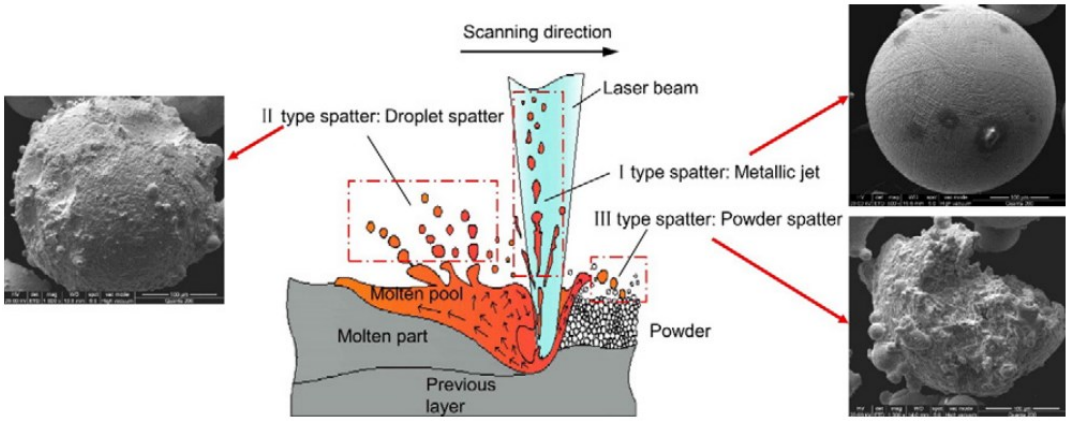

Fig. 1.12. Representative schematization of the formation mechanisms of different types of spatters [21].

These defects can be categorized as bulk defects, such as gas porosities and lack of fusion, or surface defects, such as balling and those associated with the laser spatter.

1.2.4 Last developments

Recent progresses in L-PBF have sparked considerable interest for many complex applications, with the aim of producing smart and functional structures [22]. In this regard, many studies in the biomedical field focus on the manufacture of shape memory alloys (SMAs), such as Nitinol, which are renowned for their unique ability to return to a predefined shape upon activation. The manufacture of custom-designed SMAs implants through L-PBF could in fact offer promising opportunities for innovation in medical implants.

SECTION 2.

NITINOL

2.1 INTRODUCTION

Nitinol (NiTi) is a nickel-titanium alloy characterized by the presence of its two elements in nearly equal proportions. Its name originates from the chemical composition and the laboratory where it was discovered in 1961 [23]: Ni (Nickel) + Ti (Titanium) + NOL (Naval Ordinance Laboratory).

NiTi alloy constitutes the most widespread shape memory alloy (SMA) and as such it can display two unique behaviors, i.e. the shape memory effect (SME) and the superelasticity (SE). SME consists in the recovery of the original shape after deformation by heating, while SE involves the mechanical recovery of deformation up to 6-8% on unloading. These distinctive features are related to a first-order phase transformation proper of SMAs, i.e. a martensitic transformation [24]. SME and SE of NiTi alloys are exploited in many engineering and biomedical applications [25-27]. In particular, SME is commonly used to produce motion and/or force, while SE is able to store deformation energy [28].

In addition to these peculiar features, NiTi alloys are characterized by high strength, good ductility, excellent corrosion resistance, and high biocompatibility, which makes this material the preferred among the other SMAs. Some of the main properties of NiTi alloys are reported in Table 2.1.

Table 2.1. Summary of some relevant properties of NiTi [29].

Density	6.64 kg/cm^3	
Melting point	~ 1310 °C	
Transformation temperatures	-200 to 110 °C	
Thermal Conductivity	Austenite	18 W/mK
	Martensite	9 W/mK
Coefficient of thermal expansion	Austenite	11×10^{-6} K^{-1}
	Martensite	6.6×10^{-6} K^{-1}
Resistivity	Austenite	100 Ωcm
	Martensite	70 Ωcm
Young Modulus	Austenite	70-80 GPa
	Martensite	23-41 GPa
Ultimate tensile strength	Cold worked	Up to 1900 MPa
	Fully annealed	~ 900 MPa
Elongation at fracture	Cold worked	5-10%
	Fully annealed	25-50%

2.2 MARTENSITIC TRANSFORMATION

2.2.1 Crystallographic aspects

Nitinol's martensitic transformation occurs from the parent austenitic phase (A) to the daughter martensitic phase (M). It is a *first-order phase transformation* and therefore is characterized by the presence of latent heat, which defines the amount of energy required to undergo the phase change. The martensitic transformation is a *solid-solid transformation* with *diffusionless* (or *displacive*) nature, meaning that the new phase is generated by the cooperative movements of atoms without changing the chemical composition of the matrix. This cooperative rearrangement allows a lattice structure change, even though the relative atom displacements are comparable to one interatomic distance [27]. Martensitic transformation can be either *athermal*, when proceeding with decreasing temperature, or *isothermal*, when proceeding at a constant temperature.

Unlike the classic martensitic transformation, e.g. the one occurring during the quenching of steel, Nitinol's one is *thermoelastic*, meaning that the martensite nucleates and grows steadily as the temperature is decreased, while it shrinks and vanishes reverting back to the austenite by raising temperature, conferring it a thermally reversible nature [30-32].

From a thermodynamic point of view, the driving force for the martensitic transformation is the Gibbs free energy difference between the parent phase and martensite, i.e. $\Delta G^{P\text{-}m}$ [33]. This is schematically illustrated in Fig. 2.1, which plots the Gibbs free energy of both austenite and martensite, respectively G^P and G^m, against temperature. T_0 is the equilibrium temperature between the two phases, ΔT_S is the supercooling required for the transformation. Supercooling is in fact necessary for the nucleation of martensite and superheating for the reverse transformation. M_s and M_f differs, since the elastic energy around the martensite prevents this phase from growing unless another driving force such as cooling is applied [27].

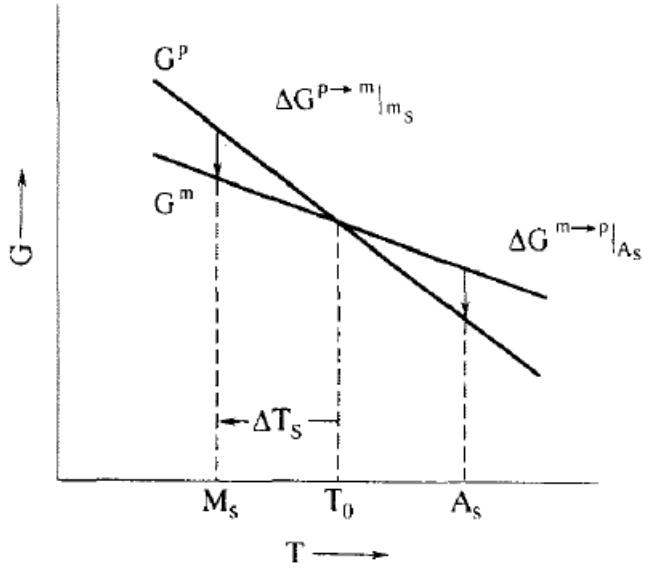

Fig. 2.1. Free energy curves for parent and martensitic phase [27].

The martensitic transformation in NiTi alloys usually occurs between austenite and martensite (A – M). However, in some cases, multiple phase transformation can occur, involving the intermediate transformation from austenite to the R-phase, and then to martensite (A – R – M). The A – R transformation is also martensitic with a thermoelastic nature. Martensitic transformations are often indicated referring to the crystal structures of phases, i.e. B2 – B19' or B2 – R – B19'.

The crystal structures of the phases existing in NiTi alloys are [33, 34]:

a) Austenite: a simple cubic B2 structure (i.e. CsCl type), shown in Fig. 2.2a[1]. It constitutes the parent phase and when undergoes the martensitic transformation turns into martensite or R-phase.
b) Martensite: monoclinic B19' structure, schematized in Fig. 2.2b. The structure relationship between austenite and B19' martensite is shown in Fig. 2.3
c) R-phase: trigonal distortion of the cubic structure, achieved through the elongation of the B2 cube along the body diagonal[2], as displayed in Fig. 2.4.

[1] In NiTi atom types are situated on specific lattice site to separate themselves as much as possible, which makes it an ordered structure. Even if the symmetry appears to be body centered cubic (bcc), the ordered structure is not bcc since the atoms at the corners are different in nature to those at the center [34]. The notation used for these crystal structures is the *Strukturbericht designation*.
[2] R-phase can be viewed as rhombohedral if considering the B2 phase being elongated along one of the body diagonal <111>. However, given the actual atom positions, its true symmetry is trigonal [33].

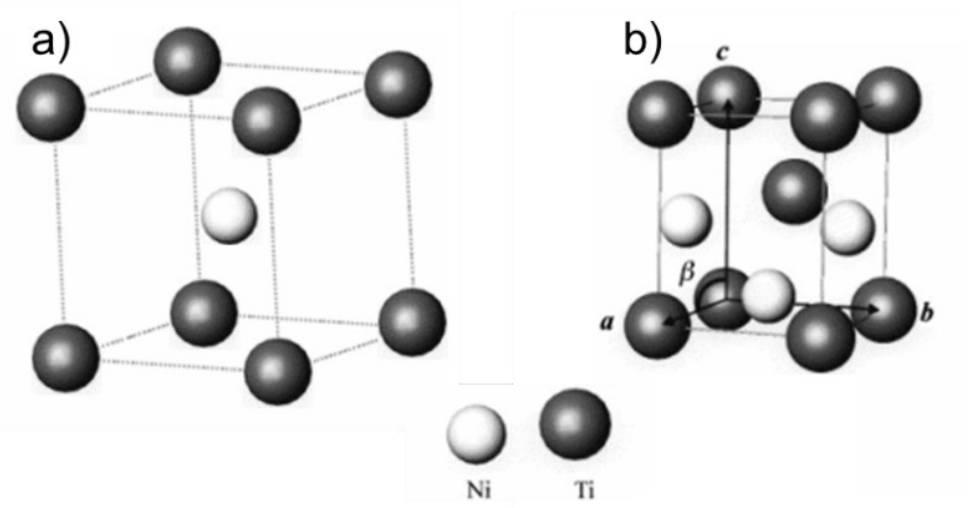

Fig. 2.2. Schematic illustration of (a) B2 cubic cell of NiTi austenite, and (b) B19' monoclinic unit cell of NiTi martensite [33].

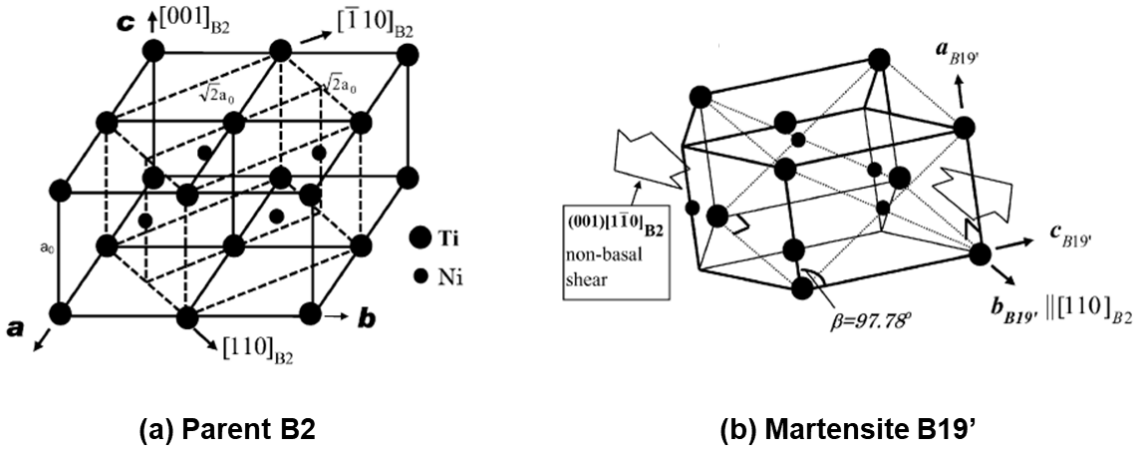

Fig. 2.3. Structure relationship between parent B2 and B19' martensite [33].

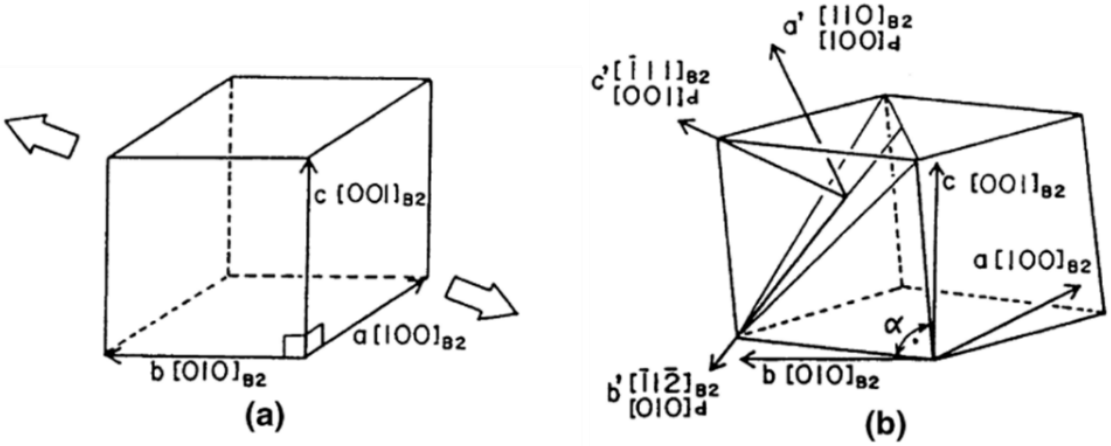

Fig. 2.4. Lattice distortion from (a) B2 to (b) R-phase. The axes a', b' and c' represent the principal axes in the lattice deformation [33].

The different arrangements of atoms in one unit cell are summarized in Fig. 2.5 for each phase.

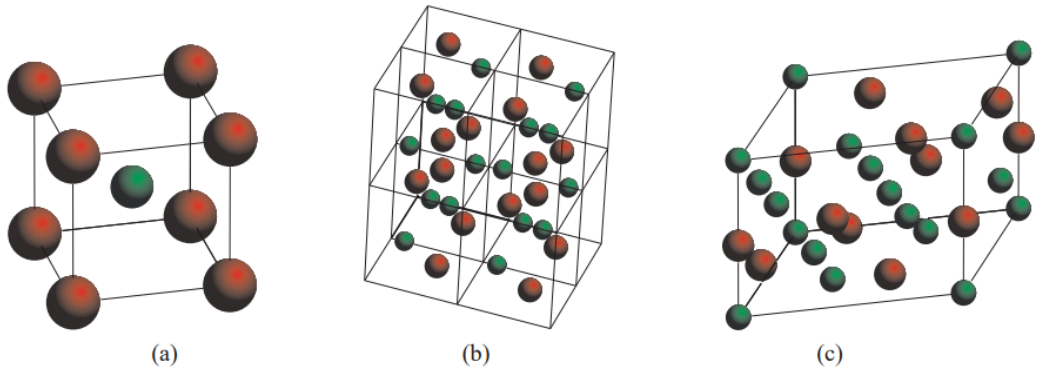

Fig. 2.5. Unit cells of the different phases in NiTi: (a) cubic lattice of B2 austenite, (b) monoclinic lattice of B19' martensite and (c) trigonal lattice of R-phase [35].

As austenite is characterized by a greater crystallographic symmetry than martensite, multiple martensite variants typically form as a result of the martensitic transformation from austenite to martensite, i.e. direct martensitic transformation A→M. This can be detected in Fig. 2.6, where square unit cell of austenite and rectangular (less symmetric) unit cell of martensite are represented. As the interfaces forming between variants must maintain coherency with unbroken rows of atoms across the interface, martensite variants are arranged coherently, leading both to peculiar patterns at small length-scale and no macroscopical net shape change [36]. Variants form as a result of the different shear planes and shear directions. The shear occurs along a specific crystallographic plane called *habit plane* that forms the interface between A and M.

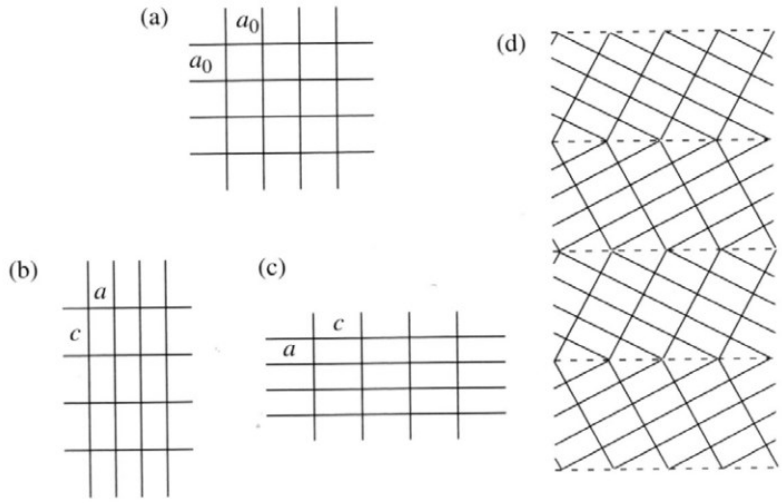

Fig. 2.6. Martensitic transformation: (a) square unit cell of austenite, (b,c) rectangular unit cells of different variants of martensite, (d) coherent rearrangement of alternating martensite variants [36].

More in detail, at the microscale, the A→M transformation normally occurs as a result of two phenomena, that are the *Bain strain* and the *lattice-invariant shear* [34]. A simplified two-dimensional approach of these is here reported. The *Bain strain*, or lattice deformation, involves the atomic movements responsible for producing the new lattice structure. This stage is shown schematically in Fig. 2.7 as the transition from the austenitic structure (Fig. 2.7a) to the martensitic structure (Fig. 2.7d) through the movement of the martensite interface of one atomic layer (Fig. 2.7b), corresponding to a very small displacement of each atom (Fig. 2.7c).

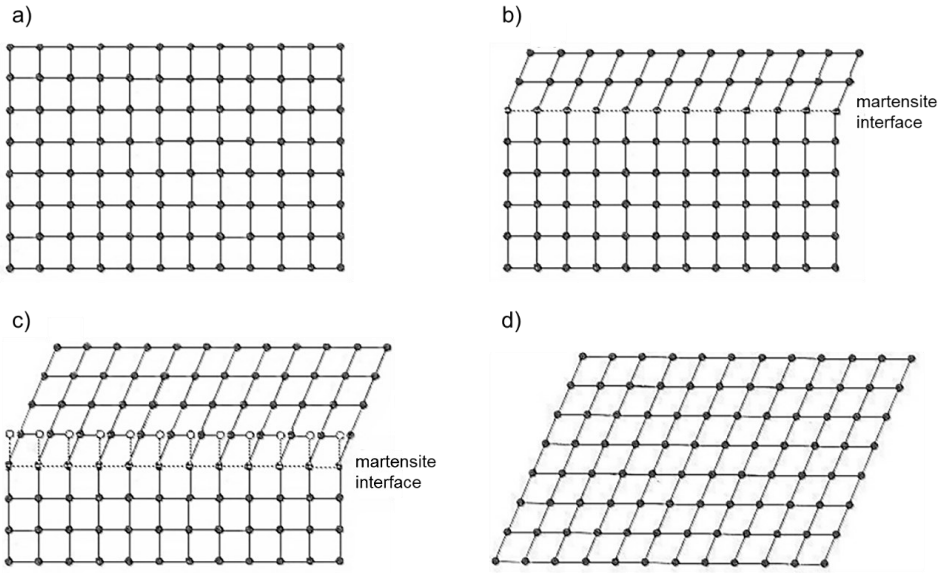

Fig. 2.7. Transformation from austenite to martensite (A→M) [34].

As the martensitic structure resulting from the Bain strain is of a different shape than the austenite, the accommodation of the new structure is required to avoid the matrix tearing. This happens in the second stage of the martensitic transformation, i.e. the *lattice invariant shear*. In general, accommodation can occur through two different mechanisms: *slip* (Fig. 2.8a) and *twinning* (Fig. 2.8b). Dislocation slip is the typical accommodation mechanism of martensite in steels, which undergoes both volumetric and shape changes. Through slip, the microstructure is permanently modified by the breaking and slipping of the atomic bonds. On the other side, for martensite in SMAs (e.g. NiTi alloys) twinning occurs, as a result of the related energy minimization, and, unlike slip, it has a reversible nature. Martensite in SMAs experiences only shape change (volume change -0.003% [36]), and through the twinning deformation mechanism it is able to accommodate it without tearing or interpenetrating the matrix. Thence, twinning accommodates shape changes in a reversible manner. Thanks to this mechanism, the result of the A→M direct martensitic transformation

is the new martensitic structure, with the same overall shape of the austenitic phase. In fact, after twinning (and also after slip) each individual cell (parallelogram in Fig. 2.8) presents the new martensitic structure (Fig. 2.8b), but the overall shape of the original austenite is preserved (compare Fig. 2.7a to Fig. 2.8b).

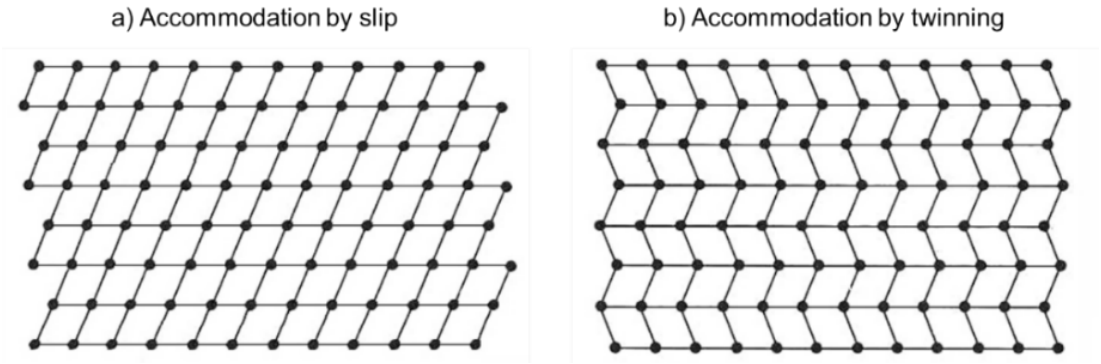

Fig. 2.8. Lattice invariant shear: (a) accommodation by slip, (b) accommodation by twinning [34].

Through the direct martensitic transformation, the produced martensite variants arrange themselves so that no macroscopic shape change happens. Since at microscopic scale the structure actually deeply modified with relative deformations, the martensite variants organize to accommodate each other's strains, thus preventing any macroscopic shape change. In other words, although every martensite plate causes a displacement, the contributions of all plates cancel when summed [34]. This phenomenon is called *self-accommodation* of martensite, and the resulting structure is a coherent arrangement of martensitic variants which occupies an area whose boundaries undergo no displacement compared to the parent phase [37].

Regarding the M→A reverse transformation, it happens upon heating (in SME) or through the release of the applied stress (in SE), as better discussed in Chapter 2.3. Since the parent phase has higher crystallographic symmetry and only one path to the parent phase is possible, the reverse transformation leads to the regain of the original shape of the parent phase after deformation.

In summary, Nitinol's capability to completely restore the original shape lies in the *thermoelastic nature* of the martensitic transformation and in the *ordered structure* of the alloy. In fact, thermoelastic alloys favor SME and SE due to both the small driving force which causes the transformation to happen (avoiding in this way the introduction of dislocations), and the presence of mobile twins, which lead to crystallographic reversibility. The effect of the ordered structure of NiTi alloys is also related to the crystallographic

reversibility, as only one path to the parent phase exists (in the case of disordered alloy three paths exist), allowing the original ordered parent structure to be restored upon the M→A reverse transformation, during which the recovery of the shape happens. Furthermore, the ordered structure also favors the avoidance of slip, as present a higher critical stress for slip than that of the disordered structure [38].

2.2.2 Transformation Temperatures

For applicative purposes, it is crucial to know the Transformation Temperatures (TTs) of NiTi alloys, which are those temperatures at which the alloy changes from the austenitic phase (stable at higher temperature) to the martensitic phase (stable at lower temperature) and vice versa. It should be noted that, for the martensitic transformation to occur, TTs are low enough to prohibit diffusive phenomena [33].

In detail, from the lowest to the highest [27]:

- *Martensite finish, M_f:* temperature at which A→M transformation completes during cooling.
- *Martensite start*, M_s: temperature at which A→M transformation starts during cooling.
- *Austenite start*, A_s: temperature at which M→A transformation starts during heating.
- *Austenite finish*, A_f: temperature at which M→A transformation completes during heating. It corresponds to the temperature above which the martensite becomes unstable.

Another temperature of practical interest is the *martensite-destruct temperature* (or *martensite-dead temperature*) M_d, which is the temperature above which the stress-induced martensite is unstable and thus its formation is impeded [27, 39-41]. This temperature is also referred to as T_s, i.e. the temperature above which the permanent plastic (slip) deformation takes place [42].

It must be noted that the temperatures at which austenite transforms to martensite (A→M forward transformation) differs from the temperatures at which martensite transforms to austenite (M→A reverse transformation). In other words, TTs change upon heating and cooling, this phenomenon is called hysteresis and for SMAs typically ranges between 20-40 °C [34]. This is mainly caused by nucleation barriers that depend on the crystallographic compatibility between austenite and martensite. Fig. 2.9 displays the phase

fraction as a function of temperature, together with the typical hysteresis related to the transformation.

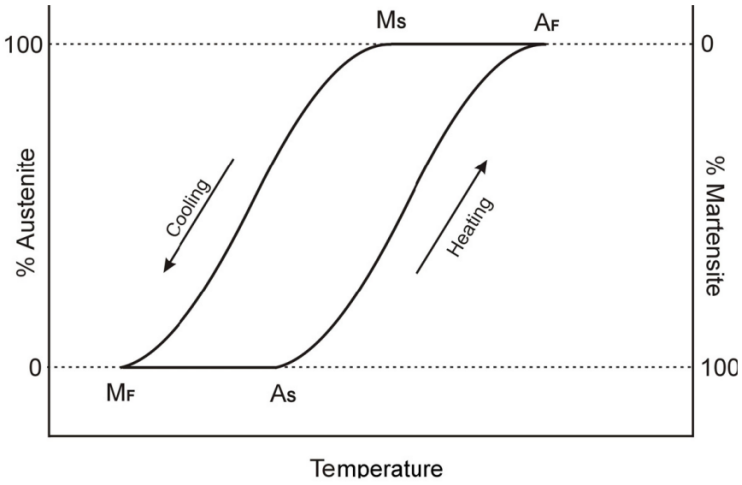

Fig. 2.9. Hysteresis of SMAs [43].

As most of the physical properties of austenite and martensite are different and drastically change during transformation (Table 2.1), TTs are commonly detected through measurements of physical properties as a function of temperature, e.g. specific heat or electrical resistance. One of the most used method for TTs determination is thermal analysis through differential scanning calorimetry (DSC) [44]. In fact, during a transformation, the sample releases or absorbs latent heat. Other common techniques are resistivity measurements, bend and free recovery tests or dilatometry.

TTs are extremely sensitive to small alloy composition changes, which therefore needs to be carefully controlled, as better analyzed in Paragraph 2.5.1.

The martensitic transformation of NiTi is reviewed in this Chapter in relation to B2→B19' transformation, however, as previously mentioned, B2→R martensitic transformation can also happen in particular circumstances prior to the transformation to B19' phase. This can occur in three cases [33, 45]:

1) in Ni-rich NiTi alloys aged around 400 °C to cause Ni_4Ti_3 precipitation (see also Paragraph 2.4.1);
2) in NiTi alloys after cold working to create rearranged dislocation structures;
3) in ternary NiTiFe(Al) alloys.

In these cases, both R-phase and B19' are affected by stress field of precipitates, stress field of dislocation and the presence of a third element (Fe or Al), respectively. B19'

martensite is usually thermodynamically preferred, but R is initially formed since in these cases it presents a lower activation energy, which makes it kinetically advantaged [46].

In contrast to B2→B19', B2→R transformation involve very small temperature hysteresis, as well as small recoverable strain associated with this transformation [46, 47]. Similarly to B19' martensite, R-phase is a low temperature phase, and its TTs, i.e. R_s, R_p, R_f, are determined from the cooling scan of DSC analyses [48].

2.3 MACROSCOPIC ASPECTS

The atoms rearrangement proper of the martensitic transformation can be triggered both by temperature or stress, generating respectively shape memory effect or superelasticity. The appearance of one or the other behavior is strongly dependent on the relative relationship between the testing temperature and TTs, and thus from the exhibited phase at the testing temperature.

2.3.1 Shape memory effect

The shape memory effect (SME) is schematically illustrated in Fig. 2.10. At a temperature below M_f, martensite is stable and present the twinned state (point A, Fig. 2.10). Upon applying load, the non-plastic detwinning deformation mode causes the detwinning of martensite, maintaining the same crystal structure (B). During detwinning, the existing preferentially oriented martensite variants grow during loading, while others "shrink" until disappearing. When the load is removed, the martensite elastically recovers but retains some residual deformation, which is actually an apparent plastic deformation (C). In fact, by heating to temperatures above A_f, the material returns to the parent phase (austenite) recovering its original shape (D). This last step corresponds to the reverse transformation M→A, responsible of the shape recovery. Then, when the austenite phase is cooled below M_f, the forward transformation A→M leads again to the obtainment of martensite (A), that preserve the parent phase shape, due to the accommodation of the martensite variants, as explained in Chapter 2.1.

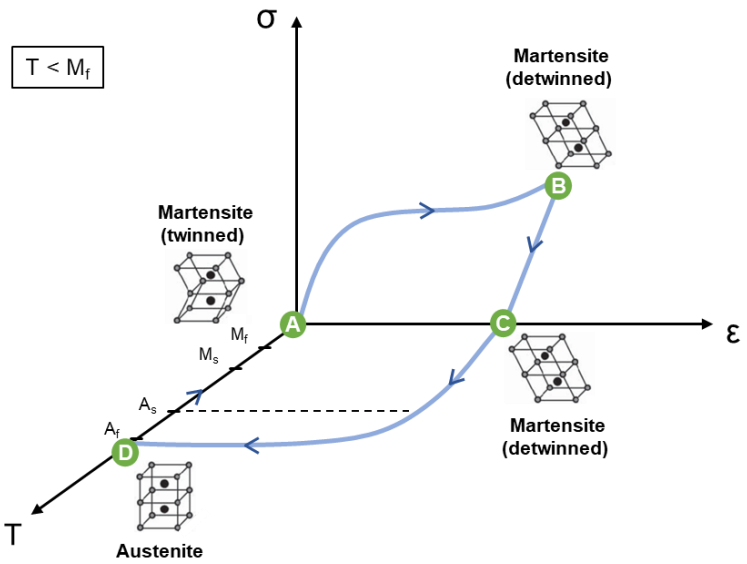

Fig. 2.10. Schematization of SME.

The corresponding changes in the crystal structures of NiTi during SME are highlighted in Fig. 2.11.

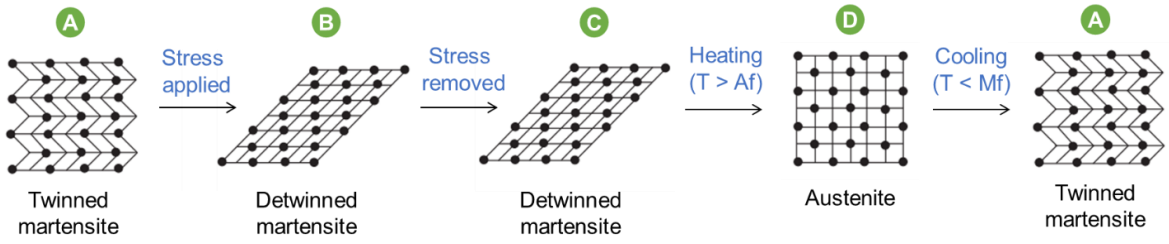

Fig. 2.11. Change of lattice structure during SME. Twinned martensite, detwinned martensite upon stress application, permanence of detwinned martensite upon stress removing, austenite upon heating above A_f, again twinned martensite upon cooling below M_f.

Generally, SME occurs starting from the martensitic phase at temperatures below M_f.

The above-described mechanism is also referred to as “One-way shape memory effect” (OWSME). As previously discussed, the material “remembers” its original parent shape by heating upon A_f. However, to start a new shape memory cycle, the material needs to be deformed again. On the other hand, the “Two-way shape memory effect” (TWSME) happens when the shape change occurs upon both heating and cooling, meaning that the material remembers both the higher temperature and the low temperature shape. In this way, the material bends in two different ways on heating and cooling, and thus no external force is required. While OWSME is an intrinsic feature of NiTi, specifical thermomechanical processes are needed to “train” NiTi parts to exhibit the TWSME.

Another unique shape memory behavior is the "All-round shape memory effect" (ARSME), which was discovered by Nishida et al. [49]. It is similar to TWSME but is associated with the R→B2 transformation and on the orientation of Ni_4Ti_3 particles with respect to the applied stress. Therefore, ARSME can be achieved by aging Ni-rich NiTi alloys due to the precipitation of Ni_4Ti_3. However, the maximum reversible strains are limited to 1% due to the very small temperature hysteresis of R→B2 transformation and thus it is not particularly attractive for many applications.

SME is commonly exploited for engineering applications to respond to a temperature change caused by a change in the ambient temperature (thermal actuator) or by electrically heating the component (electrical actuators) [28]. These are used in many different fields, such as robotic, automotive, aircraft and aerospace. Other examples include shape memory micro-grippers, shape memory thermostat or the mobile phone camera module for active image stabilization and focusing.

2.3.2 Superelasticity

Superelasticity (SE)[3] is the ability to elastically deform up to the 6% of deformation and is displayed in Fig. 2.12.

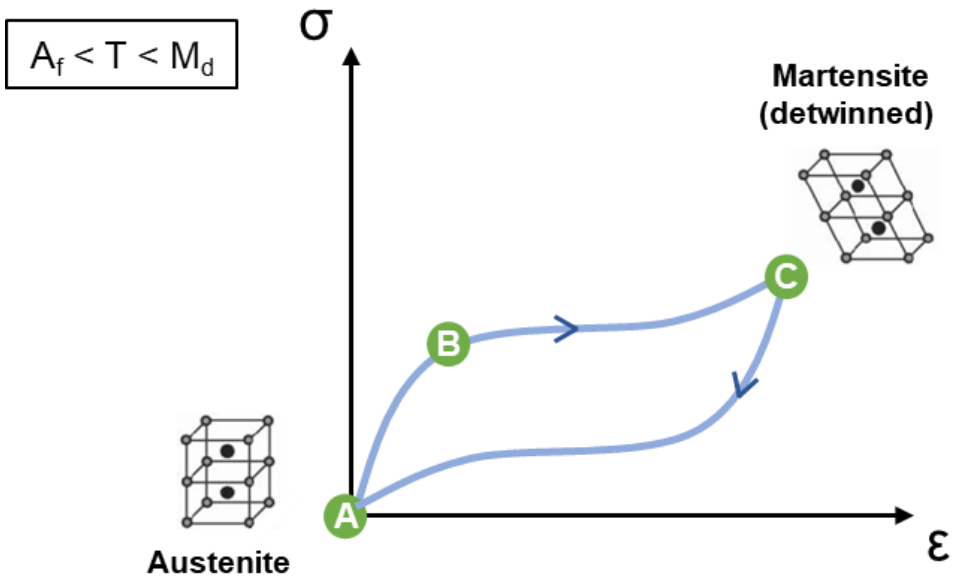

Fig. 2.12. Schematization of SE.

[3] Superelasticity is often referred to as "pseudoelasticity". *Pseudoelasticity* generally denotes when an apparent plastic deformation is recovered by unloading at a constant temperature and thus the σ-ε curve is characterized by a closed loop. *Superelasticity* specifically indicates when the closed loop originates from a stress-induced transformation upon loading and the reverse transformation upon unloading [27].

Starting from austenite (point A, Fig. 2.12), after the elastic loading, the martensitic transformation starts (B), forming martensite in twins which instantaneously detwins due to the applied load. Upon further loading it fully transforms creating a stress plateau (B-C). The formed martensite is called stress-induced martensite. The generated plateau is the result of the formation of martensite from the austenite phase ability of martensite phase to form variants during the transformation and is strongly dependent on temperature. The loading direction and the crystal orientation or texture basically determines the selection of the martensite variants. The particular variant of stress-induced martensite activated is based on which variant is oriented to accommodate the maximum strain due to the applied stress [39]. It should be noted that austenite and martensite coexist until the end of the plateau is reached. When the stress plateau ends, the stress-induced martensitic phase can elastically deform according to the martensite modulus. However, since the stress-induced martensite is not stable at $T > A_f$ without the action of stress, as the load is removed the reverse martensitic transformation M→A takes place, allowing the shape recovery by generating again the parent phase (A). It should be pointed out that if the stress-induced martensite is further loaded (above C), it will be plastically deformed and thus its deformed variants will be stabilized upon unloading, making the occurrence of SE not possible.

Concerning the localization of the transformation, for fine grained NiTi polycrystal alloys, it was found that the stress-induced martensitic transformation proceeds as Lüders deformation, thus it preferably propagates in the neighboring transformed region rather than nucleate martensite in untransformed regions in small grain, whose boundaries constrain the martensitic transformation [33].

The corresponding changes in the crystal structures of NiTi during SE are highlighted in Fig. 2.13.

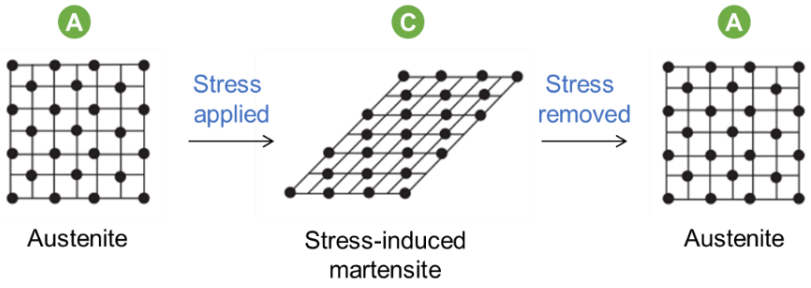

Fig. 2.13. Change of lattice structure during SE: austenite, stress-induced martensite upon the application of stress, austenite upon unloading.

SE typically occurs when the material is deformed between A_f and M_d. Above M_d, the energy required to form stress-induced martensite surpass the energy to plastically deform the austenite though slip, thus making the stress-induced martensite instable.

The main applications involving SE belong to the biomedical field (Chapter 2.6), but include also other components such as antennae or eyeglass frames [28].

2.4 NI-TI PHASE DIAGRAM

Considering the Ni-Ti phase diagram (Fig. 2.14) is essential for the understanding of its microstructural features, particularly for tuning its properties through heat treatments based on the specific application requirements.

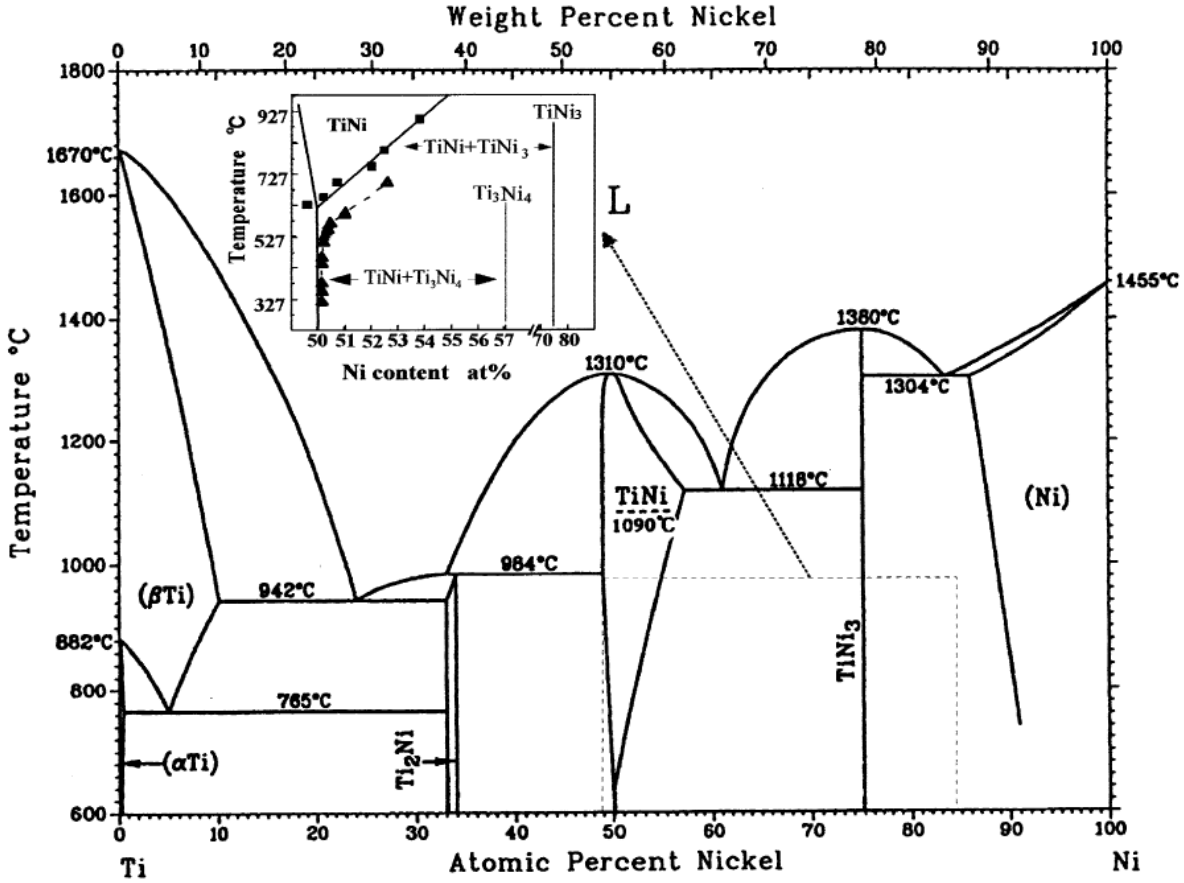

Fig. 2.14. NiTi phase diagram according to Otsuka and Ren [33], together with the phase equilibrium between B2 and Ni_4Ti_3 phases [50].

The region of interest in Ni-Ti binary diagram is the central one, which is bounded by Ti_2Ni and Ni_3Ti phases (between 55 wt% and 65 wt%), since in these ranges of composition the peculiar properties of SME and SE are revealed and can be tailored through thermo-

mechanical processes. This region corresponds to the single phase "NiTi" near the equiatomic composition, which present an order-disorder transition from B2 to body centered cubic (BCC) at 1090 °C, according to Otsuka and Ren [33]. This transformation makes NiTi commonly considered as an ordered alloy in a strict sense, despite it is also classified as an intermetallic compound [33].

2.4.1 Precipitation in NiTi alloys

The Ni-Ti system exhibits several phases. Two of these are formed through the martensitic transformation from the parent B2 cubic austenitic phase, that are monoclinic B19' martensite and trigonal R-phase (see Fig. 2.5)[4]. The aspects related to the martensitic transformation were discussed in Chapter 2.1. In addition to these phases, aging Ni-rich alloys leads to the formation of several other phases as a result of precipitation. It should be noted that precipitation through aging is possible only on Ni-rich side, since the boundary on Ti-rich side is very steep and close to 50% Ni, while on Ni-rich side there is a large solubility limit, which decreases with lowering temperature [33].

The diffusion-controlled transformations of Ni-rich 52-NiTi were extensively investigated by Nishida et al. [51] using metallography, TEM, SEM and EDS techniques. By performing different aging heat treatments, they found that three phases precipitate in sequence, depending upon aging temperature and time. These were identified as Ni_4Ti_3, Ni_3Ti_2 and Ni_3Ti. In detail, Ni_4Ti_3 phase forms at lower aging temperature and shorter aging time, Ni_3Ti_2 phase appears at intermediate temperature and time, while Ni_3Ti phase is formed at higher aging temperature and longer aging time. They also noticed that as aging progresses, the preexisting Ni_4Ti_3 is absorbed into the matrix, and both the number and dimension of Ni_3Ti_2 increase. Similarly, extending aging again causes the preexisting Ni_3Ti_2 to be absorbed in the matrix, and the quantity and size of Ni_3Ti increases. This points out that both Ni_4Ti_3 and Ni_3Ti_2 phases are intermediate phases, while Ni_3Ti is the equilibrium phase. Therefore, as the aging temperature and time increase, the diffusional transformation take place in the following order:

$$\text{NiTi B2 parent phase} \rightarrow \alpha_1 + Ni_4Ti_3 \rightarrow \alpha_2 + Ni_3Ti_2 \rightarrow \alpha_3 + Ni_3Ti$$

[4] Orthorhombic B19 martensite is also possible as intermediate phase to B19' when some amount of Ni is substituted by Cu, i.e. in Ni-Ti-Cu systems [33].

where α_1, α_2, α_3 are the matrices with different Ni concentrations as result of the formation of the other phases. These findings were summarized in the time-temperature-transformation (TTT) diagram reported in Fig. 2.15.

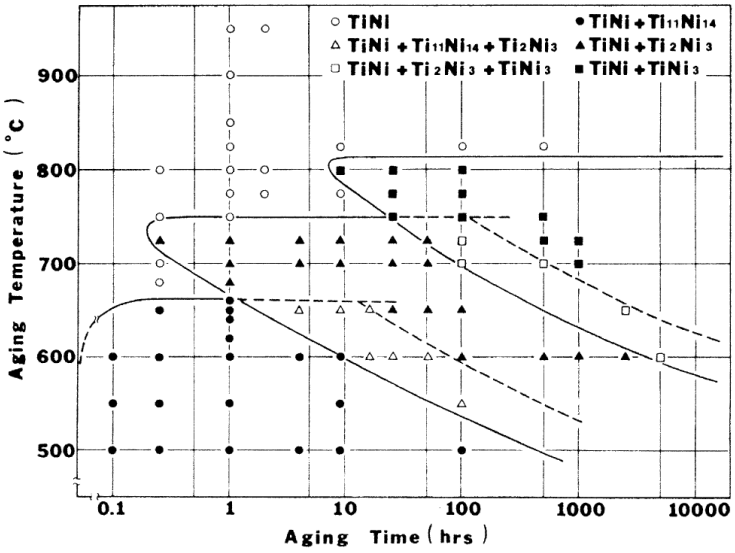

Fig. 2.15. TTT diagram of 52-NiTi alloy, describing its aging behavior[5] [51].

2.4.2 Crystal structures of precipitates

The crystal structures of NiTi precipitates are:

a) Ni_4Ti_3: rhombohedral structure (Fig. 2.16).
b) Ni_3Ti_2: it presents a higher temperature phase (stable above 100 °C) with a tetragonal structure and a lower temperature phase with an orthorhombic structure [52].
c) Ni_3Ti: hexagonal DO_{24} type ordered structure [53].

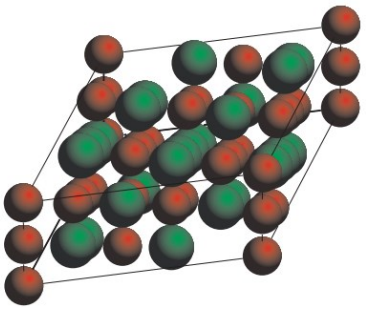

Fig. 2.16. The arrangement of atoms in one unit cell of the rhombohedral structure of Ni_4Ti_3 phase [35].

[5] It must be noted that Ni_4Ti_3 phase was initially identified as $Ni_{14}Ti_{11}$, and therefore is indicated with this stoichiometry in the Figure.

Among all NiTi phases forming through precipitation, Ni_4Ti_3 phase is very important, since it can affect the shape memory characteristics of Ni-rich alloys [33, 45, 49, 54-60]. Its morphology is typically lenticular, as shown in Fig. 2.17. In the early stage of their formation, these precipitates are coherent to the matrix and produce stress-field around them (Fig. 2.18). These stress fields in the matrix are considered to assist or arrest the formation of martensite phase and R-phase [45, 57, 58, 60]. It is well established that high-density of precipitates increases considerably the critical stress for the slip plastic deformation, thus decreasing the possibility to run into the plastic deformation and enlarging the shape memory "window" (details in Chapter 2.5) [33, 55, 56, 59]. Furthermore, the presence of Ni_4Ti_3 precipitates was found to play an essential role in the occurrence of the "all-round shape memory effect", which is a particular type of shape memory effect belonging to the two-way shape memory category [49, 54].

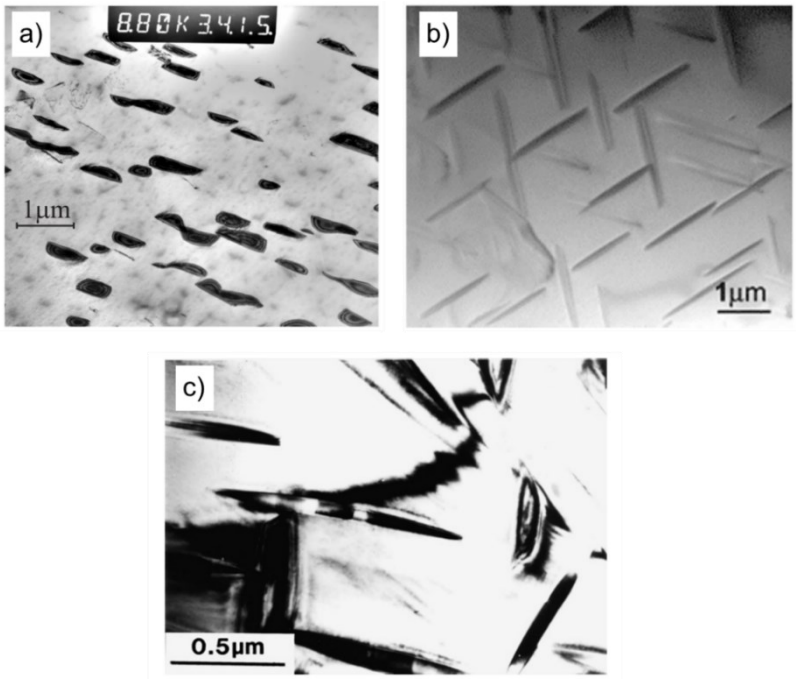

Fig. 2.17. Typical lenticular morphology revealed with TEM of Ni_4Ti_3 precipitates: (a) after aging at 530 °C for 11 hours [35], (b) after aging of at 500 °C for 150 h [61], (c) after aging at 500 °C for 150 h [54].

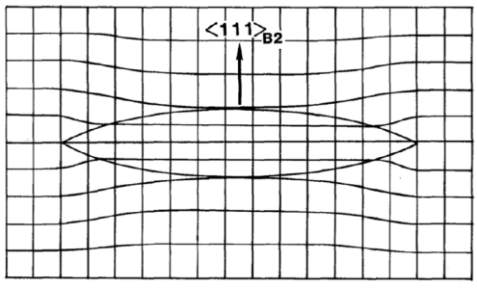

Fig. 2.18. Lattice distortion of B2 parent phase due to the presence of Ni_4Ti_3 precipitate [54].

2.5 APPEARANCE OF SHAPE MEMORY EFFECT AND SUPERELASTICITY

A SMA specimen can exhibit both superelasticity and shape memory effects, and the testing temperature has a key role in determining which one occurs. This is displayed in Fig. 2.19, where a temperature-stress diagram for a SMA is illustrated (Fig. 2.19a), together with the corresponding stress-strain curves (Fig. 2.19b-d). As previously described, the martensitic transformation proceeds by a shear-like mechanism and therefore interacts with an applied stress. In this perspective, the thermodynamic Clausius-Clapeyron relationship can be used to describe the effect of stress on the martensitic transformation [38].

In Fig. 2.19a, four martensitic transformations lines are displayed, M_s, M_f, A_s and A_f along with three kinds of stress lines as function of temperature. These are: the critical stress for slip deformation σ_{SLIP}, the stress for starting reorientation of martensite variants σ_s^{RMV} and the stress for finishing the reorientation of martensite variants σ_f^{RMV}.

The change in M_s, M_f, A_s and A_f by applied stress obeys the Clausius-Clapeyron equation [42]:

$$\frac{d\sigma}{dT} = -\frac{\Delta S^{\mathrm{P-M}}}{\varepsilon^{\mathrm{P-M}}} = -\frac{\Delta H^{\mathrm{P-M}}}{T\varepsilon^{\mathrm{P-M}}}$$

Eq. 2.1

where $\Delta S^{\mathrm{P-M}}$ is the entropy changes from the parent (austenite) to the martensite, $\Delta H^{\mathrm{P-M}}$ is the enthalpy change from the parent to the martensite, and $\varepsilon^{\mathrm{P-M}}$ is the strain caused by the transformation. This equation describes the effects of a uniaxial stress on martensitic transformation relationship between σ and T in a material in the parent phase state at a temperature T under free-stress conditions, and is transformed into the martensite state by an applied stress σ. In fact, since martensitic transformation is a shear-like mechanism, stress assists the martensitic transformation. It is therefore possible to induce martensite even at temperatures above M_s, which is the highest temperature for this phase to occur upon cooling, i.e. according to the contribution of the chemical driving force alone. This happens when the martensitic transformation is triggered through the stress, and the stress-induced martensite forms. The entropy change $\Delta S^{\mathrm{P-M}}$ is a constant negative value, while the transformation strain $\varepsilon^{\mathrm{P-M}}$ is a constant positive value, and thus the value of $-\Delta S^{\mathrm{P-M}}/\varepsilon^{\mathrm{P-M}}$ is usually a constant positive value.

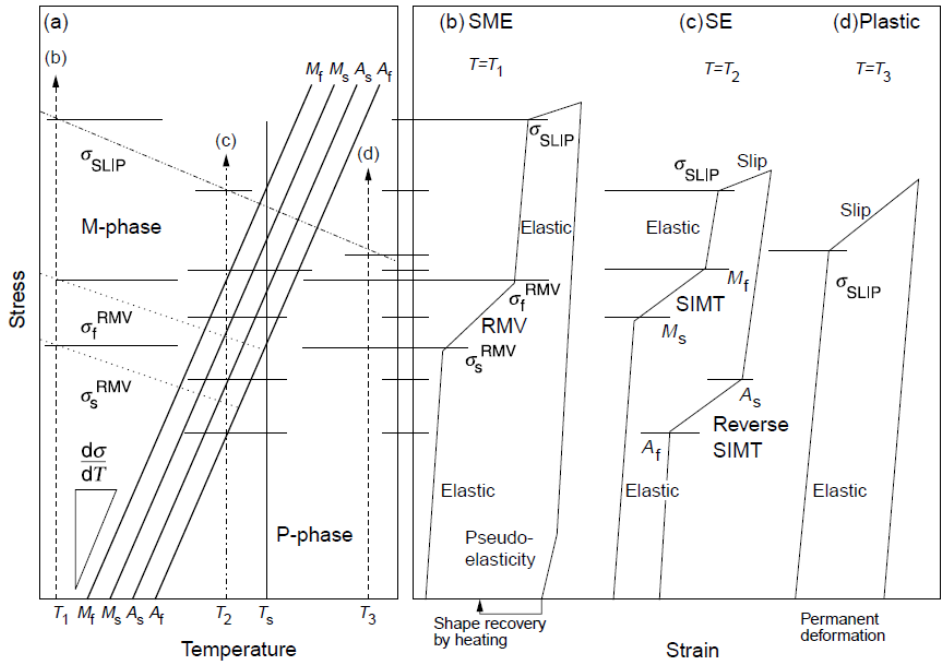

Fig. 2.19. (a) Temperature-stress diagram showing phase equilibrium in a shape memory alloy, and the corresponding stress strain-curves at (b) T=T1, SME; (c) T=T2, SE; (d) T=T3, plastic deformation. Each stress level is expressed by horizontal lines [42].

Three main temperatures are highlighted through dashed lines in Fig. 2.19, i.e. T_1, T_2, T_3, chosen as representative of the main cases of SMAs behaviors:

- $T = T_1$. The apparent phase is martensite (Fig. 2.19a). As an external stress σ is applied elastic deformation occurs followed by the reorientation of the martensitic variants (RMV), which starts as σ_s^{RMV}. RMV is a type of twin deformation and continuously takes place by increasing σ. When σ_f^{RMV} is reached almost all the material shows a single variant state. This corresponds to the maximum shape recovery strain. In fact, as σ is removed the shape change by reorientation is kept, and the strain can be recovered by heating over A_f. This is the shape memory effect. Above σ_f^{RMV}, elastic deformation takes place in the single-variant martensite. Then, plastic deformation by dislocation slip occurs as σ reaches σ_{SLIP}. After unloading and heating up to A_f, shape recovery happens but some amount of residual plastic deformation remains. As result of severe deformation, a small amount of pseudoelasticity can emerge upon unloading, which is a nonlinear shape recovery produced by a twin deformation of martensite variants due to the formation of an internal stress field caused by high density of dislocations. The corresponding stress-strain curve is displayed in Fig. 2.19b.

- $T = T_2$. The apparent phase is the austenite parent phase (Fig. 2.19a). Firstly, austenite is elastically deformed as σ is applied. When σ reaches the M_s line, the stress-induced martensitic transformation (SIMT) starts. The corresponding stress is also commonly termed as σ_{PE}, i.e. the stress at which the stress-induced martensitic transformation happens. Then deformation takes place due to the formation of preferentially oriented martensite variants up to the intersection with M_f. In this case, the reorientation of martensite variants phenomenon theoretically does not occur since as T_2 intersects M_s, the stress has already reached σ_f^{RMV}, thus preferentially oriented martensite variants are initially formed. The shape recovery occurs at the intersection of A_s line caused by the reverse martensitic transformation, and finished as A_f is reached. This is superelasticity. If σ increases and exceeds the intersection with M_f, almost all the material presents a single variant state. By further loading, elastic deformation followed by plastic deformation of single variant martensite occurs. Plastic deformation appears as σ_{SLIP} is reached. After the introduction of plastic deformation, shape recovery partially occurs upon unloading, and some amount of residual deformation persists. The corresponding stress-strain curves is displayed in Fig. 2.19c.
- $T = T_3$. In this case, plastic deformation by slip mechanism takes place. In fact, stress-induced martensitic transformation cannot occur since σ does not reach the M_s line before the intersection with σ_{SLIP}. This situation happens at temperatures higher than T_s, more frequently termed M_d. The corresponding stress-strain curves is displayed in Fig. 2.19d.

It can be stated that generally shape memory effect takes place at temperatures below M_f ($T < M_f$), while superelasticity appears above A_f, but only below M_d ($A_f < T < M_d$). Cases of more complicated behaviors, such as the coexistence of the two effects or phases, can verify at intermediate temperatures ranges. At temperatures between A_s and A_f ($A_s < T < A_f$), SE and SME coexist: the apparent phase is the parent phase, which when loaded transforms into stress-induced martensite (SE), but when the load is removed the austenite still present some residual stress that can be recovered by heating above A_f (SME). In the temperature range between M_f and A_s ($M_f < T < A_s$), SME occurs: usually both phases appear, and the already present martensite reorientates depending on the applied stress, while the austenite transforms into stress-induced martensite at the critical stress to induce

martensite, then martensite is stable and does not transform into the parent phase by removing the applied stress but only by heating above A_f (SME) [42].

The deformation mechanisms described above are summarized in Fig. 2.20.

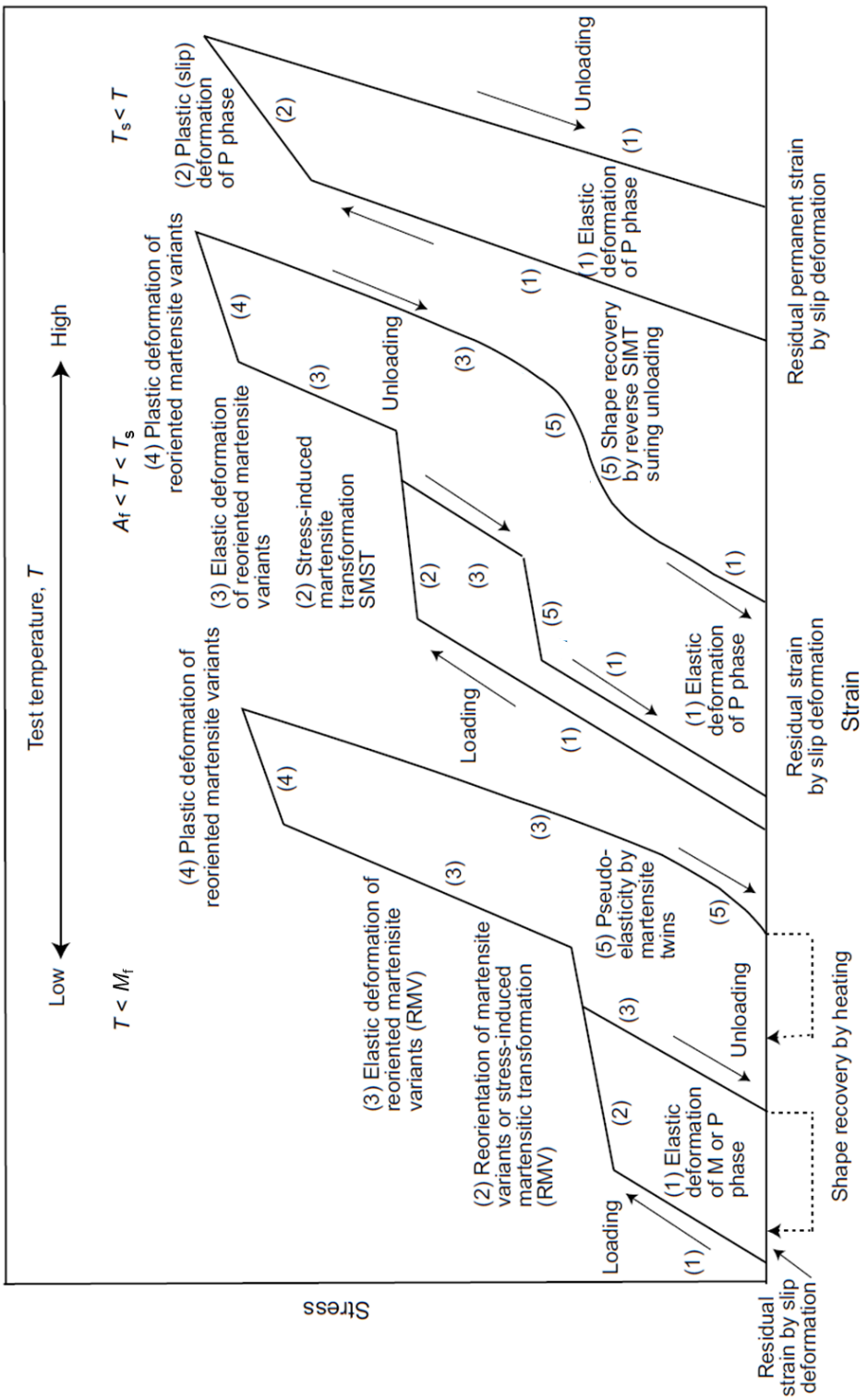

Fig. 2.20. Stress-strain curves of a SMA and the corresponding deformation mechanisms at three typical temperatures: $T<M_f$, $A_f<T<T_s$ and $T_s<T$. The mechanisms described for $T<M_f$ are referrable also for the more generic case $T<A_s$ [42].

For practical purposes, a more simplified and clear temperature-stress diagram is illustrated in Fig. 2.21, where the areas corresponding to the occurrence of shape memory effect and superelasticity (here termed "transformation pseudoelasticity") are highlighted. The line with a positive slope represents the critical stress to form stress-induced martensite, which above A_f is often called σ_{PE}. The lines with a negative slope (A, B) represent two different situations of critical stress for slip depending on the material properties. Focusing on the superelastic effect ($T > A_f$), if the considered material presents a very low critical stress (as in the case B), the irreversible slip process occurs before the critical stress for stress-induced martensite is reached. Therefore, in this case good superelasticity is not expected. On the other hand, if the critical stress for slip is high enough (as in the case A), above A_f the stress-induced transformation occurs at a stress higher than the critical stress to induce martensite. Since the formed martensite is completely unstable at temperatures above A_f in the absence of stress, upon unloading the reverse transformation takes place, forming again austenite and allowing the occurrence of the superelastic effect.

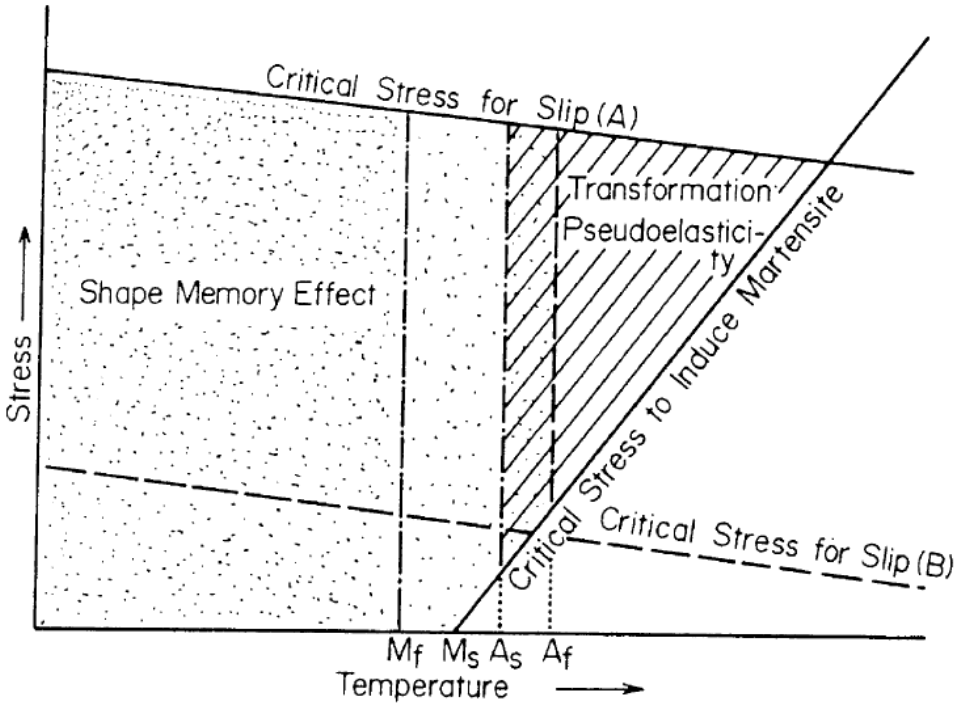

Fig. 2.21. Temperature-stress diagram of the appearance of shape memory effect and superelasticity, here termed as "Transformation Pseudoelasticity" [62].

For completeness, another temperature-stress diagram better highlighting the superelasticity window is reported in Fig. 2.22, where also M_d temperature is indicated.

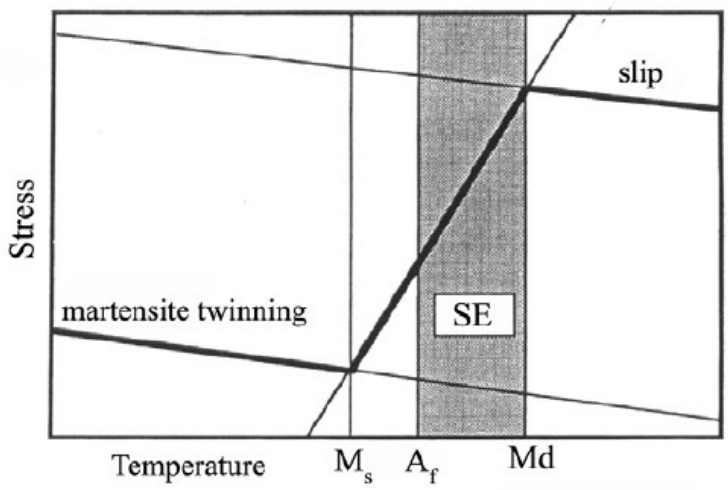

Fig. 2.22. Temperature-stress diagram pointing out the SE window bonded by M_d temperature [39].

Based on what reviewed above, it is almost impossible to see complete superelasticity in NiTi single crystal alloys in solution treated condition [63]. In fact, this case presents very low critical stress for slip compared to the critical stress to induce martensite (similarly to case B in Fig. 2.21). On the other hand, polycrystal samples can exhibit complete superelasticity at temperatures above A_f, due to the grain refinement phenomenon [47]. Superelasticity is also typically observed for aged Ni-rich alloys, where the critical stress for slip is increased due to cold working or precipitation hardening. These aspects are better discussed in Paragraph 2.5.2.

The window through which SE and SME behaviors appear is crucial for NiTi applications, and both the TTs and the critical stress for slip deformation dictate this region. Therefore, in order to improve SE and SME, control of these factors is essential.

2.5.1 Control of the transformation temperatures

The most important factors affecting TTs are Ni content, ternary alloying elements, precipitation in Ni-rich NiTi alloys, aging heat treatments, and defects [64].

The effect of Ni content on M_s is reviewed in many works, as displayed in Fig. 2.23, where it can be seen that a variation of 1% in the Ni content of Ni-rich NiTi alters M_s by 100 °C. Changing the chemical composition is thus the most effective way to change TTs. The TTs on the Ti-rich side are instead nearly constant, probably due to the limited solubility of NiTi on this side. It should be noted that the high sensitivity of TTs to chemical composition

is mainly undesirable, since it implies that a very accurate composition control is mandatory to obtain the desired TTs or properties.

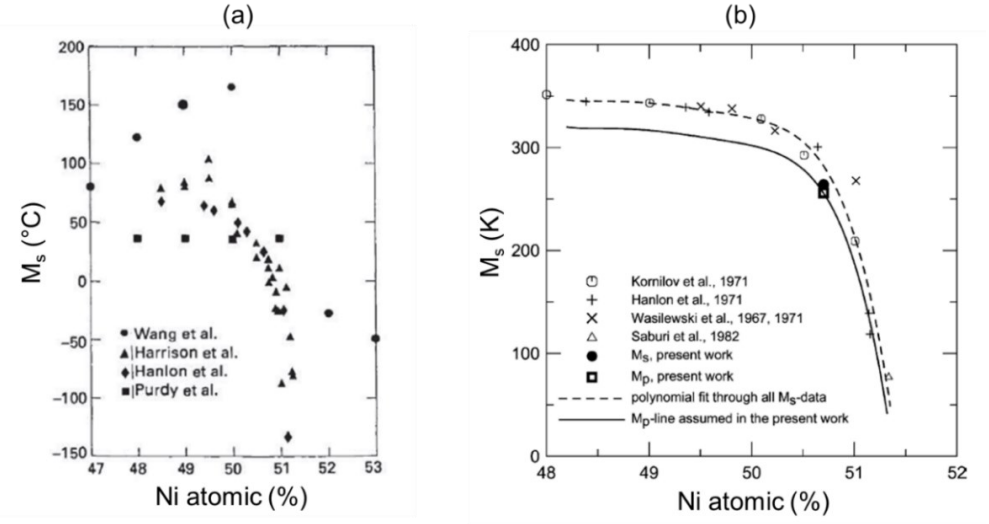

Fig. 2.23. Dependence of M_s on composition reviewed by: (a) Melton [65], and (b) Khalil-Allafi et al. [66] for a fully homogeneized alloy (i.e. solution treated).

Regarding the tertiary alloying elements, Pt, Zr, Hf, Pd and Au were found able to increase the TTs. NiTiHf, NiTiZr, NiTiPd are in fact candidates for high-temperature shape memory applications [33].

A common way to adjust TTs of Ni-rich NiTi alloys after the making of the alloy is through aging, in particular through the precipitation of particles from the quenched supersaturated NiTi solid solution. Aging causes precipitation of Ni-rich precipitates, such as Ni_4Ti_3, which alter the B2 matrix composition, typically causing an increase in TTs. Through the control of aging parameters (temperature and time) it is possible to modify the TTs of Ni-rich alloys. In fact, although the shape memory properties are based on diffusionless martensitic transformation, diffusional precipitation reactions can allow the control over it [33].

2.5.2 Control of the critical stress for slip deformation

The critical stress for slip deformation can be controlled through the following methods: work-hardening, grain-refinement, precipitation hardening or a combination of these [33]. The other strengthening mechanism commonly known in physical metallurgy is alloy-hardening, which, however, in NiTi alloys is also strongly related with the TTs and therefore is not of practical use. Examples of these various methods are discussed below for different NiTi alloys.

The effects of grain refinement on the superelastic behavior of 50.5-NiTi fully annealed at 800 °C for 1 h followed by water quenching is reported in Fig. 2.24. In this study, tensile tests were conducted at 40 °C, which corresponded to a temperature of A_f + 10 °C. The dashed lines below the x axes represents the strain recovered by heating the material above A_f. It is evident that by refining the grain size an improvement of superelasticity can be achieved [47, 67, 68].

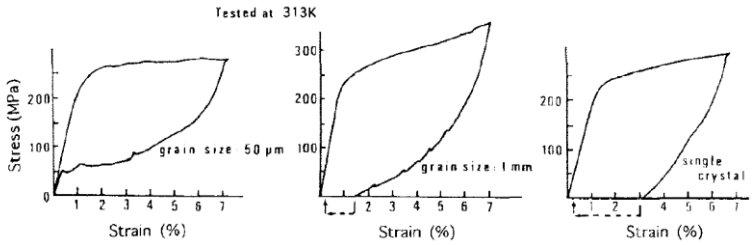

Fig. 2.24. Effect of grain refinement on the pseudoelastic behavior of NiTi alloy [68].

The influence of work-hardening on tensile stress-strain behavior as function of temperature for 49.8-NiTi is shown in Fig. 2.25. After solution annealing at 1000 °C followed by low temperature annealing at 400 °C for 1 h, the sample presents permanent strain at all temperatures and does not show superelasticity in any temperature range (Fig. 2.25a). This is because in a solution treated material the resistance to slip is low. It should be noted that the low temperature annealing did not alter the microstructure of the solution annealed and no precipitation hardening occurred, due to the Ti-rich chemical composition of the alloy. On the other hand, after cold working and annealing at 400 °C for 1 h, the specimen exhibits large superelastic deformations, as well as good SE and SME characteristics with no plastic deformation (Fig. 2.25b).

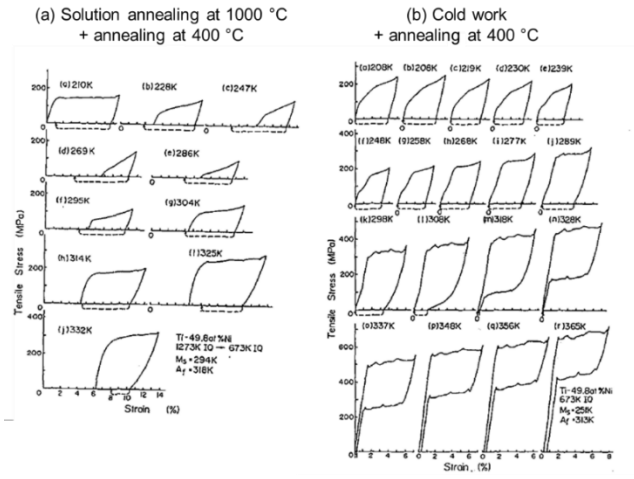

Fig. 2.25. Effects of the thermomechanical treatment on a 49.8-NiTi alloy: (a) Solution annealing at 1000 °C for 1 h and annealing at 400 °C for 1 h; (b) cold work and annealing at 400 °C for 1 h [56].

The reason for these behaviors can be understood by referring to Fig. 2.26, which displays the TEM observations of this alloy after similar thermomechanical treatments [33]. After cold working, a larger amount of tangled dislocation networks is found, that are responsible for the increase in the critical stress for slip deformation (Fig. 2.26a). By annealing at 400 °C after cold working, dislocations are re-arranged, and no recrystallization is present (Fig. 2.26b). After annealing at 500 °C recrystallization is evident (Fig. 2.26c). The specimen annealed at 500 °C showed worse superelasticity compared to the one annealed at 400 °C. After annealing at 600 °C (Fig. 2.26d), the superelastic behavior was found to be inferior, and the specimen exhibited grain growth following recrystallization.

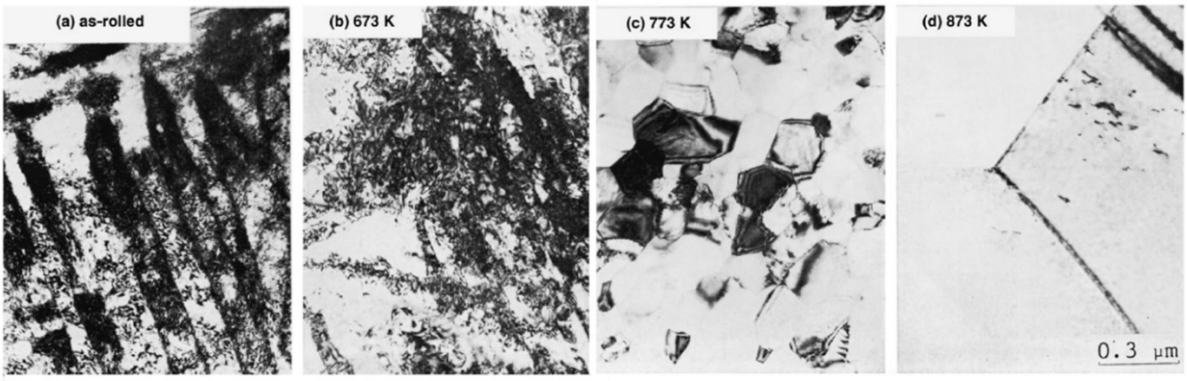

Fig. 2.26. TEM images of 49.8-NiTi: (a) cold-rolled, cold-rolled and annealed at (b) 400 °C, (c) 500 °C, (d) 600 °C [33].

Concerning the precipitation hardening in NiTi, as discussed in Paragraph 2.4.1, it commonly involves the formation of Ni_4Ti_3 through aging, which strengthens the B2 matrix [55, 56]. The effects of different aging treatments on the enlargement of the temperature window for the occurring of SME and SE can be seen in Fig. 2.27, which displays the stress-strain behavior of 50.6-NiTi alloy after solution annealing at 1000 °C and aging at both 500 °C (Fig. 2.27a) and 400 °C (Fig. 2.27b). After aging at 500 °C, SE is observed in a very narrow temperature window, and SME is incomplete due to the permanent residual deformation after heating. On the other hand, superior SE and SME features were found after aging at 400 °C, as well as a larger SE temperature window. This can be explained referring to the TEM micrographs displayed in Fig. 2.28. A higher density of small sized Ni_4Ti_3 precipitates can be observed in the sample aged at 400 °C, while a lower density of larger precipitates is seen in the specimen aged at 500 °C. Therefore, the increase of critical stress for slip is most effective with high-density small precipitates, which agrees with the physical metallurgy principles.

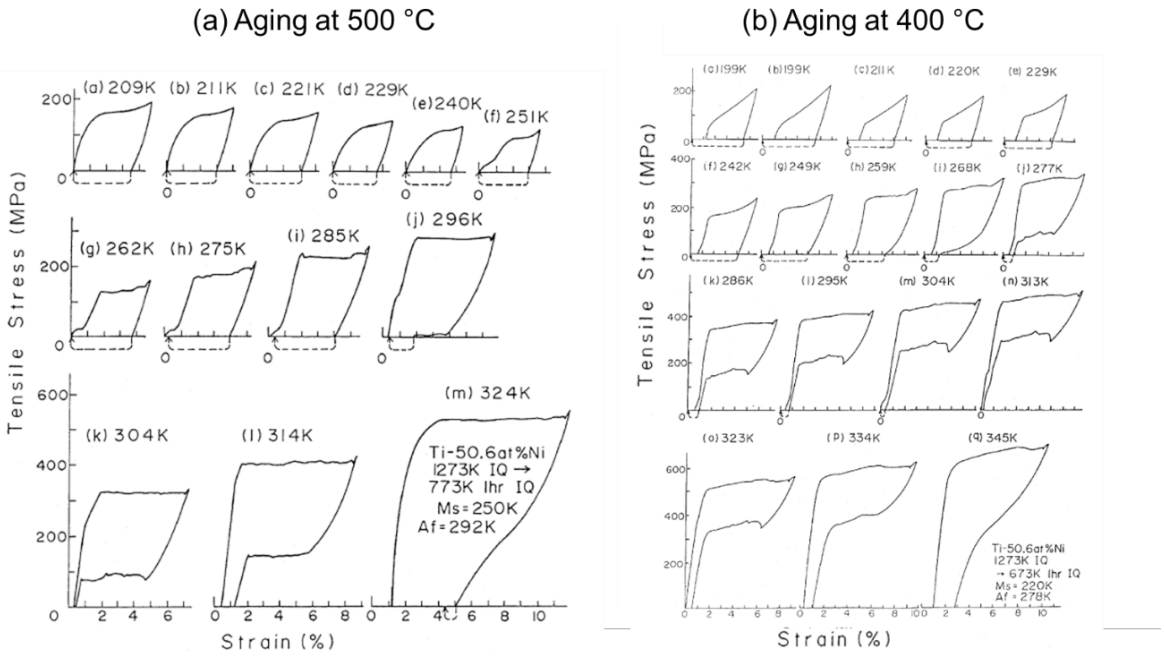

Fig. 2.27. Stress-strain curves of 50.6-NiTi alloy aged at (a) 500 °C and (b) at 400 °C for 1 h after solution annealing at 1000 °C for 1 h [33].

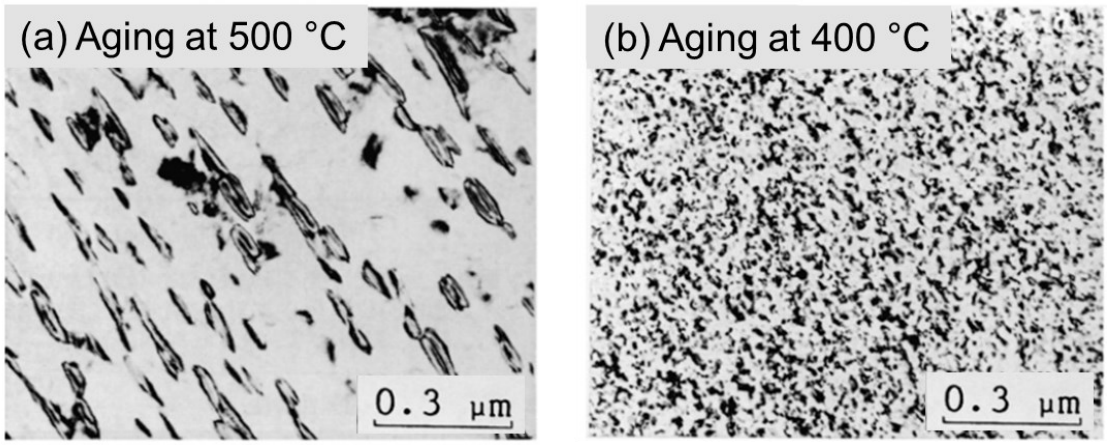

Fig. 2.28. TEM micrographs comparing 50.6-NiTi samples aged at (a) 500 °C and (b) 400 °C for 1 h after solution annealing at 1000 °C for 1 h [33].

It was reported that aging at 300 °C is not useful to improve shape memory characteristics, since at this temperature the precipitation kinetics are slow, and longer aging times is required for the formation of high density of precipitates [33].

The combination of work-hardening and age-hardening was also found to be effective in increasing the critical stress for slip. This is shown for a 50.6-NiTi cold worked and aged at 400 °C without solution treatment in Fig. 2.29. By comparing Fig. 2.29 to Fig. 2.27b, it appears that complete superelastic effect is exhibited at higher stresses after cold working and aging. However, a complex microstructure may result from the combination of work-

hardening and age hardening, where large densities of dislocations and precipitates are interwoven, since precipitates may occur mainly on dislocations (Fig. 2.30). This generates obstacles for the movement of dislocation and may hinder the recovery process [69-71].

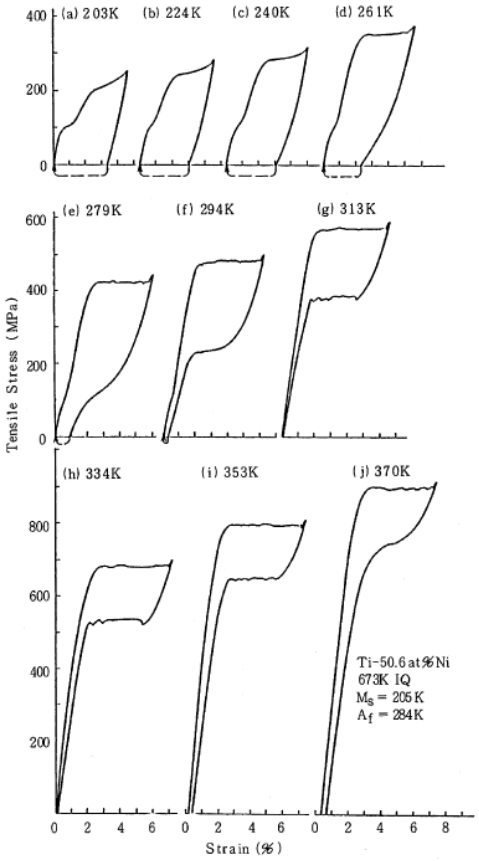

Fig. 2.29. Stress-strain curves as function of deformation temperature for 50.6-NiTi alloy cold worked and aged at 400 °C [33].

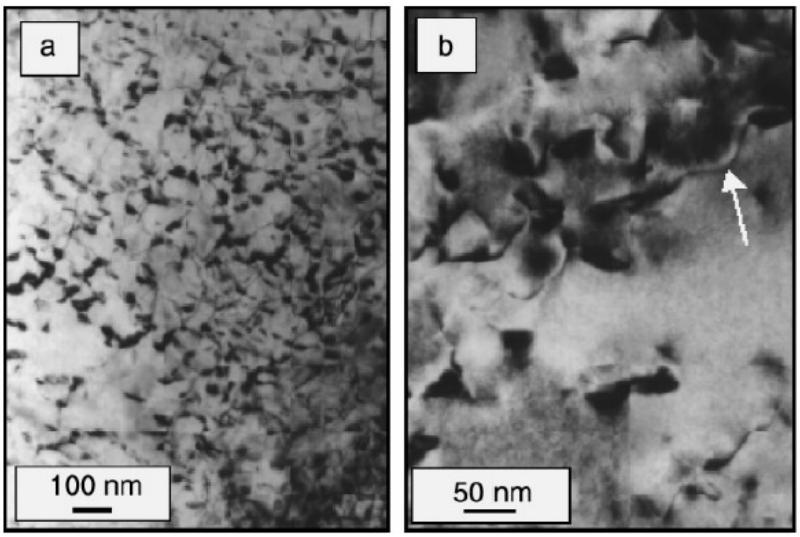

Fig. 2.30. Ni_4Ti_3 precipitates decorating the dislocations in 50.6-NiTi alloy after cold working and aging at 400 °C for (a) 2 h and (b) 4 h [69].

2.6 SUPERELASTICITY FOR BIOMEDICAL APPLICATIONS

One of the main applications for NiTi alloys involves its use in manufacturing biomedical devices. Biocompatibility is the ability of a material to perform with an appropriate host response in a specific application [72]. The biocompatibility of NiTi alloys has been widely studied according to corrosion resistance, Ni-ion release, and cytotoxicity, which are the main aspects to take into account [59]. In fact, the biocompatibility of a material is largely controlled by the surface chemistry and properties. The high biocompatibility demonstrated by NiTi is mainly attributable to the formation of a natural Ti oxide layer (TiO_2) on its surface, which provides excellent corrosion resistance and prevents toxic and allergy reactions by avoiding Ni-ion release. Furthermore, this oxide layer can be thickened through passivation procedures and other appropriate surface modifications can be also carried out on NiTi surface, such as mechanical treatments, etching, electropolishing or deposition of bioactive coatings. In addition, the nature of NiTi, which is close to that of an intermetallic, implies a strong interatomic bond between Ni and Ti with respect to other alloys, preventing the ion release and further ensuring biocompatibility.

2.6.1 The use of superelastic NiTi

Among the two peculiar properties exhibited by NiTi alloys, the superelastic effect is the most widely used in the biomedical field [73]. This because the constant temperature of human body, i.e. 37 °C, was found to be ideally suited to the superelastic temperature range of NiTi [74]. In this way, there is no need to provide external heat source or temperature variation to trigger the effect, as instead requires the shape memory effect. Furthermore, NiTi superelasticity is exploited in biomedical applications thanks to the ability to generate a constant force as well as a large shape recovery over a long activation span [75].

In addition to biocompatibility, a specific biomedical component needs to perform desirable function in contact with body tissue. This involves its mechanical behavior, also referred to as biomechanical behavior. Biomechanical compatibility is obtained when an implant is elastic, has stress-strain behavior close to that of the tissue, and exhibit similar hysteresis in the loading/unloading cycle [76]. In this regard, the elastic modulus of the implant plays a crucial role, since it must match that of the specific bone in contact, for instance in the case of an orthopedic device [76]. By matching the elastic moduli, the distribution of stresses is uniform and homogeneous for both the implant and the bone, thus stimulating the fracture healing. This, together with the density matching, prevents the stress-

shielding phenomenon[6], as well as trauma to the surrounding tissues. Some examples of biomedical devices in relation to the NiTi properties are discussed below, while the main NiTi applications are listed in Paragraph 2.6.2.

NiTi has unique properties that can reproduce those of human tissue and bones, as the stress-strain behavior is consistent with those of human bones and tendons [77]. Fig. 2.31 compares the mechanical behavior of living tissues (smooth curves) to that of various superelastic NiTi constructs (curves with experimental points) and points out their high biomechanical compatibility.

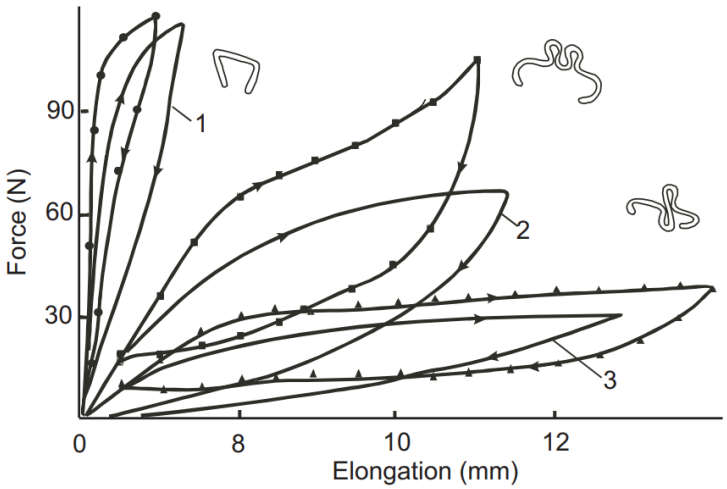

Fig. 2.31. Mechanical behavior of living tissues (smooth curves) and various NiTi constructs (curves with experimental points). Smooth curves: 1 cortical bones, 2 interspinal ligament, 3 fibrous tissue [76].

The comparison between the elastic modulus of bones to that of metallic materials commonly used for manufacturing orthopedic implants is reported in Table 2.2. Among other alloys, it is evident that porous NiTi presents the elastic modulus closest to that of bone. The development of porous NiTi has allowed this material to be used in a wide range of biomedical applications [78, 79]. Thanks to its controllable open structure, the ingrowth of the bone tissue into the implant is possible, as well as its firm fixation. The combination of superelasticity and the permeable structure of the porous implants allowed the introduction of NiTi as a soft tissue reconstruction implant in gynecology and digestive tract surgery [77], as well as in substitution to bones in oral and maxillo-facial surgery [80, 81]. Moreover, it was recently reported that porous NiTi produced by laser powder bed fusion is suitable for human mesenchymal stem cells [82].

[6] Alteration of the distribution of the human physiological stresses. This can lead to a reduction in bone density (osteopenia).

Table 2.2. Comparison between bone and biocompatible materials elastic modulus [82].

	Bone	Porous Nitinol	Titanium	Austenitic stainless steel	Co-based alloys
Elastic Modulus (GPa)	0.3-20	28	110	190	193

Fig. 2.32 compares stress-strain curves of different alloys typically used for orthodontic applications, such as archwires. The slope of the curves represents the elastic moduli of the material. Most of the biomedical devices work in a well-defined range, in which the applied force is such that it encourages the optimum biological response, i.e. the optimal force zone. Above the optimal force zone is located the excessive force zone, which can result in tissue damage. On the other hand, the range of force below the optimal force corresponds to the suboptimal force zones (ε_0), where the efficiency of the device is compromised. An effective strain range (ε_{eff}) corresponds to the optimal force zone, which varies depending on the elastic modulus of the material used. Two examples of elastic orthodontic wires produced through different materials are shown in Fig. 2.32. In detail, a high elastic modulus alloy (Fig. 2.32a) results in a reduced effective strain range compared to a low elastic modulus alloy, such as NiTi (Fig. 2.32b). Therefore, it is possible to have a greater range of activation if a low elastic modulus alloy is used. This results in the achievement of greater displacements, and therefore in the need of fewer adjustments for the archwire to move the tooths in the final position. Therefore, the low elastic modulus of NiTi makes it one of the most successfully used material in the orthodontic field [75].

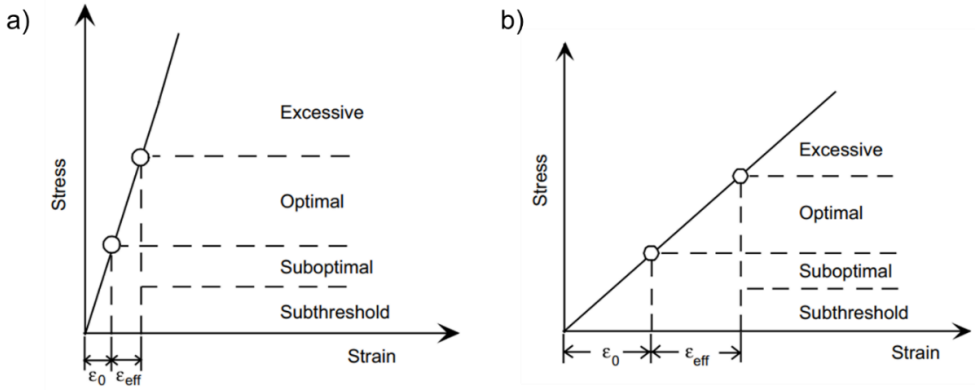

Fig. 2.32. Schematic stress-strain curves of elastic orthodontic wires with (a) high elastic modulus, (b) low elastic modulus [83].

The same aspect is shown in Fig. 2.33, where NiTi exhibiting superelastic features is compared to a conventional elastic material, that is stainless steel. As previously mentioned, an effective strain (deflection) range corresponding to the optimal force zone is larger in the

case of NiTi, resulting in the ability to accommodate a wide strain when loaded thus enabling the archwire to exert a constant stress as the teeth move [84]. Consequently, fewer archwire changes are required, as well as less painful retightening, making NiTi the preferred material for this kind of application.

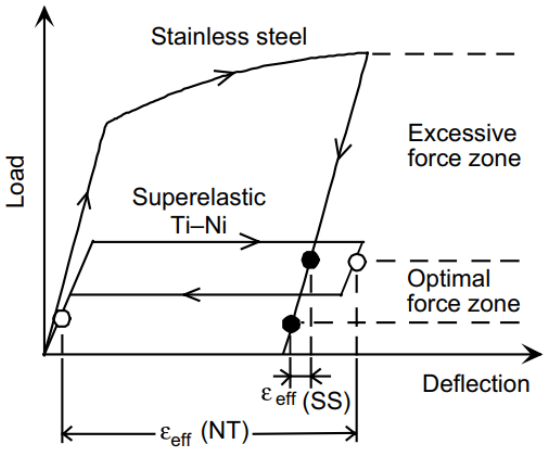

Fig. 2.33. Comparison of load-deflection curves of superelastic NiTi and conventional elastic stainless steel [83].

2.6.2 Applications

2.6.2.1 Orthopedic and dental applications

NiTi alloys have a large number of applications in the orthopedic field. It results particularly attractive for the treatment of bones fractures through bone plates, staples or smart intramedullary rods (Fig. 2.34) [85].

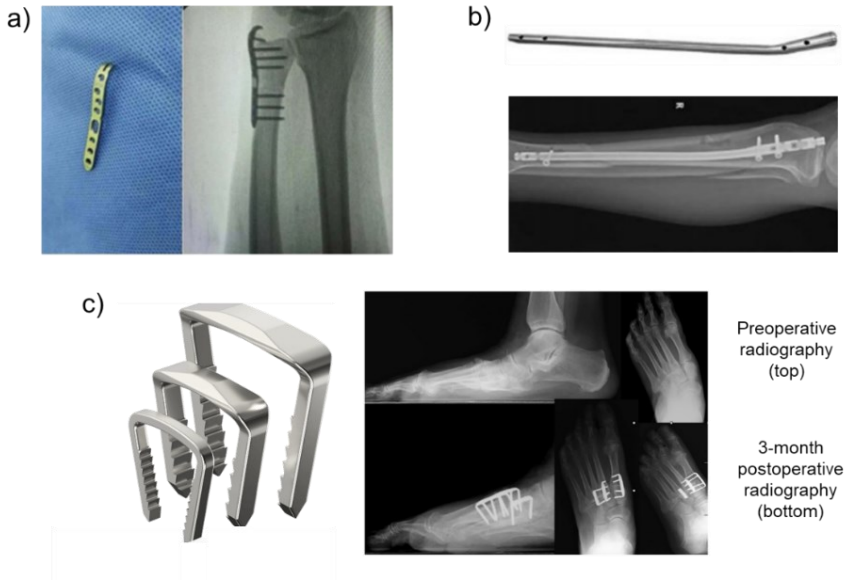

Fig. 2.34. Examples of orthopedic devices with examples of the X-ray of their placement in the human body: (a) plates [86], (b) intramedullary rods [86] and (c) staples [87, 88].

All these devices exploit the superelasticity of NiTi, as they are placed inside the edges of the two broken bones in a different ("open") configuration, thus generating low and constant stress arising from the attempt to recover the previous shape (Fig. 2.35). This is useful to join broken bones and therefore to accelerate the healing process.

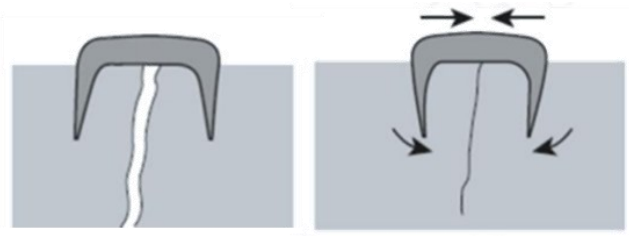

Fig. 2.35. Schematization of the working of a NiTi staple [89].

As previously discussed, NiTi is also widely used for orthodontic applications (Fig. 2.36), such as orthodontic archwires and tooth clips, fixators, implants, and devices for root channel surgery.

Fig. 2.36. Examples of orthodontic applications for NiTi [90, 91].

2.6.2.2 Self-expanding stents and other endovascular devices

Most of the applications of NiTi alloys are related to endovascular devices, with the aim of providing minimally invasive treatment instead of major surgery [85].

Self-expandable stents constitute the most popular endovascular application of NiTi. Stent devices are characterized by a tubular structure and are placed in the lumen of an anatomic vessel or duct to maintain patency. Any tubular passage can be supported by stents, some examples are the esophagus and bile duct or blood vessels, such as coronary, carotid, iliac, aorta and femoral arteries. Stents radially sustain the inner wall of vessels or organs, assuring the passageway open and preventing it from closing.

One of the most widely used types of stents are coronary stents, which are placed in the coronary arteries that supply blood to the heart. Their function is to keep the arteries open

and allow blood to flow to the heart in patients suffering from coronary heart disease. The narrowing of coronary artery can result from the buildup of abnormal plaque or cholesterol deposits on the inner walls of the arteries (atherosclerosis), as well as the progressive loss of elasticity of the walls of arteries, resulting in their abnormal thickening (arteriosclerosis). These cardiovascular diseases affect a significant portion of the global population and thus have a widespread impact on global health. In this regard, stent devices placed through angioplasty procedure offer minimally invasive alternative to the traditional procedures like coronary arteries bypass grafting (also known as bypass surgery). Bypass surgery involves the creation of a new path for blood to flow around the blocked artery in an open-heart surgery by using healthy blood vessels from another part of the body. On the other hand, the coronary angioplasty with stent placement[7] consists in the insertion of a catheter (a thin tube) into a blood vessel, usually in the wrist, arm or groin, which is then guided to the blocked coronary artery through a guide wire. Once the catheter is placed, the stent is expanded by inflating a balloon (balloon-expanding stent) or during the deployment itself (self-expanding stent). This approach has multiple advantages, due to the fact that is a minimally invasive endovascular procedure performed percutaneously, which allows the reduction of the recovery time, risk of complication and hospital stays. The comparison of the two techniques is displayed in Fig. 2.37.

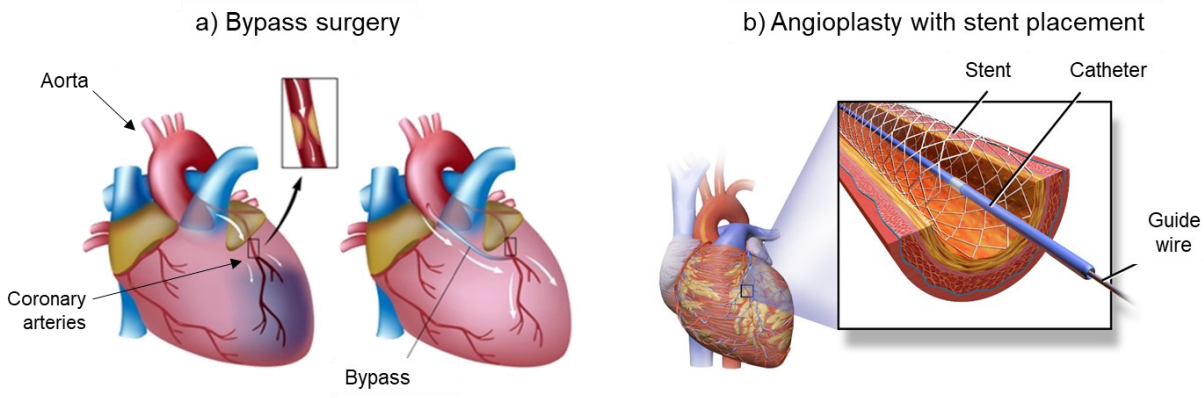

Fig. 2.37. Comparison between (a) bypass surgery [92] and (b) angioplasty with stent placement [93].

Generally, stents are classified as balloon-expanding or self-expanding depending on how the deployment is done. Balloon-expanding stents are fabricated in the crimped state and expanded to the vessel diameter by inflating in a balloon and plastically deforming the stent (Fig. 2.38a). On the other hand, self-expanding stents are manufactured with a diameter

[7] Angioplasty procedure can also be done without stent placement. In this case the expansion of blood vessel is done by the expanding of a balloon catheter passed over a guide wire and then inflated to a fixed size.

slightly higher than that of vessels and are subsequently constrained in a delivery catheter. During the deployment, the catheter (and therefore the constraint) is removed, and the stent expands elastically until it hits the vessel wall, where it continues to exert an outward force (Fig. 2.38b). Balloon-expanding stents are commonly made of stainless steel or cobalt-chrome and are sometimes subjected to failure in achieving the predicted stent diameter during deploying [94]. This makes the self-expanding stents, which are commonly made with NiTi, the preferred ones.

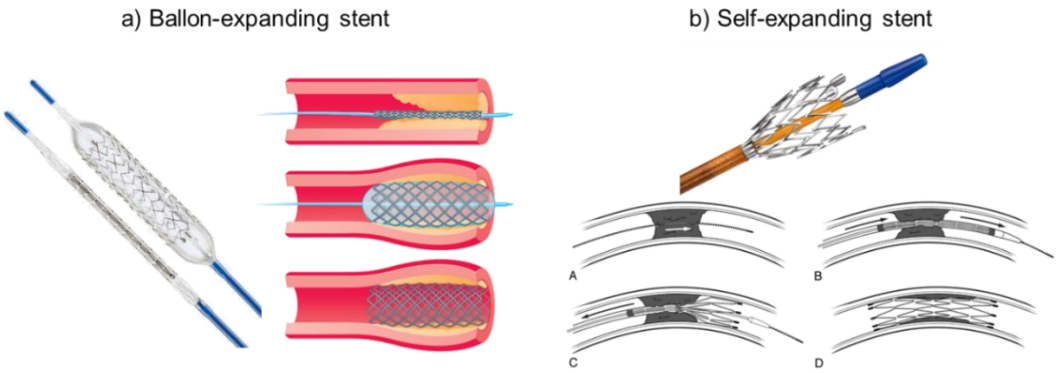

Fig. 2.38. Representation of (a) balloon-expanding [95] and (b) self-expanding stents [96, 97], together with their characteristic deployment.

One of the most unusual characteristics of NiTi is the stress hysteresis, which results in a feature named biased stiffness [98], which is shown Fig. 2.39, where a schematic stress-strain curve transposed onto a hoop force-diameter diagram of a self-expanding NiTi stent is represented. After the first linear increase in stress with strain, in the loading plateau large strains can be obtained by applying small stress increase, then, upon unloading, the stress decreases rapidly until the unloading plateau is reached, where strain is recovered with only a small decrease in stress.

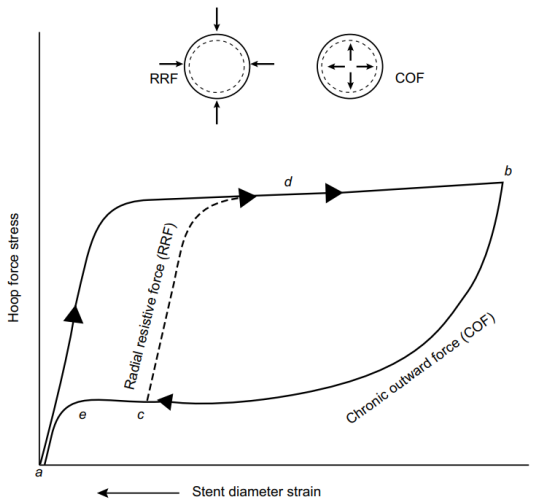

Fig. 2.39. Operating graph of a NiTi self-expanding stent [98].

By means of the graph in Fig. 2.39, the entire cycle of a NiTi self-expanding stent can be explained, i.e. its crimping into a delivery system, its deployment and the interactions with the vessels. A stent characterized by a larger diameter than the vessel for which it is intended (point a, Fig. 2.39) is crimped into a delivery system (b). Then, the stent is released into the vessel and expands from point b until it is stopped by the contact with the vessel itself (c). At this point, the stent continues to exert a low and constant force, named *chronic outward force* (COF), since it cannot completely expand to its pre-set shape due to its higher diameter compared to the vessel. Thanks to COF, NiTi self-expanding stents are able to sustain the vessel internal walls and to maintain patency. Furthermore, these devices also resist recoil pressures and any external compression forces dictated by the loading curve from point c to d, which is steeper than the unloading line (towards point e). These forces are called *radial resistive forces* (RRF). A typical example of external compression force is the one arising from the artery compression of the walls during the relaxation of the cardiac cycle (diastole).

The peculiar behavior of NiTi leads the stent to act on the vessel wall with a continuing opening force, which remains very low even through high deflections and oversizing of the stent. Generally, the diameter of the stent is 1-2 mm larger than the target vessel.

A variant of the traditional stents are graft stents, which combine the NiTi metallic structure with graft materials and thus offer enhanced support and flexibility. These devices are used in treating complex vascular conditions such as aneurysms and peripheral artery diseases.

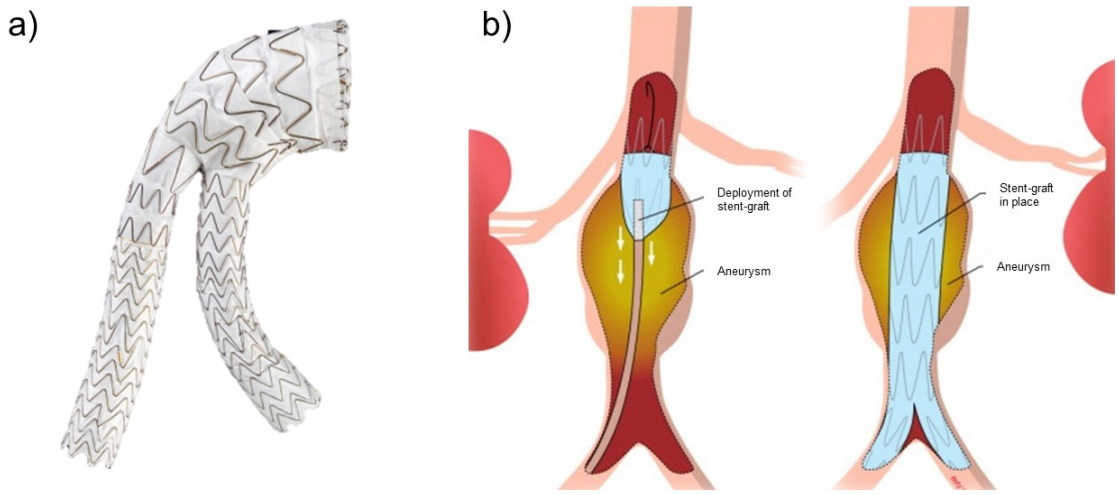

Fig. 2.40. (a) Aortic stent graft (GORE®) [99] and (b) a schematic representation of its deployment [100].

Stent applications require other properties including crush resistance, to ensure resistance to impacts that can affect the patency, kink resistance, flexibility and radiopacity. High radiopacity enables the stent to be visualized during medical surgery procedure and post-operative monitoring through imaging techniques such as X-ray radiography or CT tomography. Commonly, in NiTi self-expanding stents, tantalum radiopaque markers are added to their ends to improve radiopacity.

Similarly to self-expanding stents, NiTi is commonly used for other endovascular devices. An example is the TrapEASE® vena cava filter (Fig. 2.41), which is used to stop blood clots which migrate up from lower extremities through the vena cava and into the lungs, thus preventing the pulmonary embolisms. This filter is deployed into the vena cava through a catheter and is held on its walls by the sharp anchors. In this way, clots migrating through the vena cava are intercepted by the filter and remain there until they safely dissolve in the blood flow.

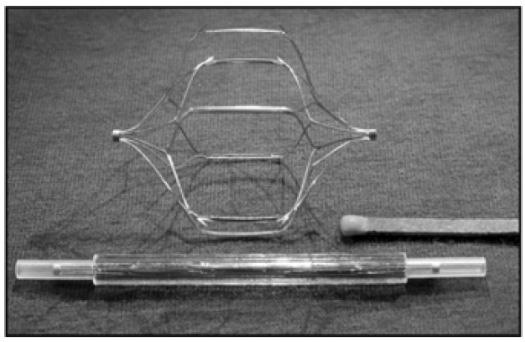

Fig. 2.41. NiTi TrapEASE® device, vena cava filter which expands to 28 mm as deployed from a sheath of 2 mm [73].

Another device intended to filter large embolized blood clots in the vena cave vein is the Simon vena cave filter, displayed in Fig. 2.42. [101].

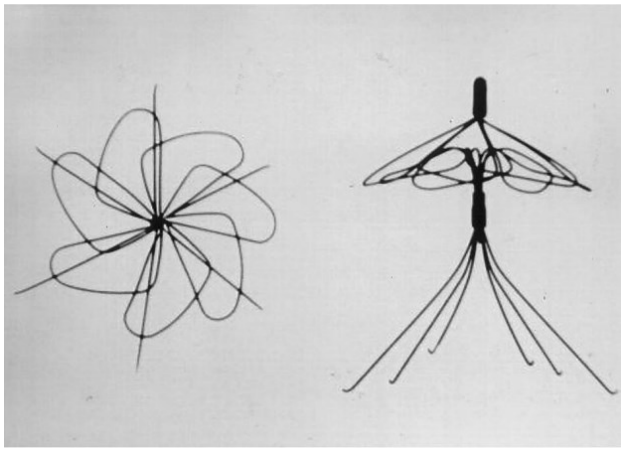

Fig. 2.42. Simon vena cava filter [101].

NiTi is also used for the GORE® CARDIOFORM Septal Occluder (Fig. 2.43), which is a device used for the closure of atrial septal defects or patent foramen ovale. Both these are congenital heart conditions that affect the structure of the heart, since they involve an abnormal opening or hole between the atria of the heart, which can lead to complications such as stroke, heart failure or arrhythmia. This device is composed of a platinum-filled NiTi wire frame covered with expanded-PTFE, forming two independent disks that are positioned before and after the defect allowing its closure. The e-PTFE enables conformability and rapid tissue ingrowth, while NiTi allows the device to adapt to the anatomy of the heart as well as to be deployed into a catheter, minimizing the risk associated with the surgery.

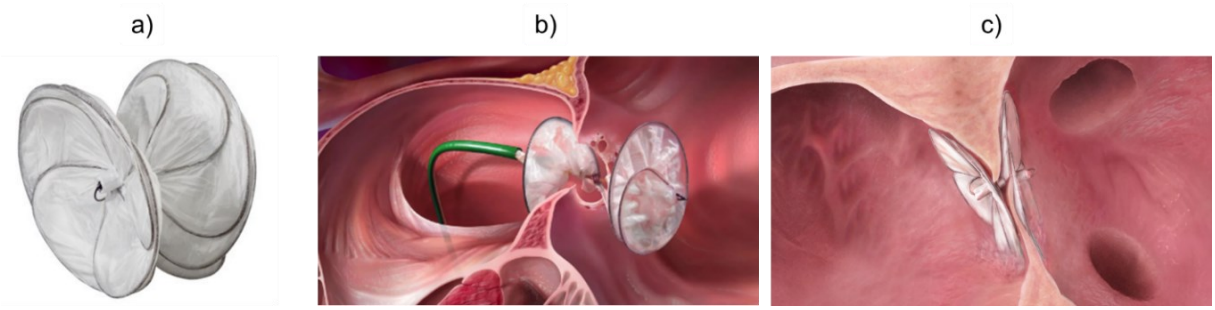

Fig. 2.43. (a) GORE® CARDIOFORM Septal Occluder, (b) its deployment through the catheter, (c) its anchoring between the two heart atria which allow the closure [102].

In general, all these devices made with NiTi or other SMAs have contributed to the implementation of the methodologies and approaches of modern medicine, by enabling the transition from invasive and complicated procedures to minimally invasive interventions done by endovascular and percutaneous way. The unique properties of these materials allowed the development of devices that can pass through blood vessels in a crimped state and expanded once in place recovering their original shape.

An additional possibility for NiTi endovascular devices that was initially considered is the deployment through the shape memory effect. The intention was to insert the device into a catheter while in the martensitic state, and upon release warming it by the surrounding blood, making it recover its “programmed” shape. However, thermal deployment has proven to be impractical because of the challenges in maintaining a device reliably cool in the martensitic state until it is correctly positioned [73].

2.6.2.3 Surgical instruments

NiTi alloy is also widely used for instruments and devices for minimally invasive procedures, such a guide wires, dilators, retrieval baskets to remove stones or fragments from

the urinary or respiratory tract, graspers or microforceps for neurosurgery (Fig. 2.44). Extreme flexibility, kink resistance, torquability, steerability and low forces required for bending are the reasons of choosing NiTi for these applications.

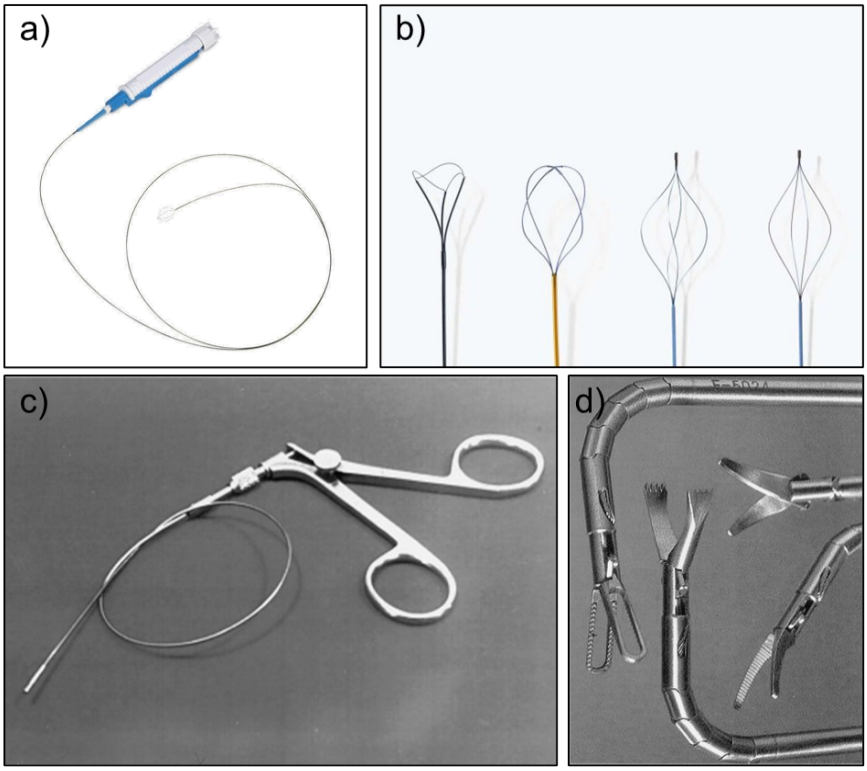

Fig. 2.44. Examples of NiTi surgical instruments: (a) retrieval basket for respiratory tract [103], (b) retrieval baskets for urinary tract [104], (c) graspers [101], (d) microforceps [101].

2.7 FABRICATION TECHNIQUES FOR NITI

The realization of NiTi devices includes a series of combinations of different and individually selected processes, and there is not a single fabrication recipe, since the processing route depends on the desired properties, shape, and application. Various fabrication methods for NiTi components are summarized in Fig. 2.45.

Regarding the raw materials, the nickel used in NiTi alloys is extracted electrolytically from nickel chloride sodium by electrowinning, while the titanium used can be either sponge titanium or ingots obtained by remelting sponge titanium [105]. Sponge titanium is produced through the Kroll Process, during which titanium is extracted from titanium ore.

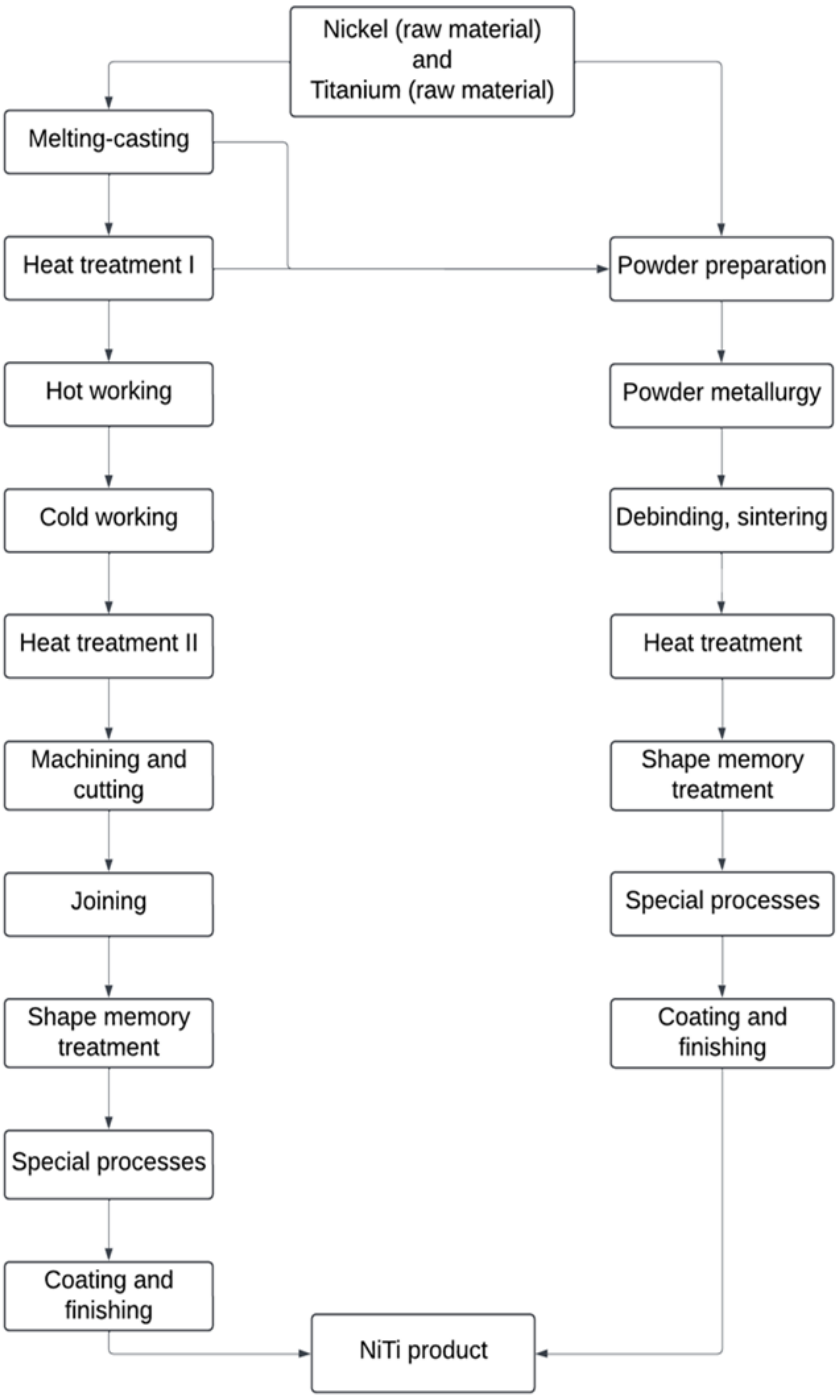

Fig. 2.45. Various routes used to fabricate NiTi products [105-107].

It is well established that process parameters and steps have a significant impact on the properties of NiTi. Therefore, considerable efforts are required for each process or process step, in order to properly take into account these sensitive properties. Each process must be properly and thoroughly understood in manufacturing high-quality NiTi parts, also considering how it affects the properties.

The main processes used for NiTi fabrication are described in the following paragraphs.

2.7.1 Melting and casting

One of the most common conventional methods to fabricate NiTi is through melting and casting. This process involves high temperature melting and alloying, which is always associated with an increase in the impurity level. As a result, these procedures require substantial precision and accuracy, since the properties of NiTi relies on the nickel-titanium ratio, which in turn is strongly influenced by the impurity content [105, 107]. Generally, the phases forming from the pickup of impurities like carbon and oxygen are TiC [108, 109] and $Ni_2Ti_4O_x$ [47, 110, 111], which are Ti-rich phases, due to the fact that B2 phase has a low solubility for these elements [47]. The formation of these secondary phases degrades the functional properties of NiTi such as the shape memory and superelastic behavior and also damage its structural properties by embrittling the material. Furthermore, such Ti-rich phases leads to a decrease of TTs, since they are responsible for reducing the Ti content in the B2 phase. Melting and casting processes often involve some amount of Ni evaporation, because Ni has a lower evaporation temperature than Ti (2913 °C and 3287 °C, respectively). This, on the other hand, contributes to a shift of chemical composition in favor of the Ti, as well as an increase in TTs.

The common routes used for melting are vacuum arc melting (VAM) and vacuum induction melting (VIM), as well as arc melting or induction melting under a pure argon atmosphere. Since the melt is high reactive, vacuum or inert gas atmosphere are in fact necessary for NiTi production [105, 107].

During VIM (Fig. 2.46a) electromagnetic induction is used as energy source for melting the metal into a crucible commonly in graphite or calcia (CaO) [105]. Graphite crucibles are cheap and durable and if good melting conditions are reached oxygen contamination is negligible and the carbon content can be kept to less than 0.05%. On the other hand, calcia does not react with molten NiTi, allowing the obtainment of pure molten alloys, however it is difficult to store since it is brittle under physical and thermal shock. VIM guarantees higher homogeneity of the chemical composition throughout the ingot thanks to the mixing effect of alternating current.

During VAM (Fig. 2.46b), an arc melts the consumable electrode constituted by the raw materials, which then drops and solidifies into a water-cooled copper mold. In this way no crucible is involved, thus avoiding the problem of contamination. However, since the melting process is limited to a small zone, one single VAM step is not sufficient for obtaining

homogeneous ingot, and therefore several additional remelting steps (usually 5-6) are required [107]. Therefore, this technique is referred to vacuum arc remelting (VAR).

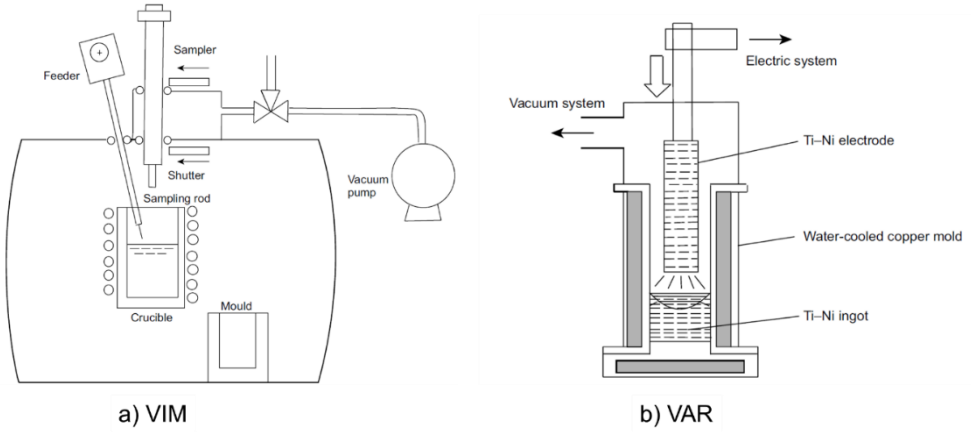

Fig. 2.46. Model of (a) VIM and (b) VAR technologies [105].

Today, a combination of VIM as primary melting followed by VAR remelt is used for NiTi production, which allows to get homogeneous and large-scale ingots [105, 107].

Thermal (homogenization and/or solution annealing) and multistage thermomechanical (hot working, cold working) treatments are carried out after the melting process to improve functional properties of NiTi.

2.7.2 Hot working and cold working

Generally, after the melting steps, the forming procedures of hot and cold forming are carried out in the conventional fabrication of NiTi parts.

Hot working is generally performed at about 800-950 °C, since in this temperature range the material is easily workable and severe oxidations are not expected [107]. Successive steps of forging, swaging, rolling and extruding at elevated temperatures are usually executed to reduce the dimension of the ingot. The microstructure of the hot worked material is coarse because of the high temperatures that lead to dynamic recrystallization processes and grain growth. This makes necessary a following reduction of the grain size for increasing mechanical properties and the functional properties of shape memory effect and superelasticity. As previously discussed, in fact, the critical stress of slip must be high to avoid the occurrence of plastic deformation instead of shape memory recovery behavior.

Cold working is therefore a common step in the conventional manufacturing route of NiTi, which typically is done through rolling and wire/tube drawing. However, cold

workability is not good in NiTi due to its intermetallic nature and therefore it is necessary to keep the cold work rate at around 30-40% [107]. Furthermore, significant springback phenomena make this phase challenging, usually requiring multiple steps with frequent intermediates annealing treatments.

After cold working, NiTi does not present the desired shape memory effect or superelasticity features due to introduction of random dislocations that cause the lower of recoverable strains [112]. It is the subsequent heat treatments that ensure that the NiTi part achieves proper functional properties [109, 112-116].

The results of these forming processes are semifinished NiTi products such as sheets, wires, rods or tube, since they are not suitable for manufacturing complex finished products [117].

2.7.3 Machining and cutting

Several machining techniques commonly used on other metals can be used for machining NiTi. However, adjustments to these methods are necessary to obtain acceptable results. In fact, NiTi presents high ductility and elasticity, which result in difficulties in removing material with cutting tools due to massive burr formation. Other critical issues include unfavorable chip breaking behavior, adhesion, work-hardening processes, stress induced martensite and springback effects [107, 118]. These phenomena usually originate considerable tool wear while degrading the quality of the workpiece [113, 118-121].

The main subtractive manufacturing processes for NiTi are:

- Milling. It constitutes one of the most challenging operations due to the intermittency of the cut and the unfavorable NiTi properties, that lead to breaking the tools, which therefore needs to be extremely hard such as highest-quality carbides [107]. The literatures reports an improvement of the effectiveness of milling by using special tools and by adjusting the process setup [122].
- Turning. It requires hard carbide tools, as well as constant flooding with coolant [107].
- Abrasive processes. These are more favorable for machining NiTi, especially grinding, sawing and erosive methods [107].

- Water-jet cutting. It is used in the manufacturing NiTi parts with intricate details, such as tubular stent due to the high resolution achievable, which is in the range of few hundred microns [123].
- EDM (electro discharge machining). It is an effective method for machining NiTi, but the surface quality after the process is not suitable for many applications due to the presence of cracks, thus requiring additional finishing processes such as electrochemical treatments [113, 124-126]. By using proper process parameters, EDM can be used for machining intricated NiTi parts [127].
- Laser cutting. It is a key technology for NiTi machining and constitutes the most widely used for manufacturing stents [113, 124, 128], due to its high accuracy. However, there are many challenges related to this technology, such as the formation of a heat affected zone (HAZ), oxides, defects, inadequate surface quality and microcracks. Therefore, post-processing is often necessary to improve the expected part life [113, 124, 128, 129]. Furthermore, a noble gas such as argon should be used in the ambient atmosphere of laser cutting. Pulsed Nd:YAG lasers (pulse durations in the order of nanoseconds) are the most common, while ultrashort pulsed lasers (pulse durations in the order of femtoseconds) are more effective for high precision machining since reducing the HAZ and the formation of thermal defects.

2.7.4 Stent fabrication

As previously discussed, self-expanding stents constitute the most widespread application of NiTi alloy. There are various production methods for NiTi stents. The most common ones typically begin with a bar obtained from an ingot. Subsequently, two main approaches are used to manufacture the final component. The first, and most common, method involves creating a microtube, which is then precisely laser cut into mesh designs. The tube is derived from the bar either through pierce extrusion or by drilling the bar to obtain a hollow interior. The other production method involves forming coils from the bar, and then braiding or knitting the resulting wire to shape the stent, which however result in increased wall thickness. After production, stent devices must undergo electropolishing and passivation, described below.

2.7.5 Heat treatments and shape setting

As previously mentioned, after the melting phase of NiTi, usually heat treatments are required to eliminate casting and solidification defects such as segregation, microscale concentration gradients and precipitates. Therefore, homogenization follow the alloying or the initial powder metallurgical processing step, with typically with maintenance at 950 °C for 24 h under vacuum followed by quenching [130].

Certain high-temperature processing methods, such as powder metallurgy (Paragraph 2.7.7), necessitate intermediate solution annealing procedure, since precipitates may form in Ni-rich NiTi alloys when processed at high temperatures. Typically, solution annealing requires temperatures similar or lower than those needed for homogenization, while the duration of solution treatment is shorter and can range from 5 min to 5.5 h depending on the processing methods [107, 113].

Cold working often requires intermediate heat treatments to create a microstructure that can tolerate further deformation, thus restoring its workability. This is done by annealing and recrystallizing the alloy, typically at temperatures ranging between 700-900 °C for 1-30 min [107, 112, 115]. In addition, NiTi parts subjected to a final cold working step require further heat treatment in the range of 350-500 °C, and this step can be combined with the shape setting treatment (analyzed below). Heat treating the alloy in this range allows to eliminate distortions and "relax" the structure full of dislocations that suppress the shape memory and superelastic responses by hindering the mobility of twin boundaries of martensite. This treatment is usually carried out between 350 and 400 °C for shape memory NiTi, while at slightly higher temperatures up to 500 °C for superelastic NiTi [113]. The difference in the heat treatment temperature is due to the different microstructural mechanisms in the two materials. As discussed in Chapter 2.5, solution annealing and aging treatment plays an important role for superelasticity, due to the formation of Ni_4Ti_3 precipitates [131]. This Ni-rich phase leads to the precipitation hardening of NiTi, increasing the stress required for slip deformation, thus promoting the occurrence of stress-induced martensite. Furthermore, Ni_4Ti_3 precipitates represent nucleation sites for the stress-induced martensitic transformation, enhancing it to take place at lower stresses [33, 47, 55, 131-137]. It is important to remark that the aging of Ni-rich NiTi alloys increases TTs since the Ni content of the matrix changes after precipitation [47, 66, 133, 138]. In addition, the presence of Ni-rich phases results in more brittleness due to the precipitation hardening effect [55,

137, 139]. As previously examined, Ni_4Ti_3 precipitates also promote the two-stage transformation involving the occurrence of R-phase [66, 132, 138, 140-144].

Shape setting (or training) is an important step that is carried out on semifinished NiTi parts. It is needed to reveal the functional properties desired in the specific application and to establish the geometrical shape, which is the one "memorized" in the material. Shape setting is done through heat-shaping techniques, during which the NiTi part is heated while being held and constrained in a fixture or mandrel of the desired shape. The heat treatment used in shape memory and superelastic NiTi are similar and usually ranges between 400-500 °C for times over 5 min followed by rapid cooling via water quench [145, 146].

It should be emphasized that heat treatments of NiTi parts (including thermomechanical treatments) are complicated practices that significantly influence both structural and functional properties of the material [118]. Several complexities and interdependencies exist in these procedures, which therefore must be optimized individually depending on the process history and the resulting microstructure, aim of the heat treatment, desired properties and application type [107].

2.7.6 Finishing and surface modification

After processing, the surface of NiTi semifinished parts present oxide coatings, contaminants, or lubricants and thus needs to be properly cleaned. At high temperatures, NiTi develops significant oxide surface layers consisting of oxides type TiO_2 and intermetallic phases Ni_3Ti, which can be removed mechanically [107].

Concerning NiTi parts intended for biomedical applications, electropolishing is a very appropriate technique for the optimization of their surfaces [113, 147-149]. For example, stents are post processed by electropolishing, which removes the oxide layer, but also smooths the surfaces and blunts sharp edges originated in the laser cutting phase. Electropolishing is thus effective in minimizing the potential trauma of tissues in contact with the stent [113]. Through this technique, the initial oxide layer is removed, but a new layer is formed immediately due to the high content of titanium. The new layer is characterized by higher homogeneity and uniformity than the former. The presence of this stable titanium oxide reduces the release of nickel in the surrounding tissues and is thus essential in NiTi biomedical components. Acting as a barrier, it enhances biocompatibility, passivity, and corrosion resistance. A further improvement of biocompatibility can be

obtained by passivation after the electropolishing step, which allow the obtainment of a stable and thin oxide layer [113].

2.7.7 Powder metallurgy

Powder metallurgy (PM) techniques result attractive for processing NiTi, since allow the obtainment of near-net-shape devices, thus contributing to a significant simplification of the manufacturing process. Also, through some PM methods, porous NiTi parts can be produced, which are very attractive for biomedical applications. However, there are challenges related to the contamination during PM route due to the high temperatures of processing and the large specific area of powder particle [113].

NiTi powders are typically prealloyed and prepared using methods such as ball milling, water or gas atomization and powder creation by laser ablation or hydriding. Among these, gas atomization is the most advantageous methods, producing nearly spherical powder with low impurities levels since it is performed in an inert atmosphere [107].

Among the conventional technologies of powder metallurgy, sintering is the most common but has limitations in component geometry. Therefore, it is not suitable for manufacturing complex NiTi components, while it is often used for producing semifinished or porous NiTi parts. Other approaches such as hot isostatic pressing (HIP) and metal injection molding (MIM) are used for parts with more complex geometries.

2.7.7.1 Additive manufacturing

Over the last years, the possibility to produce NiTi components through AM technologies has gained significant attention, with the aim of facilitating the production of highly complexed parts that cannot be processed by the conventional subtractive methods [106]. These techniques can also be exploited for fabricating tailor-made implants for biomedical applications. In addition, as previously mentioned, NiTi presents high reactivity and ductility, which results in difficulties in its conventional processing and machining. Due to these complications, the starting form of NiTi devices is limited to basic geometries, such as rod, wire, tube, bar, sheets or strip [106].

The most common AM methods to manufacture NiTi are laser powder bed fusion (L-PBF), electron beam powder bed fusion (EB-PBF) or directed energy deposition (DED) techniques [106]. During AM processes providing inert atmosphere (e.g. argon), it is required to minimize the possibility to have oxidation or impurity pick-up. AM NiTi was

found to present a very low impurity content when high quality raw material is used, allowing to meet the ASTM F2063-05 standard for medical devices [150]. This makes the AM route very attractive for applications in the biomedical field. The production of NiTi biomedical devices through AM could be supplementary to the well-established existing technologies, allowing the manufacturing of complex geometries as well as the improvement of the effectiveness of specific devices. An example concerns NiTi self-expanding stents, for which there is a general lack of customizability. These devices are in fact put on the market with serialized diameters and lengths, and clinicians must select among these based on the specific case using the patient's data (vessel sizing) obtained through clinical imaging modalities and using manufacturer's recommendation relative to the size. The match between the stent and the vessel diameters is critical, since the effectiveness of the stent can be compromised if its size is not consistent with that of vessel: small diameters imply poor adherence and displacement of the device, while large diameters lead to vascular lumen tear [151]. In some cases, the stent length may be not sufficient if the lesion extends over a longer portion of the vessel, making the overlap of multiple stents needed [152]. For instance, when performing femoropopliteal stenting, some lesions can be extended up to 30 cm in length, requiring the overlap of up to five stents with a length of 10 cm [152]. Despite these are appropriate strategies, endovascular surgery could take advantage from the use of stents with tailored lengths and diameters that better fit the patient's vessel size. In addition, stent with personalized shapes fabricated using the patient's CT scan data can be a solution for complex cardiovascular pathologies. Another example is constituted by stiffness-tailored patient-specific implant, whose production through AM makes possible the personalization of the shape and the introduction of interconnected porosities to match both the anatomical shape and the stiffness of the host tissue [106]. In addition, it should be mentioned that many studies addressed to the biocompatibility of AM NiTi have produced promising findings [82, 153-156].

Therefore, AM can be supportive to the already existing technologies in the production of NiTi biomedical components, particularly in the cases where customization is required. By enabling tailored solutions to patients' needs, the effectiveness of these devices would be strongly improved, as well as the results of the related medical operations.

Despite the promising aspects, AM NiTi biomedical devices have not been developed yet due to the still open points related to the lack of full knowledge of the process. For this reason, most of the research conducted to date has considered simple geometries rather than

actual components, with the intention to prior optimize the design, production, and post-processing phase, which is necessary for tailoring the resulting properties. Only a few works deal with NiTi actual biomedical components fabricated via AM, most of which are mainly focused on the design achievable and on the feasibility of reaching suitable A_f temperatures for the application [157-161].

Since the purpose is to exploit the advantages of AM for biomedical devices production, studies are mainly addressed to the superelastic Ni-rich NiTi. For these alloys, heat treatments such as solution annealing and aging are known to strongly affect superelasticity, acting both on TTs and final properties through the formation of precipitates [33, 59, 162, 163]. Due to the differences between conventional and AM manufacturing methods, a lot of studies are aimed at determining the optimal heat treatments for AM parts [40, 164-172], based on the features of the as-built components, which in turn strongly depend on the chemical composition of the raw material and on the process parameters used. In fact, as previously pointed out, the development of heat treatments in relation to the specific process route is sensitive and essential, and therefore needs to be carefully examined on a case-by-case basis. Among AM methods, most of the studies deal with L-PBF process, since it constitutes the most evolved and common technique due to the resulting finer microstructure and the better surface finish, both leading to higher performances [3, 6, 59, 173].

The first to report superelastic features on Ni-rich NiTi (55.88 Ni wt%, about 51 Ni at%) produced by L-PBF were Haberland et al. [40]. They investigated solution treatment at 950 °C for 5.5 h as well as solution treatment followed by different aging conditions at 350 °C and 450 °C for various durations. Multistep transformation was found in DSC thermograms of samples after aging, which was associated to the R-phase transformation due to the formation of Ni_4Ti_3 precipitates during the treatment (Fig. 2.47). Aging after solution annealing was reported to improve the superelasticity under single compression loading-unloading experiments to 1200 MPa at A_f + 10 °C temperature, in particular the treatment at 350 °C for 24 h (Fig. 2.48). This was attributed to the formation of fine Ni-rich precipitates. The aging treatment at 350 °C for 24 h was compared to conventional NiTi by performing cyclic compression tests to 600 MPa repeated 15 times at A_f + 10 °C (Fig. 2.49). For both these conditions, pseudoelastic behavior was reported, as well as a comparable degradation of the superelastic properties during cycling. Irreversible effects after loading were attributed to the formation of dislocations, which play a role in irreversible strains in two ways, i.e. directly through dislocation plasticity, and by stabilizing certain martensite

variants, preventing reverse martensitic transformation to occur. The corresponding evolution of the characteristic values during cyclic tests are reported in Fig. 2.50. In the first cycles, it appears that the ratio of reversible and maximum strain increases, while remaining on a constant level for later cycles for both the analyzed conditions. The difference between the conventional NiTi and L-PBF NiTi after heat treatment is very marginal by looking at the scaling in Fig. 2.50b. Through this study, L-PBF proved to be an attractive method to produce NiTi components, and heat treatments were found to be effective in the improvement of their superelastic features.

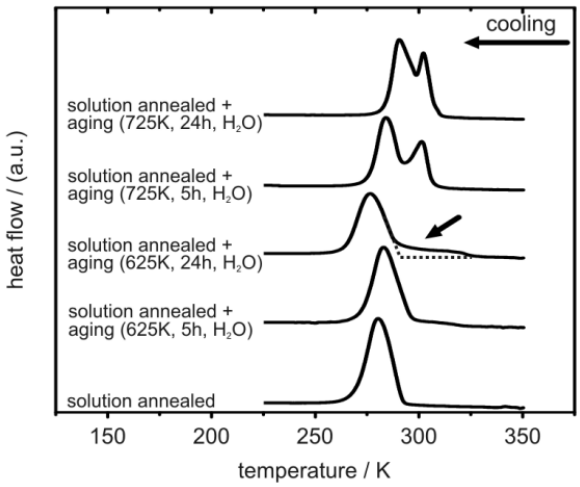

Fig. 2.47. DSC of solution annealed and solution annealed and aged L-PBF NiTi [40].

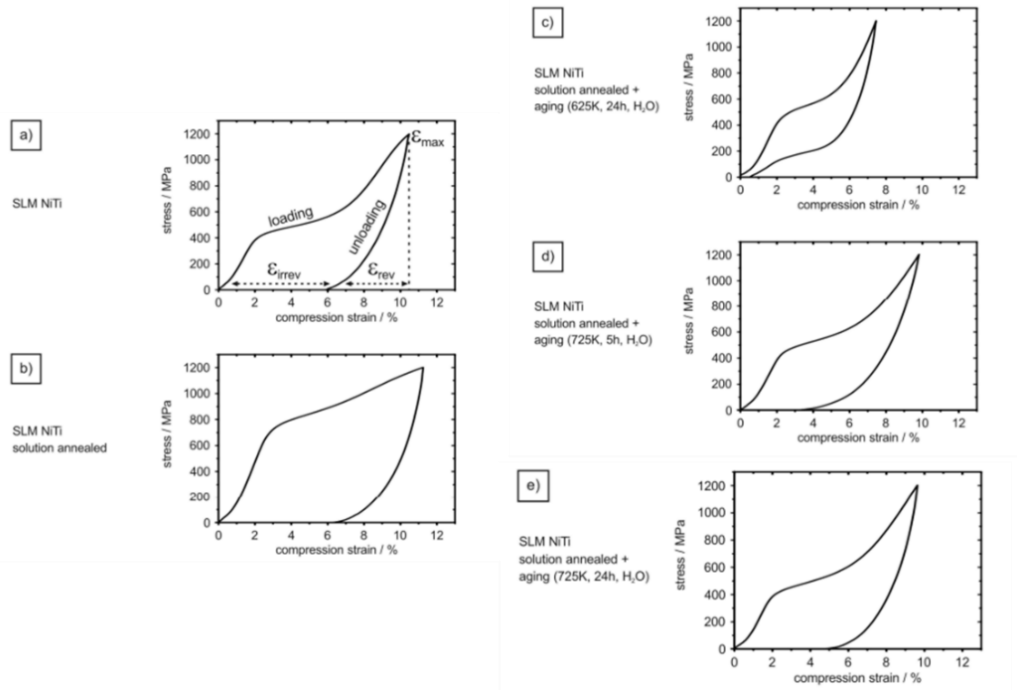

Fig. 2.48. Single loading-unloading compression tests performed on L-PBF after heat treatments, showing higher recovery after solution annealing and aging at 350 °C for 24 h [40].

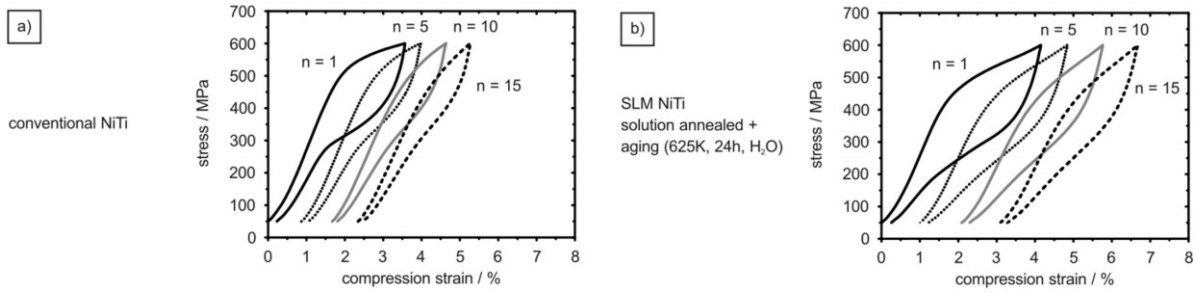

Fig. 2.49. Stress-strain plots of cyclic experiments for (a) conventional NiTi and (b) solution annealed and aged at 350 °C L-PBF NiTi [40].

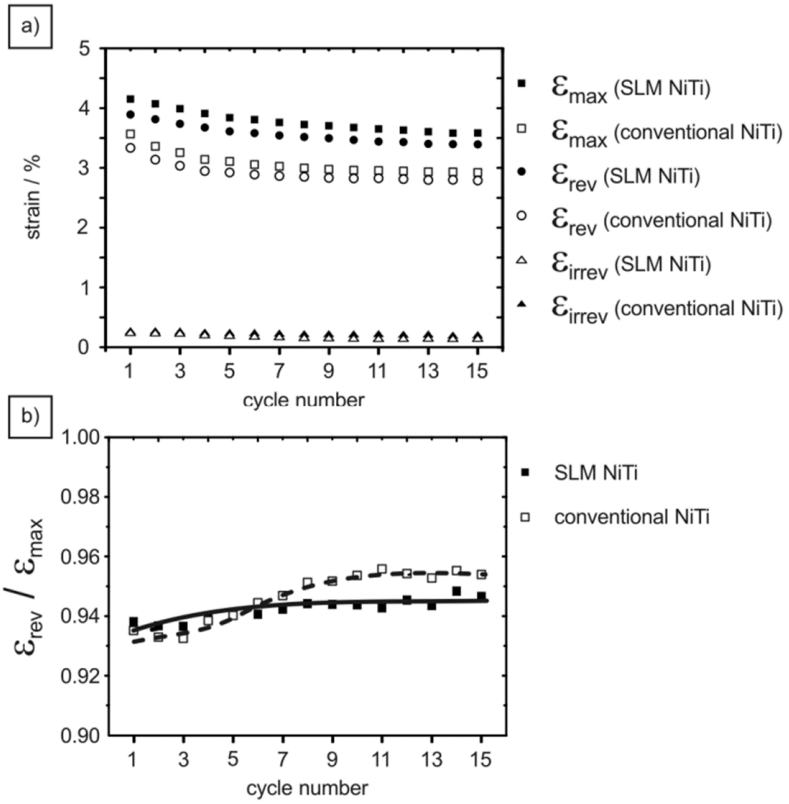

Fig. 2.50. (a) Maximum, reversible, and irreversible strain and (b) ratio of reversible and maximum strain of conventional NiTi and solution annealed and aged at 350 °C L-PBF NiTi [40].

Different conditions of heat treatment have been considered also by Saedi et al. [168, 169, 174] on 50.8Ni-49.2Ti (at%) alloy manufactured via L-PBF. To evaluate the superelastic response, different kind of compression tests were performed considering both the loading and unloading phase.

Firstly, solution annealing at 950 °C for 5.5 h followed by water quenching was examined through compression tests at different testing temperatures [174]. Results showed overall improved superelasticity after this treatment, with fully reversible strain of 3% (Fig. 2.51). The critical stress to induce martensitic transformation was also graphically determined using the tangent method, and its variation as function of temperature is reported

in Fig. 2.52. Optical micrographs of the analyzed conditions are displayed in Fig. 2.53. Inhomogeneous austenitic grains of about 90 μm are detected for the initial ingot, while after L-PBF a chessboard-like structure is formed due to alternating scanning path of the laser, which appears to dissolve after the solution treatment.

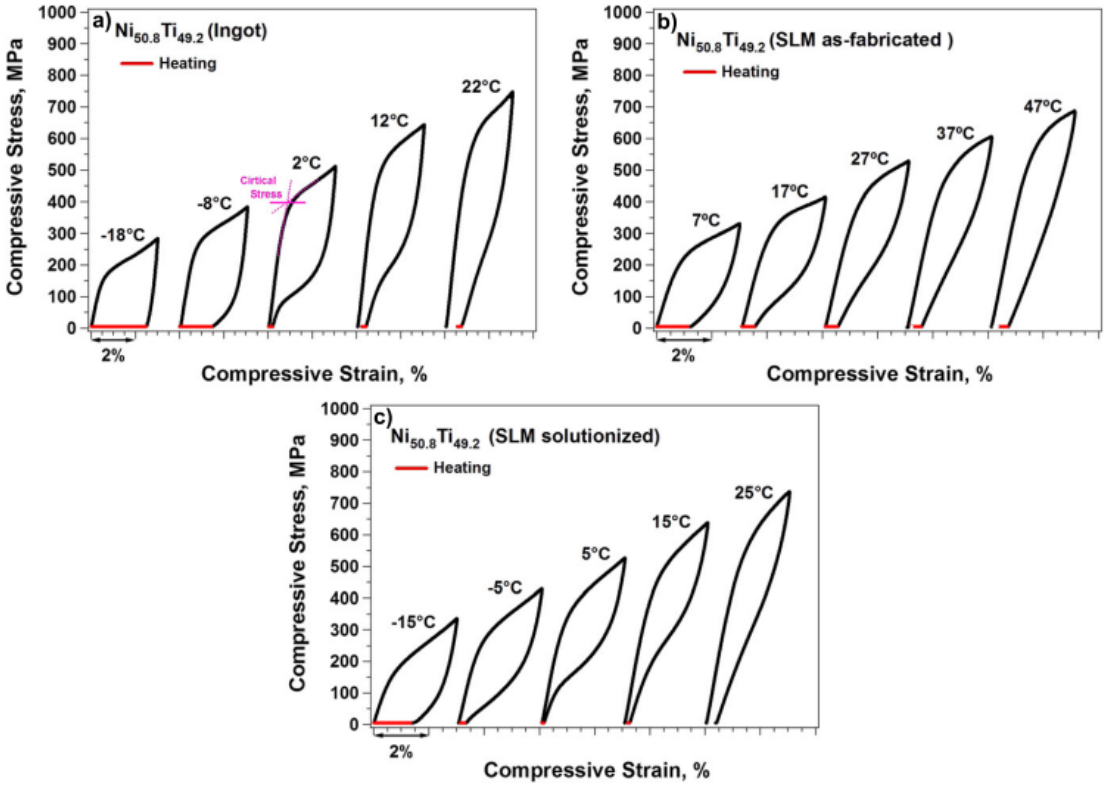

Fig. 2.51. Stress-strain responses of (a) the initial ingot, (b) the as-fabricated, and (c) the solutionized 50.8Ni-49.2Ti alloys [174].

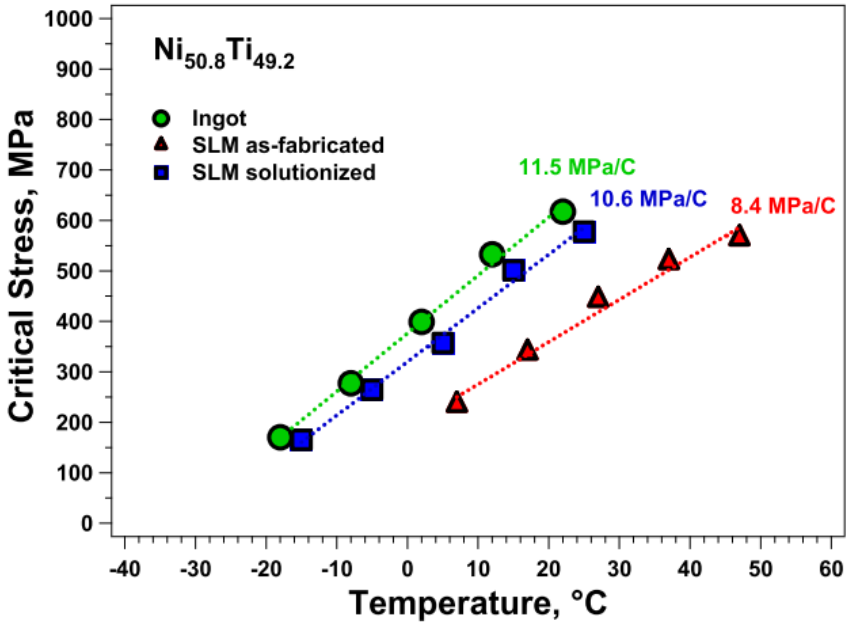

Fig. 2.52. Critical stress versus temperature of the conditions analyzed in [174].

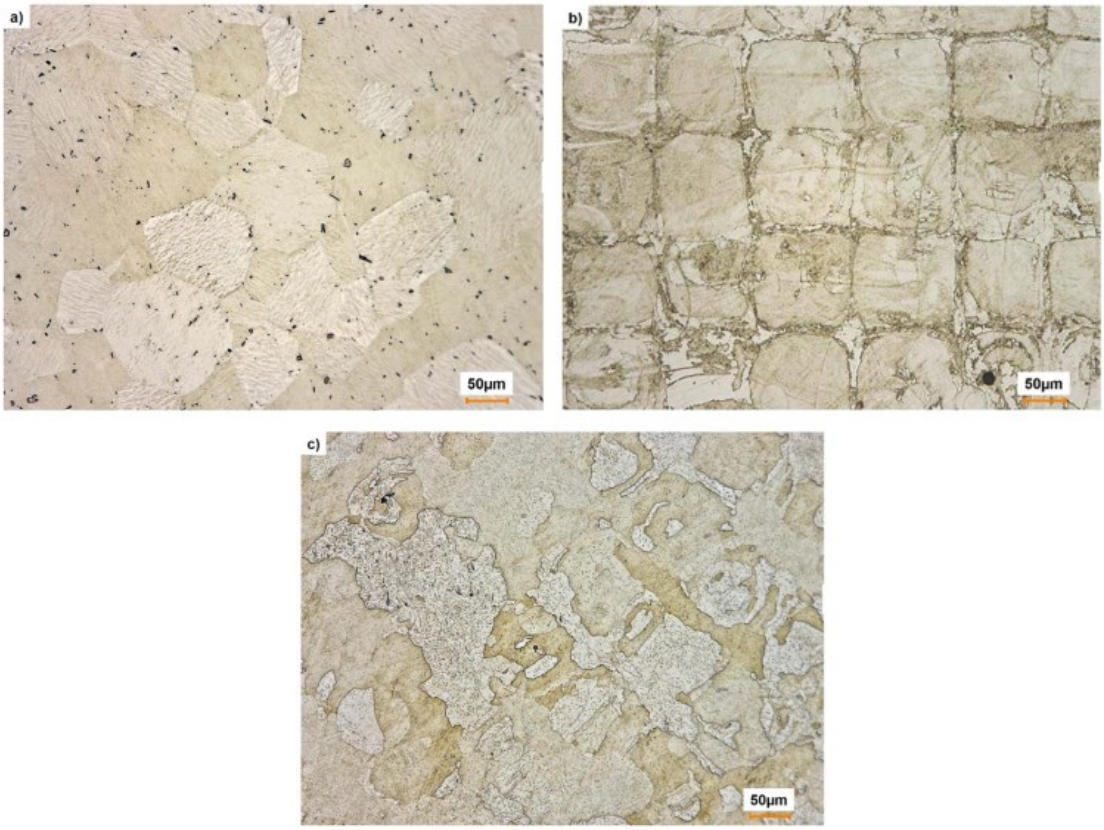

Fig. 2.53. Optical micrographs of (a) the initial ingot, (b) the as-fabricated, and (c) the solutionized 50.8Ni-49.2Ti alloys [174].

Subsequently, different aging conditions, i.e. at 350 °C and 450 °C for times ranging from 5 min to 18 h, performed after solution annealing at 950 °C for 5.5 h were examined on the same alloy [168]. The wide number of analyzed conditions lead to conclude that aging is an effective method to modify the TTs of L-PBF NiTi (Fig. 2.54). Again, the double peaks observed in DSC charts for heat treatments longer than 30 min are due to the appearance of the R-phase transformation, which witnesses the precipitation of Ni_4Ti_3 phase during such treatments. Cyclic compression tests were performed at A_f + 15 °C up to 1000 MPa, and the most representative results are show in Fig. 2.55. The best superelastic features were obtained after solution treatment followed by aging at 350 °C for 18 h and at 450 °C for 10 h, with 5.5% recoverable strain at the first cycle for both the conditions (corresponding to 95% and 69% of recoverable/total strain ratio respectively) and with a stable recoverable strain at the 10^{th} cycle of 4.2% and 3.8%, respectively. The improved superelasticity was attributed to the Ni_4Ti_3 precipitation after heat treatments, proving that the latter play a crucial role in tailoring the response of L-PBF NiTi.

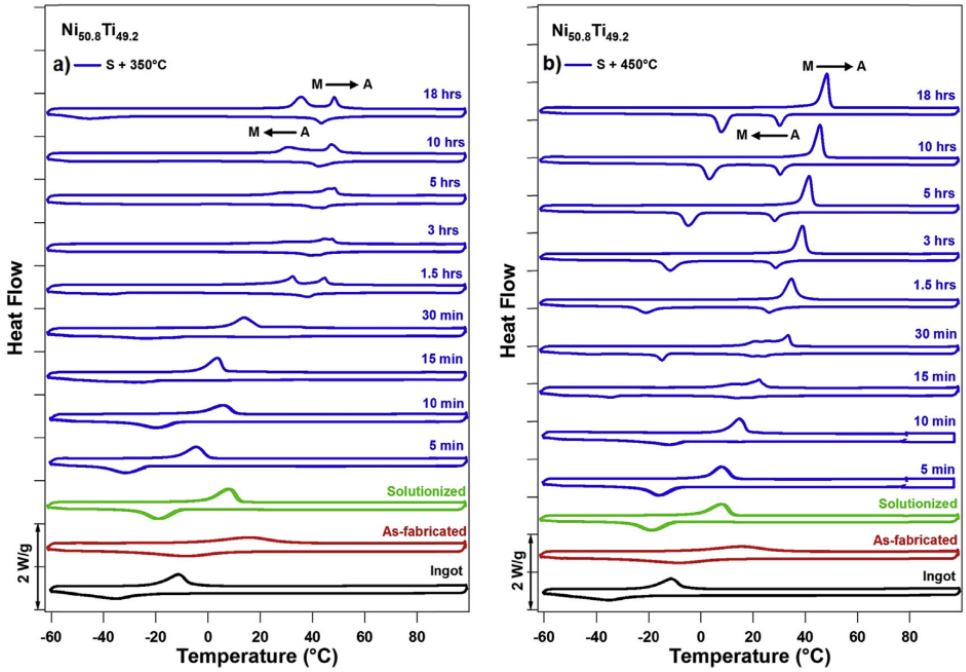

Fig. 2.54. TTs variation after solution annealing and aging for different durations at (a) 350 °C and (b) 450 °C for 50.8Ni-49.2Ti alloy, compared to the ingot, as-fabricated and solutionized conditions [168].

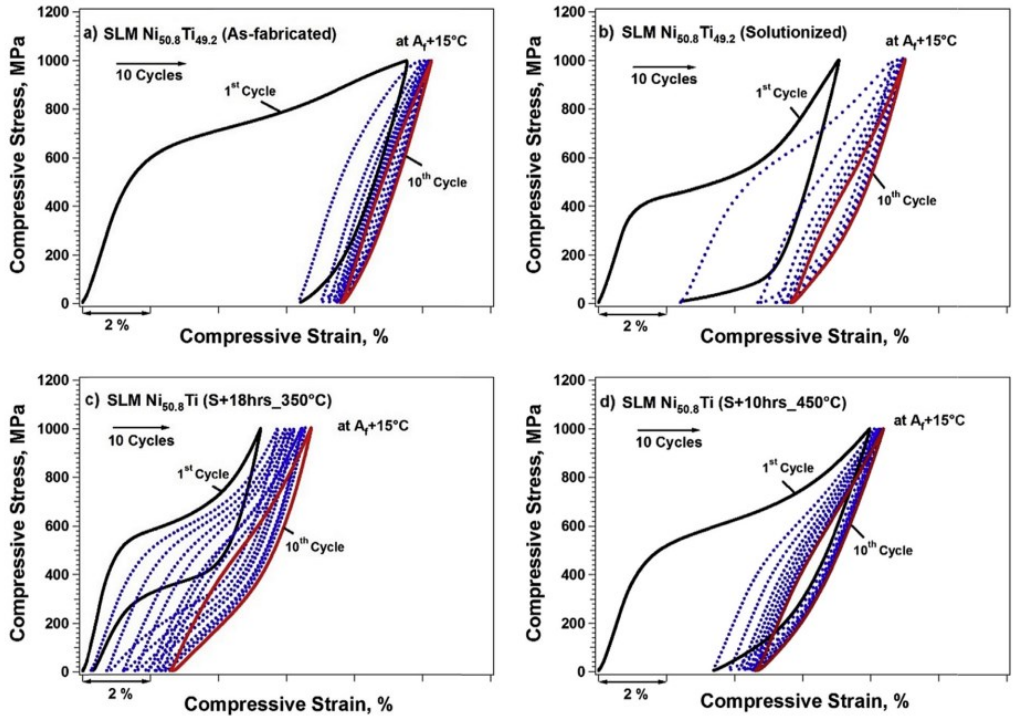

Fig. 2.55. Cyclic tests of (a) as-fabricated, (b) solution treated, (c) solution treated and aged at 350 °C for 18 h, (d) solution treated and aged at 450 °C for 10 h 50.8Ni-49.2Ti alloy [168].

Since the solution annealing process often involves unwanted outcomes such as melting and oxidation, the possibility of direct aging after L-PBF was taken into account on 50.8Ni-49.2Ti alloy (at%) [169]. Different aging temperatures (between 350 °C and 600 °C) were

considered, combined with three aging durations (30 min, 1 h and 1.5 h). The effects of the conducted treatments on the TTs of the alloy are shown in Fig. 2.56 and Fig. 2.57, compared to those of the initial ingot and the as-fabricated sample. Double peaks related to the R-phase were observed for most of the conditions considered, except for aging temperatures higher than 500 °C. Incremental compression tests were performed to 2%, 4%, 6% and 8% successively at room temperature and at 37 °C, i.e. the body temperature, to consider the possibility of biomedical applications. The corresponding stress-strain responses of the most noteworthy conditions are reported in Fig. 2.58, together with the stress-strain curves up to failure. 5.5% of strain recovery was recorded at room temperature after aging at 600 °C for 1.5 h, while 4% at 37 °C after aging at 350 °C for 1.5 h. Therefore, the study proved that even without solution annealing the appropriate aging treatment can significantly modify the TTs, as well as enhance the thermomechanical behavior of L-PBF NiTi.

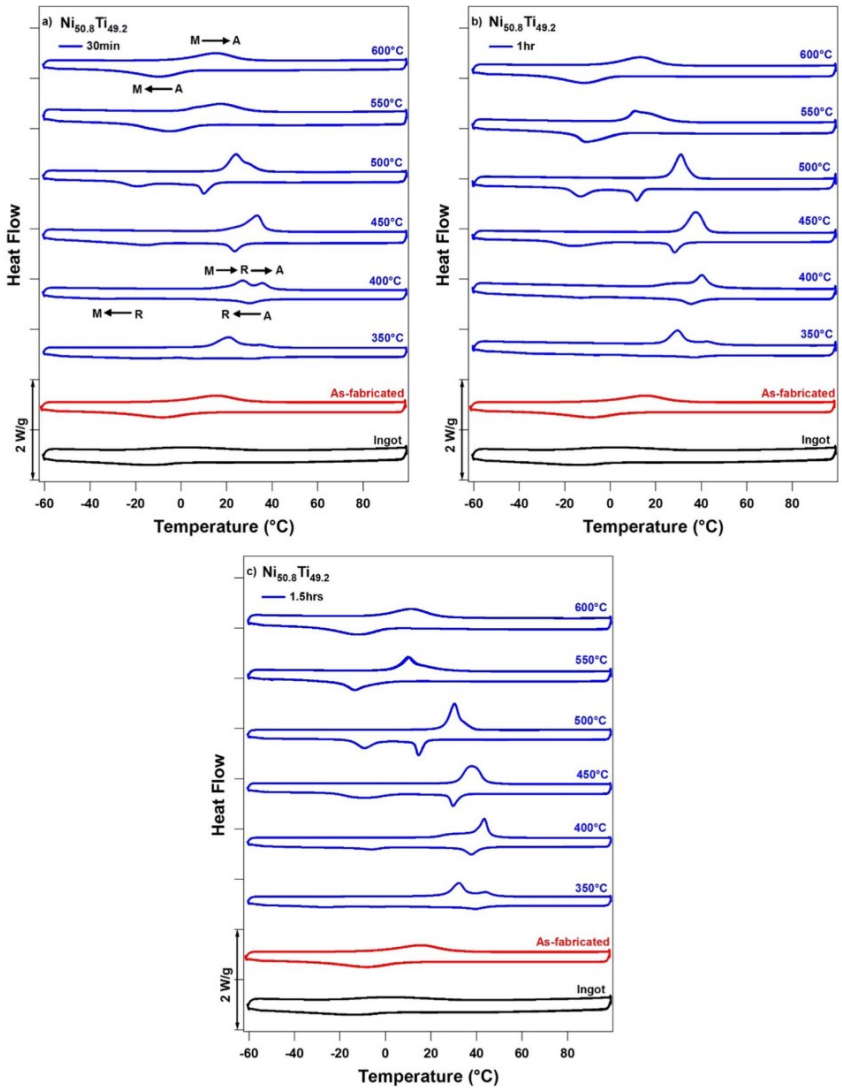

Fig. 2.56. DSC responses of 50.8Ni-49.2Ti alloy aged at 350-600 °C for (a) 30 min, (b) 1 h, (c) 1.5 h [169].

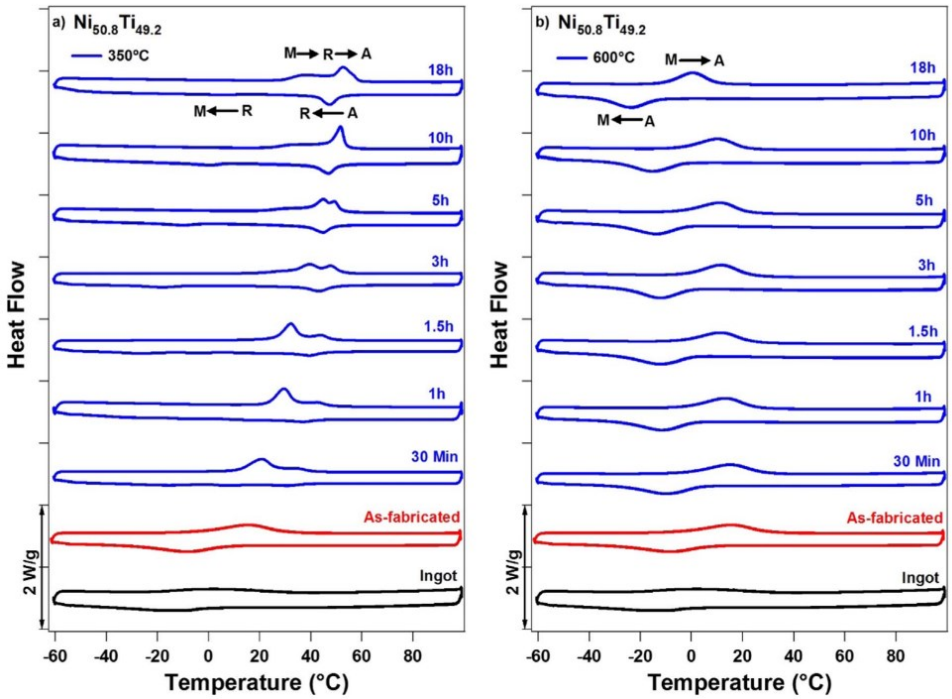

Fig. 2.57. DSC responses of 50.8Ni-49.2Ti alloy aged from 30 min to 18 h at (a) 350 °C, and (b) 600 °C [169].

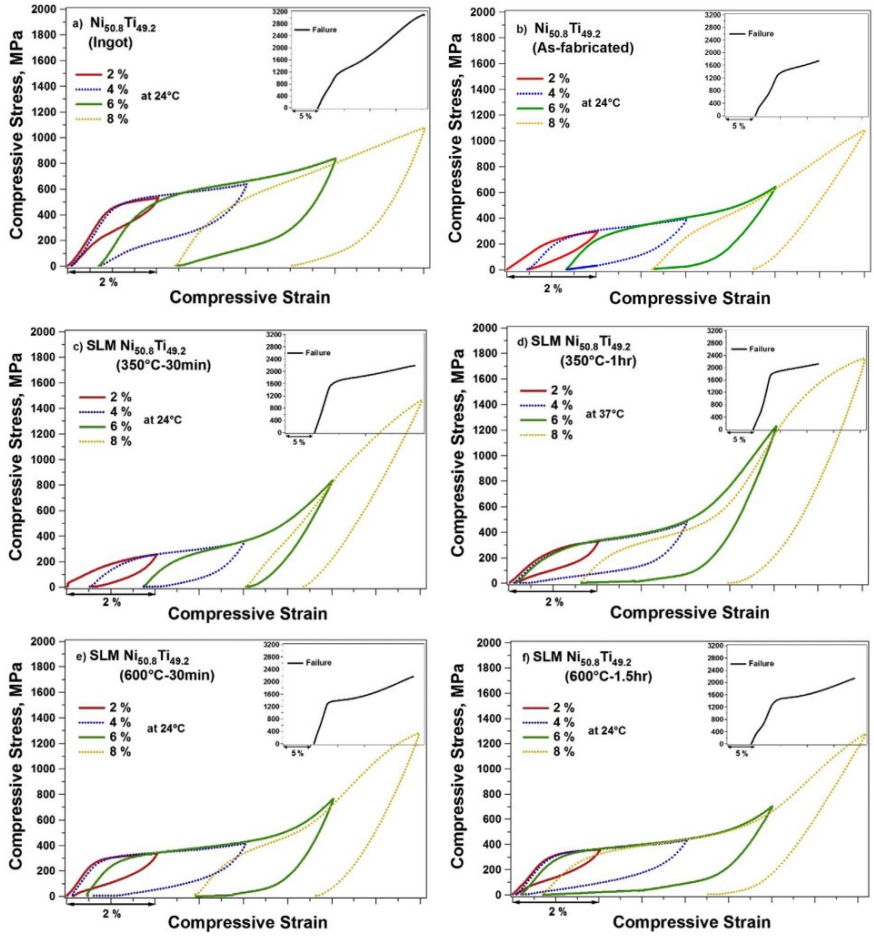

Fig. 2.58. Stress-strain responses during incremental compression tests for some of the analyzed conditions of 50.8Ni-49.2Ti alloy reported in [169], at room and body temperatures.

The same chemical composition of starting powder, i.e. 50.8Ni-49.2Ti (at%), was used by Carlucci et al. [172] to manufacture samples through L-PBF, with the aim of investigating the influence of heat treatments on the mechanical behavior under both tensile and compression tests at room temperature. The tensile specimens were manufactured in the vertical (i.e. loading direction parallel to the building direction) and horizontal direction (i.e. loading direction orthogonal to the building direction), while the compression ones only in the vertical direction. Both solution annealing followed by aging and direct aging heat treatments were analyzed, by varying temperatures and times. The examined conditions were direct aging at 400 °C and 450 °C for 15 min and at 500 °C for 1 h, solution annealing at 850 °C for 30 min, and solution annealing followed by aging at 400 °C and 450 °C for 15 min. Fig. 2.59 displays the gas-atomized powder used (Fig. 2.59a) and the microstructure of the as-built specimen, consisting in large columnar grains growing epitaxially through the building direction (Fig. 2.59b), as well as the melt pools and the cellular structure (Fig. 2.59c-d). After aging treatments, Ni_4Ti_3 precipitates were detected through XRD analysis. Results of compression and tension tests are shown in Fig. 2.60 and Fig. 2.61, respectively, together with the critical stress for the martensitic transformation (σ_{PE}) and the recovered strain due to the pseudoelastic effect ε_{PE}. σ_{PE} was determined as the onset of the stress-strain curve corresponding to a deviation from the initial linear elastic behavior of 0.2%, while ε_{PE} was calculated by subtracting the maximum strain in correspondence of a fully linear elastic unloading and the residual strain upon unloading at zero stress (Fig. 2.60b). During tests, strains were measured both at the macro-scale (named as global strain, similar to the one detected by an extensometer) and at the micro-scale (named as local strains, measured in the surface regions showing largest deformations) by using digital image correlation (DIC) technique. Heat treatments were found to strongly affect the superelastic features of the alloy, by changing σ_{PE} and the ε_{PE}. Direct aging treatments were found to be effective in the lowering of σ_{PE}, which instead was found to increase after the solution treatment. This was attributed to the presence of Ni_4Ti_3 phase, which acted as nucleation site for the formation of stress-induced martensite. Furthermore, under tension vertical samples showed better superelastic features compared to the horizontal ones. The highest strain recoverability was found for the as-built condition under compression (4.56% globally) and after solution annealing followed by aging at 450 °C under tension for the vertical sample (2.14% globally).

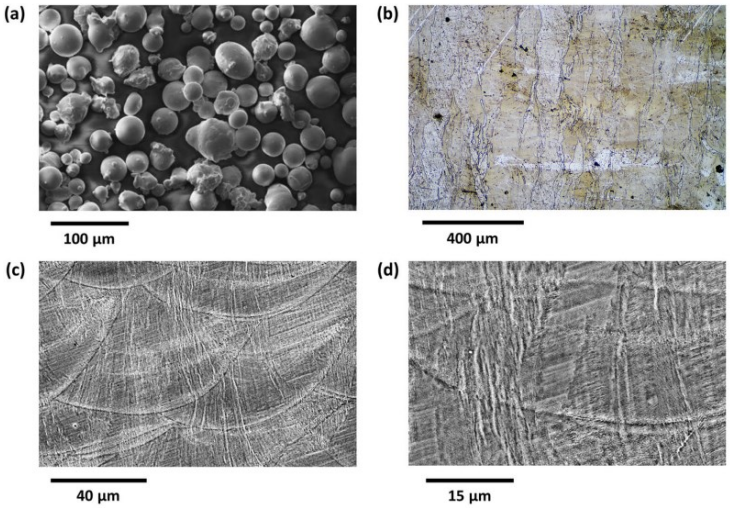

Fig. 2.59. (a) SEM micrographs of the powder used, (b) optical micrographs and (c,d) SEM images of the as-built 50.8Ni-49.2Ti alloy [172].

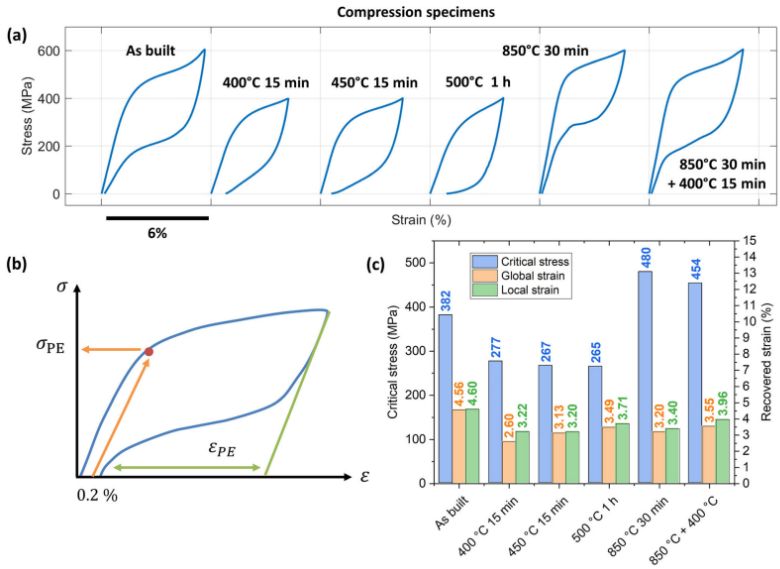

Fig. 2.60. (a) Stress-strain curves of specimens tested under compression, (b) schematic representation of the evaluation of σ_{PE} and ε_{PE}, (c) the main results obtained [172].

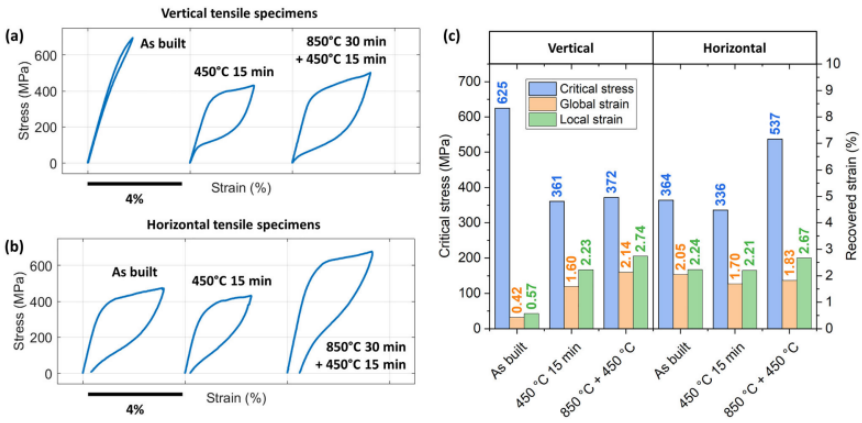

Fig. 2.61. Stress-strain curves for (a) vertical samples, (b) horizontal samples tested in tension, (c) the main results obtained [172].

All these works examine the possibility of improving the superelasticity of NiTi alloy manufactured through L-PBF using heat treatments, however only a few deal with performing aging without prior solution annealing, i.e. direct aging [169, 172], and only one involves short-time aging [172]. This kind of treatment allows the reduction of costs in L-PBF parts by avoiding solution annealing, which is a high temperature and energy-intensive step. Furthermore, the construction of the experimental temperature-stress diagram (see Fig. 2.21) has not yet been examined for NiTi alloys manufactured through L-PBF, although it would constitute a valuable resource for practical applications. Lastly, in the above reviewed experimental works, it was proved that the precipitation of Ni_4Ti_3 phase after aging enhanced the superelasticity of L-PBF NiTi, similarly to the conventional alloy. However, the presence of these precipitates is mainly witnessed by the variation of TTs (DSC analyses) or through XRD analyses, rather than a specific characterization using advanced microscopy techniques. Usually, in fact, Ni_4Ti_3 precipitates are nano-sized, and therefore are hard to detect through optical or SEM microscopy.

Besides optimizing superelasticity, numerous studies on L-PBF NiTi alloy address the issue of Ni evaporation, which may occur due to the high temperatures generated by the laser [162, 163]. In fact, the lower evaporation temperature of Ni (2913 °C) compared to Ti (3287 °C) leads to a preferential Ni evaporation, leaving a higher Ti content in the matrix. This leads to a variation of the chemical composition in the manufactured part compared to the starting powder and thus affects the TTs and the functional properties of the component. Furthermore, most of L-PBF NiTi parts are manufactured with NiTi powder with a Ni content lower than 51% (at%), as it constitutes one of the most easily commercially available chemical composition, which makes the process control over Ni evaporation even more critical.

One of the mostly considered aspects regarding the issue of Ni evaporation concerns the optimization of the process parameters.

The effects of laser power (ranging from 100 W to 250 W) and scanning speed (ranging from 125 mm/s to 1500 mm/s) on microstructure and thermomechanical response of 50.8Ni-49.2Ti (at%) alloy were investigated by Saedi et al. [170]. Optical micrographs of the different analyzed conditions are reported in Fig. 2.62, Fig. 2.63 and Fig. 2.64. It was found that energy input plays a key role in the resulting structure, as well as in the fabrication of fully dense parts. Square-shaped grains appear with moderate energy levels (55.5–79.4 J/mm^3) and laser power higher than 200 W, i.e. A3, A4, C1, C2 and C3 samples. On the

other hand, densification was achieved by combining high laser power to high scanning speed, or low laser power to low scanning speed. In addition, TTs were determined and are displayed in Fig. 2.65, together with Vickers hardness values, as function of the energy level and scanning speed for the batch of samples manufactured with 100 W and 250 W. A rise in TTs is recorded as the supplied energy increase in both the batches of specimens. This is due to a decrease of Ni content resulting from its evaporation, which increase with the energy level since the material is exposed to higher temperatures, proving that the tuning of process parameters directly affects the Ni evaporation of NiTi manufactured by L-PBF.

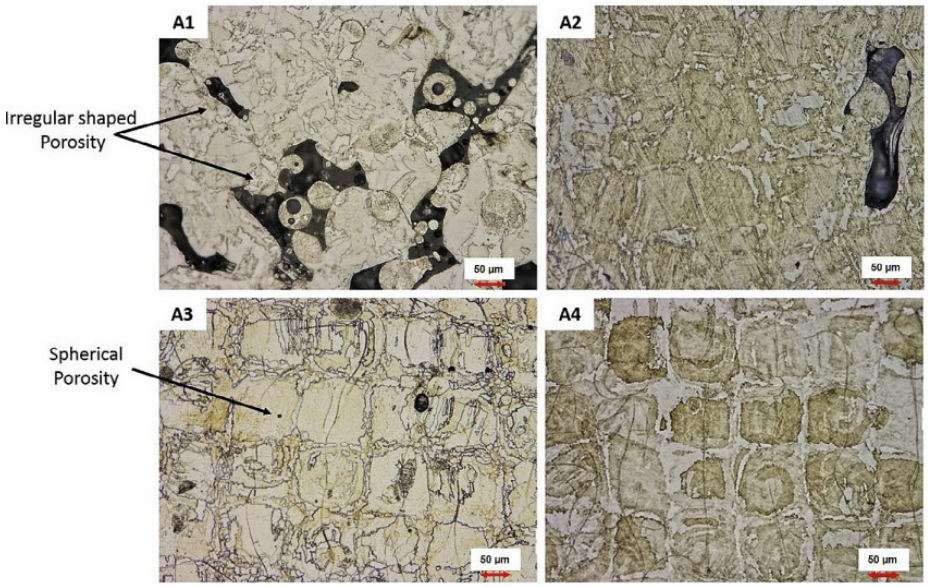

Fig. 2.62. Optical micrographs of 50.8Ni-49.2Ti alloy manufactured with constant scanning speed (1000 mm/s) and different laser powers: (A1) 100 W, (A2) 150 W, (A3) 200 W, (A4) 250 W [170].

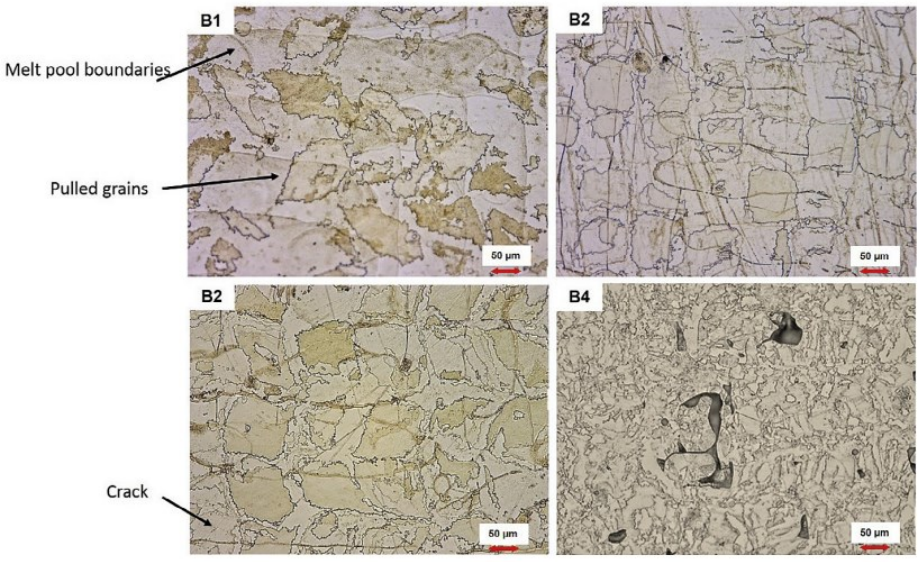

Fig. 2.63. Optical micrographs of 50.8Ni-49.2Ti alloy manufactured with low laser power (100 W) and different scanning speeds: (B1) 125 mm/s W, (B2) 175 mm/s, (B3) 225 mm/s, (B4) 500 mm/s [170].

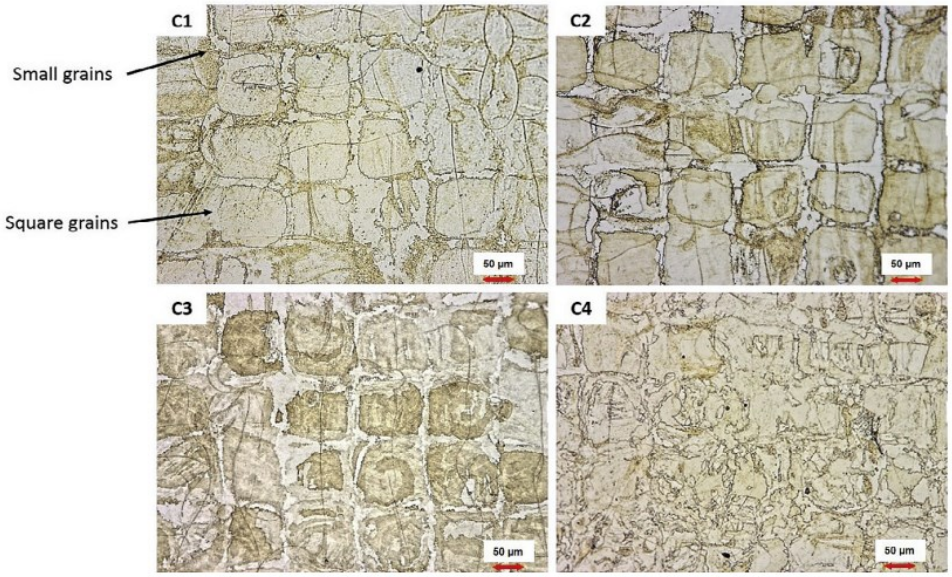

Fig. 2.64. Optical micrographs of 50.8Ni-49.2Ti alloy manufactured with low laser power (250 W) and different scanning speeds: (C1) 875 mm/s W, (C2) 1000 mm/s, (C3) 1250 mm/s, (C4) 1500 mm/s [170].

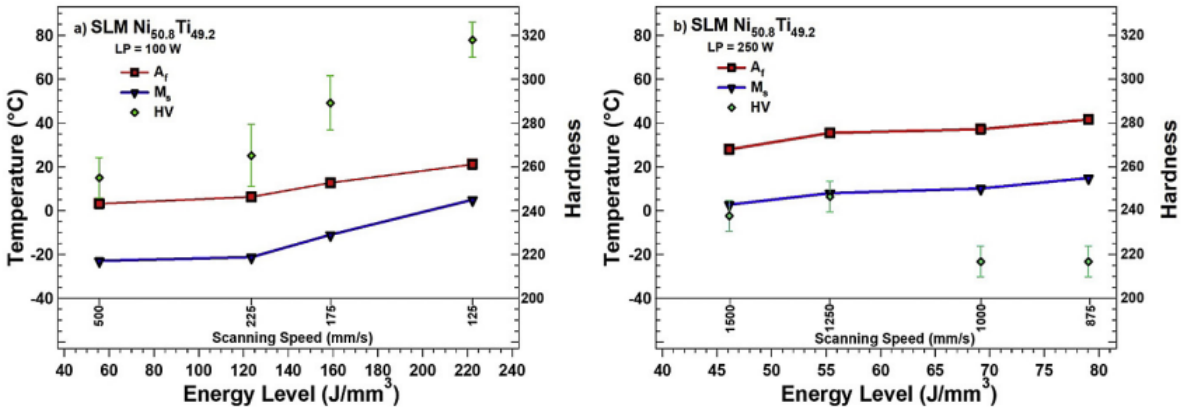

Fig. 2.65. Variation of M_s, A_f temperatures and Vickers hardness as function of energy level and scanning speed: (a) low laser power of 100 W, i.e. B1-4 and (b) high laser power of 250 W, i.e. C1-4 [170].

A design of experiment model was carried out by Obeidi et al. [175] involving the production of 81 cubes by varying four process parameters (laser power, scanning speed, focal size and hatch spacing) on three different levels, starting from 50.01Ni-49.99Ti (at%) powder. The higher volumetric energy density (VED) applied resulted in Ni evaporation, while negligible variation in Ni content and consequently in the A_s temperature were found for lower VED (J/mm^3). VED was calculated through Eq. 1.2.

The influence of various process parameters on NiTi stents produced through L-PBF was recently investigated by Yan et al. [160], for the first time using the geometry of a biomedical device. A commercially available 55.4-NiTi (wt%) batch of powder was used to

produce stents with different laser power (P) and scanning speed (v) levels. The combination of P and v leading to M_s temperature below room temperature was pointed out in Fig. 2.66. In this case, a specific VED range to obtain the desired properties could not be identified, showing that VED alone cannot provide univocal information on the printing quality and Ni evaporation. This makes the optimization of the process parameters to avoid Ni evaporation for L-PBF NiTi much more challenging.

P350	2333.3/64.7	1166.7/67.0	777.8/67.0	233.3/60.4	116.7/40.6	77.8/26.2
P320	2133.3/64.6	1066.7/66.7	711.1/66.3	213.3/60.8	106.7/31.4	71.1/27.2
P300	1999.8/64.2	999.9/64.3	666.6/67.0	200.0/56.9	100.0/30.1	66.7/25.9
P280	1866.6/67.3	933.3/67.9	622.2/47.1	186.7/33.9	93.3/27.2	62.2/24.9
P200	1333.3/24.4	666.7/25.9	444.4/26.8	133.3/33.4	66.7/23.3	44.4/19.9
P100	666.6/-7.4	333.3/-1.2	222.2/-6.8	66.7/23.2	33.3/6.5	22.2/2.4
P50	333.3/1.2	166.7/5.0	111.1/3.6	33.3/23.7	16.7/5.3	11.1/1.3
	v50	**v100**	**v150**	**v500**	**v1000**	**v1500**

Fig. 2.66. M_s temperature at different laser power (W) and scanning speed (mm/s). The energy density (J/mm^3) and M_s (°C) are summarized in the boxes. Regions marked with green color represent M_s < room temperature, with red color room temperature < M_s < body temperature, blue color M_s > body temperature, grey color failure in the printing [160].

Simulation can constitute a powerful tool for the prediction of Ni evaporation. In this regard, thermal fluid dynamics were successfully used by Jamshidi et al. [161] to simulate the selective evaporation of Ni during L-PBF of NiTi stents.

Avoiding Ni evaporation during the process is crucial, since even a small variation in the Ni content can result in a different functional behavior. Unfortunately, this can happen despite the careful setting of the process parameters or the optimization of VED. In this regard, the possibility of controlling the TTs to readjust A_f after Ni evaporation has been rarely considered so far. To date, in fact, only one study analyzed the effects of heat treatments on the modification of A_f for the production of NiTi stents through L-PBF [161]. In addition, also the possibility to add an extra 2% of Ni (at%) into the as-received equiatomic powder was examined. It was found that by using compensated powder, A_f decreased to 37 °C, while the heat treatment at 500 °C for 30 min was effective in dropping the A_f temperature to 29 °C (Fig. 2.67). This showed that the adjustment of A_f is possible

through heat treatments. However, no mechanical tests were performed to assess the mechanical behavior of the heat-treated sample.

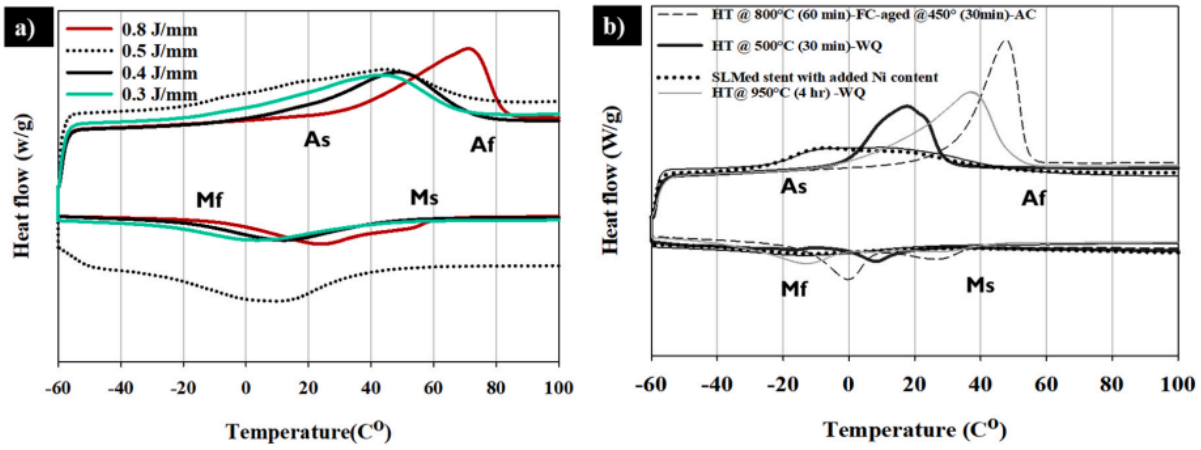

Fig. 2.67. DSC thermograms of (a) as-fabricated L-PBF NiTi stents manufactured with various energy densities, (b) L-PBF NiTi stents prepared with NiTi+Ni (extra 2% of Ni) powders together with heat treated samples at different conditions [161].

2.8 THESIS OBJECTIVES

As reviewed in the previous Chapter, heat treatments offer interesting opportunities for L-PBF NiTi parts intended for biomedical applications. Among these, short-time direct aging has been rarely considered for the obtainment of the superelastic effect. Moreover, the role of heat treatments in the possibility of modifying the transformation temperatures after Ni evaporation still requires further investigation.

In this context, the present work develops in two directions, schematized in Fig. 2.68:

- the first (Section 3) concerns the characterization of the superelastic behavior of 52.39Ni-47.61Ti (at%) alloy produced by L-PBF after short-time direct aging, through an exhaustive microstructural analysis and the construction of the experimental temperature-stress diagram, never considered so far for additively manufactured NiTi;
- the second (Section 4) investigates the possibility to adjust A_f temperature through heat treatments in 50.54Ni-49.46Ti (at%) alloy after Ni evaporation, to allow the obtainment of a microstructure suitable for superelasticity.

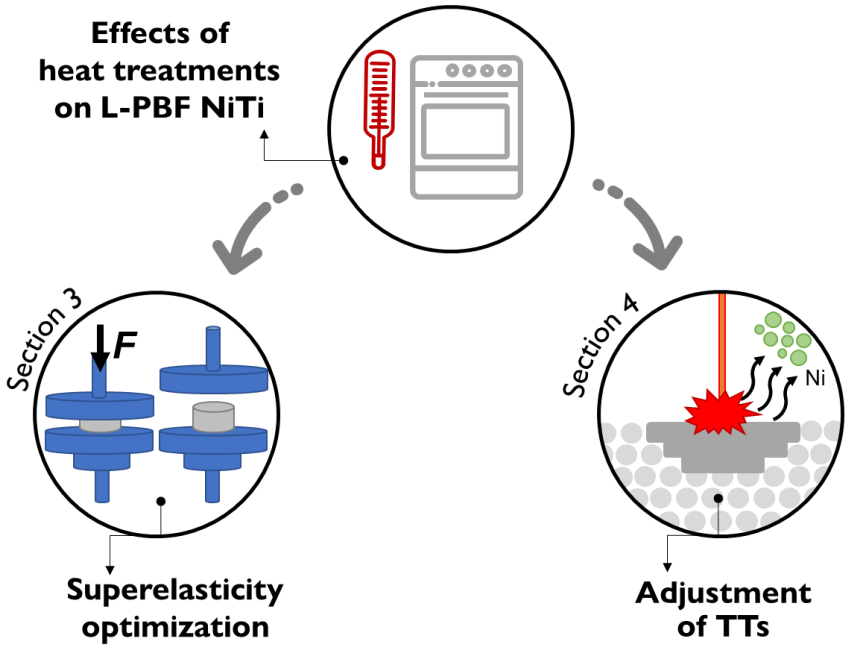

Fig. 2.68. Schematic summary of the topics addressed in the present work.

SECTION 3.

EFFECTS OF DIRECT AGING ON THE SUPERELASTIC EFFECT

In this Section, the experimental activities were carried out on samples manufactured with 52.39Ni-47.61Ti (at%) powders, with the aim of optimizing heat treatments after L-PBF production for the obtainment of superelasticity. The innovative contribution is the performing of short-time direct aging heat treatments after manufacturing, which were found to allow the obtainment of superelasticity both at RT and 37 °C, i.e. the operation temperature of biomedical devices, and not only at A_f + 10 °C temperature.

Most of the content illustrated in this Section are part of a scientific paper titled "Effects of direct aging heat treatments on the superelasticity of Nitinol produced via Laser Powder Bed Fusion" published on *Metallurgical and Material Transaction A* journal [176].

Besides, additional analyses are shown, which lead to the obtainment of the experimental temperature-stress diagram for each of the studied conditions. While this is a theoretically known aspect, it is rarely present in experimental works and to date has never been considered for additive manufactured NiTi. However, it constitutes a powerful tool for the practical use of NiTi since it allows the complete characterization of its behavior at different temperatures.

The experimental procedure is firstly described, followed by the discussion of results.

3.1 MATERIALS AND METHODS

3.1.1 Samples production and heat treatments

NiTi cylindrical samples (8 mm in diameter and 40 mm in height) were manufactured in the vertical direction starting from powder with 52.39Ni-47.61Ti nominal chemical composition (at%) with the process parameters reported in Table 3.1. Aconity MINI (Aconity 3D GmbH), a powder bed fusion system equipped with a 200 W fiber laser of 1068 nm wavelength, was used for the fabrication. The building chamber was filled with argon gas with 99.999% purity and the system was operated at < 20 ppm of oxygen level.

Table 3.1. Process parameters used for NiTi component production via L-PBF.

Laser power (W)	Scan speed (mm/s)	Hatch spacing (µm)	Spot size (µm)	Layer thickness (µm)
150-180	500-1000	80	60	60

The schematic representation of the printed samples with respect to the building platform is reported in Fig. 3.1, while an actual sample obtained after the process is displayed in Fig. 3.2 for illustrative purposes.

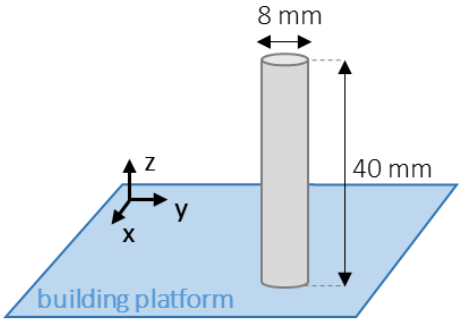

Fig. 3.1. Schematic representation of cylindrical samples.

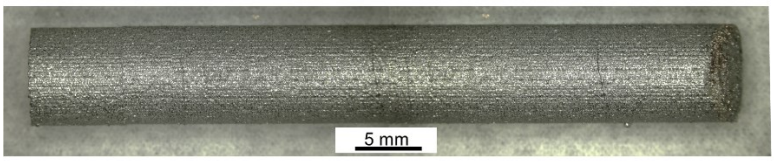

Fig. 3.2. L-PBF cylindrical sample used in the present study.

A preliminary characterization aimed at determining the effects of the different sets of process parameters used was conducted in terms of determination of the TTs and

microstructural characterization. The results showed negligible differences between samples, e.g. the microstructural observations, measured size of the chessboard pattern (between 68 and 70 μm), and the TTs were superimposable among all the samples (see the Appendix 3.4 for the detailed analyses). Therefore, the as-produced samples will be generically referred to as "as-built samples", disregarding the small differences in the process parameters.

A Nabertherm P330 furnace was used to carry out heat treatments. Aging heat treatments without prior solution annealing, i.e. direct aging, were performed. Two different temperatures were used for the aging step, 400 °C and 500 °C, for a short exposure time of 15 min followed by water quenching. For comparison, some samples were treated with solution annealing followed by aging. Solution annealing was performed at 950 °C for 5.5 h followed by water quenching. For the subsequent step, the same aging treatments described for the direct aging were used. The solution annealing specifications and the aging temperatures were selected according to the literature [33, 40, 169, 170, 174], while 15 min was chosen as aging time to investigate the effect of short time aging treatments on L-PBF NiTi.

Details of the analyzed conditions are reported in Table 3.2, where the solution annealed and aged samples are referred to as S 400 °C and S 500 °C, while the direct aged samples as DA 400 °C and DA 500 °C.

Table 3.2. Conditions investigated in the present work.

Condition	Heat treatment
As-built	-
S 400 °C	950 °C 5.5 h WQ + 400 °C 15 min WQ
S 500 °C	950 °C 5.5 h WQ + 500 °C 15 min WQ
DA 400 °C	400 °C 15 min WQ
DA 500 °C	500 °C 15 min WQ

3.1.2 Characterization procedure

The TTs were measured using differential scanning calorimetry (DSC – Q100 – TA Instruments) analyses involving subsequent thermal cycle of heating and cooling between -90 °C and 180 °C, with a heating/cooling rate of 10 °C/min. For each sample, the martensite and austenite start (M_s, A_s), finish (M_f, A_f) and peak (M_{Peak}, A_{Peak}) temperatures were identified, as well as temperatures concerning the R-phase (R_s, R_p, R_f), where present.

Crystalline structures of the samples were determined by using a Panalytical X'Pert PRO diffractometer equipped with a X'Celerator detector (X-ray source: Cu Kα, λ = 0.154nm; generator settings: 40 mA, 40 kV). XRD patterns were collected at room temperature in a 2θ range of 10° ÷ 100° (step Size: 0.0170° 2θ; scan step time: 30 s).

Microstructure was investigated through LEICA DMI 5000M optical microscope and scanning electron microscope (SEM) Leo Evo 40XVP on samples obtained using Imptech Pc10 precision cutter, cold mounted and polished with silicon carbide abrasive papers up to mirror finishing. Chemical etching was performed for 150-200 s using 10% HF, 40% HNO_3 and 50% H_2O solution, i.e. a diluted solution as suggested by Undisz et al. [177] to inhibit the formation of artefacts deriving from the hydrofluoric acid.

Porosities were characterized in terms of fraction of area, roundness and surface distribution through the analysis of eight optical microscopic images of unetched samples, each with an area of 0.6 mm^2. The fraction of porosities (%) was determined as the ratio between the total area of porosities and the analyzed area of samples. The roundness was calculated through the following equation, according to the instrument guide:

$$R = \frac{2p}{4\pi A \times 1.064}$$

Eq. 3.1

where R is the roundness, $2p$ and A are respectively the perimeter and area of the pore, and 1.064 is a corrector factor for the image digitalization.

Samples for compression tests were machined to final size of 4.5 mm in diameter (d) and 6.75 mm in length (l), to ensure a l/d of 1.5. Compression tests were performed along the building direction using an Instron mod. 3369 machine (load cell of 50 kN) with a strain rate of 10^{-3} s^{-1}, at room temperature (RT), 37 °C, and at A_f + 10 °C temperature. Experiments at RT were conducted in two different modes, i.e. cyclic loading-unloading up to a fixed level of deformation (6%) for 15 times and incremental cyclic tests from 1% to 10% of deformation and were repeated two times per condition. Deformation was measured by crosshead displacement. Compression tests at 37 °C and at A_f + 10 °C were carried out in the cyclic mode, using an environmental chamber with forced-ventilation, cooled with blowing cryogenic gas. During tests, temperature was monitored to ensure to be in the range of ± 2 °C with respect to the temperature of interest by means of thermocouples. Compression tests were chosen for the characterization since most of the biomedical devices

are compressed during exercise as well as during their delivery in the human body (e.g. vascular stents). For each cycle of each test, the maximum stress (σ_{MAX}), the pseudoelastic stress (σ_{PE}), i.e. the critical stress to induce the martensitic transformation, and the residual strain associated to each cycle (ε_{RES}) were determined according to Fig. 3.3. σ_{PE} was graphically obtained at the inflection point using the tangent method where it was visually identifiable. The total accumulated residual strain ($\varepsilon_{RES,TOT}$) was also calculated as the sum of the residual strains (ε_{RES}) of each cycle.

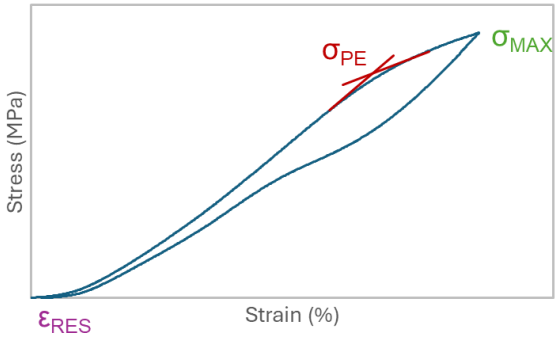

Fig. 3.3. Schematic illustration for the determination of σ_{MAX}, σ_{PE} and ε_{RES} for an example cycle.

In addition, compression tests up to failure were executed both at RT and 150 °C for each sample, for the determination of the critical stress of slip deformation σ_{SLIP}. This corresponds to the second inflection point for samples showing a superelastic behavior, i.e. tests at RT, and to the only inflection point present for samples that do not exhibit superelasticity, i.e. tests at 150 °C, and was graphically determined using the tangent method according to Fig. 3.4 (see also Fig. 2.19b). Besides RT, 150 °C was chosen as testing temperature for compression tests up to failure to better appreciate the variation of σ_{SLIP} with temperature. The obtained data were elaborated for the determination of the temperature-stress diagram, allowing the complete characterization of the superelastic behavior at different temperatures for each studied condition in relationship to the microstructural features.

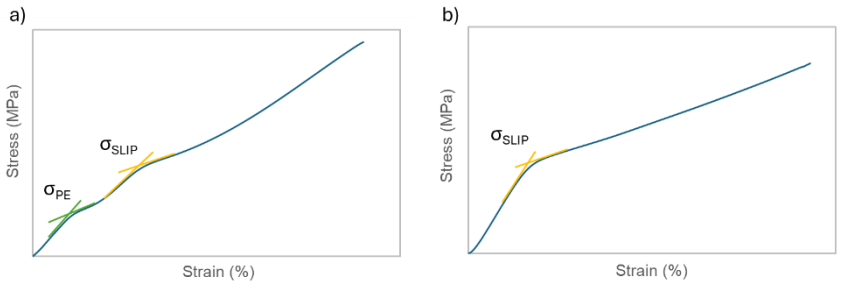

Fig. 3.4. Schematic illustration for the determination of σ_{SLIP} in two different cases of compression tests up to failure.

To provide a complete characterization of the DA samples, transmission electron microscopy (TEM) inspections were performed using a Philips™ CM20® microscope operating at 200 kV and equipped with a double tilt specimen holder and a liquid nitrogen cooling stage. Discs of 3 mm diameter were extracted from the AM cylindrical samples at the xy plane, using a precision cutting tool, and then ground to an average thickness of 100 μm. Double-side dimpling was carried out to a disc-center mean thickness of 30 μm. Final thinning to electron transparency was obtained by using a dual-beam Gatan™ Precision Ion Polishing System (PIPS).

Detected phases were identified using selected area electron diffraction (SAD). With this respect, R-phase was identified by diffraction spots occurring at 1/3<110> positions in the <111>-matrix SAD patterns. In this crystal orientation, the coherent Ni_4Ti_3 phase, whenever present, can be recognized by SAEDP additional diffraction spots at 1/7<123>-matrix positions.

Statistical evaluations of mean size, distribution, and volume fraction of the Ni_4Ti_3 phase particles were carried out by orienting the foil normal to the $[1\bar{1}0]$ direction. Foil thickness, t_{TEM}, was measured by converged electron beam diffraction (CBED). This was performed by analysing the corresponding diffracted beam intensity variation under dual beam conditions. Thence, linear interpolation of data points in a $S^2/n_{fringes}^2$ vs. $n_{fringes}^{-2}$, where S is the fringes spacing, and $n_{fringes}$ the number of counted fringes, was used to determine t_{TEM}. Crystal thickness, t_{TEM}, was measured in the areas, A, from which particle measurements were carried out.

Particle size, d, was measured by stereographic methods according to EN-112 using an image analysis software (Image pro-plus®). Particle edge-to-edge spacing, λ, was determine by stereological method through $\lambda = (N/V)^{-1/3}$, being N the total number particles measured and $V = A \cdot t_{TEM}$ the total inspected TEM crystal volume from which the measurements were taken. Particle volume fraction, f_V, was determined by Woodhead method in which the volume number fraction is determined by $N_V = N_A/d$. For each size group, $N_A(i) = n_i/(A/M^2)$ represents the thin foil are fraction recorded by tilting the thin foil at $[111]_{B2}$, that is where the longest lenticular axis of the Ni_4Ti_3 phase particles are lying, where n_i are the number of particles in specific size groups, and A is the area from which particle sizes are measured and counted at magnification M. Thence, $N_V(i) = N_A(i)/(t_{TEM} + (i\text{-}1/2)\Delta)$, being t_{TEM} the thin

foil thickness measured in the area of acquisition and $(i\text{-}1/2)\Delta$ is the mean diameter in the size group (i).

Using this stereological approach, the Ni_4Ti_3 particle volume fraction is calculated as follows:

$$f_V = \frac{\pi}{6}\Delta^3 \sum N_{V(i)}(i - 1/2)^3$$

Eq. 3.2

and the related values were obtained by evaluating more than 2500 particles from several TEM disc areas and from three different TEM discs per experimental condition.

Vickers microhardness tests were also performed on the DA samples, with the aim of providing a deeper understanding of their mechanical behavior in relationship to the microstructure. Microhardness measurements were carried out on the xy plane for each sample with a Mitutoyo HM-200 hardness tester, using a load of 100 g applied for 15 s, for a total number of ten indentations. Results of Vickers microhardness tests were discussed with respect to the stress-strain behavior up to failure for the DA samples.

3.2 RESULTS AND DISCUSSION

3.2.1 Phase transformation

Fig. 3.5 displays the DSC thermograms of virgin powder, as-built and heat-treated samples, and Table 3.3 shows the resulting TTs.

The DSC curve of the powder presents large and adjacent peaks during both the heating and cooling scan, due to the A ↔ M (B2 cubic ↔ monoclinic B19' lattice [178]) phase transformation occurring at multiples and continuous temperatures, as a result of the compositional heterogeneity of powder [179]. The as-built alloy exhibits only a single peak on both cooling and heating, which corresponds to the A→M direct transformation and M→A reverse transformation respectively. It should be noted that the leftmost peak detected in the cooling scans of powder and as-built sample is not completely observable, due to the limited examined temperature range. These peaks are associated to the A→M transformation, which in these cases did not complete in the examined range and therefore M_f could not be accurately determined due to the instrument limits. Both the powder and the

as-built sample are characterized by an A_f lower than room temperature, thus denoting the presence of the austenitic phase at room temperature.

TTs were also determined for the as-built sample after solution annealing to estimate the chemical composition of the alloy after L-PBF process. This is possible due to the extreme sensitivity of the TTs to the Ni content, as shown in Fig. 2.23. The results, not reported here for the sake of brevity, showed a M_s temperature of -9 °C, which, compared to the literature [65, 66], suggests a Ni content (at%) approximately between 50.5% and 51%, pointing out that likely more than 1% of Ni evaporated during the process.

The double peaks observed in the DSC scans for all the heat-treated alloys suggest the presence of the R-phase (R). This is an intermediate phase appearing sometimes in the transformation of austenite into martensite, resulting from the trigonal distortion of the B2 structure. The R-phase transformation can be classified as symmetric (A→R→M on cooling, M→R→A on heating) for S 400 °C, DA 400 °C and DA 500 °C samples, while asymmetric (A→R→M on cooling, M→A on heating) for S 500 °C [46]. The second cooling peak (R→M) is not evident for S 400 °C, DA 400 °C and DA 500 °C. However, the two-step transformation during heating and the very small temperature hysteresis between the austenite peak and the R-phase peak ($|A_p - R_p| < 10$ °C) allow the identification of the R-phase. In fact, the A ↔ R transformation is characterized by a very small temperature hysteresis compared to the A ↔ M transformation [46]. Since the R→M transformation is not completely observable for S 400 °C, DA 400 °C and DA 500 °C, the relative Mf temperature was not accurately determinable due to the instrument limits.

R-phase is connected to the presence of Ni_4Ti_3 precipitates, which are known to form after solution annealing and aging between 400-600 °C in the conventionally manufactured NiTi components [33, 59]. The presence of these particles, if nano-sized and placed at small relative distances, generates strain fields able to promote A→R transformation over A→M. This is due to the smaller transformation strain involved by the R-phase compared to martensite if precipitates are present [66, 180]. The increase of the TTs in the heat-treated alloys compared to the as-built also confirms the presence of Ni_4Ti_3, as their formation involves a decrease in the Ni content of the matrix. It is in fact well established that the increase of the TTs is associated to the loss of Ni content in the matrix, which can originate by the formation of Ni-rich secondary phases during heat treatment or by the Ni evaporation during the process [33, 173, 181-183].

By comparing the samples aged at the same temperature, with and without solution annealing, it appears that the TTs are almost superimposable, especially for S 400 °C and DA 400 °C. The small variation observed between S 500 °C and DA 500 °C is mainly attributed to the asymmetric nature of the R transformation recorded for S 500 °C. However, the austenite TTs, which determine the superelastic behavior, appears similar also between S 500 °C and DA 500 °C. This denotes that the effect of solution annealing on TTs is negligible compared to the effect of the aging for the purpose of obtaining TTs suitable for the superelasticity.

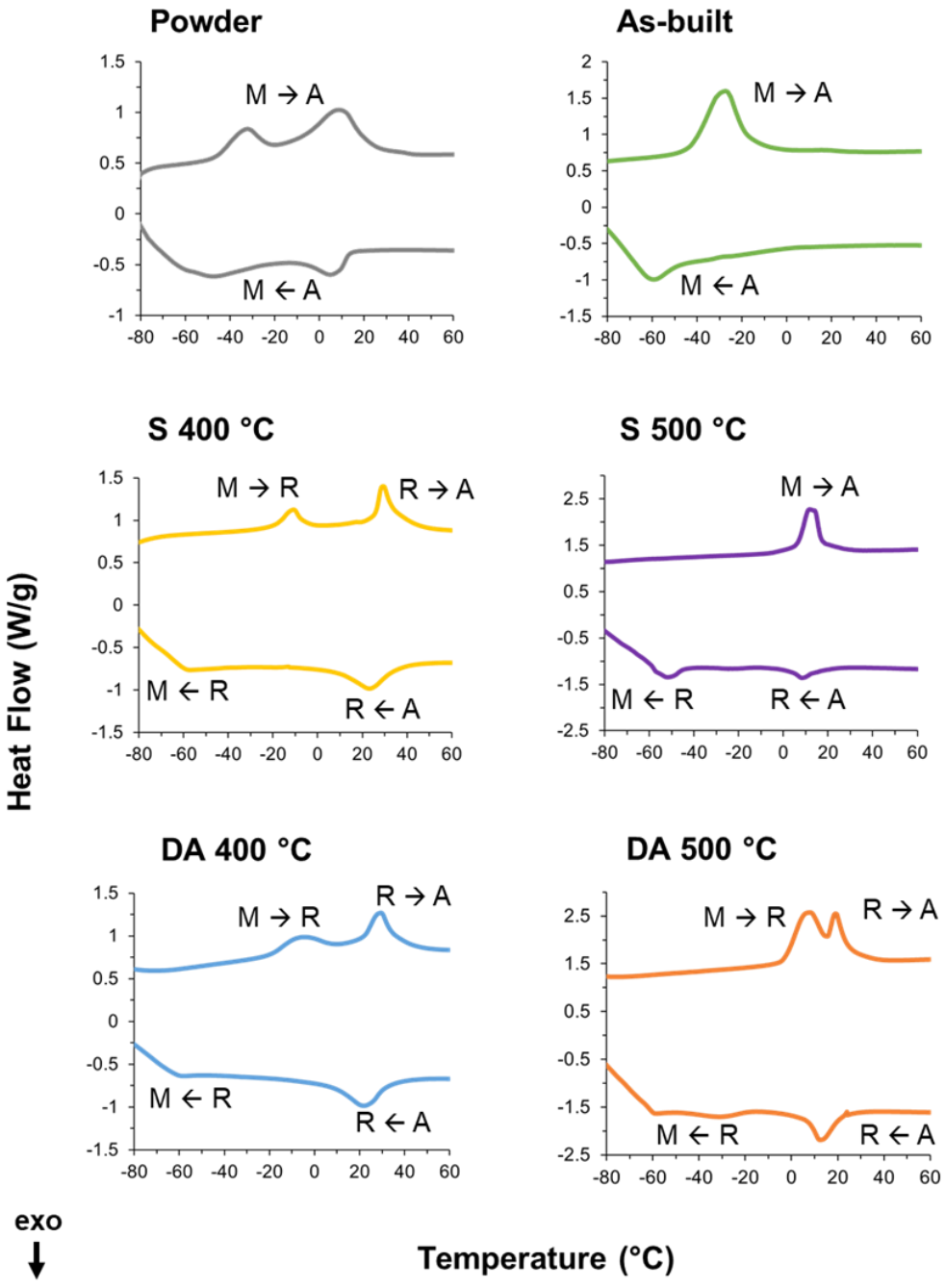

Fig. 3.5. DSC thermograms for powder, as-built and heat-treated samples.

Table 3.3. Transformation temperatures of powder, as-built and heat-treated samples.

Material	Temperature (°C)								
	M_f	M_p	M_s	R_f	R_p	R_s	A_s	A_p	A_f
Powder	<-70	-48	-14	-	-	-	-48	8	23
As-built	<-70	-60	-31	-	-	-	-43	-27	-16
S 400 °C	<-70	-58	-40	9	23	36	25	29	35
S 500 °C	<-70	-57	-42	2	8	16	6	12	17
DA 400 °C	<-70	-60	-44	4	22	33	21	29	37
DA 500 °C	-46	-31	-19	6	12	22	16	19	25

3.2.2 Phase analysis and microstructure

Fig. 3.6 displays the XRD spectra of the specimens. According to the literature, all samples show the principal peaks of B2 austenite [184, 185]. In the case of the heat-treated alloys, B19' martensite can also be detected [185, 186], which is attributable to residual martensite due to the non-completed M→A transformation at room temperature. This is in agreement with the DSC analysis (Fig. 3.5). The peaks related to Ni_4Ti_3 overlap with those of B2 phase [179, 187-190], therefore it is not easy to clearly identify their presence. However, based on the literature, the formation of Ni_4Ti_3 can be reasonably assumed for the heat-treated samples. This is further confirmed by the DSC scans, which show the presence of the R-phase and the increase of TTs after the heat treatments (Fig. 3.5).

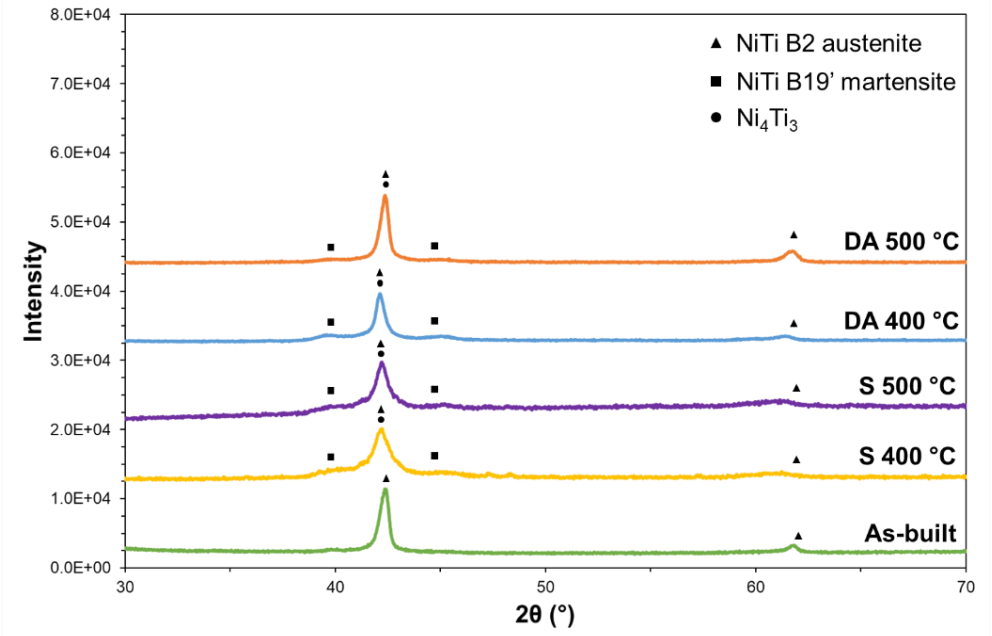

Fig. 3.6. XRD spectra of the as-built, S 400 °C, S 500 °C, DA 400 °C and DA 500 °C samples.

Micrographs along the xy plane at are reported in Fig. 3.7 for all the investigated conditions. The observable structure has a chessboard shape, which reflects the alternating laser scanning path used during production [170, 191]. Similar textures have already been detected in L-PBF NiTi [192-197]. The substructures ("islands") observable within the chessboard texture are characterized by squared shape. The main influence on their shape is generally attributed to the hatch spacing parameter, whose variation leads to changes from squared to polygonal or irregular shape [195-197].

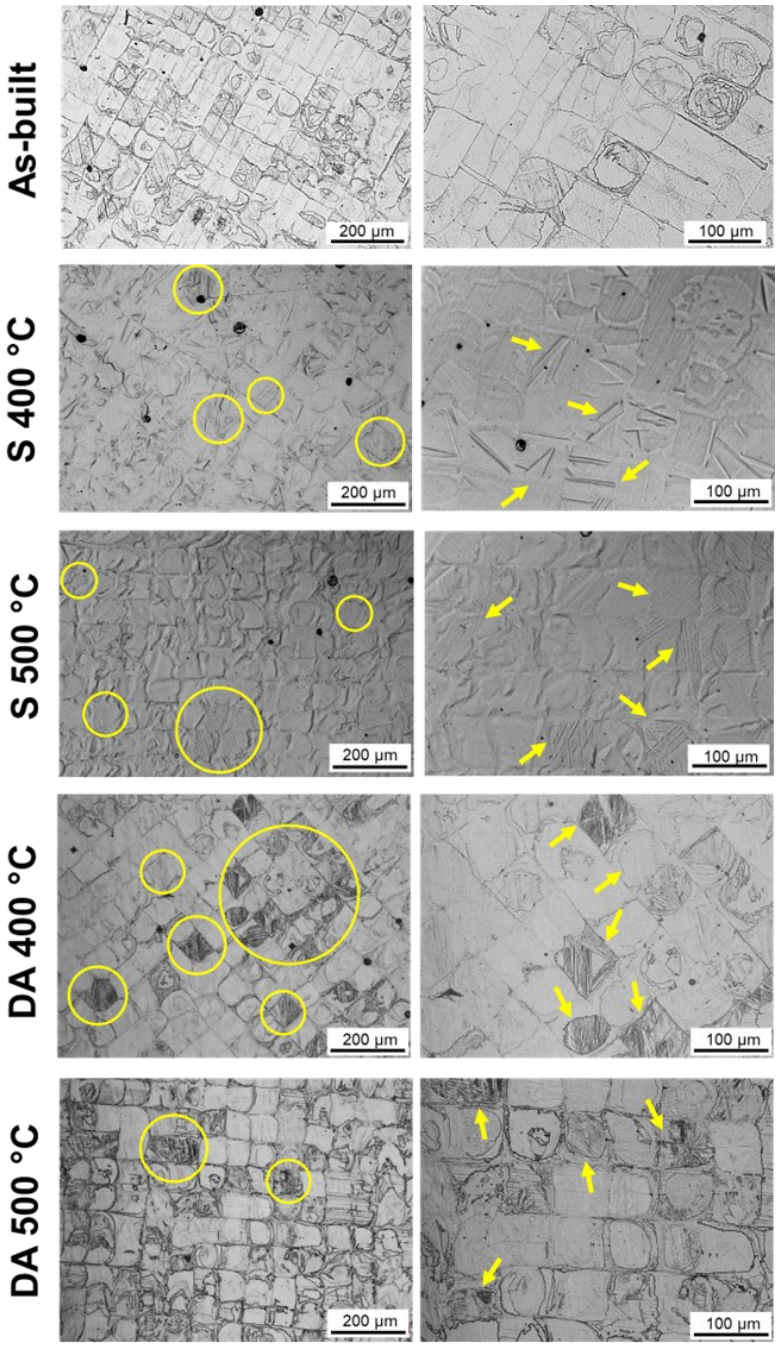

Fig. 3.7. Micrographs of as-built cylinders, as well as the S 400 °C, S 500 °C, DA 400 °C and DA 500 °C at different magnifications.

The chessboard texture in the as-built alloy is characterized by a width of the substructures of 70 ± 6 µm, which is slightly smaller than the hatch spacing, i.e. 80 µm. This can be attributed to a smaller spot size relative to the hatch spacing and denotes that no scan overlap occurred [59].

The chessboard structure was maintained after all the heat treatments performed. The width of the islands was found to be 70 ± 4 µm for S 400 °C, 70 ± 3 µm for S 500 °C, 70 ± 5 µm for DA 400 °C and 71 ± 4 µm for DA 500 °C, thus pointing out that no significant modifications in the chessboard texture took place after heat treatments.

Within the chessboard pattern of the as-built alloy, only "smooth" squares are observed, with no martensitic structures. In fact, according to the XRD and DSC analyses, this sample only presents the B2 austenite phase at room temperature. On the other hand, all the heat-treated samples show some martensitic structures inside the chessboard pattern, pointed out by the yellow circles and arrows. These, according to the XRD analysis, can be identified as the B19' martensitic phase. Ni_4Ti_3 precipitates are not observable at these magnifications for either solution annealed or direct aged alloys due to their nanometric dimensions.

From the comparison of the direct aged specimens, it appears that martensite is more evident in the DA 400 °C sample compared to the DA 500 °C. This is due to the different A_f temperatures (37 °C and 25 °C respectively), which point out that especially for DA 400 °C sample the transformation is still occurring at room temperature and thus more martensite is present in this case.

Details of an island of the chessboard texture and martensite structures at higher magnification are provided in Fig. 3.8 for some of the analyzed conditions, for illustrative purposes.

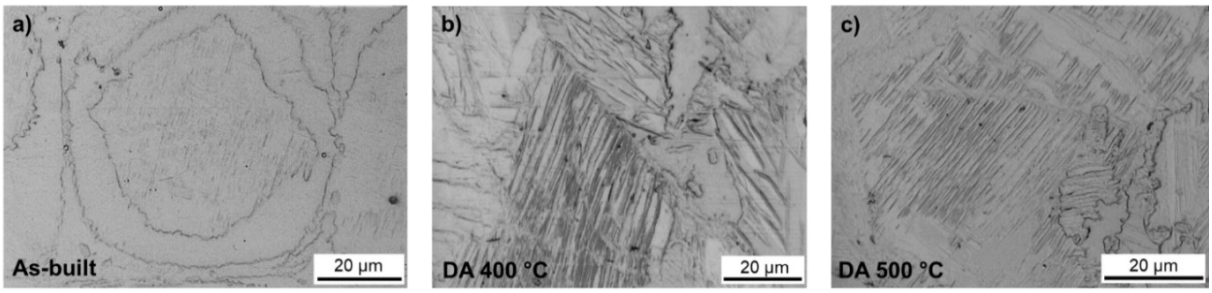

Fig. 3.8. Microstructural details of a chessboard substructure (a), and martensitic structures (b-c).

Fig. 3.9 reports the results of the SEM analyses, which reveal the same structures identified through the optical microscope, i.e. squared-shape chessboard texture for all the conditions and the presence of the martensitic phase in the heat-treated ones.

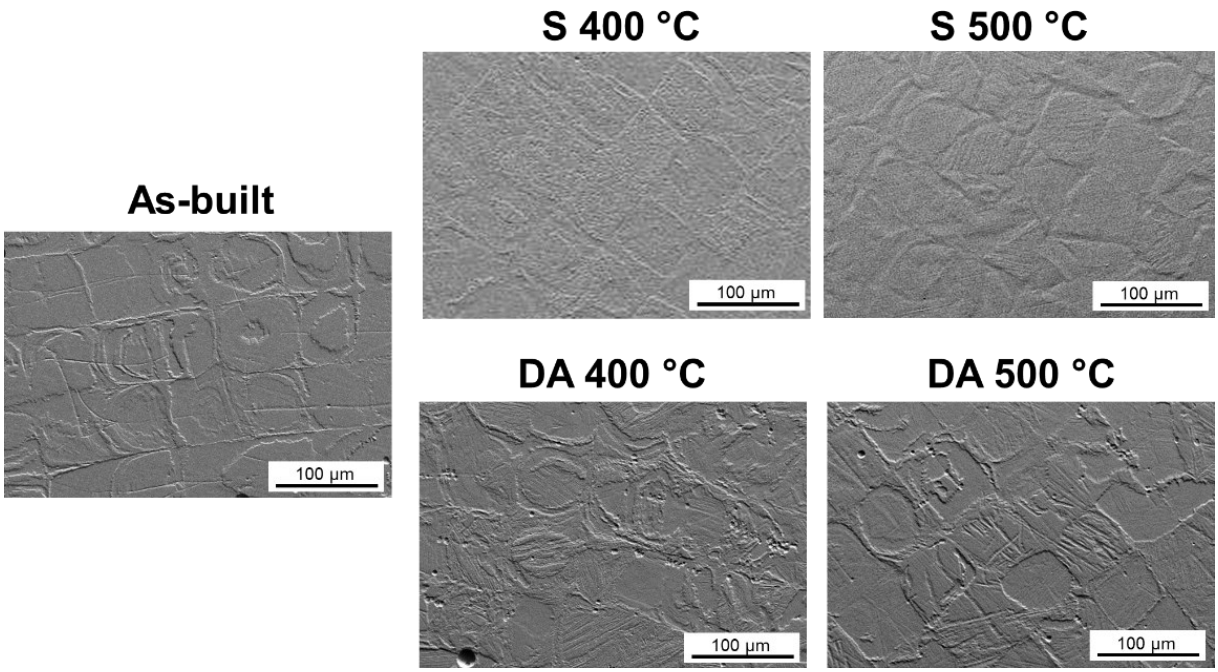

Fig. 3.9. SEM micrographs of as-built cylinders, as well as S 400 °C, S 500 °C, DA 400 °C and DA 500 °C.

Results of the porosity analysis for the as-built, S 400 °C, S 500 °C, DA 400 °C and DA 500 °C conditions are reported in Fig. 3.10. A very low porosity fraction can be observed for the as-built alloy, which remains negligible after the direct aging heat treatments, while increases after solution annealing and aging. This is due to the high temperature of the solution annealing treatment, which promotes the growth of the existing gas pores, resulting in the rise of the fraction of area of porosities. The analysis of the surface distribution showed that most of the porosities present an area lower than 50 μm^2. Furthermore, the roundness of pores was found to be close to 1 for each of the samples analyzed, denoting their spheric morphology. This demonstrates that most of the generated pores are mainly due to the absorption of the gas surrounding the material during the L-PBF process rather than lack of fusion defects [6, 198].

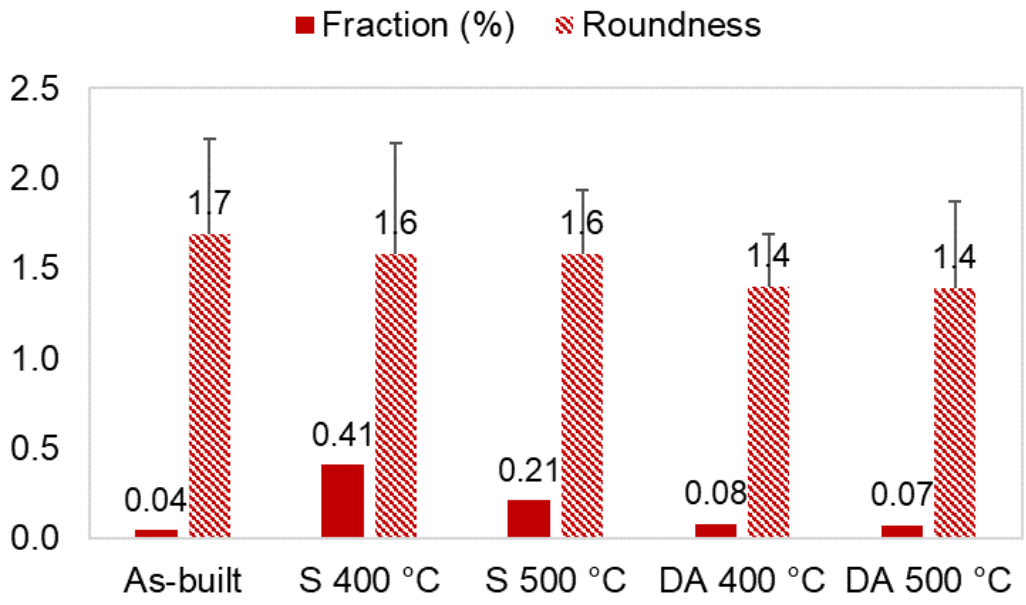

Fig. 3.10. Fraction of area and roundness of the porosities for as-built and heat-treated cylinders.

3.2.3 Stress-strain response at RT

3.2.3.1 Cyclic compression tests

Stress-strain curves obtained from cyclic compression tests at RT for the as-built and heat-treated samples are reported in Fig. 3.11, where solution annealed and direct aged samples are grouped by the aging temperature for a better comparison. Each specimen underwent 15 cycles of loading up to 6% strain, commonly considered as the limit for superelasticity, and unloading to 0%.

A pseudoelastic behavior can be observed in each condition (Fig. 3.11), with the formation of stress-induced martensite from the austenitic phase during the application of load, pointed out by the flattening of the curve, which is commonly shown also during both tension and torsion tests [199]. This part of the curve is commonly referred to as "Luders-like" deformation and is associated with martensite reorientation and detwinning processes [200, 201]. Stress-strain behavior is almost superimposable for the heat treatments carried out at the same temperature (i.e. aging), thus pointing out the minor effects of the presence of the solution annealing step compared to the aging temperature.

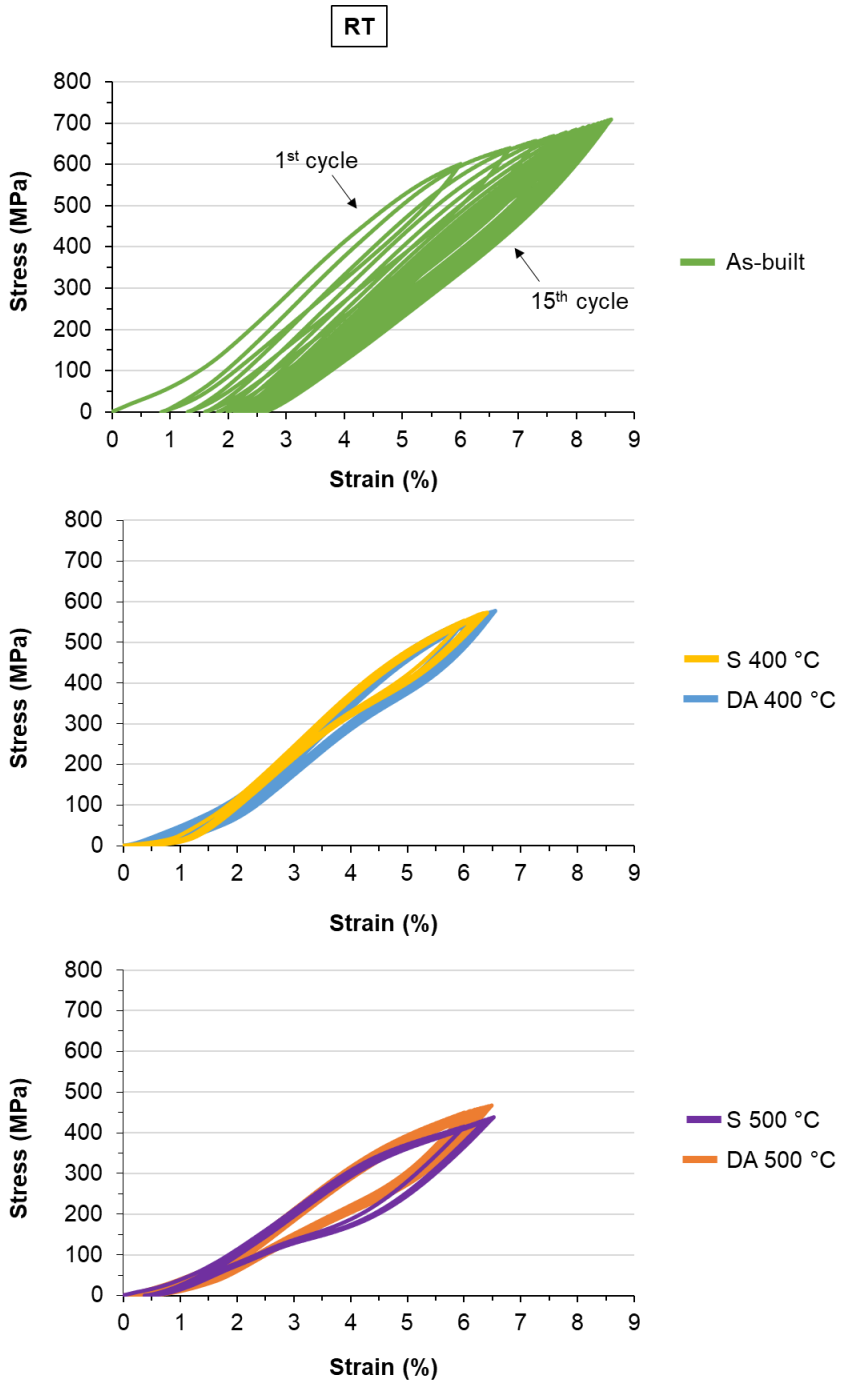

Fig. 3.11. Stress-strain responses of as-built and heat-treated samples tested under cyclic tests at RT.

For every cycle, the maximum stress (σ_{MAX}), the pseudoelastic stress (σ_{PE}), i.e. the critical stress to induce the martensitic transformation, and the residual strain associated to each cycle (ε_{RES}) were determined, and the results are summarized in Fig. 3.12. σ_{PE} was graphically determined at the inflection point using the tangent method where it was visually identifiable.

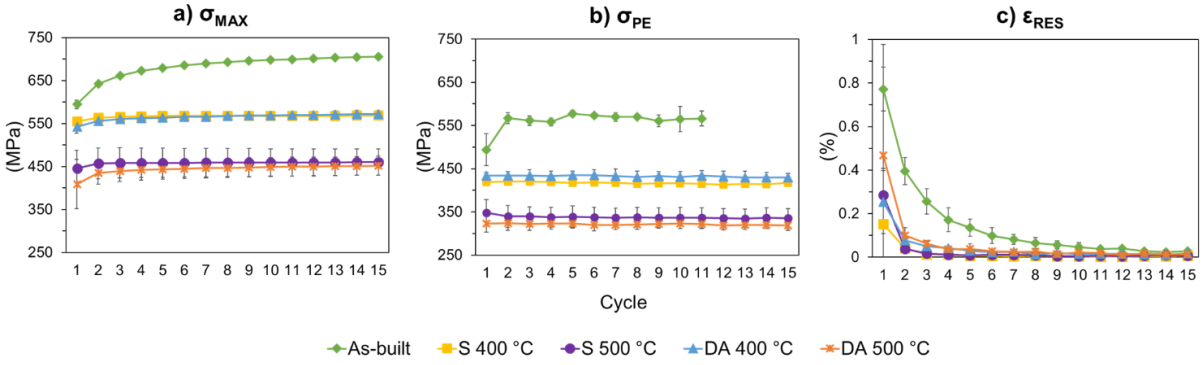

Fig. 3.12. Results of cyclic compression tests at RT: (a) maximum stress, (b) pseudoelastic stress and (c) residual strain as function of each cycle.

By analyzing σ_{MAX} and σ_{PE} (Fig. 3.12a-b), it emerges that higher values are reached by the as-built alloy, followed by S 400 °C and DA 400 °C and then by S 500 °C and DA 500 °C. The σ_{MAX} and σ_{PE} of the heat treatments performed at the same aging temperature are almost equal one to each other, reflecting what seen in Fig. 3.11.

During the first cycles, the as-built specimen shows an increasing trend for σ_{MAX}, which then stabilizes at about 700 MPa from cycle 6, while a lower σ_{PE} value is recorded only in the first cycle due to the marked difference in the shape of the first curve (Fig. 3.11). It should be noted that σ_{PE} could not be determined for cycles from 12 to 15 for the as-built condition, due to the gradual disappearance of the inflection point in the curves, pointing out an instability of the pseudoelastic behavior as the number of cycle increases.

On the other hand, all the heat-treated alloys show a lower σ_{MAX} value in cycle 1 (S 400 °C 555 ± 1 MPa, DA 400 °C 542 ± 15 MPa and S 500 °C 445 ± 42 MPa, DA 500 °C 409 ± 58 MPa), which then increases and remains constant from cycle 2 (around 570 MPa for both S 400 °C and DA 400 °C, and 450 MPa for both S 500 °C and DA 500 °C). Thus, for all the heat-treated samples σ_{MAX} settles after cycle 1, while σ_{PE} is stable from the first cycle. This denotes an overall greater stability in the stress-strain responses for the heat-treated conditions compared to the as-built. For each sample, a difference between σ_{MAX} and σ_{PE} in the range 120-150 MPa is recorded, considered after stabilization.

All the heat-treated samples show lower values of σ_{PE} compared to the as-built (Fig. 3.12b). In detail, heat treatments at 400 °C lowered σ_{PE} by approximately 135 MPa, while heat treatments at 500 °C by about 240 MPa compared to the as-built condition. As reported previously, this is because after aging austenite easily transforms into martensite due to the presence of local stress intensification field around Ni-rich precipitates, thus acting as nucleation sites for the transformation [57, 202]. Lower σ_{PE} values can be also associated to

the increase of TTs respect to the as-built alloy [168, 172], which agrees with the DSC results (Table 3.3).

By comparing the σ_{MAX} values of the as-built and heat-treated alloys (Fig. 3.12a), it appears that lower values are reached by the heat-treated ones. This points out that up to 6% of deformation the performed heat treatments enhanced the superelastic properties in compression by lowering σ_{PE} rather than increasing the maximum stress reached at 6% of strain.

Concerning ε_{RES} (Fig. 3.12c), the as-built sample exhibits the highest values, denoting poor superelastic features. In this case dislocations formed during deformation, generating plasticity as well as stabilizing some martensite variants during loading, which inhibits the reverse transformation upon unloading and the consequent total recovery of the deformation [40]. On the contrary, all the heat-treated conditions present comparable negligible values of irreversible strain (lower than 0.1% for each cycle after stabilization, which occurred after the first cycle).

The total accumulated strain after 15 cycles at 6% of deformation at RT is summarized in Table 3.4, where the higher superelasticity of the heat-treated alloys is confirmed.

Table 3.4. Residual deformation after 15 cycles at 6% of strain for all samples tested at RT.

	$\varepsilon_{RES,TOT,RT}$ (%)
As-built	2.24 ± 0.49
S 400 °C	0.28 ± 0.18
S 500 °C	0.43 ± 0.12
DA 400 °C	0.62 ± 0.12
DA 500 °C	0.89 ± 0.58

The remarkable superelastic features obtained after the heat treatments are attributed to the presence of the Ni_4Ti_3 precipitates resulting from aging. The latter favor the superelastic features of the alloy by raising the stress required for slip plastic deformation. In this way, the achievement of the critical stress to induce the martensitic transformation (σ_{PE}) is eased, since from a thermodynamic point of view it is easier to form martensite when the stress is applied rather than causing plastic deformation. The formation of stress-induced martensite is therefore favored before the occurrence of slip [117, 133, 203]. Furthermore, Ni_4Ti_3 precipitates are known to act as nucleation sites for the formation of martensite, thus promoting the martensitic transformation [40, 57, 172].

3.2.3.2 Incremental compression tests

The effect of incremental cyclic loading (from 1 to 10% of strain) at RT was also investigated and the stress-strain curves for each condition are reported in Fig. 3.13.

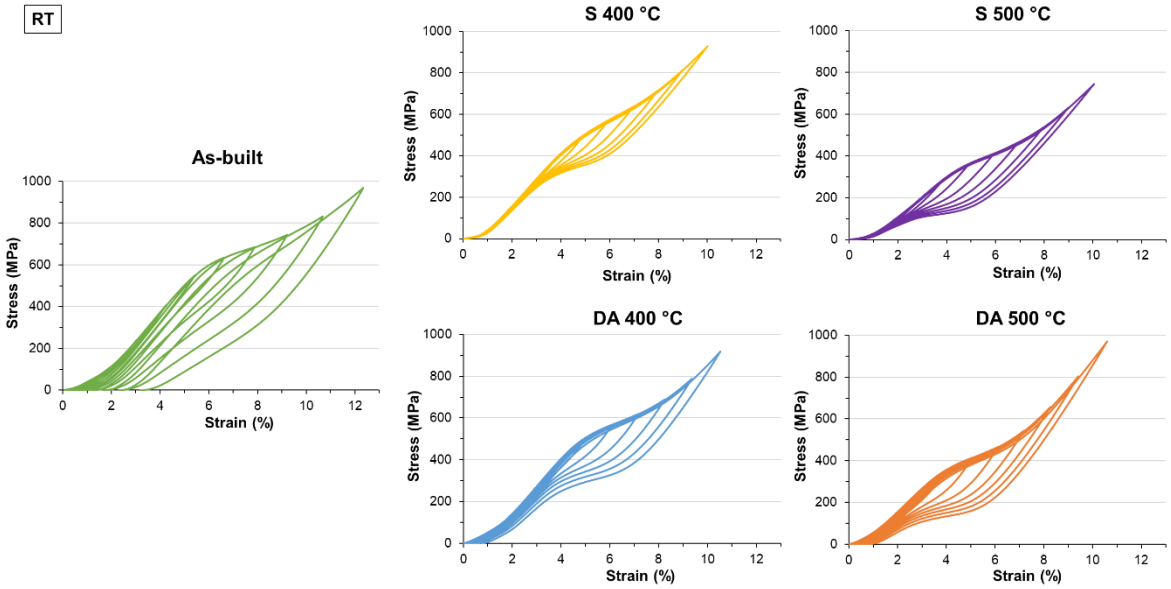

Fig. 3.13. Stress-strain responses tested under incremental tests at RT for as-built and heat-treated samples.

The general trend previously observed for cyclic tests is confirmed, with an overall pseudoelastic behavior emerging from each condition. Improved superelastic features are evident for the heat-treated alloys, which show a similar behavior by comparing the conditions at the same aging temperature. Also, similarly to the cyclic tests, the lowering of the curves is detected as the aging temperature increases, as well as a greater definition of the pseudoelastic behavior.

Results of σ_{MAX}, σ_{PE} and ε_{RES} are reported in Fig. 3.14 as function as the number of cycles, which in this case corresponds to the applied strain.

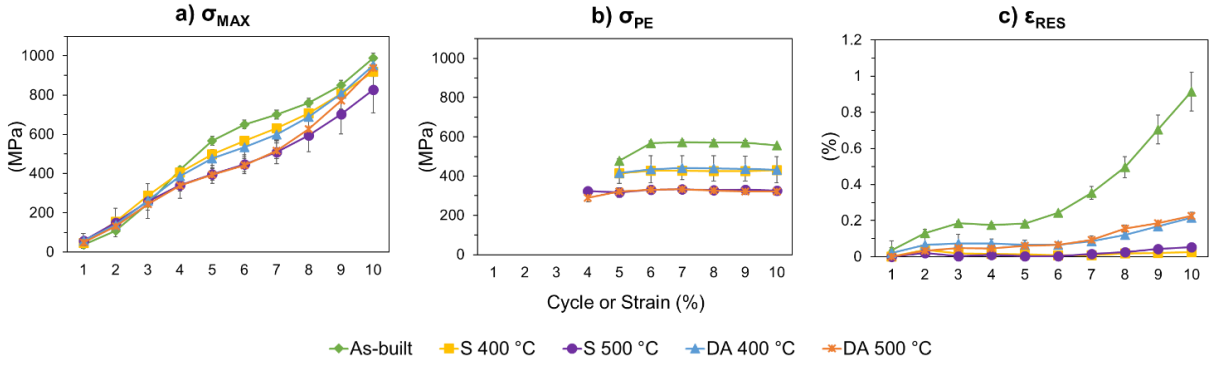

Fig. 3.14. Results of incremental compression tests at RT: (a) maximum stress, (b) pseudoelastic stress and (c) residual strain as function of each cycle.

The σ_{MAX} and σ_{PE} (Fig. 3.14a-b) for samples aged at the same temperature, with and without solution annealing, are nearly identical to one another, as previously detected in the cyclic tests.

As expected, σ_{MAX} raises as the number of cycles increases, as each cycle corresponds to an increase of the applied deformation (Fig. 3.14a). The as-built specimen reaches higher σ_{MAX} compared to heat-treated samples from cycle 4 to 9, while results are almost superimposed for the other cycles.

For each condition, σ_{PE} was not clearly identifiable in the early cycles, where in fact samples present a linear behavior due to the very low strains involved, and consequently it could not be determined (Fig. 3.14b). In this regard, it should be noted that both S 500 °C and DA 500 °C exhibits pseudoelastic behavior starting from 4%, while others from 5%. Values of σ_{PE} are higher in the as-built alloy, followed by S 400 °C and DA 400 °C and then by S 500 °C and DA 500 °C, confirming the general trend observed during cyclic compression tests. For each condition, σ_{PE} does not vary as the applied deformation increases, which is in agreement to what observed during incremental compressive tests by Saedi et al. [169]. σ_{PE} stabilizes at values around 570 MPa for the as-built sample, 430 MPa for both S 400 °C and DA 400 °C and 320 MPa for both S 500 °C and DA 500 °C. Heat treatments at 400 °C and 500 °C lowers σ_{PE} of about 135 MPa and 240 MPa compared to the as-built condition, which agrees to what found during cyclic compressive tests.

At equal applied deformation, ε_{RES} appears higher for the as-built, reaching 0.9 ± 0.1% in cycle 10, while both heat-treated specimens remain at values lower than 0.2% for each cycle, denoting a negligible irrecoverable strain (Fig. 3.14c).

The total cumulative strain after 10 cycles of incremental deformation is 3.4 ± 0.3% for the as-built alloy, 0.2 ± 0.1% for S 400 °C, 0.2 ± 0.1% for S 500 °C, 1.0 ± 0.2% for DA 400 °C and 0.9 ± 0.1% for DA 500 °C, thus indicating the improvement of the superelastic behavior thanks to heat treatments. Therefore, it can be stated that superelasticity is achieved up to 10% of strain after all the heat treatments. This value is higher than both the limit of superelasticity, commonly identified as 6%, and what found in previous studies on additively manufactured components [40, 168, 169, 172].

3.2.4 Stress-strain response at 37 °C

Cyclic compression tests were repeated at the body temperature (37 °C) to investigate the feasibility of achieving superelasticity for possible biomedical applications. The corresponding stress-strain curves are displayed in Fig. 3.15, while Table 3.5 summarizes the total accumulated residual strain at 37 °C ($\varepsilon_{RES,TOT,37\ °C}$) at the end of the 15 cycles for each condition as the main result of the test.

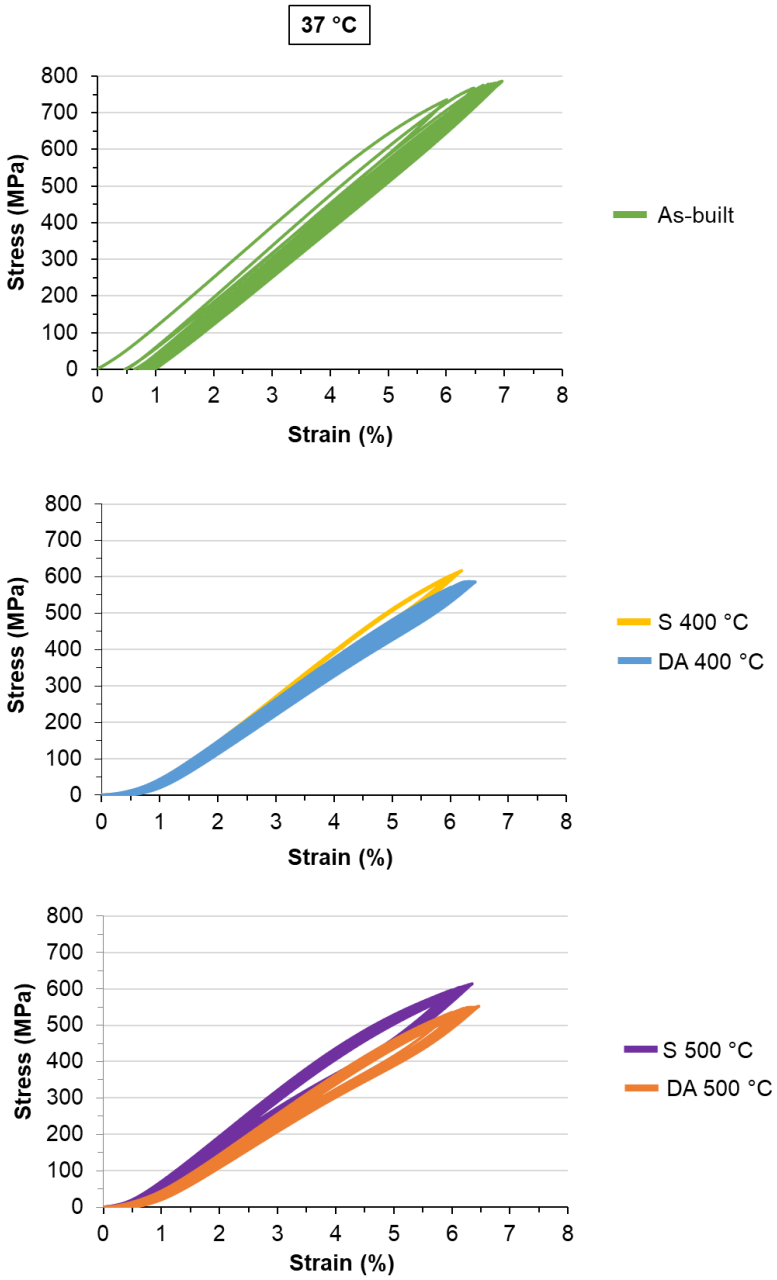

Fig. 3.15. Stress-strain responses of as-built and heat-treated samples tested under cyclic tests at 37 °C.

Similarly to what previously observed in RT tests, the as-built alloy shows higher stress at equal strain compared to the heat-treated. The comparison among samples aged at the same temperature shows that solution annealed and aged samples reach slightly higher stresses compared to the direct aged ones.

The as-built alloy is characterized by poor superelastic features, while all the heat-treated alloys show higher stability of the superelastic effect (Fig. 3.15), as well as negligible $\varepsilon_{RES,TOT,37\ °C}$ (Table 3.5). This is analogous to what was previously found at RT due to the non-significant microstructural differences experienced at 37 °C by the alloys. In fact, Ni_4Ti_3 precipitates are preserved at 37 °C, and their sizes and distribution are not expected to change. Furthermore, according to the TTs (Table 3.3), no substantial variations are expected at 37 °C in the matrices of the analyzed alloys. At this temperature both S 400 °C and DA 400 °C should again present austenite and martensite, while in both S 500 °C and DA 500 °C the austenite should be the solely phase present, and this is expected to further enhance the superelastic effect. Thence, heat treatments with aging at 500 °C appear to be preferable to those with aging at 400 °C in the perspective of biomedical applications. This is also confirmed by the more pronounced pseudoelastic behavior observed in Fig. 3.15.

Each of the curves obtained at 37 °C shows slightly higher levels of stress (σ_{MAX} and σ_{PE}) compared to those at RT (compare Fig. 3.15 to Fig. 3.11). This is due to the higher stability of the austenitic phase as the temperature rises, which leads to the need of greater stress for triggering the stress-induced martensitic transformation [204]. This is especially true for samples treated at 500 °C, i.e. S 500 °C and DA 500 °C, which at 37 °C are likely fully formed by austenite, rather than a mixed austenite-martensite structure as occurs at RT (A_f is of 17 °C and 25 °C, respectively).

Table 3.5. Residual deformation after 15 cycles at 6% strain for all samples tested at 37 °C.

	$\varepsilon_{RES,TOT,37\ °C}$ (%)
As-built	0.90 ± 0.09
S 400 °C	0.18 ± 0.02
S 500 °C	0.35 ± 0.01
DA 400 °C	0.44 ± 0.01
DA 500 °C	0.48 ± 0.02

3.2.5 Stress-strain response at A_f + 10 °C

To provide a comprehensive characterization of all the analyzed conditions, cyclic compression tests were performed at A_f + 10 °C temperature, which differs for each of the analyzed alloys (Table 3.3). This allowed the samples to be situated at identical thermodynamic conditions for a more detailed comparison. The corresponding stress-strain curves are displayed in Fig. 3.16, while Table 3.6 summarizes the total accumulated residual strain at A_f + 10 °C ($\varepsilon_{RES,TOT,Af+10\ °C}$) at the end of the 15 cycles for each condition as the main result of the test. It should be noted that for DA 500 °C sample, the A_f + 10 °C temperature corresponds to the condition of tests at 37 °C, illustrated in the above Paragraph.

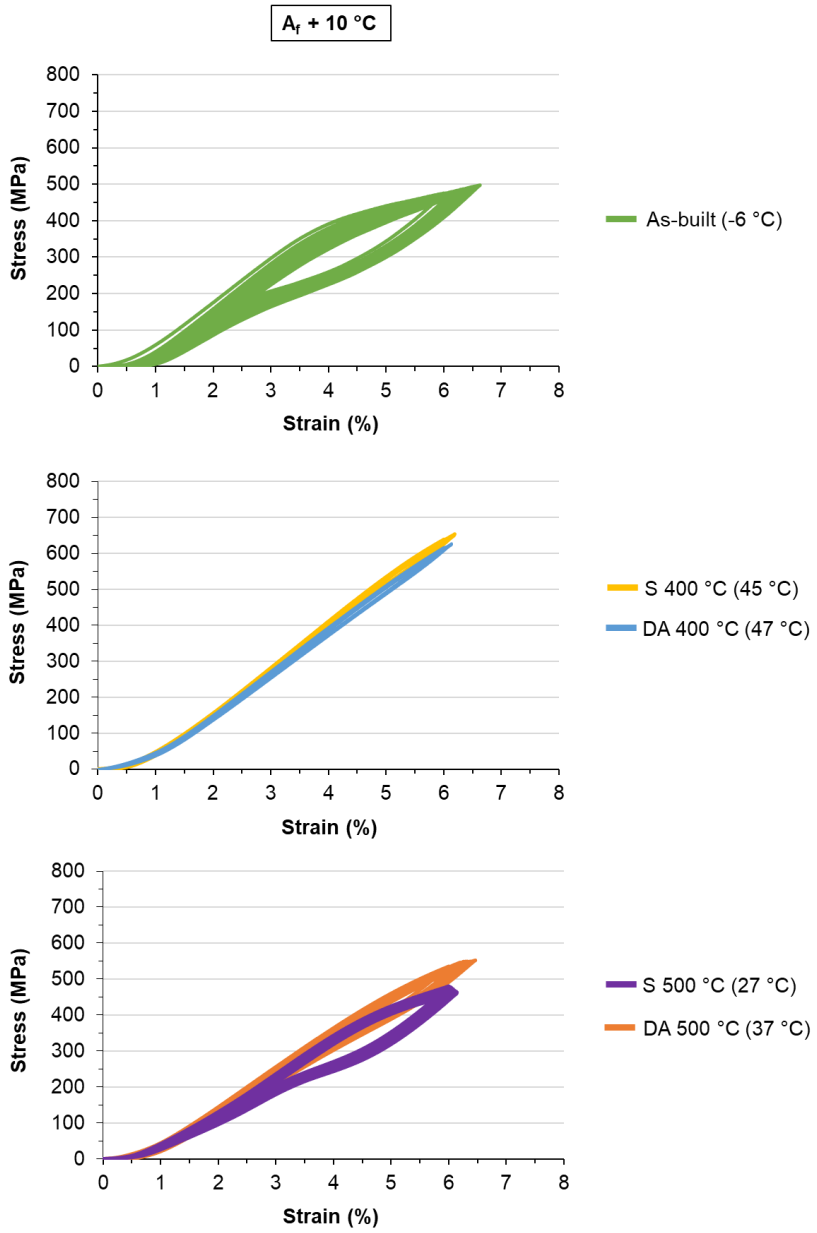

Fig. 3.16. *Stress-strain responses of as-built and heat-treated samples tested under cyclic tests at A_f + 10 °C. The testing temperature is indicated in brackets for each condition.*

Contrary to what previously found in RT and 37 °C tests, the as-built alloy shows lower or comparable stress at equal strain with respect to the heat-treated conditions, as well as improved superelastic features compared to the same condition tested at RT and 37 °C. In fact, the behavior of the as-built alloy appears to be deeply changed at its A_f + 10 °C, while the heat-treated alloys show a similar behavior for all the testing temperatures. This can be attributed to the greater differences in the testing temperatures for the as-built condition, which was of -6 °C in this case, and therefore much lower than the previously tests at RT and 37 °C. A_f + 10 °C temperatures for all the heat-treated alloys are instead closer both to RT and 37 °C. In this regard, it should be noted that testing all the samples at their A_f + 10 °C means that they are in the same thermodynamic condition since the thermodynamic driving force for the martensitic transformation is the same and therefore the selected testing temperature is expected to generate superelastic response in all the samples. This is confirmed by the $\varepsilon_{RES,TOT,Af+10\,°C}$ values reported in Table 3.6 for all the analyzed conditions, which points out the enhancement of superelastic features for the as-built sample at this temperature (compare Table 3.6 to Table 3.4 and Table 3.5).

Concerning the samples treated at 400 °C, i.e. S 400 °C and DA 400 °C, the slightly higher stresses reached at their A_f + 10 °C temperature compared to 37 °C is due to the fact that at this temperature they are fully formed from austenite, rather than a mixed austenite-martensite structure as occurs at RT and 37 °C. On the other hand, S 500 °C tested at A_f + 10 °C (i.e. 27 °C) shows lower levels of stress reached (σ_{MAX} and σ_{PE}) compared to S 500 °C tested at 37 °C, because the austenite is more stable as the temperature increases, and more stress is needed to induce the martensitic transformation [204]. This also explains the lower stresses reached at A_f + 10 °C compared to the other testing temperatures for the as-built alloy.

Table 3.6. Residual deformation after 15 cycles at 6% strain for all samples tested at A_f + 10 °C.

	$\varepsilon_{RES,TOT,Af+10\,°C}$ (%)
As-built	0.67 ± 0.03
S 400 °C	0.18 ± 0.01
S 500 °C	0.25 ± 0.16
DA 400 °C	0.07 ± 0.09
DA 500 °C	0.48 ± 0.02

3.2.6 Comparison of stress-strain responses at different testing temperatures

For better clarity, Fig. 3.17 provides the comparison of σ_{MAX}, σ_{PE} and ε_{RES} at the different analyzed temperatures for each sample, i.e. RT, 37 °C and A_f + 10 °C. The different scaling values on the y-axis should be noted for ε_{RES}. For the as-built sample, σ_{PE} at 37 °C could not be determined except for the very first cycle of the curves (see Fig. 3.15), and therefore was not reported in the graph below and could not be used for the construction of temperature-stress diagram in the following paragraph. It should be remarked that for DA 500 °C sample the resulting data for tests at A_f + 10 °C and 37 °C coincide. For DA 500 °C condition tested at RT, the high scattering value in the first cycle of loading is due to the fact that one of the tested samples exhibited an abnormal ε_{RES} during the first cycle (0.83% compared to 0.11% for the other sample), which however settles immediately from the next cycle. Therefore, this was considered to be not relevant for the superelastic features of the sample.

As previously mentioned, the higher the testing temperature the higher the σ_{PE}, due to a greater stability of the austenitic phase with temperature, as well as, from a thermodynamic point of view, more efforts required in inducing martensitic transformation. This also results in higher σ_{MAX} as the testing temperature rises.

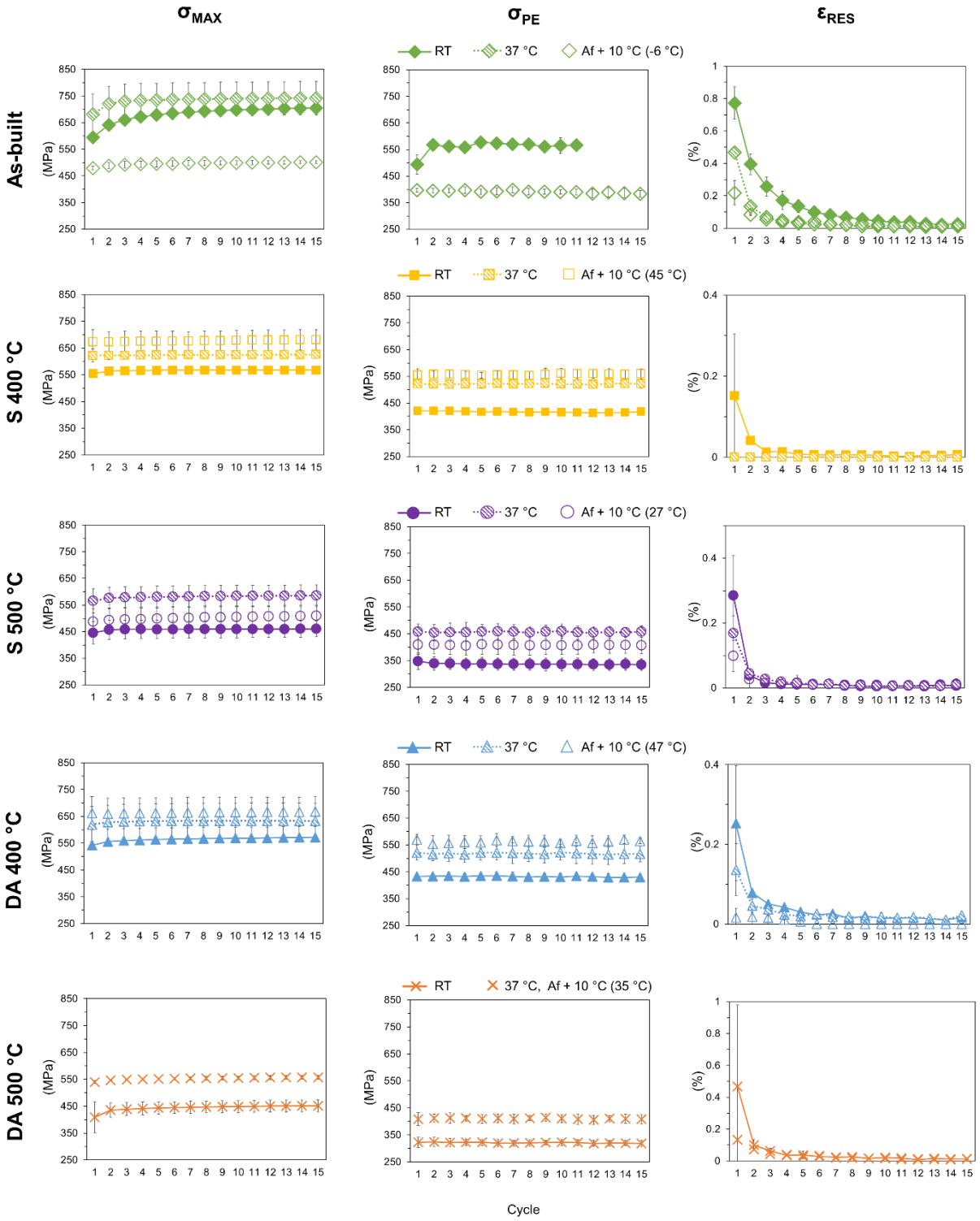

Fig. 3.17. σ_{MAX}, σ_{PE} and ε_{RES} variation with testing temperatures for each analyzed condition.

3.2.7 Construction of the temperature-stress diagrams

The elaboration of the σ_{PE} data obtained during cyclic compression tests at different temperatures together with the M_s temperature measured from the DSC analyses and the σ_{SLIP} obtained from compression test up to failure at RT and 150 °C allowed the construction of the experimental temperature-stress diagrams for each of the analyzed conditions, similarly to the one displayed in Fig. 2.21. Results are summarized in Fig. 3.18**,** where the superelastic (SE) window is highlighted in green, while the region corresponding to the shape memory effect (SME) in grey. It should be noted that the standard deviations are barely observable in the graphs due to the fact for that for σ_{PE} they range between 3 and 25 MPa, while for σ_{SLIP} between 50 and 62 MPa.

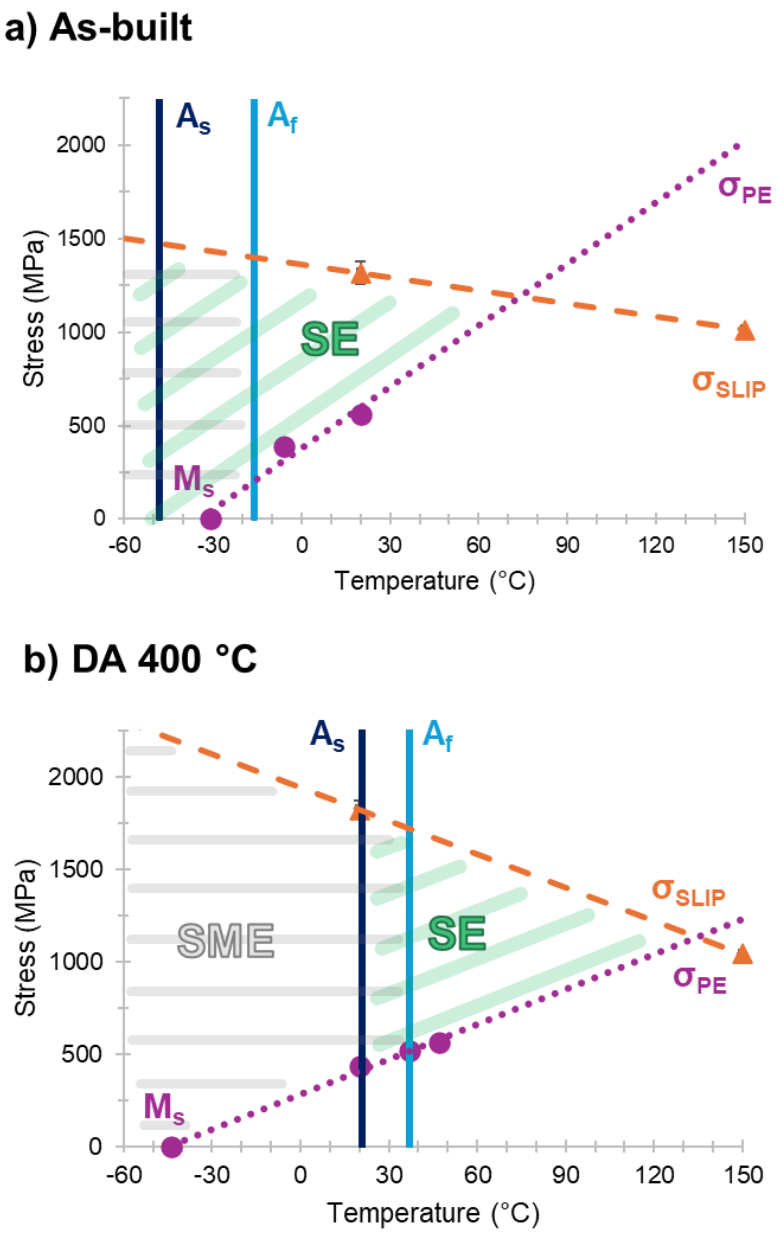

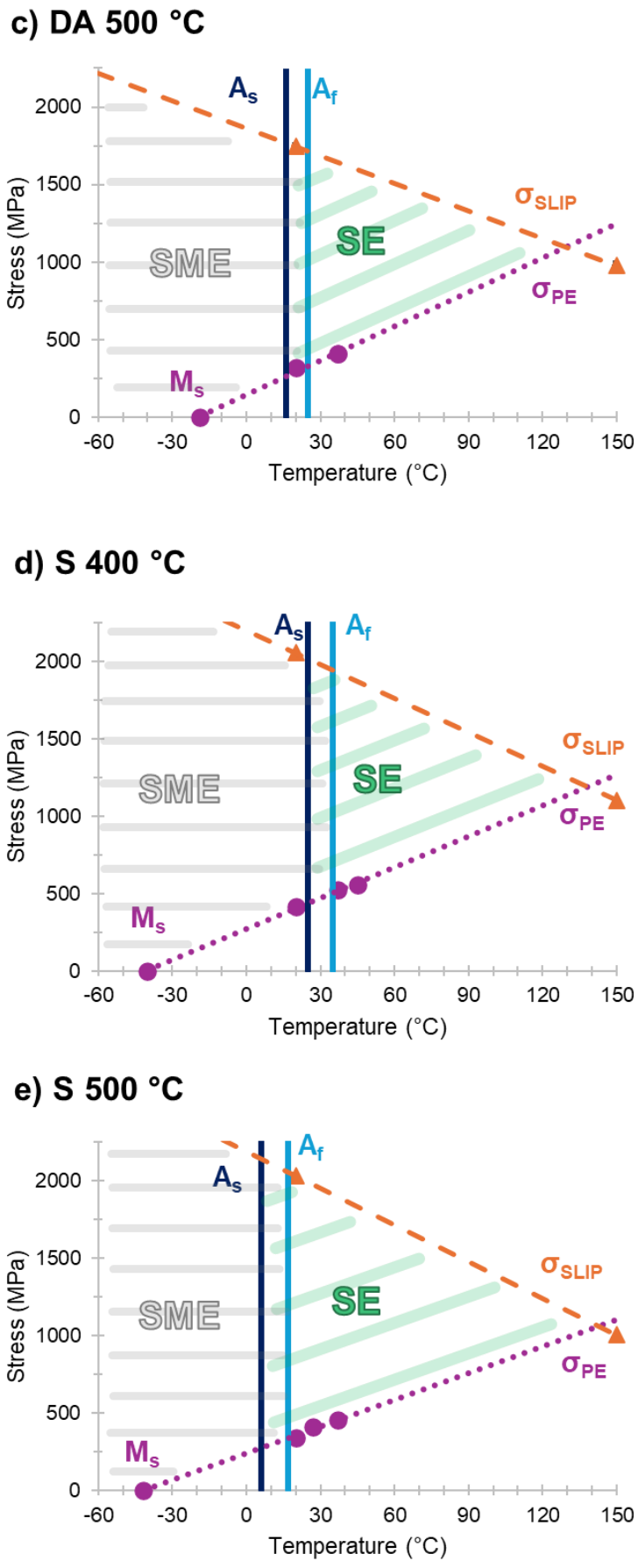

Fig. 3.18. Temperature-stress diagrams for each analyzed condition.

The diagrams allowed the determination of the effects of heat treatments, which can be summarized as follows:

- shifting the TTs to higher temperatures,
- increasing the critical stress for slip deformation (σ_{SLIP}),
- decreasing the critical stress to induce the martensitic transformation (σ_{PE}).

Therefore, the superelastic window expanded after all the heat treatments in the temperature range of interest for biomedical applications, thus contributing in significantly enhancing the superelastic behavior of the alloy.

Furthermore, by comparing the different conditions summarized in Fig. 3.18, it can be stated the direct aged samples produced the same overall behavior compared to the solution annealed and aged ones, making the solution step unnecessary for the purposes of the superelasticity obtainment. This, together with the negligible residual strain observed both at RT and 37 °C, proves the effectiveness of short-time direct aging heat treatments on the superelasticity of NiTi parts produced through L-PBF. To completely characterize the microstructural features responsible for the improvement of the superelastic response, TEM analysis was carried out on the direct aged alloys, as constituting the innovative conditions proposed in the present work.

3.2.8 Direct aging characterization

3.2.8.1 Precipitates analysis

Fig. 3.19 displays representative TEM micrographs showing B2 austenite and B19' martensite phases in the direct aged samples, that is DA 400 °C (Fig. 3.19a-b) and DA 500 °C (Fig. 3.19c-d). B2 austenite grained structure in both conditions is characterized by high density of tangled dislocations. In fact, Fig. 3.20 shows the typical dislocation morphology observed in the two direct aging conditions. DA 500 °C alloy tends to show a slightly higher tangled dislocation density compared to DA 400 °C. The austenite mean grain size is 1.2 μm and 0.9 μm after direct aging at 400 °C and after 500 °C, respectively (Fig. 3.19). B19' martensite is shown in Fig. 3.21 for both the direct aged samples. It was found that the volume fraction of B19' martensite in DA 400 °C sample was up to 50% more compared to the amount of it found in DA 500 °C. In addition, the R-phase was detected for each condition, and was observed at the B19' martensite lath edges, as reported in Fig. 3.21 and Fig. 3.22. A greater amount of R-phase was found in DA 500 °C specimen.

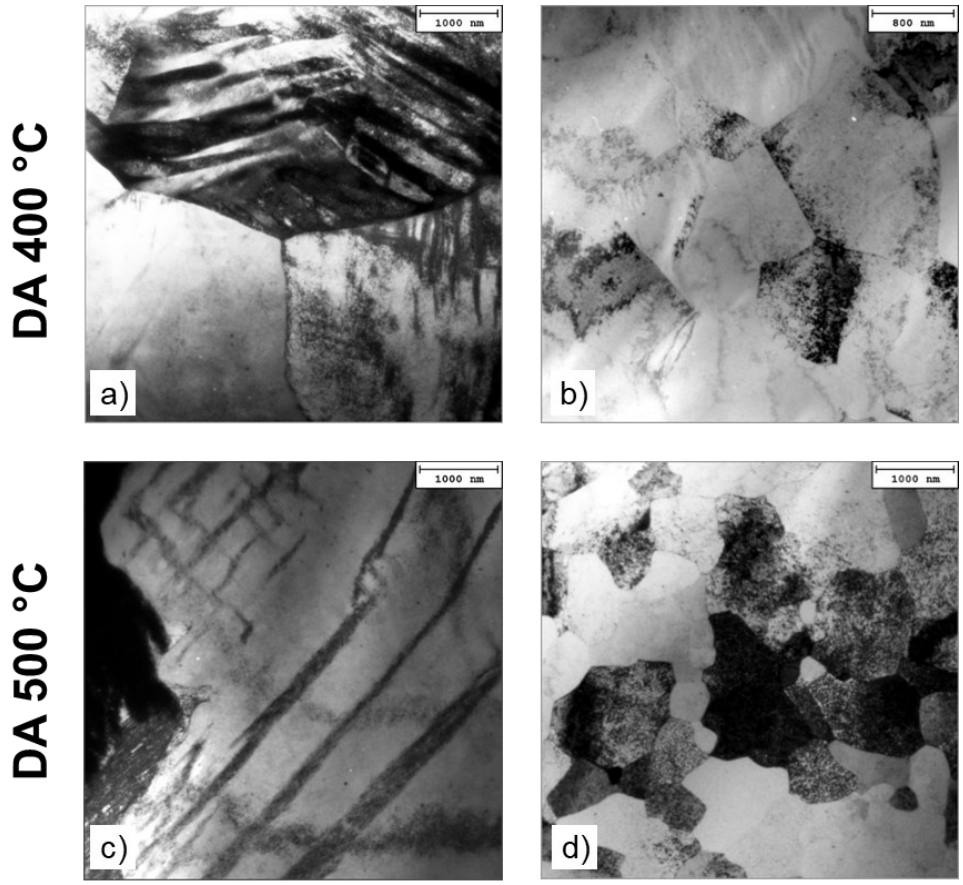

Fig. 3.19. Low magnification of: (a-b) DA 400 °C, (c-d) DA 500 °C.

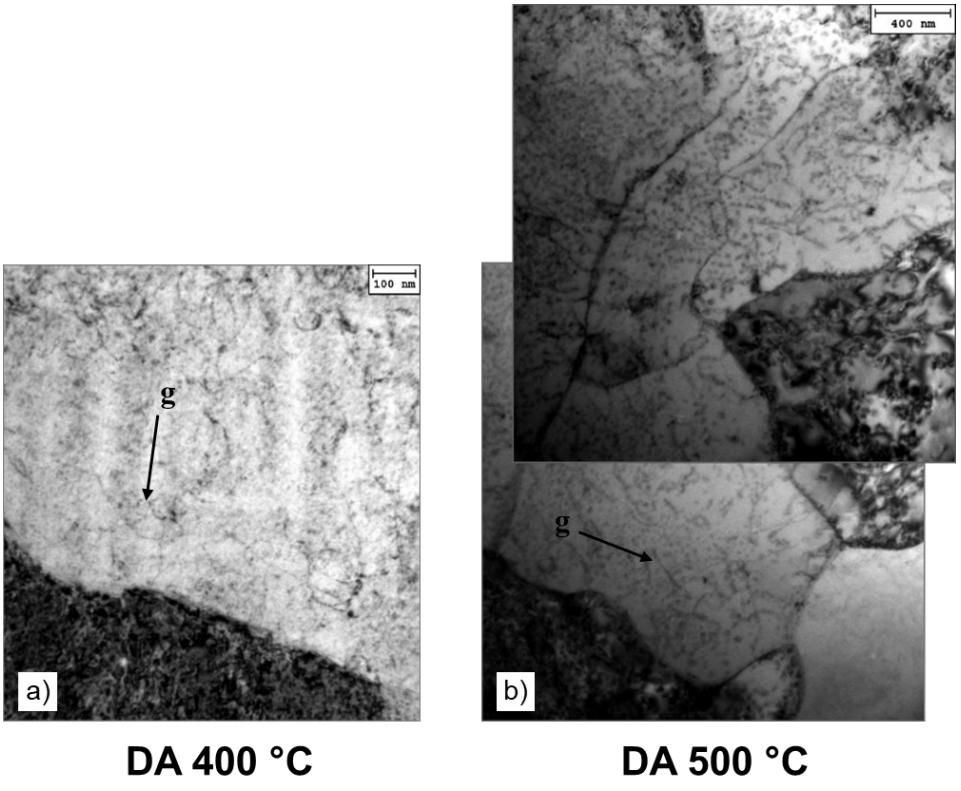

Fig. 3.20. TEM bright-field showing dislocation network obtained under $[110]_{B2}$ g-vector in (a) DA 400 °C sample, (b) DA 500 °C.

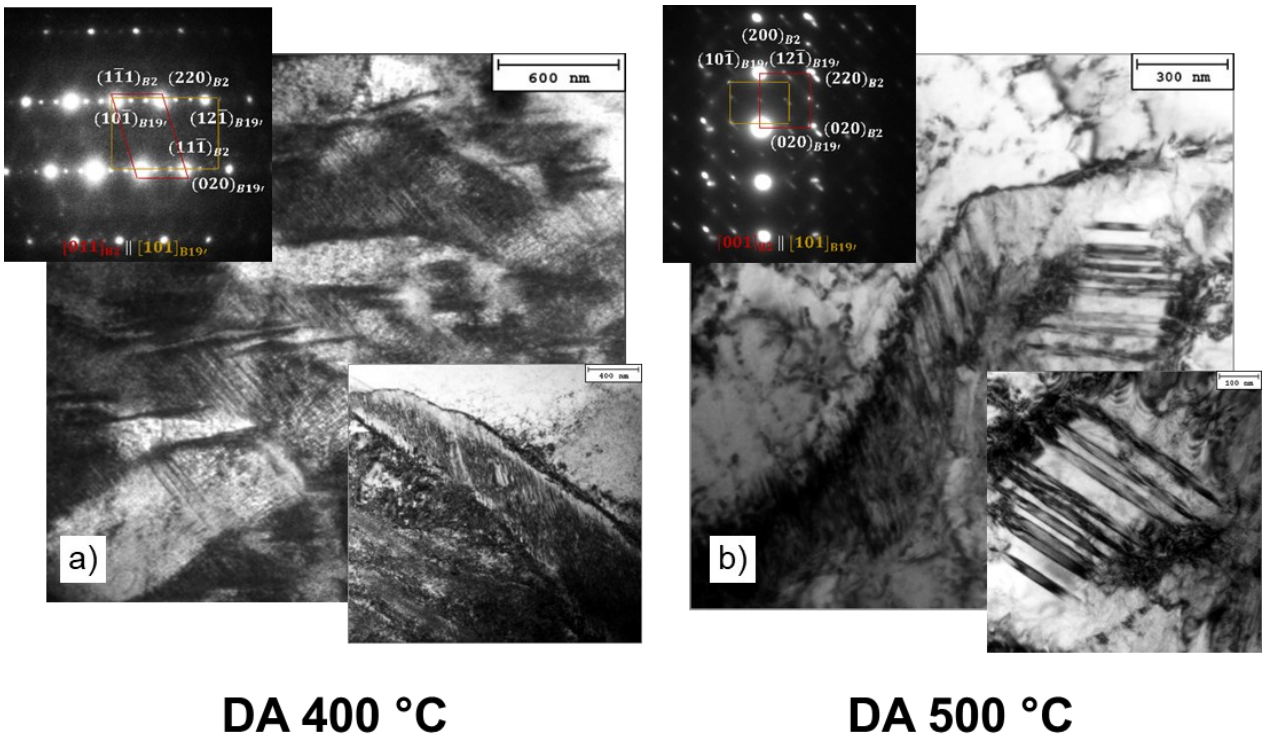

Fig. 3.21. B19' martensite phase in (a) DA 400 °C, (b) DA 500 °C.

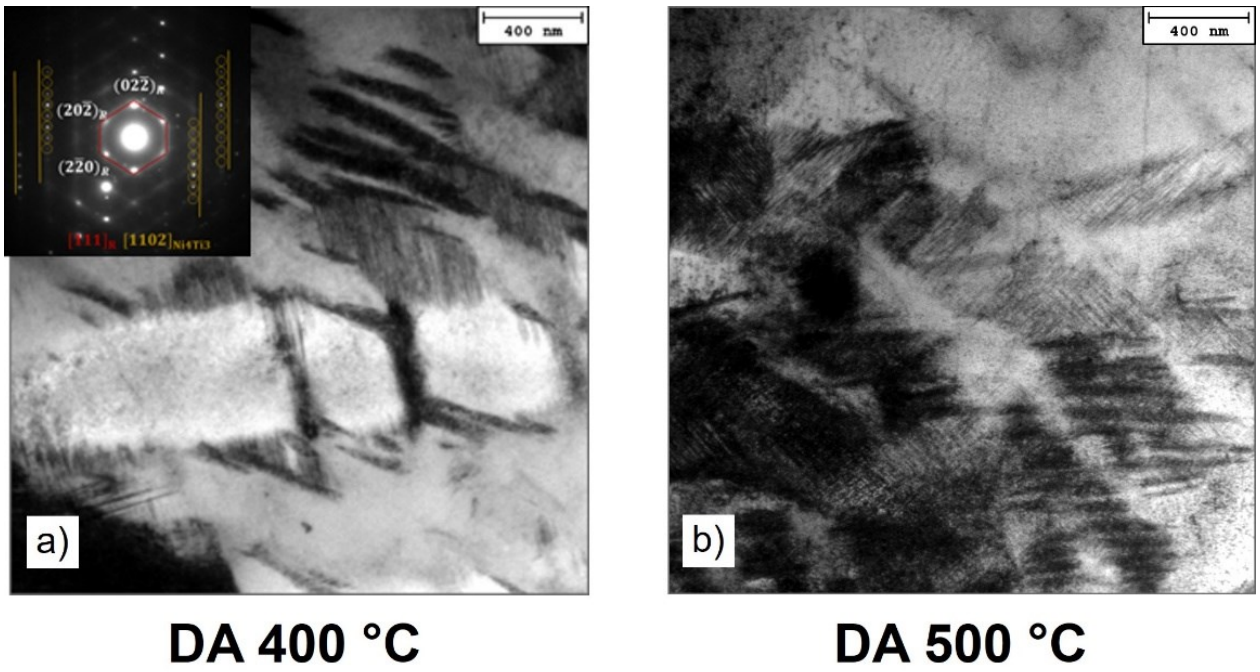

Fig. 3.22. Smooth constrained growth of R-phase induced by the presence of Ni_4Ti_3 precipitates. The micrographs document (a) the occurrence of early stages of R-phase formation in DA 400 °C sample, and (b) its evolution in DA 500 °C sample.

In the B2 austenite grains several nanometric spheroidal oxide particles were found in both the DA samples, these are identified as Ni_4Ti_3O oxides. Yet, their size and distribution did not appear to be affected by the aging temperature (Fig. 3.23).

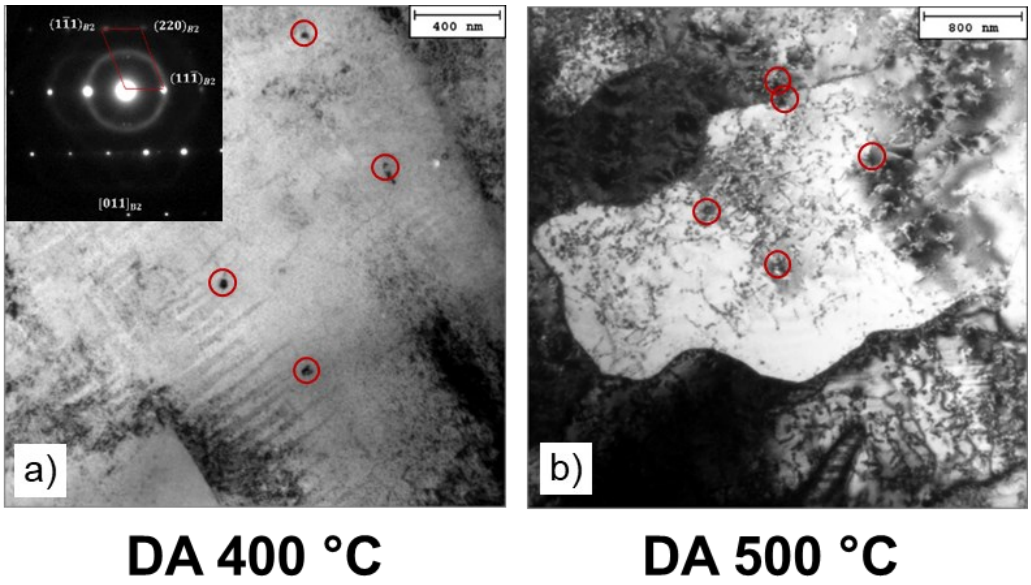

Fig. 3.23. Typical nanometer Ni_4Ti_3O oxide particles detected in (a) DA 400 °C, (b) DA 500 °C.

One of the marked microstructure aspects that differentiate the two direct aging conditions is the presence and distribution of nanometric Ni_4Ti_3 phase precipitates. Fig. 3.24 shows the typical distribution of these particles in the two direct aged alloys. It appears that the volume fraction and quantity of Ni_4Ti_3 particles were significantly higher after direct aging at 500 °C compared to the 400 °C condition. In the DA 400 °C sample, the size distribution of the Ni_4Ti_3 precipitates tends to be uniform, with minimum-to-maximum sizes of ~8-to-60 nm. On the other hand, in the DA 500 °C sample, the Ni_4Ti_3 precipitates appeared to be less homogeneous, with minimum-to-maximum sizes of ~5-to-80 nm.

Histogram and statistic data reported in Fig. 3.25 show that formation of Ni_4Ti_3 particles after direct aging at 500 °C is largely promoted accounting to 4-times higher volume fraction compared to the alloy direct aged at 400 °C for the same duration. At the same time particle spacing reduced to almost half from DA 500 °C with respect to DA 400 °C, being the mean size unaltered. TEM inspections showed that the higher presence of the Ni_4Ti_3 particles after direct aging at 500 °C is rather inhomogeneous throughout the material microstructure. In fact, these particles were found to preferentially precipitate within the B2 austenite grains and at their grain boundaries.

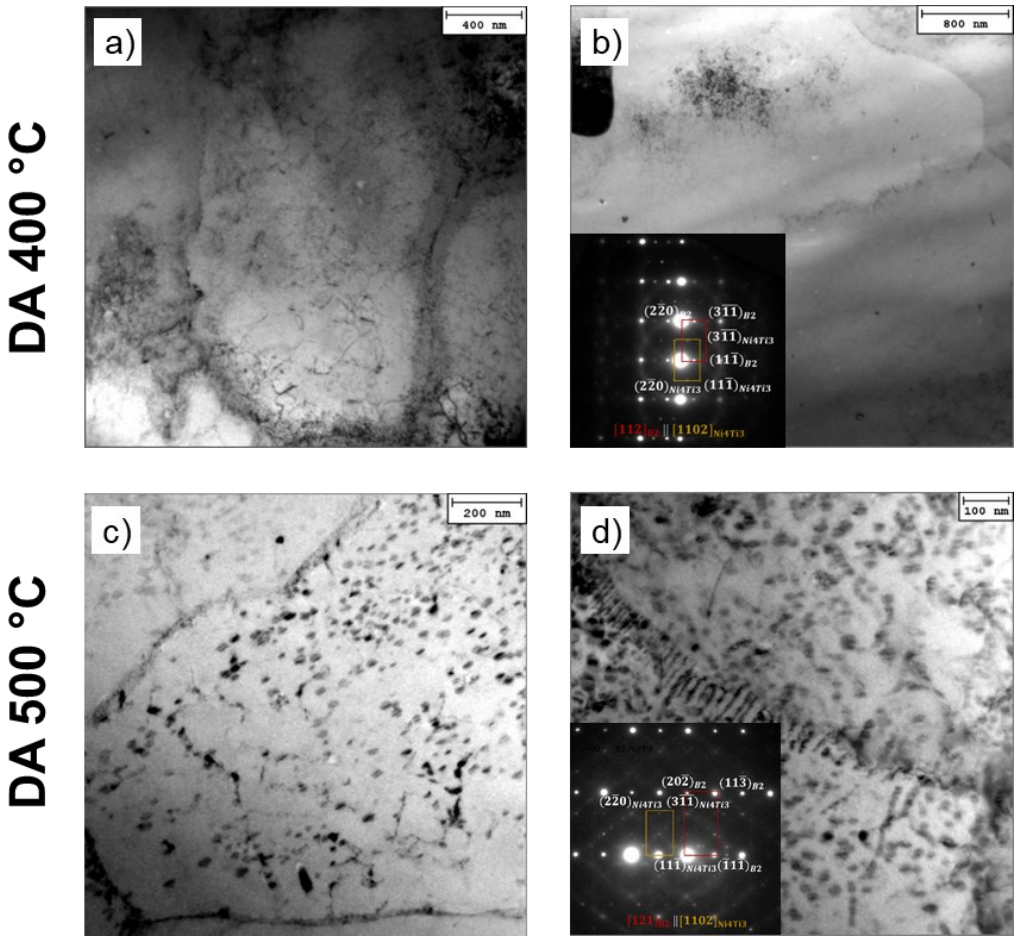

Fig. 3.24. Ni_4Ti_3 phase particles detected in: (a-b) DA 400 °C, (c-d) DA 500 °C.

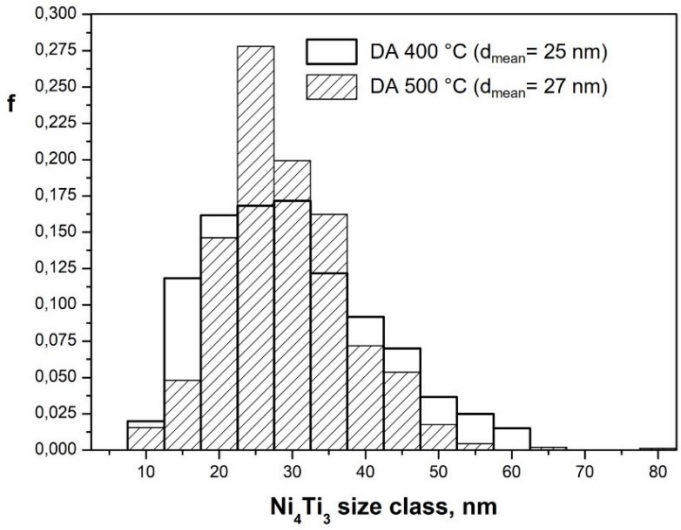

experimental condition	d_{av} (nm)	λ (nm)	f_V (%)
DA 400 °C	25 ± 3	134 ± 6	2.4 ± 0.8
DA 500 °C	27 ± 2	88 ± 6	12 ± 3

Fig. 3.25. Ni_4Ti_3 size distribution and statistic evaluation: mean size (d_{av}), mean edge-to-edge spacing (λ), volume fraction (f_V).

Ni_4Ti_3 is a metastable phase that is known to precipitate in NiTi shape memory alloy below 700 °C. Ni_4Ti_3 phase has a R3-space group with a rhombohedral unit cell structure (in which six Ti atoms alternate to eight Ni atoms [205, 206]). The Ni_4Ti_3 particles habit plane is along $[111]_{B2}$ austenite matrix, with a total of eight variants [205, 206].

Ni_4Ti_3 phase typically has an orientation relationship to B2 matrix as $[121]_{B2}$ || $[1102]_{Ni4Ti3}$ and $[112]_{B2}$ || $[1102]_{Ni4Ti3}$ [205]. Moreover, Ni_4Ti_3 phase and B2 austenite phase reflections overlap in the $[011]_{B2}$ and $[001]_{B2}$ orientations (see also [207]).

It was reported that Ni_4Ti_3 particles with size below ~100 nm generate coherency and semi-coherency with the B2 austenite matrix [58, 141, 208]. Ni_4Ti_3 precipitates have lenticular shape with lateral spacing increasing with ageing time [138].

On cooling from high temperatures, the B2 austenite phase can directly transform into the B19' martensite phase. On the other hand, the presence of Ni_4Ti_3 precipitates promotes the B2 to R-phase transformation [138], as also reported in Fig. 3.21. Thence, the presence of the Ni_4Ti_3 phase is likely to inhibit and eventually suppress the occurrence of martensitic transformation, thus promoting formation of R-phase. That is, the occurrence of two-stage phase transformation of B2-R-B19' is mainly driven by the formation of Ni_4Ti_3 phase. In general, the R-phase nucleates at the interface between Ni_4Ti_3 phase and B2 austenite matrix, as well as B19' martensite nucleates at the interface between Ni_4Ti_3 phase and R-phase [132, 142].

The intermediate R-phase has a trigonal crystal structure [132]. This phase can be recognized by SAEDP as superlattice reflections are located at 1/3 positions along $[110]_{B2}$ and $[111]_{B2}$ austenite matrix directions, in addition, $[111]_{B2}$ || $[111]_R$ variants can also be considered for the R-phase identification.

The existing supersaturation of Ni atoms within the B2 matrix promotes the homogeneous nucleation of the Ni_4Ti_3 precipitates, at first stages of aging, and the particle growth, at the second stage of aging. The supersaturation of Ni can be attributed to the extremely high cooling rates and thermal gradients experienced by the alloys after the L-PBF process [6], which made the solution annealing step unnecessary for Ni_4Ti_3 precipitation. The nucleation of Ni_4Ti_3 is likely to occur not only at the grain and subgrain boundaries but also at oxide interfaces, oxide particles being of Ni_4Ti_3O or Ti_4Ni_2O type (Fig. 3.23). Particle local inhomogeneities in terms of distribution and location sites strongly depend on the short aging times (15 min). This microstructure aspect was partially overcome

by increasing the aging temperature from 400 °C to 500 °C, as documented by the TEM inspections and, in particular, as reported in Fig. 3.24.

With the increase in aging time, or aging temperature, the Ni_4Ti_3 precipitates keep growing at grain and subgrain boundaries and in the grain interior. The particle coarsening typically progresses along the coherent B2 matrix interface. The Ni_4Ti_3 particle coarsening proceeds by absorbing Ni atoms from the B2 matrix around them. This explains the increasing of TTs temperature found for DA samples (see Fig. 3.5 and Table 3.3).

Fig. 3.24 shows heterogeneous nucleation of Ni_4Ti_3 phase precipitates as an important factor in the early stages of direct aging, especially in the higher temperature of 500 °C. It appears that precipitation of small lenticular Ni_4Ti_3 particles only occurs at and near grain and subgrain boundaries, as well as at oxide particle locations. Anyway, especially in the DA 400 °C alloy, vast portions of the grains appear free of precipitates. Only increasing the aging temperature to 500 °C, Ni_4Ti_3 precipitation become significant, and particles start coarsening even after the short aging time of 15 min. The higher volume fraction of Ni_4Ti_3 after direct aging at 500 °C promoted the greater formation of R-phase.

A further interesting aspect refers to the coherency/semi-coherency and non-coherency of the Ni_4Ti_3 phase to the B2 austenite matrix at the two aging temperatures. That is, in the DA 400 °C sample, Ni_4Ti_3 are mostly coherent and semi-coherent, with a low fraction of incoherent particles, while in DA 500 °C coherent, semi-coherent, and incoherent particles equally coexist.

The effects of these precipitates on the superelastic features of the samples are complex. Firstly, their presence in the heat-treated alloys was found to increase the TTs by reducing the Ni content of the matrix (see Fig. 3.5 and Table 3.3). This allowed the stress-induced martensitic transformation to happen for these samples both at RT and 37 °C at the reached stresses during tests. On the other hand, in fact, for the as-built alloy both RT and 37 °C are much higher than A_f (-16 °C), and the superelastic behavior is not appreciable. It is therefore reasonable to assume that the stress-induced martensite formation is impeded at these temperatures, which could be due to the fact that the stress required for its formation is higher than those reached during the compression tests, or to the exceeding of the martensite-destruct temperature (M_d) [38, 40, 47].

Another aspect to consider is that Ni_4Ti_3 precipitates act as nucleation sites for martensite as the load is applied, thus promoting the stress-induced martensitic

transformation [40, 57, 172]. In this regard, the higher volume fraction of precipitates found in the DA 500 °C sample explains the lower σ_{PE} recorded during compression tests respect to DA 400 °C (see Fig. 3.12b, Fig. 3.14b and Fig. 3.17). In fact, at the interface between coherent Ni_4Ti_3 particles and B2 matrix, a coherent stress field is generated, which makes the transformation happen near these regions to relax the coherent stresses [141].

Lastly, Ni_4Ti_3 precipitates are also known to increase the critical stress for the slip deformation mechanism (σ_{SLIP}) due to their precipitation hardening effect. In this way, since the chance of the occurring of plastic deformation is decreased, the stress-induced martensitic transformation necessary for SE is promoted [33, 56, 59].

The combination of these effects due to the presence of Ni_4Ti_3 precipitates contributed to significantly enlarging the SE window for direct aged samples compared to the as-built, as discussed above (Fig. 3.17).

3.2.8.2 Microhardness and compression up to failure

Vickers microhardness results of the direct aged samples compared to the as-built are reported in Fig. 3.26. It should be mentioned that the hardness of NiTi is complex and strongly dependent on the testing temperature and the exhibited phases. Moreover, during hardness test, stress-induced transformations or variant reorientation can happen, as well as the formation of dislocations [199].

Both the performed direct aging treatments increase the microhardness compared to the as-built sample, with a slightly decreasing trend with aging temperature, which is also in agreement with the literature [169, 209]. In detail, hardness increases from 344 ± 23 HV to 437 ± 27 HV by direct aging at 400 °C and then decreases to 410 ± 16 HV by direct aging at 500 °C. The austenitic phase in NiTi has higher hardness than martensite [196, 199, 210]. Therefore, the higher hardness measured for direct aged alloys compared to the as-built is imputable to the presence of Ni_4Ti_3 precipitates and their precipitation hardening effect. It is in fact commonly known that hardness is strongly affected by the presence of precipitates, with a complex dependence on their size and distance.

Several reasons could explain the slightly lower hardness found after direct aging at 500 °C. Firstly, it may be ascribed to the precipitates dimension which was found to grow and consequently some become incoherent (Fig. 3.25), which may have contributed to slightly decrease hardness [209, 211]. Another explanation can be found by referring to the σ_{PE} parameter. In fact, for superelastic materials, a higher σ_{PE} corresponds to a higher force that

can be recovered without causing a permanent deformation. Therefore, since DA 400 °C exhibits the greatest σ_{PE} (Fig. 3.12b and Fig. 3.14b), it will result in a lower permanent deformation and thus in a smaller indentation and higher Vickers hardness [212]. This only applies to material exhibiting superelastic responses, such as the direct aged samples, while it is not valid for the as-built condition.

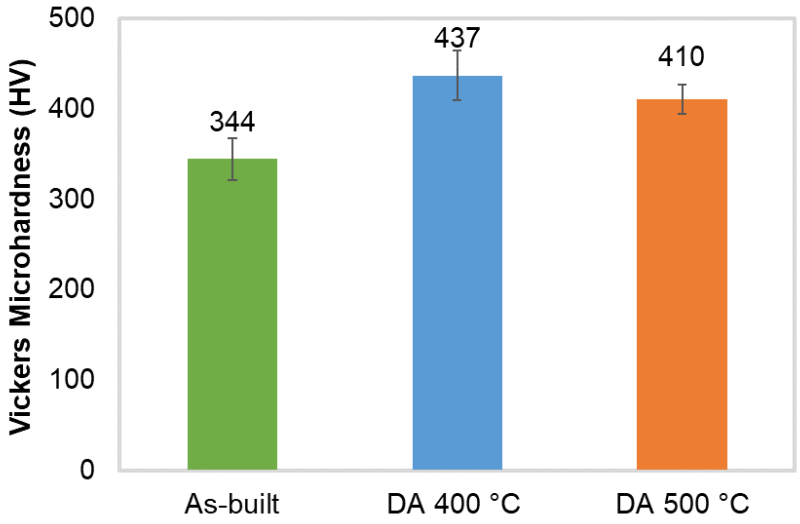

Fig. 3.26. Vickers microhardness of as-built, DA 400 °C and DA 500 °C samples.

Since hardness is commonly recognized as an indication of the strength and is mainly concerned to the plastic behavior of the material, compression tests until failure at RT were performed to deeply understand the mechanical behavior of direct aged alloys. Fig. 3.27 reports the results of the complete compression tests. The details for the determination of σ_{PE} and σ_{SLIP} from this type of curve are shown in Fig. 3.4a.

The first region of the curves is related to the elastic deformation of the initial structure, i.e. austenite for the as-built sample and austenite and martensite for the direct aged samples. By loading up to the first inflection point of each curve, which corresponds to σ_{PE}, stress-induced martensite forms from austenite. Then, a decrease in slope occurs between 5% and 10% of strain. Up to this point, the behavior of samples reflects what previously found during cyclic and incremental compressive tests (Fig. 3.11 and Fig. 3.13): the as-built sample shows higher σ_{PE}, as well as higher stress at the same strain value, followed by DA 400 °C and DA 500 °C. After, the formed martensite is firstly elastically and then plastically deformed up to failure. The plastic deformation by dislocation slip takes place as the stress reaches σ_{SLIP}, that is the critical stress for the slip deformation mechanism and corresponds to the second inflection point of the curve [42]. Beyond this point, at the same strain value, both the direct aged alloys reach higher stresses compared to the as-built condition. This is consistent with

the hardness results reported in Fig. 3.26. It should be noted that in this region all the samples present the same phase (i.e. martensite), and therefore the hardening effect of direct-aged alloys with respect to the as-built can be attributed to the presence of Ni_4Ti_3 precipitates and to their precipitation hardening effect. It is therefore evident that Ni_4Ti_3 phase increased σ_{SLIP} in the direct aged samples. Lastly, the Ni_4Ti_3 precipitates present in the DA samples lead to a slight reduction of both stress and strain at failure compared to the as-built alloy. This is due to the precipitation hardening effect of Ni-rich phases and to their brittle nature [40, 213].

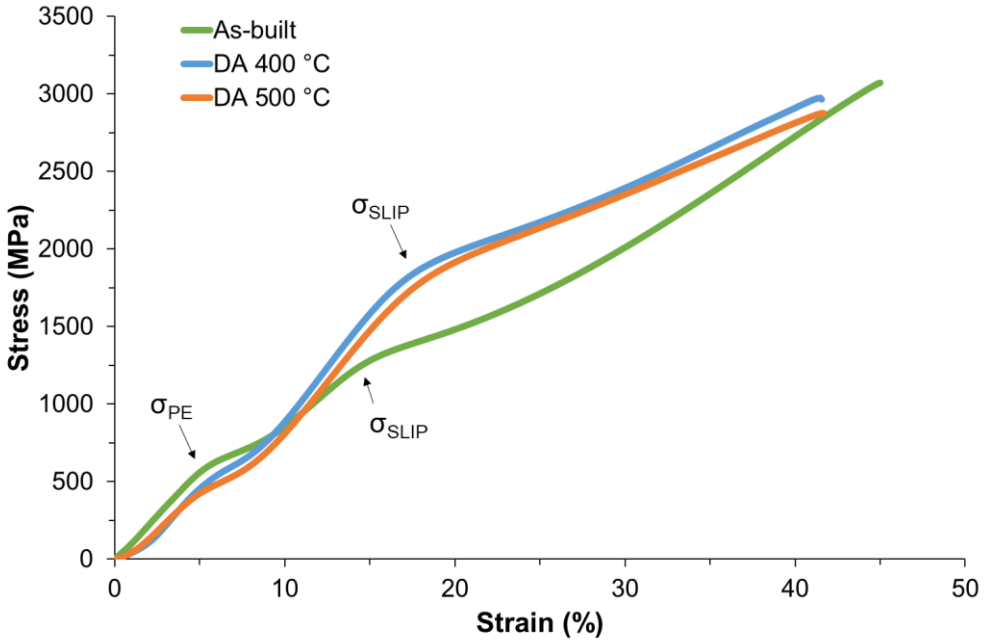

Fig. 3.27. Stress-strain plots for as-built and direct aged samples loaded until failure at RT.

3.3 CONCLUSIONS

Direct aging heat treatments were performed at 400 °C and 500 °C for a short exposure time of 15 min on NiTi cylinders (52.39Ni-47.61Ti at%) produced by laser powder bed fusion. Their properties were compared to those of samples that underwent the traditional treatment involving solution annealing and aging.

Cyclic compression tests were carried out to characterize the superelastic behavior at different testing temperatures. At room temperature, all the heat-treated samples showed negligible residual strain values after 15 cycles up to 6% of deformation. Furthermore, after 10 cycles of incremental deformation from 1% to 10% at room temperature, the total cumulative strain was found to be lower than 2%. This, together with the high stability

exhibited during compression cycles, proves the obtainment of the superelastic effect at room temperature up to 10% of strain for all the heat-treated alloys. The superelastic features achieved after the performed heat treatments were found to be preserved at 37 °C. Cyclic compression tests were also carried out on each sample at its A_f + 10 °C temperature, while compression tests up to failure were executed both at room temperature and at 150 °C. The elaboration of data obtained from all tests allowed the determination of the experimental temperature-stress diagram, representative of the behavior of the material in the different analyzed conditions. Heat treatments were found to significantly enlarge the superelastic window in the temperature range of interest compared to the as-built alloy. Furthermore, the solution treatment was found to be not required to reach superelasticity after laser powder bed fusion, due to the comparable results obtained with and without this step.

Due to the promising results obtained at 37 °C, short-time direct aging heat treatments at 400 °C and 500 °C can be exploited to enhance properties of NiTi components intended for biomedical applications.

The reason of the improved superelastic behavior after heat treatments was attributed to the formation of Ni_4Ti_3 phase. Transmission electron microscopy analyses showed that the alloy direct aged at 500 °C exhibited a significantly higher precipitation of Ni_4Ti_3 nano-precipitates compared to the one direct aged at 400 °C. Moreover, the large presence of this phase after direct aging at 500 °C promoted the greater formation of R-phase at the B19' martensite lath boundaries. On the other hand, martensite volume fraction was higher in the alloy direct aged at 400 °C compared to samples treated at 500 °C. Lastly, direct aged alloys resulted in higher microhardness compared to the as-built, due to the presence of Ni_4Ti_3 phase and the resulting precipitation hardening effect. Ni_4Ti_3 precipitates were also found to enhance the critical stress at which the slip plastic deformation occurs, as well as the resistance during plastic deformation for both the direct aged alloys.

3.4 APPENDIX

In this Chapter, the preliminary characterization on the cylindrical specimens after manufacturing (i.e. "as-built samples") is reported.

3.4.1 Materials and methods

Samples named A, B and C were produced through L-PBF with the sets of process parameters listed in Table 3.7 starting from powder 52.39Ni-47.61Ti nominal chemical composition (at%). Specifics on the production phase can be found in Paragraph 3.1.1.

Table 3.7. Process parameters used for cylindrical samples production via L-PBF.

Sample	Laser Power (W)	Scan Speed (mm/s)	Hatch Spacing (µm)	Spot size (µm)	Layer thickness (µm)
A	150	500	80	60	60
B	180	1000	80	60	60
C	180	500	80	60	60

The preliminary characterization was conducted by examining the transformation temperatures (TTs) through DSC analyses, the microstructure by means of optical microscopy and the phases through XRD. The details on the related characterization procedure can be find in Paragraph 3.1.2.

3.4.2 Results and discussion

Almost superimposable values of TTs were detected for the as-built samples, as reported in Table 3.8. Despite the slight differences observed for A_f temperatures, which is the temperature of interest for superelasticity, these are all very below both room temperature and 37 °C, pointing out that samples are situated in the same thermodynamic condition in the temperatures of interest of the work. For the purpose of the study, the three conditions of as-built samples were thus considered equal one to each other.

Table 3.8. Transformation temperatures of samples A, B, and C.

Sample	Temperature (°C)					
	M_f	M_p	M_s	A_s	A_p	A_f
A	<-70	-60	-31	-43	-27	-16
B	<-70	-63	-31	-43	-29	-20
C	<-70	-57	-23	-41	-21	-9

Micrographs of samples A, B and C are displayed in Fig. 3.28. The chessboard structure is found on the xy plane, while melt pools appear along the building (z) direction for all the specimens. The width of the islands constituting the structure is 70 ± 4 μm, 71 ± 6 μm, and 69 ± 8 μm for sample A, B and C respectively, pointing out no significant microstructural differences for the as-built specimens.

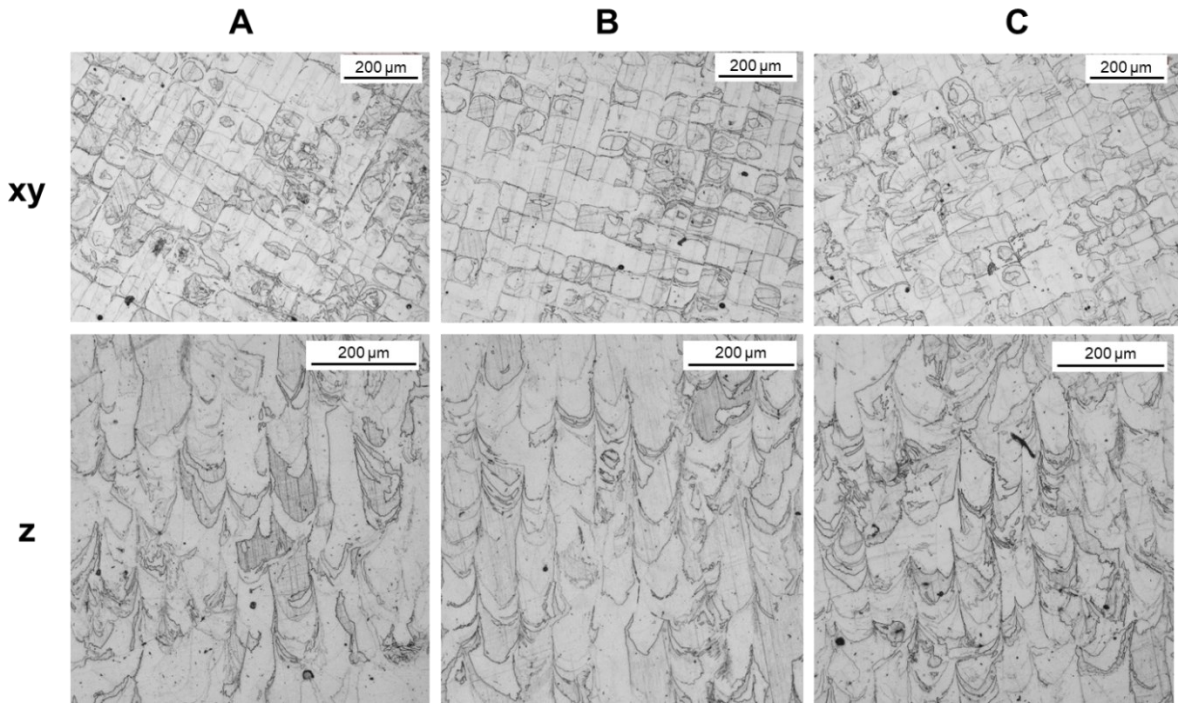

Fig. 3.28. Optical micrographs of as-built samples on the xy plane and along z (building) direction.

The XRD spectra of samples A and C are reported in Fig. 3.29. Specimens show superimposable spectra with austenite and either no martensite or presence of precipitation phases, confirming what previously observed from DSC analyses.

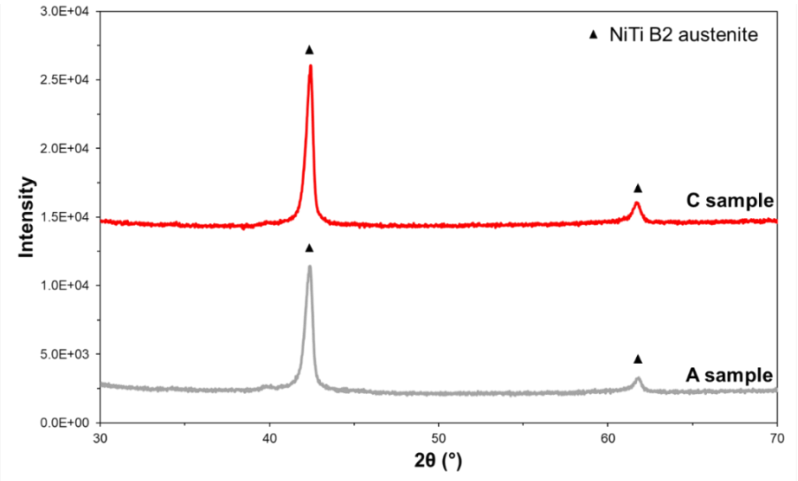

Fig. 3.29. XRD spectra for A and C as-built samples.

SECTION 4.

EFFECTS OF HEAT TREATMENTS ON THE ADJUSTMENT OF TRANSFORMATION TEMPERATURES

In this Section, the experimental activities were carried out on samples manufactured with 50.54Ni-49.46Ti (at%) powders, with the aim of investigating the effects of heat treatments on the modification of TTs after Ni evaporation during production of components with stent geometry. The loss of Ni content during L-PBF is a critical issue, which in the literature is mainly addressed through the tuning of process parameters, as reviewed in Paragraph 2.7.7.1. However, since some unwanted Ni evaporation can occur despite the preventive arrangements, it is worth considering the possibility of modifying A_f temperature through heat treatments, with the aim of restoring a microstructure suitable for the obtainment of superelasticity.

Most of the content illustrated in this Section are part of a scientific paper titled "Effect of Heat Treatments on Microstructure and Mechanical Properties of Nitinol Prototype Stents Produced by Laser Powder Bed Fusion" published on *Key Engineering Materials* journal [214].

The experimental procedure is firstly described, followed by the discussion of results.

4.1 MATERIALS AND METHODS

4.1.1 Samples production and heat treatments

NiTi gas-atomized powder with nominal composition of 50.54Ni-49.46Ti (at%) was used to produce protype stents via L-PBF. Particle size distribution (PSD) was measured using Malvern Mastersizer 3000 laser diffraction particle size analyzer, while morphology was analyzed with scanning electron microscope (SEM) Leo Evo 40XVP.

The PSD of powder ranges from 10 to 70 µm (Fig. 4.1), with $D_{10} = 18.5$ µm; $D_{50} = 32.5$ µm and $D_{90} = 51.3$ µm, where D_x represents the diameter of particle size for "x" percentage. The reflective and particle absorption index were 2 and 3.5 respectively. The powder was analyzed under 1 bar pressure to avoid particles agglomeration.

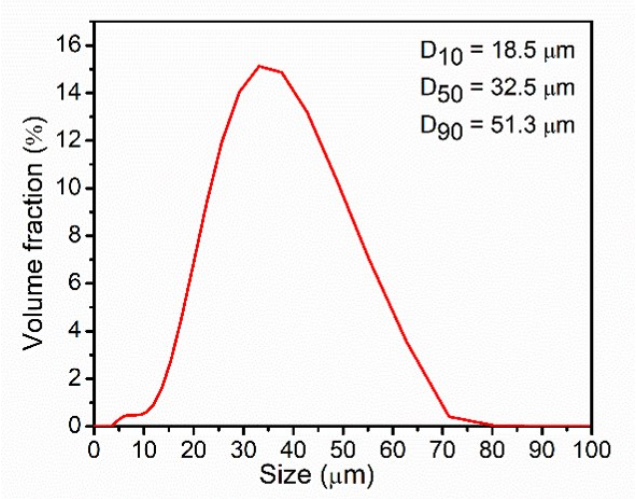

Fig. 4.1. Particle size distribution of the powder used.

NiTi prototype stents were produced using Aconity MINI (Aconity 3D GmbH), a powder bed fusion system equipped with a 200 W fiber laser of 1068 nm wavelength. The building chamber was filled with argon gas with 99.999% purity and the system was operated at < 20 ppm of oxygen level. Stents were produced along the vertical direction with length of 40 mm, nominal internal diameter of 7 mm, thickness of 0.4 mm and a Tigris stent mesh type. A schematization of the orientation of L-PBF stents respect to the building platform is reported in Fig. 4.2.

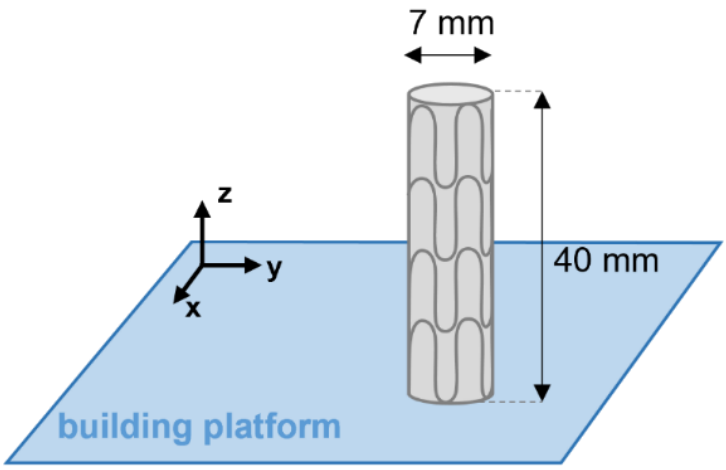

Fig. 4.2. Schematization of the prototype stent samples.

Prototype stents were manufactured using three different combinations of process parameters to identify their effect on samples qualities. Table 4.1 shows the three sets of process parameters used, indicated as A, B, and C.

Table 4.1. Process parameters used for prototype stents production via L-PBF.

Sample	Laser Power (W)	Scan Speed (mm/s)	Hatch Spacing (µm)	Spot size (µm)	Layer thickness (µm)
A	150	900	55	40	40
B	180	1200	70	40	40
C	180	900	70	40	40

A preliminary characterization aimed at identifying the effects of the process parameters was conducted by evaluating TTs, microstructure and compression behavior. The results regarding the results of the as-built condition are reported in Paragraph 4.2.2.

After production, each stent was cut into 4 parts to obtain 12 samples to achieve statistically reliable results. Fig. 4.3a displays the geometry of a L-PBF sample obtained after stent cutting. A commercially available NiTi self-expanding stent (Fig. 4.3b) manufactured with conventional technique was tested to compare its properties to those of stents manufactured via L-PBF. The conventional stent was supplied by Medtronic (Italy) and is characterized by 7 mm of diameter, 20 mm of length and a diamond design. The commercial name of this stent is Complete SE SFA Stent©, abbreviated as SFA stent in the present study. Its aim is to improve luminal diameter of the superficial femoral artery (SFA) and/or proximal popliteal artery (PPA) in symptomatic patients. This sample also includes eight tantalum radiopaque markers, fours on each end, for correct anatomical placement during the delivery phase.

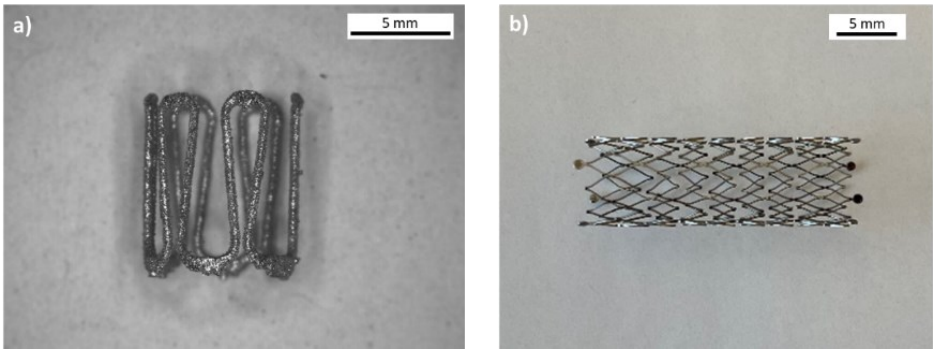

Fig. 4.3. The two stent samples used in the present study: a) sample sectioned from the L-PBF prototype stent, b) commercial stent (SFA Stent).

Heat treatments were performed on the L-PBF samples under high vacuum and with argon partial pressure of 1 mbar. Two different heat treatments named T1 and T2 were performed, whose details are reported in Table 4.2. 600 °C was chosen for T1 temperature since it was previously reported to decrease the transformation temperatures, and the duration of 1.5 h allowed the achievement of the best superelastic effect [169]. The reduction of the transformation temperatures was also found after heat treatments at 1100 °C, which was therefore chosen for T2 [171].

Table 4.2. Details of the performed heat treatments on the L-PBF prototype stents.

	Temperature	**Time**	**Cooling**
T1	600 °C	1.5 h	Furnace cooling
T2	1100 °C	1.5 h	Furnace cooling

4.1.2 Characterization procedure

Differential scanning calorimetry (DSC – TA Instruments) analyses were performed to evaluate the TTs of virgin powder, SFA stent, as-built and heat-treated samples. For each condition, the martensite and austenite start (M_s, A_s), finish (M_f, A_f) and peak (M_{Peak}, A_{Peak}) temperatures were identified, as well as temperatures concerning the R-phase (R_s, R_p, R_f), where present. Tests involved subsequent thermal cycles consisting in heating and cooling between -90 °C and 180 °C, with a heating/cooling rate of 10 °C/min. Specimens with mass between 5 and 10 mg were used. As a preliminary analysis aimed at verifying thermal stability of samples, two subsequent DSC runs (named 1st and 2nd experiment) were performed on selected samples. Each of these consists of three successive scans (heating, cooling and heating). The resulting TTs and their variation were monitored to assess the thermal stability of samples after L-PBF.

To investigate the microstructure of L-PBF prototype stents, some sample rods were cut and cold mounted to allow the subsequent metallographic preparation. Specimens were polished with silicon carbide abrasive papers and then fine polished with 3 μm and 1 μm diamond suspension. Subsequently, samples were chemically etched for a variable time between 30 and 120 s with 5 ml of HF, 20 ml HNO_3, 25 ml of H_2O, i.e. a diluted solution as suggested by Undisz et al. [177] to inhibit the formation of artefacts deriving from the hydrofluoric acid. Following this, microstructural analyses were performed using both LEICA DMI 5000M optical microscope and scanning electron microscope (SEM) Leo Evo 40XVP.

Compression tests with parallel flat plates (or crush tests) were performed using a Searle Physica MCR501 Anton Paar rheometer, set in a plate-to-plate configuration as shown in Fig. 4.4. Tests were performed according to the ISO 25539-2:2020 [215], at 37 ± 2 °C under a cross head speed of 1 mm/min (strain rate of 2.35×10^{-3}) for a minimum of two repetitions. Samples were compressed from the expanded state up to 20% of the nominal diameter. The choice of the instrument was based on its high precision, which allowed the continuous measurement of normal force with a resolution of 0.002 N and an accuracy of 2.5% of measured value, ±0.03 N, and displacement with a resolution of 0.01 mm. No rotation but only vertical movement of the shaft was set to compress the stent, measuring meanwhile both the position of the head and the normal force. This experiment set up allowed performing tests which otherwise would not have been carried out with the same accuracy, due to the extremely low involved forces. To monitor the temperature, the support plate was holed to insert a thermocouple, whose position is shown in Fig. 4.4. During the test, the furnace is closed to maintain the proper temperature, which is monitored during the test by the thermocouple placed close to the sample. Performing this test is appropriate for self-expanding stents, in particular for venous, non-aortic, non-coronary and non-renal arterial located, because they are more exposed thus they might be subjected to compressing forces that can affect patency [215]. The experiment allows the determination of the force per unit axial length related to the pre-specified displacement and helps to establish whether the stent recovers its original geometry once the load is removed. Compression resistance (CR) was determined as the force per unit axial length and plotted as a function of the normalized diameter (D/D_0).

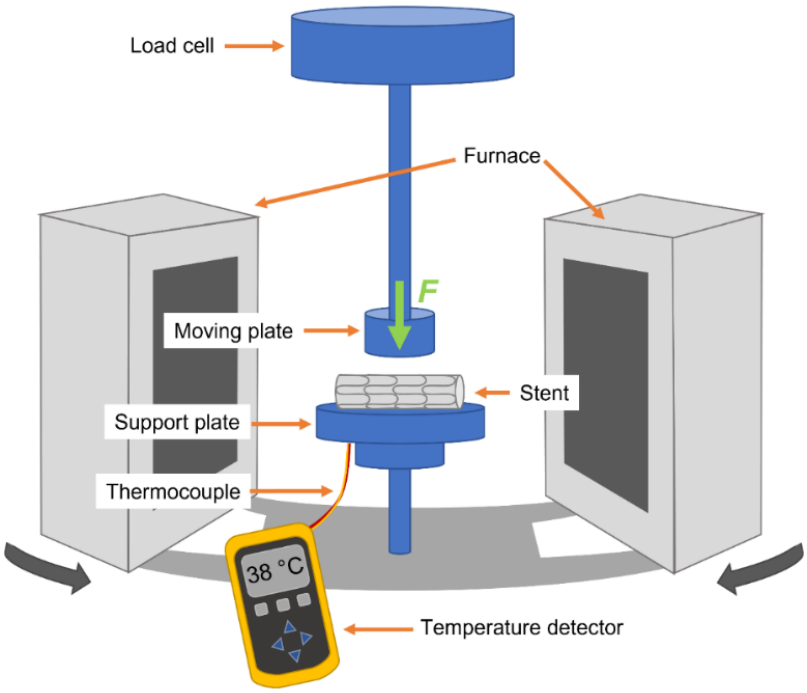

Fig. 4.4. Configuration of compression test with parallel plates.

4.2 RESULTS AND DISCUSSION

4.2.1 Powder

SEM images showing the morphology of the gas-atomized powder used are reported in Fig. 4.5. Powder is characterized by good overall sphericity. However, some defects such as irregularly shaped particles can be also detected, as well as satellite and agglomeration of powder.

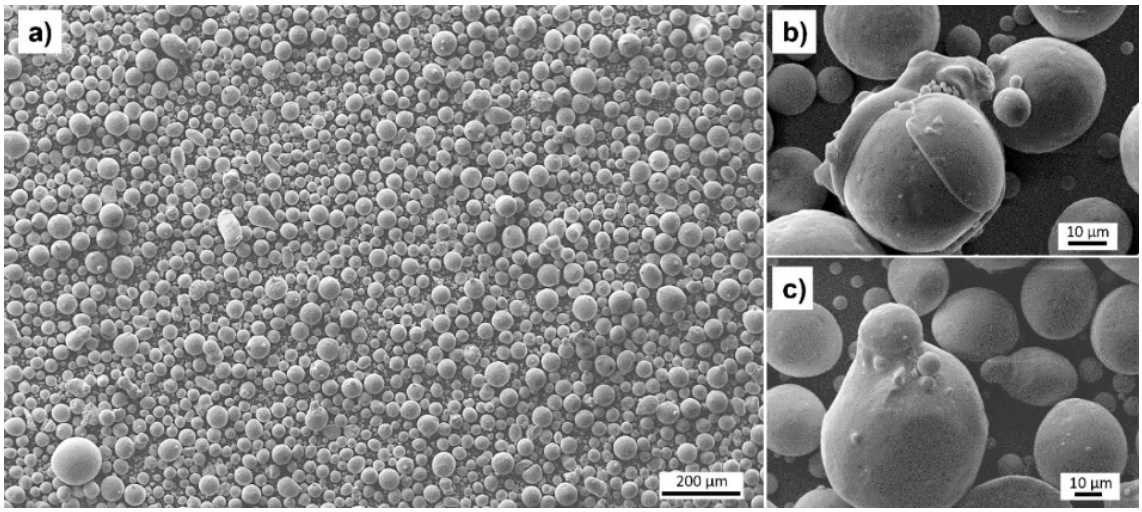

Fig. 4.5. SEM micrographs of NiTi gas atomized powder.

4.2.2 As-built samples

4.2.2.1 Phase transformation

The evolution of the DSC thermogram with subsequent cycles of heating and cooling can be observed in Fig. 4.6 for sample A, as representative of the behavior of all the samples. It is evident that the first heating scan (Scan 1) is characterized by a less regular and clean curve in shape as compared to the other ones. The following heating scans (Scan 3, 4 and 6) appear regular and basically overlapping, denoting the thermal stability of the alloy after the first heating run.

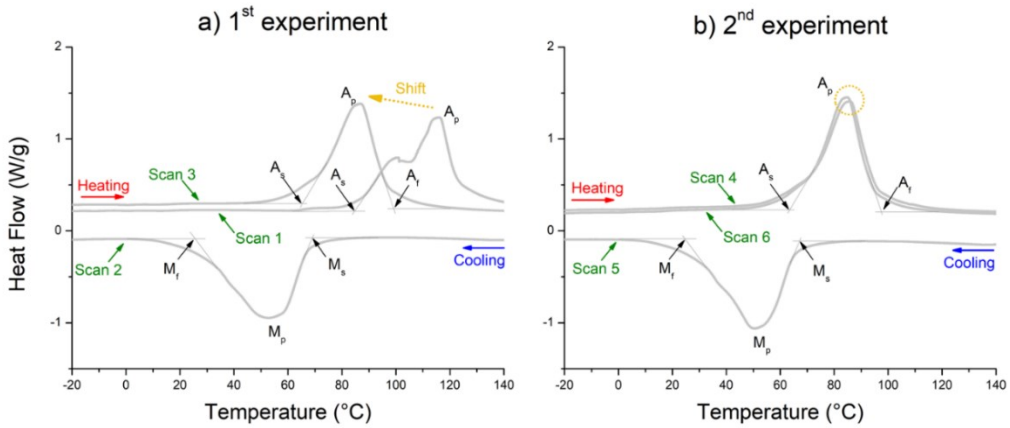

Fig. 4.6. DSC curves of Sample A in as-built conditions: a) first experiment, b) second experiment.

This fact is also highlighted in Fig. 4.7, which displays the austenite TTs values for each heating scan of Sample A. The austenite TTs decreased by 25 °C on average during the second heating run. Conversely, on subsequent heating, no significant changes can be detected, pointing out the achievement of stability.

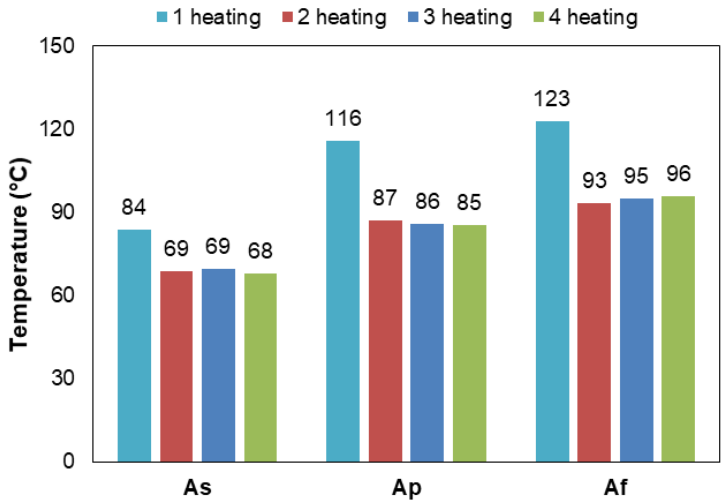

Fig. 4.7. Comparison of the austenite TTs for sample A after subsequent heating scans.

The TTs decrease is commonly associated to a change in the chemical composition, which, however, must be excluded at these low temperatures. Therefore, the most likely hypothesis is that during the first heating run, the as-built samples underwent a relief of the residual stresses, which were present due to the nature of the process. It is in fact well established that L-PBF process involves extremely high cooling rates and thermal gradients, which generate residual stresses that can result in crack formation [6, 163]. This phenomenon in NiTi as-built samples can shift the TTs to higher temperatures [216]. After the first heating scan, these residual stresses relax and thus the structure is more stable, with no longer variable TTs.

Regarding martensite TTs, no changes were noticed between the different cooling scans (Scan 2 and 5), as the scattering between values ranged from 2 to 4 °C. This is attributed to the fact that the stress-relief condition is achieved right after the first heating scan, and the martensite TTs are determined during the subsequent cooling scans.

Table 4.3 lists the TTs of the as-built samples, along with those of the powder and SFA stent for comparison. Based on the previous findings, the austenite TTs values emerging from the second heating and the martensite TTs values emerging from the first cooling are reported, as found to be representative of L-PBF samples in the as-built condition.

Table 4.3. Transformation temperatures of powder, as-built alloys and the commercial SFA stent.

Material	**Temperature (°C)**								
	M_f	**M_p**	**M_s**	**R_f**	**R_p**	**R_s**	**A_s**	**A_p**	**A_f**
Powder	31	37	49	-	-	-	58	66	77
Sample A	28	53	68	-	-	-	69	87	93
Sample B	35	57	86	-	-	-	71	88	98
Sample C	28	47	68	-	-	-	65	84	97
SFA stent	<-70	-60	-40	10	18	27	19	23	31

By observing the TTs of A, B and C samples, it appears that those of the austenite are quite constant, while a larger scattering can be detected for M_s in Sample B. However, it must be noted that all the L-PBF stents present the same microstructure at the temperature of interest, i.e. martensite and austenite at 37 °C. Therefore, for the purpose of the work, the L-PBF samples can be considered overall superimposable one to the other.

Shape memory features rather than superelasticity are expected to emerge at 37 °C for all the as-built sample, since $M_f < 37$ °C $< A_s$ in samples A, B, C. On the other hand, in fact, TTs of SFA stent point out the presence of solely the austenite phase at 37 °C and the

consequent appearance of superelastic features (A_f < 37 °C). For this reason, in order to modify the microstructure at the operation temperature as the main scope of this part of the work, two different heat treatments were performed on L-PBF samples (Table 4.2) and the corresponding results are discussed in Paragraph 4.2.3.

To better analyze and compare the TTs, Fig. 4.8 compares the DSC thermograms of virgin powder, Sample B and SFA stent. Only Sample B is reported for comparison, as L-PBF samples showed almost superimposable curves.

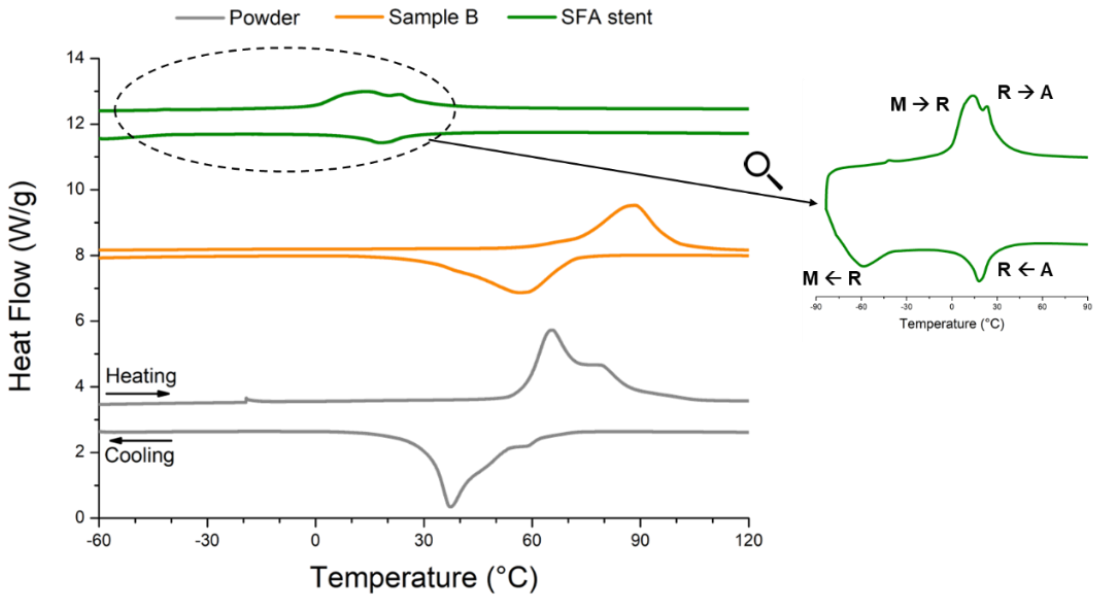

Fig. 4.8. DSC curves comparison between powder, sample B and SFA stent.

The powder is characterized by broad and adjacent peaks near A_f and M_s, which may be attributed to compositional heterogeneity of powder and which thus causes transformation to happen in multiple continuous temperatures [179]. This phenomenon is favored by decreasing heating or cooling rates [217]. On the contrary, clear phase transformations are noticed for Sample B, as only a single peak is detected for both the heating and the cooling phase. A noteworthy shift to the right can be observed by comparing the curve of Sample B to that of virgin powder, which corresponds to the conditions after and before the L-PBF process respectively. In detail, M_p, M_s, A_p and A_f significantly increased after the L-PBF process, of about 20 °C. Commonly, an increase in M_s is associated to a loss of the Ni content that can occur during manufacturing. In L-PBF process this happens more significantly with VED values higher than 45 J/mm^3 [163], as those used in the present work (Table 4.1). By comparing values of Table 4.3 with those reported in [65, 162], it can be stated that 1% of loss in Ni content occurred during L-PBF. This is also confirmed by a previous study [218]

where TTs very close to those of the present work are reported, and are attributed to a NiTi alloy with 49% Ni (at%).

On the other hand, by comparing Sample B and SFA stent, differences even up to 100 °C can be detected for TTs values. This likely denotes that the NiTi alloy used to manufacture the SFA stent had a different chemical composition compared to the one of Sample B achieved after the L-PBF process. Furthermore, the SFA stent was probably subjected to heat treatments after manufacturing, which lead to further modification of the TTs and resulting phases. DSC scans very similar to those of the SFA stent were found in [46, 216], where superelastic wires used to fabricate stents were analyzed. Therefore, it is reasonable to assume that the chemical composition of the SFA stent is close to those reported in [46, 216], i.e. 50.8% (at%) and 50.6% (at%). From the magnification of the DSC curve of the SFA stent reported in Fig. 4.8, the occurrence of two separate peaks during cooling is evident. This fact reveals the presence of the R-phase and thus of the two-step martensitic transformation A→R and R→M. This is confirmed by the small thermal hysteresis between A and R transformation, which is typical of the R phase ($|A_P - R_P| < 10$ °C) [46, 217]. The R-phase was also identified in [46, 216], which showed DSC scans superimposable to those of the present work. R-phase is associated to the presence Ni_4Ti_3 particles, as the strain fields around these precipitates make the A→R transformation favored over the direct A→M [33]. Upon heating, the austenite peak shows a double hump, which denotes that M→R and R→A transformations happened as separate but overlapping peaks. Since there are temperature ranges in which the R-phase is thermodynamically favored over both A and M, the R-phase transformation can be classified as symmetric [46]. Lastly, it should be mentioned that the martensitic transformation is not completely observable in the examined temperature range, which indicates that M_f is lower than -70 °C, as reported in Table 4.3.

4.2.2.2 Microstructural characterization

Micrographs of Sample B along the building direction is reported in Fig. 4.9 as representative of the L-PBF samples. The typical structure obtained from the process is detected, i.e. semi-circular melt pools partially overlapped with each other (white dotted lines), marked with the dotted line, as well as columnar grains oriented from the boundary to the center of the melt pool (yellow arrows). Some typical process defects such as porosities (white arrows) are noticed, moreover, the surface is characterized by partially welded

particles, which denotes the typical surface finishing of additively manufactured samples in as-built conditions.

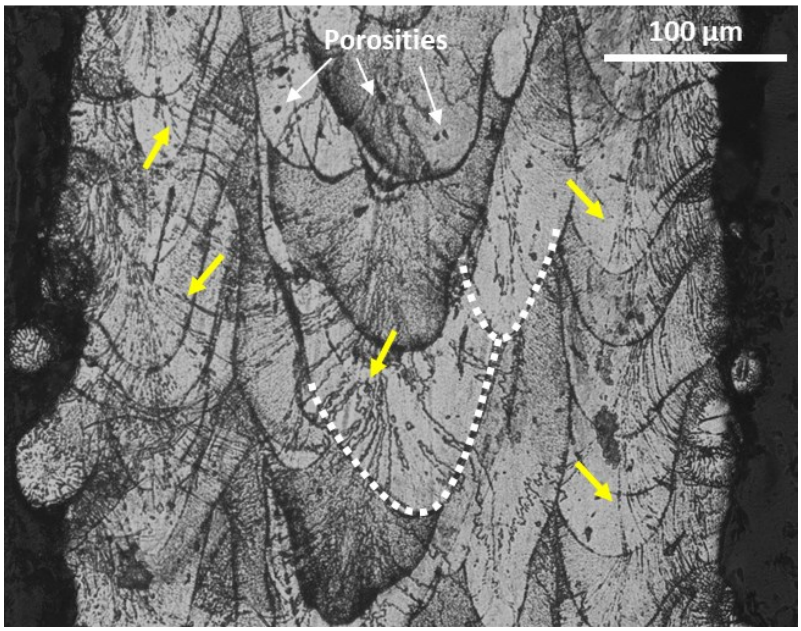

Fig. 4.9. Micrographs of an L-PBF sample.

Results of the EDS analyses performed on Sample A are reported in Fig. 4.10 and Table 4.4 as representative of all L-PBF samples. The chemical composition after manufacturing changed to 51.09 ± 0.15% of Ti and 48.92 ± 0.15% of Ni (at%), meaning that Ni content dropped by about 1% after L-PBF, confirming the previous hypothesis based on the DSC analyses.

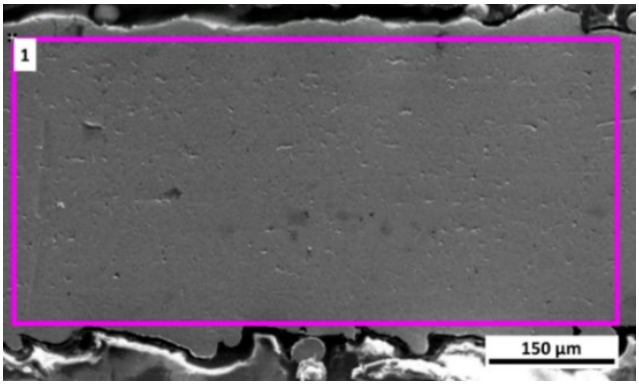

Fig. 4.10. Representative SEM image of the one of the areas analyzed with EDS.

Table 4.4. EDS (at%) of the area indicated in Fig. 4.10.

	Ti	**Ni**
1	51.02	48.98

4.2.3 Heat-treated samples

Heat treatments were performed with the aim of modifying the microstructure of the as-built samples to obtain the one suitable for superelasticity at 37 °C. In fact, for the as-built alloy M_f < 37 °C < A_s, which results in shape memory effect rather than superelasticity, required for stent application. Since the previous analyses showed no influence of the investigated process parameters on the TTs of L-PBF samples, results regarding heat-treated samples were selected regardless of the process parameters.

4.2.3.1 Phase transformation

Results of DSC analyses of T1 and T2 samples compared to the as-built and SFA stent are reported in Fig. 4.11, while the corresponding TTs are listed in Table 4.5. Similarly to the criterion used for as-built samples, results of the second heating scans are reported.

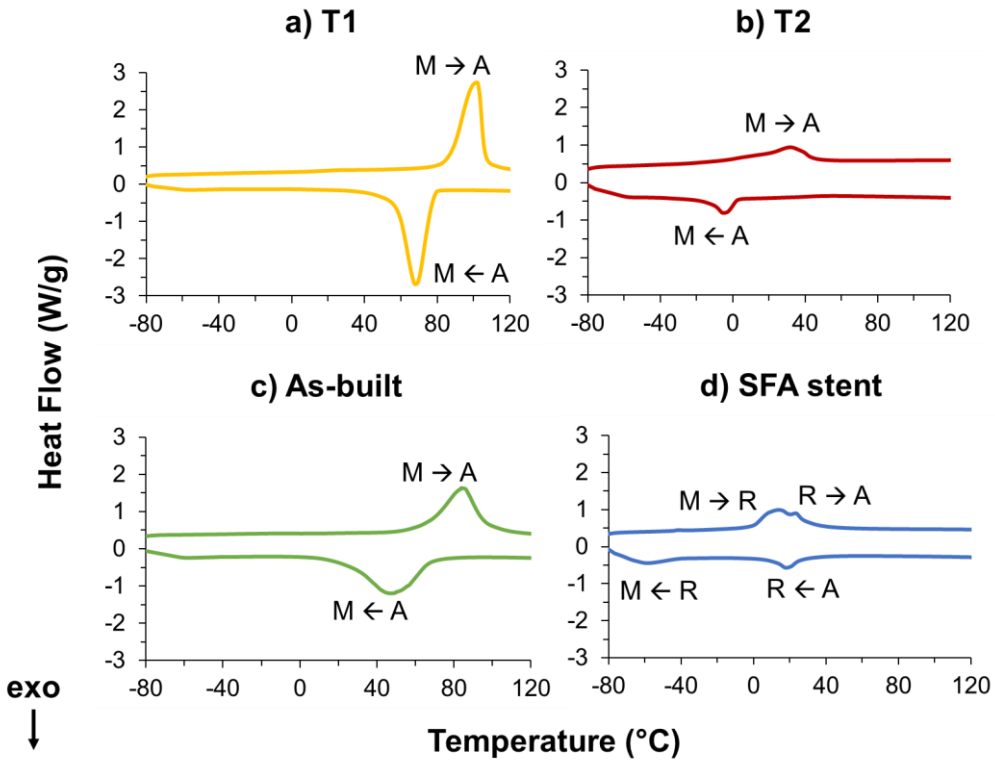

Fig. 4.11. DSC thermogram of T1, T2 samples compared to the as-built sample and SFA stent.

Table 4.5. TTs of as-built, T1, T2 samples and SFA stent.

Material	Temperature (°C)								
	M_f	M_p	M_s	R_f	R_p	R_s	A_s	A_p	A_f
As-built	28	47	68	-	-	-	65	84	97
T1	58	68	78	-	-	-	86	102	106
T2	-13	-5	3	-	-	-	-17	32	45
SFA stent	<-70	-60	-40	10	18	27	19	23	31

For T1 and T2 samples only a single peak is detected for both the heating and the cooling scans, which corresponds respectively to the M→A and A→M transformations. The structure occurring at the stent operation temperature (i.e. 37 °C) is martensite for T1 sample, and mixed austenite-martensite for T2 sample and austenite for the SFA stent.

T1 sample presents the martensitic phase at the stent operation temperature (37 °C), similarly to the as-built alloy. The slight increase of TTs after T1 made this condition of heat treatment to present $M_f > 37$ °C, meaning that the shape memory effect is exhibited rather than superelasticity, further distancing the as-built sample (for which $M_f < 37$ °C $< A_s$) from obtaining superelasticity at 37 °C. This appears to be in contrast with previous findings [169], possibly due to the slight difference in the Ni content before the heat treatment compared to the present work.

On the other hand, after T2, DSC curves were shifted to lower values of about 60 °C compared to the as-built, making the TTs of the alloy to be $A_s < RT < A_f$ and also $A_s < 37$ °C $< A_f$. This fact may be attributed to the formation of Ti-rich precipitates during the slow cooling of the heat treatment, which lowered the Ti level in the matrix, thus enriching that of Ni. In addition, T1 heat treatment produces sharper DSC thermograms, indication of a homogenous structure, while T2 resulted in wider and more rounded curves, which reflects instead a heterogeneous structure likely related to precipitates formation [59]. T2 sample came very close to the DSC curve and TTs values of the SFA stent. However, in this case it was not possible to detect any double peak related to R-phase, and the temperature range in which the transformation occurs during heating ($|A_f-A_s|$) is much wider. Furthermore, the obtained TTs should result in the coexistence of shape memory and superelastic effect at the operation temperature ($A_s < 37$ °C $< A_f$), in contrast to the shape memory features emerging for the as-built alloy ($M_f < 37$ °C $< A_s$). On the other hand, in the case of SFA stent, a full superelastic behavior is expected since $A_f < 37$ °C.

4.2.3.2 Microstructure

Micrographs of the T1 and T2 samples are reported in Fig. 4.12, while the corresponding EDS analyses are listed in Table 4.6.

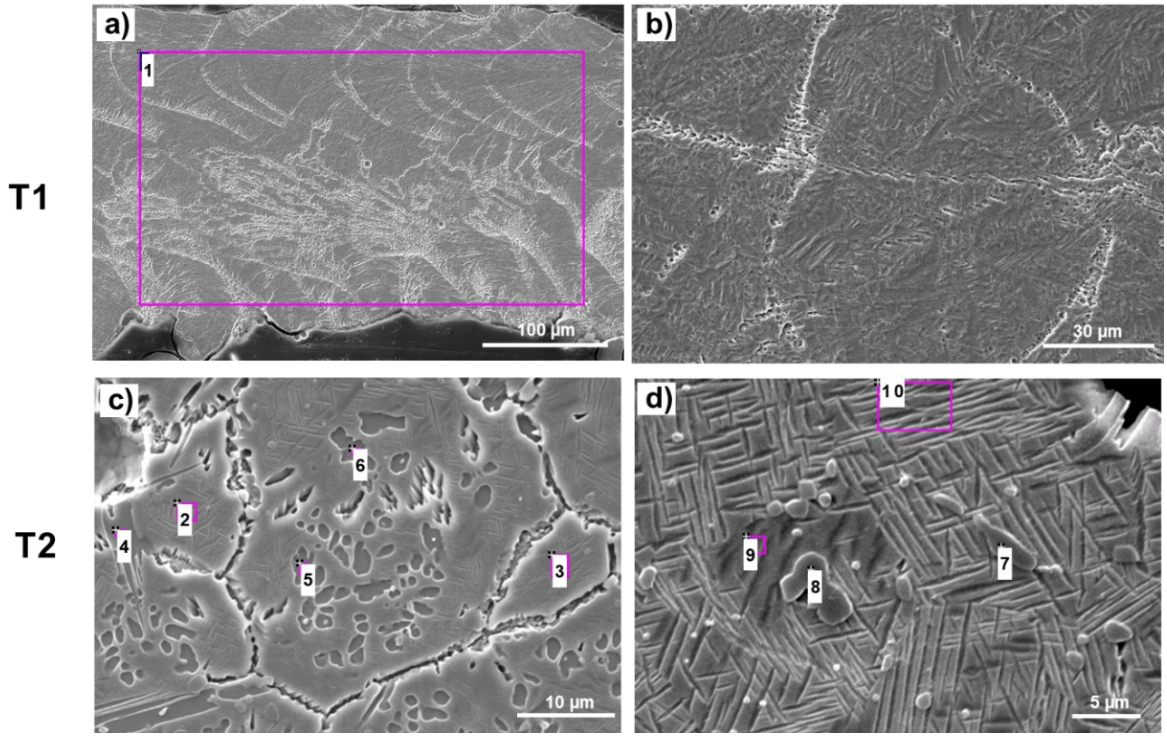

Fig. 4.12. SEM micrographs of a-b) T1 sample, c-d) T2 sample.

Table 4.6. EDS analyses (at%) of areas indicated in Fig. 4.12 for T1 and T2 samples.

	Ti	Ni
1	50.99	49.01
2	48.66	51.34
3	49.49	50.51
4	41.94	58.06
5	43.65	56.35

	Ti	Ni
6	41.86	58.14
7	63.84	36.16
8	60.80	39.20
9	48.06	51.94
10	48.23	51.77

The L-PBF structure and the chemical composition recorded through EDS are preserved after T1 heat treatment (Fig. 4.12a, row 1 of Table 4.6) as well as the martensite (Fig. 4.12b). In fact, for both the as-built alloy and T1 sample, the martensite is present at room temperature, as shown by the DSC results ($RT < M_f$). No precipitates are present after T1. The formation of Ni-rich phases, which typically occurs around 600 °C in Ni-rich NiTi alloys, is excluded in this case due to the insufficient Ni content in the matrix. The presence of nanometric Ni_4Ti_3 precipitates, although potentially too small to be detected using SEM, is also excluded, due again to the low Ni content, as well as the slow cooling rate of the heat treatment. Furthermore, DSC analysis of the T1 sample (Fig. 4.11) revealed no R-phase peak, thus further proving the absence of Ni_4Ti_3.

A mixed structure is detected for T2 sample, confirming the results of DSC analyses. Austenite grains are found preferably close to the sample surface (Fig. 4.12c), while martensite increases moving inward (Fig. 4.12d). After T2, the chemical composition of the matrix changed to higher values of Ni (row 2, 3, 9, 10 of Table 4.6) compared to the as-built sample. Moreover, particles with chemical composition near to Ti_2Ni (from about 0.60:0.40 to about 0.75:0.25 at% [219]) can be found in the inner area (Fig. 4.12d, row 7, 8 of Table 4.6), while other particles richer in Ni can be found near the surface (Fig. 4.12c, row 4, 5, 6 of Table 4.6).

Ti_2Ni phase was generated during heat treatment, as it forms at 984 °C by a peritectic reaction [33], and the low rate of furnace cooling allowed its growth. Therefore, its formation resulted in Ni enrichment of the matrix and thus in the lowering of TTs. As consequence of this chemical variation, other diffusive phenomena likely occurred during the heat treatment, leading to the formation of Ni-rich precipitates. The stoichiometry of these particles is near Ni_3Ti_2 phase, a metastable phase forming from Ni_4Ti_3 and which subsequently evolves into the Ni_3Ti equilibrium phase [33, 51]. Ni_3Ti_2 presence is confirmed by the morphology, i.e. plate and indefinite block shape located both at grain boundaries and within the grains [51]. On the contrary, Ni_4Ti_3 particles were not detected: their formation has probably occurred between 400-600 °C during cooling after Ni enrichment of the matrix, however the slow cooling in the furnace likely promoted their evolution in Ni_3Ti_2. The contribution of small and fine-dispersed Ni_4Ti_3 precipitates is effective in the improvement of superelastic behavior, while Ti_2Ni and Ni_3Ti_2 phases are known to be detrimental for this purpose. This indicates a non-optimal microstructure for the superelasticity, even though the TTs approached those of the SFA stent, thus suggesting that this heat treatment requires further optimization.

4.2.3.3 Compression tests

Fig. 4.13 displays the curves obtained from compression tests performed on the as-built, T1 and T2 samples compared to the SFA stent. The compression resistance (CR) in force per unit axial length is plotted against the normalized displacement of the compression.

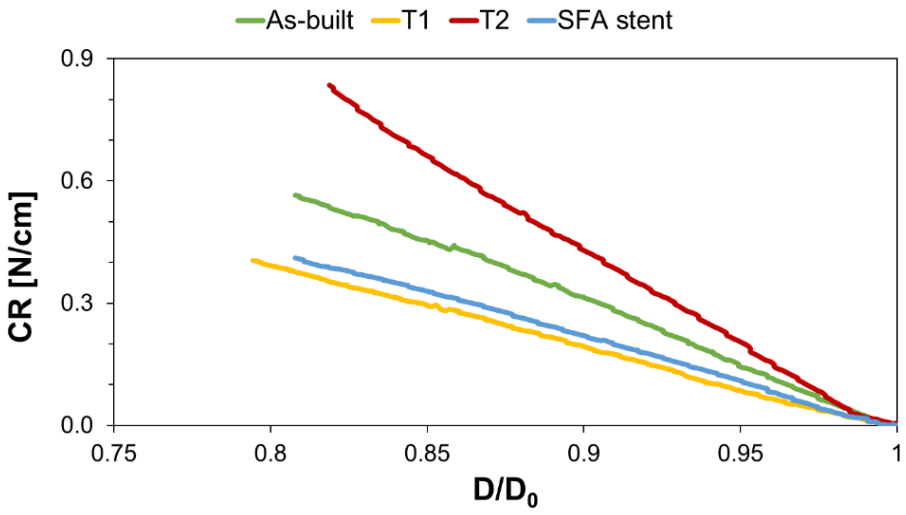

Fig. 4.13. Comparison of compression curves of as-built, T1, T2 samples and SFA stent.

A nearly linear behavior can be detected for all the investigated samples, in accordance with previous studies [220-222]. The as-built sample exhibits a higher slope than the SFA stent, denoting higher resistance to compression, as with the same applied force a lower deformation occurs. T1 treatment results in a decrease in slope compared to the as-built, due to its effect as stress-relieving heat treatment on the martensite structure. This allowed T1 sample to get closer to SFA stent curves despite the different microstructures. On the contrary, the curve for T2 sample shows a slope increase, which reflects the microstructural changes occurred, i.e. the formation of Ti_2Ni and Ni_3Ti_2 precipitates. The higher CR demonstrates that T2 sample can undercome higher external loads, but this constitutes a risk for vascular overdilatation and lesions [220]. In fact, T2 sample exhibits a higher stiffness than the SFA stent. Despite approaching the microstructure of the SFA stent, T2 sample still differs as neither R-phase nor Ni_4Ti_3 were detected, and instead Ti_2Ni and Ni_3Ti_2 were found. These differences are attributed to the mismatch of Ni content between the SFA stent and the as-built sample, emphasized by the Ni evaporation during L-PBF. T2 proved to only partially compensate for the loss of Ni, further demonstrating the importance of tailoring the appropriate process parameters on NiTi parts when produced via L-PBF to contain Ni evaporation.

Because CR was found to be directly correlated with radial resistive force (RRF) [220], which is another key property indicator for stents measured during radial compression tests, the same overall results are reasonably expected also for the radial compression behavior of samples.

4.3 CONCLUSIONS

After manufacturing of prototype stents starting from 50.54Ni-49.46Ti (at%) powder, about 1% of Ni loss was recorded in the as-built sample, as well as the presence of the martensitic phase rather than austenite at 37 °C, i.e. the operation temperature of stents. The heat treatment at 600 °C for 1.5 h acted as a stress-relief treatment, thus not modifying the microstructure at room temperature, and reducing the mechanical properties under compression testing. After this treatment, at 37 °C only the martensitic phase appears, making this condition farther from the obtainment of superelasticity. On the contrary, heat-treating samples at 1100 °C for 1.5 h allowed a significant modification of the microstructure at room temperature, partially restoring the austenitic phase. This was possible thanks to the modification of TTs, which brought the samples to be in the A_s < 37 °C < A_f region, where, however the coexistence of the shape memory and superelastic effect is expected rather than full superelasticity. Furthermore, the mechanical behavior of samples after this heat treatment showed higher compression resistance and higher stiffness compared to the conventional stent, which could be dangerous for blood vessel integrity. Table 4.7 provides for each analyzed condition a summary of the TTs, expected behavior and phases present both at room temperature, corresponding to the microstructural analyses, and 37 °C, corresponding to the compression testing temperature.

Table 4.7. TTs, expected behavior and phases exhibited in the temperature of interest of the present study: i.e. RT for microstructural analyses, and 37 °C for compression tests.

Sample	at RT	at 37 °C
As-built	$RT < M_f$ SME Martensite	$M_f < 37\ °C < A_s$ SME Martensite and austenite
T1	$RT < M_f$ SME Martensite	$37\ °C < M_f$ SME Martensite
T2	$A_s < RT < A_f$ SE + SME Martensite and austenite	$A_s < 37\ °C < A_f$ SE + SME Martensite and austenite
SFA stent	$A_s < RT < A_f$ SE + SME Martensite and austenite	$37\ °C < A_f$ SE Austenite

Even for T2 treatment, the complete achievement of superelasticity at 37 °C is not expected to occur, since for this aim a slightly lower A_f is required. Nevertheless, even if lower A_f was reached, the microstructural modification involved for this purpose, i.e. the

formation of Ti_2Ni, is detrimental for the occurrence of superelasticity, as well as the presence of Ni_3Ti_2 phase. In fact, the presence of these phases is known to hinder the superelastic features. Therefore, heat treating at 1100 °C for 1.5 h was found to be effective in adjusting TTs after Ni evaporation, but the microstructural modifications involved are not suitable for the obtainment of superelasticity, thus requiring further optimization.

FINAL REMARKS

In the present work, NiTi samples produced by laser powder bed fusion were characterized after performing heat treatments with two different aims, which are the obtainment of superelasticity and the modification of the transformation temperatures after Ni evaporation.

For the first scope, direct aging heat treatments at 400 °C and 500 °C were performed on 52.39Ni-47.61Ti (at%) cylindrical samples for a short time of 15 minutes and compared to the corresponding solution treated and aged conditions. Cyclic compression tests of loading and unloading up to 6% of strain were performed at different temperatures, i.e. room temperature, 37 °C, and A_f + 10 °C. Comparable results were found at all the testing temperatures between direct aged samples and solution annealed and aged samples, with negligible residual strains and high cyclic stability, in contrast to the as-built alloy, which only showed superelastic features at its A_f + 10 °C temperature. The results of direct aging are thus promising for integrating this treatment into the additive manufacturing production route of NiTi, making it more attractive thanks to the reduction of the associated costs, bypassing the need of solution annealing. Direct aging was found to directly exploit the supersaturated condition resulting from the process itself, which allowed the precipitation of Ni_4Ti_3 phase to happen.

The compression tests performed at different temperatures allowed the determination of a map of the material behavior as function of the temperature and the applied stress, providing a comprehensive characterization of each analyzed condition. Thanks to the presence of Ni_4Ti_3 nano-precipitates, all the performed heat treatments resulted in raised transformation temperatures, increased critical stress for slip deformation and decreased critical stress to induce martensitic transformation. This deeply improved the superelastic features of the alloy within the temperature range of interest, also allowing a recoverable strain of 10%. This value is higher than the commonly recognized limit of the superelastic effect (6-8%), as well as than what reported in the literature for NiTi alloy fabricated via L-PBF.

For the purpose of adjusting the transformation temperatures after Ni evaporation, different heat treatments were performed on prototype stents manufactured from 50.54Ni-49.46Ti (at%) powder. Among these, heat treatment at 1100 °C for 1.5 h was found to be

effective in lowering A_f temperature, bringing it closer to that of a conventionally produced stent. However, this reduction in the transformation temperatures was associated with the decrease of Ti in the matrix after the formation of the Ti_2Ni phase, which is undesirable for the achieving the superelastic behavior. In addition, compression tests with parallel flat plates showed that this heat treatment resulted in higher stresses values compared to those reached of the commercially available stent, which could prove harmful to the vessel integrity. Therefore, although the heat treatment at 1100 °C for 1.5 h was effective in tuning A_f after Ni evaporation, the resulting microstructure did not lead to mechanical properties suitable for the application and, furthermore, would not be appropriate in achieving superelasticity, thus pointing out the need for further optimization.

REFERENCES

[1] A. International, "ASTM F2792-12a "Standard Terminology for Additive Manufacturing Technologies", 2012.

[2] L. Yang, K. Hsu, B. Baughman, D. Godfrey, F. Medina, M. Menon, and S. Wiener, *Additive Manufacturing of Metals: The Technology, Materials, Design and Production*: Springer, 2017.

[3] J. O. Milewski, *Additive Manufacturing of Metals: From Fundamental Technology to Rocket Nozzles, Medical Implants, and Custom Jewelry*, 2017.

[4] M. Guide. https://www.manufacturingguide.com/en/selective-laser-melting-and-milling-slmm.

[5] C. Y. Yap, C. K. Chua, Z. L. Dong, Z. H. Liu, D. Q. Zhang, L. E. Loh, and S. L. Sing, "Review of selective laser melting: Materials and applications", *Applied Physics Reviews,* vol. 2, no. 4, 2015.

[6] T. DebRoy, H. L. Wei, J. S. Zuback, T. Mukherjee, J. W. Elmer, J. O. Milewski, A. M. Beese, A. Wilson-Heid, A. De, and W. Zhang, "Additive manufacturing of metallic components – Process, structure and properties", *Progress in Materials Science,* vol. 92, pp. 112-224, 2018.

[7] L. Zhou, J. Miller, J. Vezza, M. Mayster, M. Raffay, Q. Justice, Z. Al Tamimi, G. Hansotte, L. D. Sunkara, and J. Bernat, "Additive Manufacturing: A Comprehensive Review", *Sensors,* 24, 2024.

[8] M. Ruffo, C. Tuck, and R. Hague, "Cost estimation for rapid manufacturing - Laser sintering production for low to medium volumes", *Proceedings of the Institution of Mechanical Engineers, Part B: Journal of Engineering Manufacture,* vol. 220, no. 9, pp. 1417-1427, 2006.

[9] X. H. Liu, C. C. Zhao, X. Zhou, Z. J. Shen, and W. Liu, "Microstructure of selective laser melted AlSi10Mg alloy", *Materials & Design,* vol. 168, Apr, 2019.

[10] J. Zhang, B. Song, Q. Wei, D. Bourell, and Y. Shi, "A review of selective laser melting of aluminum alloys: Processing, microstructure, property and developing trends", *Journal of Materials Science & Technology,* vol. 35, no. 2, pp. 270-284, 2019.

[11] W. Shifeng, L. Shuai, W. Qingsong, C. Yan, Z. Sheng, and S. Yusheng, "Effect of molten pool boundaries on the mechanical properties of selective laser melting parts", *Journal of Materials Processing Technology,* vol. 214, no. 11, pp. 2660-2667, 2014.

[12] S. Kou, "Welding Metallurgy", John Wiley & Sons, Inc., 2002.

[13] K. Kempen, L. Thijs, J. Van Humbeeck, and J. P. Kruth, "Processing AlSi10Mg by selective laser melting: parameter optimisation and material characterisation", *Materials Science and Technology,* vol. 31, no. 8, pp. 917-923, 2015.

[14] U. Scipioni Bertoli, A. J. Wolfer, M. J. Matthews, J. P. R. Delplanque, and J. M. Schoenung, "On the limitations of Volumetric Energy Density as a design parameter for Selective Laser Melting", *Materials and Design,* vol. 113, pp. 331-340, 2017.

[15] L. Cao, S. Chen, M. Wei, Q. Guo, J. Liang, C. Liu, and M. Wang, "Effect of laser energy density on defects behavior of direct laser depositing 24CrNiMo alloy steel", *Optics and Laser Technology,* vol. 111, pp. 541-553, 2019.

[16] S. Ghods, R. Schur, E. Schultz, R. Pahuja, A. Montelione, C. Wisdom, D. Arola, and M. Ramulu, "Powder reuse and its contribution to porosity in additive manufacturing of Ti6Al4V", *Materialia,* vol. 15, 2021.

[17] F. Chu, K. Zhang, H. Shen, M. Liu, W. Huang, X. Zhang, E. Liang, Z. Zhou, L. Lei, J. Hou, and A. Huang, “Influence of satellite and agglomeration of powder on the processability of AlSi10Mg powder in Laser Powder Bed Fusion”, *Journal of Materials Research and Technology,* vol. 11, pp. 2059-2073, 2021.

[18] C. Weingarten, D. Buchbinder, N. Pirch, W. Meiners, K. Wissenbach, and R. Poprawe, “Formation and reduction of hydrogen porosity during selective laser melting of AlSi10Mg”, *Journal of Materials Processing Technology,* vol. 221, pp. 112-120, 2015.

[19] Q. C. Liu, J. Elambasseril, S. J. Sun, M. Leary, M. Brandt, and P. K. Sharp, "The effect of manufacturing defects on the fatigue behaviour of Ti-6Al-4V specimens fabricated using selective laser melting." pp. 1519-1524.

[20] R. Li, J. Liu, Y. Shi, L. Wang, and W. Jiang, “Balling behavior of stainless steel and nickel powder during selective laser melting process”, *The International Journal of Advanced Manufacturing Technology,* vol. 59, no. 9, pp. 1025-1035, 2012.

[21] D. Wang, S. Wu, F. Fu, S. Mai, Y. Yang, Y. Liu, and C. Song, “Mechanisms and characteristics of spatter generation in SLM processing and its effect on the properties”, *Materials & Design,* vol. 117, pp. 121-130, 2017.

[22] S. L. Sing, and W. Y. Yeong, “Laser powder bed fusion for metal additive manufacturing: perspectives on recent developments”, *Virtual and Physical Prototyping,* vol. 15, no. 3, pp. 359-370, 2020.

[23] W. Buehler, and R. Wiley, *Nickel-Based Alloys. USA Patent No. 3, 147, 851*, 1965.

[24] S. Miyazaki, "Development and Characterization of Shape Memory Alloys”, *Shape Memory Alloys*, M. Fremond and S. Miyazaki, eds., pp. 69-147, Vienna: Springer Vienna, 1996.

[25] M. H. Elahinia, M. Hashemi, M. Tabesh, and S. B. Bhaduri, “Manufacturing and processing of NiTi implants: A review”, *Progress in Materials Science,* vol. 57, no. 5, pp. 911-946, 2012.

[26] J. Van Humbeeck, “Non-medical applications of shape memory alloys”, *Materials Science and Engineering: A,* vol. 273-275, pp. 134-148, 1999.

[27] K. Otsuka, and C. M. Wayman, *Shape Memory Materials*: Cambridge University Press, 1998.

[28] D. Stöckel, "The shape memory effect: phenomenon, alloys, applications”, *Shape memory alloys for power systems* pp. 1–13, 1995.

[29] J. Matthey. "Nitinol technical properties”, April, 2024; https://matthey.com/products-and-markets/other-markets/medical-components/resource-library/nitinol-technical-properties.

[30] L. Delaey, R. V. Krishnan, H. Tas, and H. Warlimont, “Thermoelasticity, pseudoelasticity and the memory effects associated with martensitic transformations - Part 1 Structural and microstructural changes associated with the transformations”, *Journal of Materials Science,* vol. 9, no. 9, pp. 1521-1535, 1974.

[31] R. V. Krishnan, L. Delaey, H. Tas, and H. Warlimont, “Thermoplasticity, pseudoelasticity and the memory effects associated with martensitic transformations - Part 2 The macroscopic mechanical behaviour”, *Journal of Materials Science,* vol. 9, no. 9, pp. 1536-1544, 1974.

[32] H. Warlimont, L. Delaey, R. V. Krishnan, and H. Tas, “Thermoelasticity, pseudoelasticity and the memory effects associated with martensitic transformations - Part 3 Thermodynamics and kinetics”, *Journal of Materials Science,* vol. 9, no. 9, pp. 1545-1555, 1974.

[33] K. Otsuka, and X. Ren, “Physical metallurgy of Ti-Ni-based shape memory alloys”, *Progress in Materials Science,* vol. 50, no. 5, pp. 511-678, 2005.

[34] C. M. Wayman, and T. W. Duerig, "An Introduction to Martensite and Shape Memory", *Engineering Aspects of Shape Memory Alloys*, T. W. Duerig, K. N. Melton, D. Stöckel and C. M. Wayman, eds., pp. 3-20: Butterworth-Heinemann, 1990.

[35] D. Holec, "On the precipitation in NiTi based Shape Memory Alloys", Masaryk University, Brno, 2005.

[36] K. Bhattacharya, *Microstructure of martensite: why it forms and how it gives rise to the shape-memory effect*: Oxford University Press, 2004.

[37] K. Bhattacharya, "Self-accommodation in martensite", *Archive for Rational Mechanics and Analysis,* vol. 120, no. 3, pp. 201-244, 1992.

[38] O. K., and C. M. Wayman, "Mechanism of Shape Memory and Superelasticity", *Shape Memory Materials*, C. U. Press, ed., pp. 27-48, 1999.

[39] T. W. Duerig, and R. Zadno, "An Engineer's Perspective of Pseudoelasticity", *Engineering Aspects of Shape Memory Alloys*, T. W. Duerig, K. N. Melton, D. Stöckel and C. M. Wayman, eds., pp. 369-393: Butterworth-Heinemann, 1990.

[40] C. Haberland, H. Meier, and J. Frenzel, "On the properties of Ni-rich NiTi shape memory parts produced by selective laser melting." pp. 97-104.

[41] S. Gollerthan, M. L. Young, A. Baruj, J. Frenzel, W. W. Schmahl, and G. Eggeler, "Fracture mechanics and microstructure in NiTi shape memory alloys", *Acta Materialia,* vol. 57, no. 4, pp. 1015-1025, 2009.

[42] H. Hosoda, and T. Inamura, "Mechanical properties of shape memory alloys", *Shape Memory Alloys for Biomedical Applications*, T. Yoneyama and S. Miyazaki, eds., pp. 20-36: Woodhead Publishing, 2009.

[43] D. Mândru, I. Lungu, S. Noveanu, and O. Tatar, "Shape memory alloy wires as actuators for a minirobot." pp. 333-336.

[44] A. International, "ASTM F2004-16 Transformation Temperature of Nickel-Titanium Alloys by Thermal Analysis", 2016.

[45] S. Miyazaki, and K. Otsuka, "Deformation and transition behavior associated with the R-phase in Ti-Ni alloys", *Metallurgical Transactions A,* vol. 17, no. 1, pp. 53-63, 1986.

[46] T. W. Duerig, and K. Bhattacharya, "The Influence of the R-Phase on the Superelastic Behavior of NiTi", *Shape Memory and Superelasticity,* vol. 1, no. 2, pp. 153-161, 2015.

[47] T. Saburi, "Ti-Ni Shape Memory Alloys", *Shape Memory Materials*, C. U. Press, ed., pp. 49-96: Cambridge University Press, 1999.

[48] A. International, "F2005-21 Standard Terminology for Nickel-Titanium Shape Memory Alloys", 2021.

[49] M. Nishida, and T. Honma, "All-round shape memory effect in Ni-rich TiNi alloys generated by constrained aging", *Scripta Metallurgica,* vol. 18, no. 11, pp. 1293-1298, 1984.

[50] K. Otsuka, and T. Kakeshita, "Science and Technology of Shape-Memory Alloys: New Developments", *MRS Bulletin,* vol. 27, no. 2, pp. 91-100, 2002.

[51] M. Nishida, C. M. Wayman, and T. Honma, "Precipitation processes in near-equiatomic TiNi shape memory alloys", *Metallurgical Transactions A,* vol. 17, no. 9, pp. 1505-1515, 1986.

[52] T. Hara, T. Ohba, K. Otsuka, and M. Nishida, "Phase transformation and crystal structures of Ti2Ni3 precipitates in Ti-Ni alloys", *Materials Transactions, JIM,* vol. 38, no. 4, pp. 277-284, 1997.

[53] A. Taylor, and R. W. Floyd, "Precision measurements of lattice parameters of non-cubic crystals", *Acta Crystallographica,* vol. 3, no. 4, pp. 285-289, 1950.

[54] T. Tadaki, Y. Nakata, K. i. Shimizu, and K. Otsuka, “Crystal structure, composition and morphology of a precipitate in an aged Ti-51 at. %Ni shape memory alloy”, *Transactions of the Japan Institute of Metals,* vol. 27, no. 10, pp. 731-740, 1986.

[55] T. Saburi, T. Tatsumi, and S. Nenno, "Effects of heat treatment on mechanical behavior of Ti-Ni alloys", *Journal de Physique*, pp. c4.261-c4.266, 1982.

[56] S. Miyazaki, Y. Ohmi, K. Otsuka, and Y. Suzuki, "Characteristics of deformation and transformation pseudoelasticity in Ti-Ni alloys", *Journal de Physique*, pp. c4.255-c4.260, 1982.

[57] S. Y. Jiang, Y. Q. Zhang, Y. N. Zhao, S. W. Liu, L. Hu, and C. Z. Zhao, “Influence of Ni4Ti3 precipitates on phase transformation of NiTi shape memory alloy”, *Transactions of Nonferrous Metals Society of China (English Edition),* vol. 25, no. 12, pp. 4063-4071, 2015.

[58] J. I. Kim, and S. Miyazaki, “Effect of nano-scaled precipitates on shape memory behavior of Ti-50.9at.%Ni alloy”, *Acta Materialia,* vol. 53, no. 17, pp. 4545-4554, 2005.

[59] K. Safaei, H. Abedi, M. Nematollahi, F. Kordizadeh, H. Dabbaghi, P. Bayati, R. Javanbakht, A. Jahadakbar, M. Elahinia, and B. Poorganji, “Additive Manufacturing of NiTi Shape Memory Alloy for Biomedical Applications: Review of the LPBF Process Ecosystem”, *JOM,* vol. 73, no. 12, pp. 3771-3786, 2021.

[60] Q. Chen, X. F. Wu, and T. Ko, “The effects of Ti3Ni4 precipitates on the R-phase transformation”, *Scripta Metallurgica et Materialia,* vol. 29, no. 1, pp. 49-53, 1993.

[61] T. Saburi, S. Nenno, and T. Fukuda, “Crystal structure and morphology of the metastable X phase in shape memory Ti-Ni alloys”, *Journal of the Less Common Metals,* vol. 125, pp. 157-166, 1986.

[62] K. Otsuka, and K. Shimizu, “Pseudoelasticity and shape memory effects in alloys”, *International Metals Reviews,* vol. 31, no. 1, pp. 93-114, 1986.

[63] F. Takei, T. Miura, S. Miyazaki, S. Kimura, K. Otsuka, and Y. Suzuki, “Stress-induced martensitic transformation in a Ti-Ni single crystal”, *Scripta Metallurgica,* vol. 17, no. 8, pp. 987-992, 1983.

[64] K. Otsuka, and X. Ren, "Factors affecting the Ms temperature and its control in shape-memory alloys", *Material Science Forum*, vol. 394, pp. 177-184, 2002.

[65] K. N. Melton, "Ni-Ti Based Shape Memory Alloys”, *Engineering Aspects of Shape Memory Alloys*, T. W. Duerig, K. N. Melton, D. Stöckel and C. M. Wayman, eds., pp. 21-35: Butterworth-Heinemann, 1990.

[66] J. Khalil-Allafi, A. Dlouhy, and G. Eggeler, “Ni4Ti3-precipitation during aging of NiTi shape memory alloys and its influence on martensitic phase transformations”, *Acta Materialia,* vol. 50, no. 17, pp. 4255-4274, 2002.

[67] T. Saburi, M. Yoshida, and S. Nenno, “Deformation behavior of shape memory TiNi alloy crystals”, *Scripta Metallurgica,* vol. 18, no. 4, pp. 363-366, 1984.

[68] T. Saburi, S. Nenno, Y. Nishimoto, and M. Zeniya, “Effects of thermomechanical treatment on the shape-memory effect and pseudoelasticity of Ti-50.2Ni and Ti-47.5Ni-2.5Fe alloys”, *J. Iron and Steel Inst. Japan,* vol. 72(6), pp. 571-578, 1986.

[69] D. Chrobak, D. Stróż, and H. Morawiec, “Effect of early stages of precipitation and recovery on the multi-step transformation in deformed and annealed near-equiatomic NiTi alloy”, *Scripta Materialia,* vol. 48, no. 5, pp. 571-576, 2003.

[70] D. Chrobak, and D. Stróż, “Two-stage R phase transformation in a cold-rolled and annealed Ti–50.6at.%Ni alloy”, *Scripta Materialia,* vol. 52, no. 8, pp. 757-760, 2005.

[71] C. P. Frick, A. M. Ortega, J. Tyber, A. E. M. Maksound, H. J. Maier, Y. Liu, and K. Gall, “Thermal processing of polycrystalline NiTi shape memory alloys”, *Materials Science and Engineering: A,* vol. 405, no. 1, pp. 34-49, 2005.

[72] D. F. Williams, "Definitions in biomaterials", *Proceedings of a consensus conference of the european society for biomaterials,* vol. 4, 1987.
[73] T. W. Duerig, "The use of superelasticity in modern medicine", *MRS Bulletin,* vol. 27, no. 2, pp. 101-104, 2002.
[74] J. L. Hughes, *Evaluation of Nitinol for Use as a Material in the Construction of Orthopaedic Implants*, 1976.
[75] T. Yoneyama, and S. Miyazaki, *Shape Memory Alloys for Biomedical Applications*: Woodhead Publishing, 2009.
[76] S. Shabalovskaya, and J. Van Humbeeck, "Biocompatibility of Nitinol for biomedical applications", *Shape Memory Alloys for Biomedical Applications*, pp. 194-233, 2008.
[77] S. A. Shabalovskaya, "On the nature of the biocompatibility and on medical applications of NiTi shape memory and superelastic alloys", *Bio-Medical Materials and Engineering,* vol. 6, no. 4, pp. 267-289, 1996.
[78] V. I. Itin, V. E. Gyunter, S. A. Shabalovskaya, and R. L. C. Sachdeva, "Mechanical properties and shape memory of porous nitinol", *Materials Characterization,* vol. 32, no. 3, pp. 179-187, 1994.
[79] M. Z. Mirgazizov, V. Gyunter., and V. I. Itin, *Superelastic Implants and Constracts from Shape Memory Alloys in Dentistry*: Quintessenz Verlag., GmbH., 1993.
[80] V. Polenichkin, "Treatment of fractures of the facial bone sceleton with NiTi shape memory devices", in *The Proceedings of 1st International Conference on Shape Memory and Superelastic Technologies*, California, USA, March 7-10, 1994.
[81] A. Starokha, V. E. Gyunter, P. Sysolyatin, and V. I. Itin, "Shape memorizing implants in otorhinolaryngology", in *The Proceedings of 1st International Conference on Shape Memory and Superelastic Technologies*, California, USA, March 7-10, 1993, pp. pp. 509-513.
[82] T. Habijan, C. Haberland, H. Meier, J. Frenzel, J. Wittsiepe, C. Wuwer, C. Greulich, T. A. Schildhauer, and M. Köller, "The biocompatibility of dense and porous Nickel–Titanium produced by selective laser melting", *Materials Science and Engineering: C,* vol. 33, no. 1, pp. 419-426, 2013.
[83] S. Miyazaki, and R. L. Sachdeva, "1 - Shape memory effect and superelasticity in Ti—Ni alloys", *Shape Memory Alloys for Biomedical Applications*, T. Yoneyama and S. Miyazaki, eds., pp. 3-19: Woodhead Publishing, 2009.
[84] D. Kapoor, "Nitinol for Medical Applications: A Brief Introduction to the Properties and Processing of Nickel Titanium Shape Memory Alloys and their Use in Stents", *Johnson Matthey Technology Review,* vol. 61, no. 1, pp. 66-76, 2017.
[85] L. H. Yahia, F. Rayes, and A. O. Warrak, "Regulation, orthopedic, dental, endovascular and other applications of Ti-Ni shape memory alloys", *Shape Memory Alloys for Biomedical Applications*, pp. 306-326, 2008.
[86] J. Li, L. Qin, K. Yang, Z. Ma, Y. Wang, L. Cheng, and D. Zhao, "Materials evolution of bone plates for internal fixation of bone fractures: A review", *Journal of Materials Science and Technology,* vol. 36, pp. 190-208, 2020.
[87] M. UNITE. "REFLEX® Nitinol Staples", https://medlineunite.com/product/reflex-nitinol-staples/.
[88] O. N. Schipper, S. E. Ford, P. W. Moody, B. Van Doren, and J. K. Ellington, "Radiographic Results of Nitinol Compression Staples for Hindfoot and Midfoot Arthrodeses", *Foot and Ankle International,* vol. 39, no. 2, pp. 172-179, 2018.
[89] F. Auricchio, E. Boatti, and M. Conti, "Chapter 11 - SMA Biomedical Applications", *Shape Memory Alloy Engineering*, L. Lecce and A. Concilio, eds., pp. 307-341, Boston: Butterworth-Heinemann, 2015.

[90] T. Duerig. "Nitinol: The Shape of Things to Come", April, 2024; https://www.medicaldevice-network.com/features/feature116/?cf-view.
[91] S. A. Materials. "NT0407 Nitinol Dental Brace (Nickel Titanium)", April, 2024; https://www.samaterials.com/nitinol/407-nitinol-dental-braces.html.
[92] "Bypass aorto-coronarico", April, 2024; https://www.ihy-ihealthyou.com/salute/trattamenti/bypass-aorto-coronarico/.
[93] K. Gupta, and K. Meena, "A novel double arrowhead auxetic coronary stent", *Computers in Biology and Medicine,* vol. 166, 2023.
[94] S. Aziz, J. L. Morris, R. A. Perry, and R. H. Stables, "Stent expansion: a combination of delivery balloon underexpansion and acute stent recoil reduces predicted stent diameter irrespective of reference vessel size", *Heart,* vol. 93, no. 12, pp. 1562-6, Dec, 2007.
[95] A. health. "ParaMount™ Mini GPS™", April, 2024; https://aventinhealth.com/en/urunler/medtronic-products/peripheral-products/paramount-mini-gps-balonla-genisletilebilir-periferik-stent-sistemi/.
[96] B. B. Medical. "VascuFlex® 5 and 6 F: Peripheral self-expanding nitinol stent system", April, 2024; https://www.bbraun.co.uk/en/products/b50/vascuflex-peripheralstent.html.
[97] E. I. Levy, R. Mehta, R. Gupta, R. A. Hanel, A. J. Chamczuk, D. Fiorella, H. H. Woo, F. C. Albuquerque, T. G. Jovin, M. B. Horowitz, and L. N. Hopkins, "Self-expanding stents for recanalization of acute cerebrovascular occlusions", *American Journal of Neuroradiology,* vol. 28, no. 5, pp. 816-822, 2007.
[98] D. Stoeckel, A. Pelton, and T. Duerig, "10 - Self-expanding Nitinol stents for the treatment of vascular disease", *Shape Memory Alloys for Biomedical Applications*, T. Yoneyama and S. Miyazaki, eds., pp. 237-256: Woodhead Publishing, 2009.
[99] G. Medical. "GORE® EXCLUDER® Conformable AAA Endoprosthesis: Annual Clinical Update", April, 2024; https://www.goremedical.com/resource/22831460-en.
[100] I. Santos, A. Sepúlveda, J. Viana, A. Pontes, B. Wardle, S. Sampaio, R. Albuquerque, J. Tavares, and L. Rocha, "Improving Post-EVAR Surveillance with a Smart Stent-Graft", 2012.
[101] T. Duerig, A. Pelton, and D. Stöckel, "An overview of nitinol medical applications", *Materials Science and Engineering: A,* vol. 273-275, pp. 149-160, 1999.
[102] G. Medical. "GORE® CARDIOFORM Septal Occluder", April, 2024; https://www.goremedical.com/products/cardioform/septal-occluder.
[103] B. Scientific. "Zero Tip™ Cestelli per il recupero per le vie respiratorie", April, 2024; https://www.bostonscientific.com/products/IT/it-IT/all-products/pulmonology/airway-retrieval-baskets/zero-tip-/p/FP00000126?pc=M00513200#Prodottocontent-0.
[104] VIREN. "Retrieval Baskets", April, 2024; https://virencorp.com/portfolio/retrieval-baskets/.
[105] T. Habu, "Fabrication of shape memory alloy parts", *Shape Memory Alloys for Biomedical Applications*, pp. 86-100, Cambridge, England: Woodhead Publishing Limited, 2008.
[106] M. Elahinia, N. Shayesteh Moghaddam, M. Taheri Andani, A. Amerinatanzi, B. A. Bimber, and R. F. Hamilton, "Fabrication of NiTi through additive manufacturing: A review", *Progress in Materials Science,* vol. 83, pp. 630-663, 2016.
[107] C. Haberland, and M. H. Elahinia, "Fabricating NiTi SMA Components", *Shape Memory Alloy Actuators: Design, Fabrication, and Experimental Evaluation*, L. John Wiley & Sons, ed., 2016.

[108] Z. Zhang, J. Frenzel, C. Somsen, J. Pesicka, and J. Eggeler, "On the Formation of TiC Crystals during Processing of NiTi Shape Memory Alloys", pp. 71-99, 2005.
[109] J. Frenzel, K. Neuking, G. Eggeler, and C. Haberland, *On the Role of Carbon during Processing of NiTi Shape Memory Alloys*, 2007.
[110] M. V. Nevitt, "Stabilization of certain Ti2Ni-type phases by oxygen", vol. Vol: 218, 1960.
[111] P. Olier, F. Barcelo, J.-L. Béchade, J.-C. Brachet, E. Lefevre, and G. Guenin, "Effects of Impurities Content (Oxygen, Carbon, Nitrogen) on Microstructure and Phase Transformation Temperatures of Near Equiatomic TiNi Shape Memory Alloys", *Journal de Physique IV,* vol. 7, 1997.
[112] D. A. Miller, and D. C. Lagoudas, "Influence of cold work and heat treatment on the shape memory effect and plastic strain development of NiTi", *Materials Science and Engineering: A,* vol. 308, no. 1, pp. 161-175, 2001.
[113] M. Wu, "Fabrication of Nitinol Materials and Components", *Materials Science Forum,* vol. 394, pp. 285-292, 2002.
[114] Y. Suzuki, "Fabrication of shape memory alloys", *Shape Memory Materials*, pp. 133-148, Cambridge, UK: Cambridge University Press, 1998.
[115] C. Grossmann, J. Frenzel, S. Vedamanickam, T. Depka, A. Oppenkowski, C. Somsen, K. Neuking, W. Theisen, and G. Eggeler, "Processing and property assessment of NiTi and NiTiCu shape memory actuator springs", *Materialwissenschaft und Werkstofftechnik,* vol. 39, pp. 499-510, 2008.
[116] M. E. Mitwally, and M. Farag, "Effect of cold work and annealing on the structure and characteristics of NiTi alloy", *Materials Science and Engineering: A,* vol. 519, no. 1, pp. 155-166, 2009.
[117] A. R. Pelton, J. DiCello, and S. Miyazaki, "Optimisation of processing and properties of medical grade Nitinol wire", *Minimally Invasive Therapy and Allied Technologies,* vol. 9, no. 2, pp. 107-118, 2000.
[118] D. E. Hodgson, "Fabrication, heat treatment and joining of nitinol components", in *Proceedings of the International Conference on Shape Memory and Superelastic Technologies*, Pacific Grove, CA, USA, April 30–May 4, 2000, 2001, pp. 11-24.
[119] S. K. Wu, H. C. Lin, and C. C. Chen, "A study on the machinability of a Ti49.6Ni50.4 shape memory alloy", *Materials Letters,* vol. 40, no. 1, pp. 27-32, 1999.
[120] D. Biermann, F. Kahleyss, E. Krebs, and T. Upmeier, "A Study on Micro-Machining Technology for the Machining of NiTi: Five-Axis Micro-Milling and Micro Deep-Hole Drilling", *Journal of Materials Engineering and Performance,* vol. 20, pp. 745-751, 2011.
[121] K. W. Weinert, and V. Petzold, "Micromachining of NiTi shape memory alloys", *Prod Eng,* vol. 13, 2006.
[122] D. Biermann, F. Kahleyss, E. Krebs, and T. Upmeier, "A Study on Micro-Machining Technology for the Machining of NiTi: Five-Axis Micro-Milling and Micro Deep-Hole Drilling", *Journal of Materials Engineering and Performance,* vol. 20, no. 4, pp. 745-751, 2011.
[123] M. Frotscher, F. Kahleyss, T. Simon, D. Biermann, and G. Eggeler, "Achieving Small Structures in Thin NiTi Sheets for Medical Applications with Water Jet and Micro Machining: A Comparison", *Journal of Materials Engineering and Performance,* vol. 20, no. 4, pp. 776-782, 2011.
[124] L. M. Schetky, and M. H. Wu, "Issues in the further development of nitinol properties and processing for medical device applications", pp. 271-276, 2003.

[125] W. Theisen, and A. Schuermann, "Electro discharge machining of nickel–titanium shape memory alloys", *Materials Science and Engineering: A,* vol. 378, no. 1, pp. 200-204, 2004.

[126] D. Stöckel, "Forming nitinol - A challenge", in *New Developments in Forging Technology*, Frankfurt/Main: MAT-INFO-Werkstoff-Informationsgesellschaft mbH, 2001, pp. 119–134.

[127] H. Huang, H. Y. Zheng, and Y. Liu, "Experimental investigations of the machinability of Ni50.6Ti49.4 alloy", *Smart Materials and Structures,* vol. 14, no. 5, pp. S297, 2005.

[128] A. Schüssler, and M. Strobel, "Status and trends of nitinol micromachining techniques", *Proceedings of the International Conference on Shape Memory and Superelastic Technologies, Pacific Grove, CA, USA, May 5–8, 2003*, pp. 135-141, 2003.

[129] M. Frotscher, F. Schreiber, L. Neelakantan, T. Gries, and G. Eggeler, "Processing and Characterization of Braided NiTi Microstents for Medical Applications", *Materialwissenschaft und Werkstofftechnik,* vol. 42, pp. 1002-1012, 2011.

[130] J. Frenzel, E. P. George, A. Dlouhy, C. Somsen, M. F. X. Wagner, and G. Eggeler, "Influence of Ni on martensitic phase transformations in NiTi shape memory alloys", *Acta Materialia,* vol. 58, no. 9, pp. 3444-3458, 2010.

[131] K. Gall, and H. J. Maier, "Cyclic deformation mechanisms in precipitated NiTi shape memory alloys", *Acta Materialia,* vol. 50, no. 18, pp. 4643-4657, 2002.

[132] J. Michutta, C. Somsen, A. Yawny, A. Dlouhy, and G. Eggeler, "Elementary martensitic transformation processes in Ni-rich NiTi single crystals with Ni4Ti3 precipitates", *Acta Materialia,* vol. 54, no. 13, pp. 3525-3542, 2006.

[133] X. Huang, and Y. Liu, "Effect of annealing on the transformation behavior and superelasticity of NiTi shape memory alloy", *Scripta Materialia,* vol. 45, no. 2, pp. 153-160, 2001.

[134] A. Ortega, J. Tyber, C. Frick, K. Gall, and H. Maier, "Cast NiTi Shape-Memory Alloys", *Advanced Engineering Materials,* vol. 7, pp. 492-507, 2005.

[135] S. Miyazaki, S. Kimura, F. Takei, T. Miura, K. Otsuka, and Y. Suzuki, "Shape memory effect and pseudoelasticity in a Ti-Ni single crystal", *Scripta Metallurgica,* vol. 17, no. 9, pp. 1057-1062, 1983.

[136] S. Miyazaki, T. Imai, Y. Igo, and K. Otsuka, "Effect of Cyclic Deformation on the Pseudoelasticity Characteristics of Ti-Ni Alloys", *Metallurgical Transactions A,* vol. 17, pp. 115-120, 1986.

[137] F. Jiang, Y. Liu, H. Yang, L. Li, and Y. Zheng, "Effect of ageing treatment on the deformation behaviour of Ti–50.9 at.% Ni", *Acta Materialia,* vol. 57, no. 16, pp. 4773-4781, 2009.

[138] J. Khalil Allafi, X. Ren, and G. Eggeler, "The mechanism of multistage martensitic transformations in aged Ni-rich NiTi shape memory alloys", *Acta Materialia,* vol. 50, no. 4, pp. 793-803, 2002.

[139] S. Miyazaki, Y. Kohiyama, K. Otsuka, and T. W. Duerig, "Effects of Several Factors on the Ductility of the Ti-Ni Alloy", *Materials Science Forum - MATER SCI FORUM,* vol. 56-58, pp. 765-770, 1990.

[140] J. Khalil-Allafi, G. Eggeler, A. Dlouhy, W. W. Schmahl, and C. Somsen, "On the influence of heterogeneous precipitation on martensitic transformations in a Ni-rich NiTi shape memory alloy", *Materials Science and Engineering: A,* vol. 378, no. 1, pp. 148-151, 2004.

[141] N. Zhou, C. Shen, M. F. X. Wagner, G. Eggeler, M. J. Mills, and Y. Wang, "Effect of Ni4Ti3 precipitation on martensitic transformation in Ti-Ni", *Acta Materialia,* vol. 58, no. 20, pp. 6685-6694, 2010.

[142] A. Dlouhý, O. Bojda, C. Somsen, and G. Eggeler, "Conventional and in-situ transmission electron microscopy investigations into multistage martensitic transformations in Ni-rich NiTi shape memory alloys", *Materials Science and Engineering: A,* vol. 481-482, no. 1-2 C, pp. 409-413, 2008.

[143] M. C. Carroll, C. Somsen, and G. Eggeler, "Multiple-step martensitic transformations in Ni-rich NiTi shape memory alloys", *Scripta Materialia,* vol. 50, no. 2, pp. 187-192, 2004.

[144] G. Fan, W. Chen, S. Yang, J. Zhu, X. Ren, and K. Otsuka, "Origin of abnormal multi-stage martensitic transformation behavior in aged Ni-rich Ti–Ni shape memory alloys", *Acta Materialia,* vol. 52, no. 14, pp. 4351-4362, 2004.

[145] J. M. Components. "Nitinol Shape Setting", April, 2024; https://matthey.com/products-and-markets/other-markets/medical-components/resource-library/nitinol-shape-setting/.

[146] C. Medical. "Nitinol Facts", April, 2024; https://conf.hxmbox.com/tech-center/nitinol-facts/.

[147] S. Shabalovskaya, J. Anderegg, and J. Van Humbeeck, "Critical overview of Nitinol surfaces and their modifications for medical applications", *Acta Biomater,* vol. 4, no. 3, pp. 447-67, May, 2008.

[148] M. Pohl, C. Heßing, and J. Frenzel, "Electrolytic processing of NiTi shape memory alloys", *Materials Science and Engineering: A,* vol. 378, no. 1, pp. 191-199, 2004.

[149] J. F. Decker, C. Trépanier, L. Vien, and A. R. Pelton, "The Effect of Material Removal on the Corrosion Resistance and Biocompatibility of Nitinol Laser-Cut and Wire-Form Products", *Journal of Materials Engineering and Performance,* vol. 20, no. 4, pp. 802-806, 2011.

[150] C. Haberland, M. Elahinia, J. M. Walker, H. Meier, and J. Frenzel, "On the development of high quality NiTi shape memory and pseudoelastic parts by additive manufacturing", *Smart Materials and Structures,* vol. 23, no. 104002, 2014.

[151] G. Coppi, R. Pacchioni, R. Moratto, S. Gennai, G. A. Farello, G. Bergamaschi, C. Rabbia, D. Rossato, F. Ponzio, V. Stancanelli, and E. Piccinini, "Experience with the Stentor endograft at four Italian centers", *Journal of Endovascular Surgery,* vol. 5, no. 3, pp. 206-215, 1998.

[152] A. A. Giannopoulos, D. Mitsouras, S. J. Yoo, P. P. Liu, Y. S. Chatzizisis, and F. J. Rybicki, "Applications of 3D printing in cardiovascular diseases", *Nature Reviews Cardiology,* vol. 13, no. 12, pp. 701-718, 2016.

[153] I. V. Shishkovsky, L. T. Volova, M. V. Kuznetsov, Y. G. Morozov, and I. P. Parkin, "Porous biocompatible implants and tissue scaffolds synthesized by selective laser sintering from Ti and NiTi", *Journal of Materials Chemistry,* vol. 18, no. 12, pp. 1309-1317, 2008.

[154] J. J. Marattukalam, A. K. Singh, S. Datta, M. Das, V. K. Balla, S. Bontha, and S. K. Kalpathy, "Microstructure and corrosion behavior of laser processed NiTi alloy", *Materials Science and Engineering: C,* vol. 57, pp. 309-313, 2015.

[155] H. Ibrahim, A. Jahadakbar, A. Dehghan, N. S. Moghaddam, A. Amerinatanzi, and M. Elahinia, "In Vitro Corrosion Assessment of Additively Manufactured Porous NiTi Structures for Bone Fixation Applications", *Metals,* 8, 2018.

[156] Z. Yu, B. Liu, S. Yu, H. Chi, Z. Wang, H. Yang, Z. Xu, Z. Zhang, Y. Guo, and L. Ren, "Enhancing the surface finish and corrosion resistance of laser powder bed

fusion NiTi surfaces through chemical polishing", *Journal of Materials Research and Technology,* vol. 29, pp. 5507-5516, 2024.

[157] S. Maffia, V. Finazzi, F. Berti, F. Migliavacca, L. Petrini, B. Previtali, and A. G. Demir, "Selective laser melting of NiTi stents with open-cell and variable diameter", *Smart Materials and Structures,* vol. 30, no. 10, 2021.

[158] V. Finazzi, F. Berti, R. J. Guillory, L. Petrini, B. Previtali, and A. G. Demir, "Patient-specific cardiovascular superelastic NiTi stents produced by laser powder bed fusion", *Procedia CIRP*, vol. 110, pp. 244-248, 2022.

[159] S. V. Chernyshikhin, I. A. Pelevin, F. Karimi, and I. V. Shishkovsky, "The Study on Resolution Factors of LPBF Technology for Manufacturing Superelastic NiTi Endodontic Files", *Materials,* vol. 15, no. 19, 2022.

[160] L. Yan, S. L. Soh, N. Wang, Q. Ma, W. F. Lu, S. T. Dheen, A. S. Kumar, and J. Y. H. Fuh, "Evaluation and characterization of nitinol stents produced by selective laser melting with various process parameters", *Progress in Additive Manufacturing,* vol. 7, no. 6, pp. 1141-1153, 2022.

[161] P. Jamshidi, C. Panwisawas, E. Langi, S. C. Cox, J. Feng, L. Zhao, and M. M. Attallah, "Development, characterisation, and modelling of processability of nitinol stents using laser powder bed fusion", *Journal of Alloys and Compounds,* vol. 909, 2022.

[162] E. Farber, J. N. Zhu, A. Popovich, and V. Popovich, "A review of NiTi shape memory alloy as a smart material produced by additive manufacturing", *Materials Today: Proceedings*, vol. 30, pp. 761-767, 2020.

[163] J. C. Chekotu, R. Groarke, K. O'Toole, and D. Brabazon, "Advances in selective laser melting of Nitinol shape memory alloy part production", *Materials,* vol. 12, no. 5, 2019.

[164] P. R. Halani, I. Kaya, Y. C. Shin, and H. E. Karaca, "Phase transformation characteristics and mechanical characterization of nitinol synthesized by laser direct deposition", *Materials Science and Engineering A,* vol. 559, pp. 836-843, 2013.

[165] J. Lee, and Y. C. Shin, "Effects of Composition and Post Heat Treatment on Shape Memory Characteristics and Mechanical Properties for Laser Direct Deposited Nitinol", *Lasers in Manufacturing and Materials Processing,* vol. 6, no. 1, pp. 41-58, 2019.

[166] J. Dutkiewicz, Ł. Rogal, D. Kalita, M. Węglowski, S. Błacha, K. Berent, T. Czeppe, A. Antolak-Dudka, T. Durejko, and T. Czujko, "Superelastic Effect in NiTi Alloys Manufactured Using Electron Beam and Focused Laser Rapid Manufacturing Methods", *Journal of Materials Engineering and Performance,* vol. 29, no. 7, pp. 4463-4473, 2020.

[167] B. Lu, X. Cui, M. Dong, W. Ma, and G. Jin, "The Influence of Solution Treatments on the Microstructure, Phase Transformation Behavior, and Superelastic Characteristics of Nitinol Synthesized by Plasma Arc Deposition", *Journal of Materials Engineering and Performance,* vol. 29, no. 4, pp. 2491-2498, 2020.

[168] S. Saedi, A. S. Turabi, M. T. Andani, C. Haberland, H. Karaca, and M. Elahinia, "The influence of heat treatment on the thermomechanical response of Ni-rich NiTi alloys manufactured by selective laser melting", *Journal of Alloys and Compounds,* vol. 677, pp. 204-210, 2016.

[169] S. Saedi, A. S. Turabi, M. T. Andani, N. S. Moghaddam, M. Elahinia, and H. E. Karaca, "Texture, aging, and superelasticity of selective laser melting fabricated Ni-rich NiTi alloys", *Materials Science and Engineering A,* vol. 686, pp. 1-10, 2017.

[170] S. Saedi, N. Shayesteh Moghaddam, A. Amerinatanzi, M. Elahinia, and H. E. Karaca, "On the effects of selective laser melting process parameters on microstructure and

thermomechanical response of Ni-rich NiTi", *Acta Materialia,* vol. 144, pp. 552-560, 2018.

[171] K. Khanlari, Q. Shi, K. Li, K. Hu, P. Cao, and X. Liu, "Effects of printing volumetric energy densities and post-processing treatments on the microstructural properties, phase transformation temperatures and hardness of near-equiatomic NiTinol parts fabricated by a laser powder bed fusion technique", *Intermetallics,* vol. 131, 2021.

[172] G. Carlucci, L. Patriarca, A. G. Demir, J. N. Lemke, A. Coda, B. Previtali, and R. Casati, "Building Orientation and Heat Treatments Effect on the Pseudoelastic Properties of NiTi Produced by LPBF", *Shape Memory and Superelasticity,* vol. 8, no. 3, pp. 235-247, 2022.

[173] Z. X. Khoo, Y. Liu, J. An, C. K. Chua, Y. F. Shen, and C. N. Kuo, "A Review of Selective Laser Melted NiTi Shape Memory Alloy", *Materials,* vol. 11, no. 4, 2018.

[174] S. Saedi, A. S. Turabi, M. T. Andani, C. Haberland, M. Elahinia, and H. Karaca, "Thermomechanical characterization of Ni-rich NiTi fabricated by selective laser melting", *Smart Materials and Structures,* vol. 25, no. 3, 2016.

[175] M. A. Obeidi, M. Monu, C. Hughes, D. Bourke, M. N. Dogu, J. Francis, M. Zhang, I. U. Ahad, and D. Brabazon, "Laser beam powder bed fusion of nitinol shape memory alloy (SMA)", *Journal of Materials Research and Technology,* vol. 14, pp. 2554-2570, 2021.

[176] M. B. Abrami, M. Tocci, D. Brabazon, M. Cabibbo, and A. Pola, "Effects of Direct Aging Heat Treatments on the Superelasticity of Nitinol Produced via Laser Powder Bed Fusion", *Metallurgical and Materials Transactions A*, 2024.

[177] A. Undisz, K. Reuther, H. Reuther, and M. Rettenmayr, "Occurrence and origin of non-martensitic acicular artifacts on NiTi", *Acta Materialia,* vol. 59, no. 1, pp. 216-224, 2011.

[178] X. Zhang, and H. Sehitoglu, "Crystallography of the B2 → R → B19′ phase transformations in NiTi", *Materials Science and Engineering: A,* vol. 374, no. 1-2, pp. 292-302, 2004.

[179] K. Khanlari, M. Ramezani, P. Kelly, P. Cao, and T. Neitzert, "Mechanical and microstructural characteristics of as-sintered and solutionized porous 60NiTi", *Intermetallics,* vol. 100, pp. 32-43, 2018.

[180] X. Ren, N. Miura, J. Zhang, K. Otsuka, K. Tanaka, M. Koiwa, T. Suzuki, Y. I. Chumlyakov, and M. Asai, "A comparative study of elastic constants of Ti-Ni based alloys prior to martensitic transformation", *Materials Science and Engineering: A,* vol. 312, no. 1-2, pp. 196-206, 2001.

[181] Y. Zheng, F. Jiang, L. Li, H. Yang, and Y. Liu, "Effect of ageing treatment on the transformation behaviour of Ti-50.9 at.% Ni alloy", *Acta Materialia,* vol. 56, no. 4, pp. 736-745, 2008.

[182] K. Kazemi-Choobi, J. Khalil-Allafi, and V. Abbasi-Chianeh, "Influence of recrystallization and subsequent aging treatment on superelastic behavior and martensitic transformation of Ni50.9Ti wires", *Journal of Alloys and Compounds,* vol. 582, pp. 348-354, 2014.

[183] E. Henderson, D. H. Nash, and W. M. Dempster, "On the experimental testing of fine Nitinol wires for medical devices", *Journal of the Mechanical Behavior of Biomedical Materials,* vol. 4, no. 3, pp. 261-268, 2011.

[184] H. Sitepu, "Texture and structural refinement using neutron diffraction data from molybdite (MoO3) and calcite (CaCO3) powders and a Ni-rich Ni50.7Ti49.30 alloy", *Powder Diffraction,* vol. 24, no. 4, pp. 315-326, 2009.

[185] A. Chmielewska, B. Wysocki, P. Kwaśniak, M. J. Kruszewski, B. Michalski, A. Zielińska, B. Adamczyk-Cieślak, A. Krawczyńska, J. Buhagiar, and W.

Święszkowski, “Heat Treatment of NiTi Alloys Fabricated Using Laser Powder Bed Fusion (LPBF) from Elementally Blended Powders”, *Materials,* vol. 15, no. 9, 2022.

[186] Y. Kudoh, M. Tokonami, S. Miyazaki, and K. Otsuka, “Crystal structure of the martensite in Ti-49.2 at.%Ni alloy analyzed by the single crystal X-ray diffraction method”, *Acta Metallurgica,* vol. 33, no. 11, pp. 2049-2056, 1985.

[187] B. Bertheville, M. Neudenberger, and J. E. Bidaux, “Powder sintering and shape-memory behaviour of NiTi compacts synthesized from Ni and TiH2”, *Materials Science and Engineering: A,* vol. 384, no. 1, pp. 143-150, 2004.

[188] J. C. Hey, and A. P. Jardine, “Shape memory TiNi synthesis from elemental powders”, *Materials Science and Engineering: A,* vol. 188, no. 1, pp. 291-300, 1994.

[189] B.-Y. Li, L.-J. Rong, X.-H. Luo, and Y.-Y. Li, “Transformation behavior of sintered porous NiTi alloys”, *Metallurgical and Materials Transactions A,* vol. 30, no. 11, pp. 2753-2756, 1999.

[190] S. M. Green, D. M. Grant, and N. R. Kelly, “Powder metallurgical processing of Ni-Ti shape memory alloy”, *Powder Metallurgy,* vol. 40, no. 1, pp. 43-47, 1997.

[191] M. Neikter, A. Huang, and X. Wu, “Microstructural characterization of binary microstructure pattern in selective laser-melted Ti-6Al-4V”, *International Journal of Advanced Manufacturing Technology,* vol. 104, no. 1-4, pp. 1381-1391, 2019.

[192] T. Bormann, B. Müller, M. Schinhammer, A. Kessler, P. Thalmann, and M. de Wild, “Microstructure of selective laser melted nickel–titanium”, *Materials Characterization,* vol. 94, pp. 189-202, 2014.

[193] L. Xue, K. C. Atli, S. Picak, C. Zhang, B. Zhang, A. Elwany, R. Arroyave, and I. Karaman, “Controlling martensitic transformation characteristics in defect-free NiTi shape memory alloys fabricated using laser powder bed fusion and a process optimization framework”, *Acta Materialia,* vol. 215, 2021.

[194] S. Ehsan Saghaian, M. Nematollahi, G. Toker, A. Hinojos, N. Shayesteh Moghaddam, S. Saedi, C. Y. Lu, M. Javad Mahtabi, M. J. Mills, M. Elahinia, and H. E. Karaca, “Effect of hatch spacing and laser power on microstructure, texture, and thermomechanical properties of laser powder bed fusion (L-PBF) additively manufactured NiTi”, *Optics and Laser Technology,* vol. 149, 2022.

[195] N. Shayesteh Moghaddam, S. Saedi, A. Amerinatanzi, A. Hinojos, A. Ramazani, J. Kundin, M. J. Mills, H. Karaca, and M. Elahinia, “Achieving superelasticity in additively manufactured NiTi in compression without post-process heat treatment”, *Scientific Reports,* vol. 9, no. 1, 2019.

[196] M. Zamani, M. Kadkhodaei, M. Badrossamay, and E. Foroozmehr, “Adjustment of the scan track spacing and linear input energy to fabricate dense, pseudoelastic Nitinol shape memory alloy parts by selective laser melting”, *Journal of Intelligent Material Systems and Structures*, 2021.

[197] J. N. Zhu, E. Borisov, X. Liang, R. Huizenga, A. Popovich, V. Bliznuk, R. Petrov, M. Hermans, and V. Popovich, “Controlling microstructure evolution and phase transformation behavior in additive manufacturing of nitinol shape memory alloys by tuning hatch distance”, *Journal of Materials Science,* vol. 57, no. 10, pp. 6066-6084, 2022.

[198] A. Poudel, M. S. Yasin, J. Ye, J. Liu, A. Vinel, S. Shao, and N. Shamsaei, “Feature-based volumetric defect classification in metal additive manufacturing”, *Nature Communications,* vol. 13, no. 1, 2022.

[199] A. S. Turabi, S. Saedi, S. M. Saghaian, H. E. Karaca, and M. H. Elahinia, "Experimental Characterization of Shape Memory Alloys”, *Shape Memory Alloy Actuators: Design, Fabrication and Experimental Evaluation*, pp. 239-277, 2015.

[200] Y. Liu, Y. Liu, and J. Humbeeck, "Lüders-like deformation associated with martensite reorientation in NiTi", *Scripta Materialia,* vol. 39, no. 8, pp. 1047-1055, 1998.

[201] Y. Liu, Z. Xie, J. Van Humbeeck, and L. Delaey, "Some results on the detwinning process in NiTi shape memory alloys", *Scripta Materialia,* vol. 41, no. 12, pp. 1273-1281, 1999.

[202] P. Chowdhury, L. Patriarca, G. Ren, and H. Sehitoglu, "Molecular dynamics modeling of NiTi superelasticity in presence of nanoprecipitates", *International Journal of Plasticity,* vol. 81, pp. 152-167, 2016.

[203] R. R. Adharapurapu, and K. S. Vecchio, "Superelasticity in a new bioImplant material: Ni-rich 55NiTi alloy", *Experimental Mechanics,* vol. 47, no. 3, pp. 365-371, 2007.

[204] S. Nemat-Nasser, and W. G. Guo, "Superelastic and cyclic response of NiTi SMA at various strain rates and temperatures", *Mechanics of Materials,* vol. 38, no. 5-6, pp. 463-474, 2006.

[205] M. Nishida, C. M. Wayman, R. Kainuma, and T. Honma, "Further electron microscopy studies of the Ti11 Ni14 phase in an aged Ti52at%Ni shape memory alloy", *Scripta Metallurgica,* vol. 20, no. 6, pp. 899-904, 1986.

[206] M. Nishida, and C. M. Wayman, "Electron microscopy studies of precipitation processes in near-equiatomic TiNi shape memory alloys", *Materials Science and Engineering,* vol. 93, no. C, pp. 191-203, 1987.

[207] B. Chad Hornbuckle, X. X. Yu, R. D. Noebe, R. Martens, M. L. Weaver, and G. B. Thompson, "Hardening behavior and phase decomposition in very Ni-rich Nitinol alloys", *Materials Science and Engineering: A,* vol. 639, pp. 336-344, 2015.

[208] W. H. Zou, X. D. Han, R. Wang, Z. Zhang, W. Z. Zhang, and J. K. L. Lai, "TEM and HREM study of the interphase interface structure of Ti3Ni4 precipitates and parent phase in an aged TiNi shape memory alloy", *Materials Science and Engineering: A,* vol. 219, no. 1-2, pp. 142-147, 1996.

[209] H. E. Karaca, S. M. Saghaian, G. Ded, H. Tobe, B. Basaran, H. J. Maier, R. D. Noebe, and Y. I. Chumlyakov, "Effects of nanoprecipitation on the shape memory and material properties of an Ni-rich NiTiHf high temperature shape memory alloy", *Acta Materialia,* vol. 61, no. 19, pp. 7422-7431, 2013.

[210] X. Huang, J. Nohava, B. Zhang, and A. G. Ramirez, "Nanoindentation of NiTi shape memory thin films at elevated temperatures", *International Journal of Smart and Nano Materials,* vol. 2, no. 1, pp. 39-49, 2011.

[211] K. Gall, K. Juntunen, H. J. Maier, H. Sehitoglu, and Y. I. Chumlyakov, "Instrumented micro-indentation of NiTi shape-memory alloys", *Acta Materialia,* vol. 49, no. 16, pp. 3205-3217, 2001.

[212] M. J. Mahtabi, A. Yadollahi, M. Rahmati, and T. W. Stone, "Correlation Between Hardness and Loading Transformation Stress of Superelastic NiTi", *Arabian Journal for Science and Engineering,* vol. 43, no. 9, pp. 5029-5033, 2018.

[213] J. Mentz, M. Bram, H. P. Buchkremer, and D. Stöver, "Influence of heat treatments on the mechanical properties of high-quality Ni-rich NiTi produced by powder metallurgical methods", *Materials Science and Engineering: A,* vol. 481-482, no. 1-2 C, pp. 630-634, 2008.

[214] M. B. Abrami, M. Tocci, K. Tamilselvam, D. Brabazon, and A. Pola, "Effect of Heat Treatments on Microstructure and Mechanical Properties of Nitinol Prototype Stents Produced by Laser Powder Bed Fusion", *Key Engineering Materials,* vol. 967, pp. 143-149, 2023.

[215] "ISO 25539-2 Cardiovascular implants - Endovascular devices - Part 2: Vascular stents", *Cardiovascular implants - Endovascular devices - Part 2: Vascular stents*, 2021.

[216] J. A. Shaw, C. B. Churchill, and M. A. Iadicola, "Tips and tricks for characterizing shape memory alloy wire: Part 1-differential scanning calorimetry and basic phenomena", *Experimental Techniques,* vol. 32, no. 5, pp. 55-62, 2008.

[217] A. Baran, and M. Polanski, "Microstructure and properties of LENS (laser engineered net shaping) manufactured Ni-Ti shape memory alloy", *Journal of Alloys and Compounds,* vol. 750, pp. 863-870, 2018.

[218] D. B. Chernov, Y. I. Paskal, V. E. Gyunter, L. A. Monasevich, and E. M. Savitskii, "The Multiplicity of Structural Transitions in Alloy Based on TiNi", *Doklady Akademii Nauk SSSR,* vol. 247, pp. 854-857, 1979.

[219] C. Della Corte, and G. Glennon, *Ball Bearings Comprising Nickel-Titanium and Methods of Manufacturing Thereof*, 2012.

[220] C. Brandt-Wunderlich, W. Schmidt, N. Grabow, M. Stiehm, S. Siewert, R. Andresen, and K. P. Schmitz, "Support function of self-expanding nitinol stents - Are radial resistive force and crush resistance comparable?", *Current Directions in Biomedical Engineering,* vol. 5, no. 1, pp. 465-467, 2019.

[221] G. P. Kumar, K. Zuo, L. B. Koh, C. W. Ong, Y. Zhong, H. L. Leo, P. Ho, and F. Cui, "Effect of number of crowns on the crush resistance in open-cell stent design", *Journal of Mechanics of Materials and Structures,* vol. 15, no. 1, pp. 75-86, 2020.

[222] D. Dabir, A. Feisst, D. Thomas, J. A. Luetkens, C. Meyer, A. Kardulovic, M. Menne, U. Steinseifer, H. H. Schild, and D. L. R. Kuetting, "Physical Properties of Venous Stents: An Experimental Comparison", *CardioVascular and Interventional Radiology,* vol. 41, no. 6, pp. 942-950, 2018.